

University of Nevada, Reno

**The Geology, Alteration, and Mineralization of the True North Gold Deposit,  
Fairbanks, Alaska**

A dissertation submitted in partial fulfillment of the  
requirements of the degree of Doctor of Philosophy in  
Geology

by

Keith B. Campbell

Dr. Tommy B. Thompson/Dissertation Advisor

December, 2006

UMI Number: 3239880

### INFORMATION TO USERS

The quality of this reproduction is dependent upon the quality of the copy submitted. Broken or indistinct print, colored or poor quality illustrations and photographs, print bleed-through, substandard margins, and improper alignment can adversely affect reproduction.

In the unlikely event that the author did not send a complete manuscript and there are missing pages, these will be noted. Also, if unauthorized copyright material had to be removed, a note will indicate the deletion.

**UMI**<sup>®</sup>

---

UMI Microform 3239880

Copyright 2007 by ProQuest Information and Learning Company.

All rights reserved. This microform edition is protected against unauthorized copying under Title 17, United States Code.

ProQuest Information and Learning Company  
300 North Zeeb Road  
P.O. Box 1346  
Ann Arbor, MI 48106-1346

We recommend that the dissertation  
prepared under our supervision by

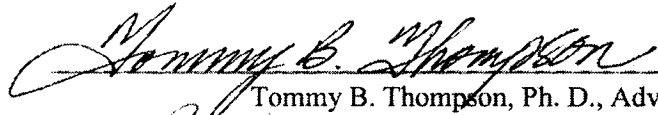
**KEITH BRYAN CAMPBELL**

entitled

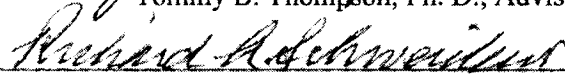
The Geology, Alteration, and Mineralization of the True North Gold Deposit, Fairbanks  
District, Alaska

Be accepted in partial fulfillment of the  
requirements for the degree of

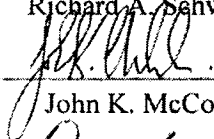
**DOCTOR OF PHILOSOPHY**



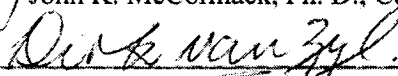
Tommy B. Thompson, Ph. D., Advisor



Richard A. Schweickert, Ph. D., Committee Member



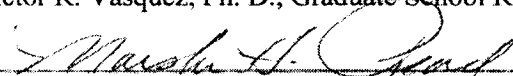
John K. McCormack, Ph. D., Committee Member



Dirk J. A. van Zyl, Ph. D., Committee Member



Victor R. Vasquez, Ph. D., Graduate School Representative



Marsha H. Reed, Ph. D. Associate Dean, Graduate School

December, 2006

## ABSTRACT

The True North gold deposit is a unique epithermal system, hosted in a klippe of eclogite grade metasediments (Chatanika terrane) that rests on the Fairbanks schist about 28 km northeast of Fairbanks, Alaska. Host rocks are predominately biotite to quartz-biotite schist, locally graphitic, in the Hindenberg Pit (northeastern part of the deposit) and graphitic slate-argillite in the Shepard Pit (southwestern part of the deposit). Mineralization associated with the intrusion of the Pedro Dome stock (Gilmore Dome intrusive complex) at ~92 Ma and is localized within two set of faults. A low-angle fault set is sub-parallel to and related to thrust faults that emplaced the Chatanika sub-Terrane over the Fairbanks Schist. Mineralized high angle faults include faults sub-parallel to and related to district scale northeast-trending left lateral oblique-slip faults, and several north to north-east striking faults. All mineralized faults have tens of centimeters to meters of graphitic gouge with a well-developed planar, anastomosing fabric concentrated along slip planes with evidence of multiple stages of movement. The graphite is physically remobilized from graphitic host rocks.

Mineralization consists of multiple generations of quartz-gold-arsenopyrite- pyrite veins and several generations of carbonate veins occurring within the fault zones. Carbonate veining locally extends out into relatively unaltered host rocks for several tens of meters. Veins are crushed and dismembered within the fault zones by repeated fault movement, and intact veins are only rarely preserved. Alteration consists of a halo of fuchsite-ankerite-arsenopyrite and pyrite around veins. Where veins are closely spaced, or veins intersect host rock foliation at high angles, large volumes of rock are altered.

Quartz fluid inclusion mean homogenization temperatures, pressure corrected for an estimated 1km formation depth, are 240°C for Hindenberg Pit veins (biotite schist host rocks) and 270°C for Shepard Pit veins (slate-argillite host rocks). Quartz inclusion fluids are dilute, ~4 weight percent NaCl equivalent, with as much as 3 mole percent CO<sub>2</sub>. Carbon and oxygen isotopic data suggests that the fluid source was either igneous or groundwater isotopically equilibrated with the host rocks and that carbonate veins were precipitated in equilibrium with graphite in the faults that contain the veins.

## ACKNOWLEDGEMENTS

This project would not have been possible without support from Dr. Tommy Thompson, the Ralph J. Roberts Center for Research in Economic Geology (CREG), Ted Wilton, and Kinross Gold Corporation. The faculty and staff at the University of Nevada, Reno Department of geology provided a great deal of support and assistance, in particular Dr. Richard Schweikert for helping me begin to understand the history and assembly of the North American Cordillera, Dr. Greg Arhert for help in understanding isotopic systems, Dr. Jim Carr who assisted by specially modifying his statistical programs and helped with interpreting the results, and Dr. John McCormack who helped me see really small aspects of the deposit. Dr. Simon Poulson (Nevada Stable Isotope Laboratory), Dr. Terry Spell (University of Nevada, Las Vegas Geochronology Laboratory), and Rich Goldfarb (USGS) all provided invaluable assistance and discussion.

No research project of this type and magnitude is the work of a single person and nowhere is that more true than at a producing deposit. The geologic work contained herein stands on the shoulders of the many geologists who worked in the True North area of the Fairbanks District, Alaska, as well as the companies for whom they worked. The 'Exploration History Section' was originally conceived as a way to acknowledge the many people and companies who have worked on or had a hand in working out the geology of the gold deposit at True North and whom have yet to have their story well and accurately told. However, time, distance, and the births, deaths, and merging of companies and the subsequent movement of people have made that goal impossible. However the lack of an individual or company in this list does not imply that a person or

company did not contribute, only that the author failed to find mention of them in the reports available to him.

Among those to whom I owe a personal thanks (at least!) are Bob Morrell (who saw True North from exploration to production, AMAX to Kinross); John Woodman (Project geologist for True North through 2004) who spent endless hours discussing True North with me; Paul Jensen (former True North Mine Geologist) whose ideas kept me on my toes; Paul Buisseret (former Kinross geologist) who shared with me what it was like to drill into the True North deposit and try and figure out the lithologies and structure (from chips and core); Larry Snider (former Kinross geologic and ore reserve modeler) who showed me through the True North 3D model and helped me see how things fit together; John Galey, who worked for AMAX and was involved in the early exploration effort (1990-1993) and who generously took his valuable time to put together a history for the years he was involved; Randy Vance, who was with Newmont while they had True North and Richard Harris, who worked with Newmont and Kinross, both of whom assisted with discussions and providing historical materials and information; Richard Swainbank who kindly took time to discuss his work on the eclogite facies rocks and his past and continuing ideas about the Chatinika Terrane; Bill Duncan (former AMAX to Kinross Exploration Geologist) who shared a house and many, many ideas with me during my first summer in Alaska; and Dave Emmons (former Kinross Exploration Geologist) who shared an apartment and his geologic experience during my second summer in Alaska. Because many (most?) of the reports by the people who worked on the discovery and development of True North are not available, the names and work done

by many geologists can not be recorded nor directly acknowledged here. This in no way lessens their contributions. Thank you to all of you as well.

Thanks go to all those with whom I had conversations and for whom I made attempts at explanations of ideas and concepts, all of the Kinross geologists in Alaska, graduate students at UNR and at various conferences, and many mining and exploration geologists at Geologic Society of Nevada and CREG meetings, you all helped clarify and refine my ideas about True North and helped eliminate inconsistencies.

A huge thank you goes to my family. To Soraya for putting up with being hauled away from her home in the tropics and into the desert, my late nights on campus, and all of the struggle that comes from doing a project of this scale. To my parents, an even bigger thank you, for support, encouragement, and the occasional push.



**TABLE OF CONTENTS**

<b>Abstract</b>	<b>i</b>
<b>Acknowledgements</b>	<b>iii</b>
<b>Table of Contents</b>	<b>vi</b>
<b>List of Tables</b>	<b>x</b>
<b>List of Figures</b>	<b>xi</b>
<b>INTRODUCTION</b>	<b>1</b>
<b>TECTONIC SETTING</b>	<b>2</b>
<b>Physical Setting</b>	<b>2</b>
<b>The North American Continental Margin</b>	<b>4</b>
<b>The Yukon-Tanana Composite Terrane</b>	<b>9</b>
<b>DISTRICT GEOLOGY</b>	<b>14</b>
<b>District Exploration History</b>	<b>17</b>
<b>True North Property</b>	<b>17</b>

<b>MAPPABLE LITHOLOGIC UNITS AT TRUE NORTH</b>	<b>22</b>
<b>Introduction</b>	<b>22</b>
<b>The Physical and Mineralogical Aspects of Biotite Weathering</b>	<b>25</b>
<b>Characterization of Biotite Weathering at True North</b>	<b>31</b>
<b>Summary of Schists and Definition of Map Units</b>	<b>41</b>
<b>DESCRIPTIONS OF MAP UNITS</b>	<b>47</b>
<b>Lithologic Units</b>	<b>47</b>
<b>Slate-Argillite Unit</b>	<b>47</b>
<b>Eclogite</b>	<b>50</b>
<b>Actinolite Schist</b>	<b>54</b>
<b>Marble</b>	<b>54</b>
<b>Biotite Schist</b>	<b>58</b>
<b>Graphitic Biotite Schist</b>	<b>62</b>
<b>White Mica Schist</b>	<b>62</b>
<b>Amphibolite (Amphibole Biotite Schist)</b>	<b>66</b>
<b>Distribution of Units</b>	<b>66</b>
<b>STRUCTURE</b>	<b>68</b>
<b>Metamorphic Foliation and Folds</b>	<b>68</b>
<b>Faults</b>	<b>74</b>

<b>VEINS</b>	<b>77</b>
<b>Paragenesis</b>	<b>81</b>
<b>Quartz-sulfide Vein Paragenesis</b>	<b>84</b>
<b>Fluid Inclusions</b>	<b>89</b>
<b>ALTERATION</b>	<b>96</b>
<b>STRUCTURE, VEINING AND GOLD GRADES</b>	<b>104</b>
<b>STABLE ISOTOPE DATA</b>	<b>107</b>
<b>Carbonate <math>\delta^{13}\text{C}</math> and <math>\delta^{18}\text{O}</math> Values</b>	<b>107</b>
<b>Interpretation</b>	<b>110</b>
<b>Calcite-Graphite Geothermometer</b>	<b>112</b>
<b>Oxygen Isotope Values for Carbonate Precipitating Waters</b>	<b>113</b>
<b>Carbon Isotopes of Graphite</b>	<b>115</b>
<b>Sulfur Isotopes</b>	<b>117</b>
<b>GEOCHRONOLOGY</b>	<b>117</b>
<b>Review of Data Available From Previous Work</b>	<b>117</b>
<b>Dates Generated in This Study</b>	<b>119</b>
<b>Interpretation</b>	<b>121</b>
<b>MULTI-ELEMENT GEOCHEMISTRY</b>	<b>123</b>

<b>CONCLUSIONS</b>	<b>142</b>
<b>Summary and Interpretation of Regional Tectonic Setting</b>	<b>146</b>
<b>Summary and Interpretation of the True North Gold Deposit</b>	<b>146</b>
<b>Deposit Model</b>	<b>150</b>
<b>Suggestions for Further Work</b>	<b>151</b>
<b>REFERENCES CITED</b>	<b>152</b>
<b>APPENDIX A: X-Ray Data</b>	<b>158</b>
<b>Part 1: Comparison Patterns</b>	<b>159</b>
<b>Part 2: Biotite (phlogopite) Weathering</b>	<b>172</b>
<b>Part 3: Alteration</b>	<b>184</b>
<b>Part 4: Amphibolite</b>	<b>213</b>
<b>APPENDIX B: Petrographic Summary</b>	<b>217</b>
<b>APPENDIX C: Stable Isotope Data Tables</b>	<b>225</b>
<b>APPENDIX D: Age Dates and Argon Release Data</b>	<b>229</b>
<b>APPENDIX E: Geochemical Data</b>	<b>236</b>
<b>APPENDIX F: SEM and EDX Data</b>	<b>252</b>

**LIST OF TABLES**

<b>Table 1. Weathering Stages of Biotite to Kaolinite or Gibbsite (from Wilson, 1966).</b>	<b>28</b>
--	-----------

## LIST OF FIGURES

<b>Figure 1. Location map and regional geologic map of central Alaska and part of the Yukon. Showing locations of geologic units and features. After Dusel-Bacon et al. (2006).</b>	<b>3</b>
<b>Figure 2. Reconstruction of the offset of the Charley River fold and thrust belt by the Tintina and Kaltag faults. After Dover (1994) and Foster and Keith (1994).</b>	<b>5</b>
<b>Figure 3. Map of parts of Alaska, Yukon Territory, and British Columbia. Shows the Yukon-Tanana (YTT), bounding faults, assemblages within the YTT including eclogite/blueschist occurrences, and reference political boundaries and cities. The explanation is on the following page. After Nelson et al. (2006) and Dover (1994).</b>	<b>6</b>
<b>Figure 3a. Explanation for Figures 3 and 4. After Nelson et al. (2006).</b>	<b>7</b>
<b>Figure 4. Map showing the same area as Figure 4 after restoration of ~425 km of movement on the Tintina fault. Same units as Figure 4. Dotted red line is inferred suture between N. America and YTT. After Nelson et al. (2006) and Dover (1994).</b>	<b>8</b>
<b>Figure 5. Tectonic assemblages for the Yukon-Tanana terrane, CO<sub>3</sub> is carbonate, BAB is Back-Arc-Basin. From Colpron et al., 2006.</b>	<b>11</b>
<b>Figure 6. Geologic sketch map of part of the Fairbanks district. After Newberry et al., 1996.</b>	<b>15</b>
<b>Figure 7. Map of True North showing geology, area names, and key geographic names.</b>	<b>18</b>
<b>Figure 8. Kinross (2002) lithologic units and descriptions (Note: CBX= calcareous breccia).</b>	<b>23</b>
<b>Figure 6. Sample site for the XRD samples. On the right is unweathered biotite schist, center and to the left, is variably weathered biotite schist (Hindenberg Pit 1340 bench).</b>	<b>26</b>
<b>Figure 10. TEM images of biotite-vermiculite. A) Showing the layer spacing. 10Å layers are biotite, 14Å layers are vermiculite. B) Showing the interlayering of biotite and vermiculite. B= biotite, V= vermiculite (from Banfield and Eggleton, 1988).</b>	<b>29</b>
<b>Figure 11. TEM image showing gradual change from biotite, left, to vermiculite, right. The layer spacing changes from 10Å to 14Å as biotite converts to vermiculite. (from Banfield and Eggleton, 1988).</b>	<b>30</b>
<b>Figure 12. Diagrammatic illustration of biotite converting to vermiculite, showing relationship between fronts of vermiculite and the biotite being replaced, B= biotite, V= vermiculite. (from Banfield and Eggleton, 1988).</b>	<b>30</b>
<b>Figure 13. A) TEM image of packets of 7Å kaolinite sheets parallel to biotite layers. B) Showing Goethite, halloysite, and kaolinite from biotite (from Banfield and Eggleton, 1988).</b>	<b>32</b>

<b>Figure 14. Fresh, fine-grained biotite (phlogopite)-quartz schist. Top photo is natural surface, lower photo is sawed surface.</b>	<b>35</b>
<b>Figure 15. Powder diffraction pattern for sample 200703-2, unweathered biotite schist.</b>	<b>36</b>
<b>Figure 16. X-ray powder diffraction pattern for sample 200703-1, weakly weathered biotite schist.</b>	<b>37</b>
<b>Figure 17. Weakly weathered biotite schist, sample 200703-1.</b>	<b>38</b>
<b>Figure 18. Weakly weathered biotite schist, with vermiculite. Sample 040903-3</b>	<b>38</b>
<b>Figure 19. X-ray powder diffraction pattern for sample 040903-3, weakly weathered biotite schist with vermiculite.</b>	<b>39</b>
<b>Figure 20. X-ray powder diffraction pattern for sample 060802-3, muscovite schist.</b>	<b>40</b>
<b>Figure 21. Muscovite schist, sample 060802-3.</b>	<b>43</b>
<b>Figure 22. Coarse-grained muscovite schist (white mica schist), sample 260802-2</b>	<b>43</b>
<b>Figure 23. X-ray powder diffraction pattern for sample 260802-2 coarse-grained muscovite schist (white mica schist).</b>	<b>44</b>
<b>Figure 24. Photomicrograph of biotite-garnet schist sample 270802-2a. Top photo is crossed polars. Bottom is plane polarized light. Field of view is 1.33 mm. At lower left is a fragmented garnet. The phlogopite is non-pleochroic, and almost colorless.</b>	<b>45</b>
<b>Figure 25. 'white mica schist' (260802-1) Top photo is hand specimen. Lower is a photomicrograph in plane light, field of view of 2mm, showing the lack of color and iron-oxides/hydroxides between mica layers.</b>	<b>46</b>
<b>Figure 26. Shepard pit, 1300 bench: photo of slate-argillite, looking west. Bench height is 20'.</b>	<b>48</b>
<b>Figure 27. Detail of slate-argillite, 1300 bench, Shepard pit. Hammer is 32" tall.</b>	<b>48</b>
<b>Figure 28. Slate-argillite hand specimen.</b>	<b>49</b>
<b>Figure 29. Photomicrograph of slate-argillite, plane light 2mm field of view.</b>	<b>49</b>
<b>Figure 30. Eclogite, Hindenberg 1420 bench looking north. Top shows eclogite pod in core of recumbent isoclinal fold, hammer is 32" in length. Lower photo shows detail of surface textures.</b>	<b>51</b>
<b>Figure 31. Hand specimen of eclogite. Top photo is broken surface, lower photo shows sawed surface showing large pink garnets and groundmass of chlorite, pyroxene, amphibole, calcite, and albite.</b>	<b>52</b>
<b>Figure 32. Photomicrographs of sample EG-1 (same as previous figure). Shows garnet, amphibole, calcite, mica, and iron oxides. Field of view is 1.33 mm. Upper photo in crossed Nicols, lower photo in plane light.</b>	<b>53</b>

<b>Figure 33. Actinolite schist, sample 230903-5.</b>	<b>55</b>
<b>Figure 34. Photomicrograph of actinolite schist showing fine-grained actinolite and carbonate, crossed Nicols, 2 mm field of view. Same sample as above.</b>	<b>55</b>
<b>Figure 35. Marble, 1340 bench, Shepard pit. 20' bench height. The marble is the blocky material cropping out on the left side of the photo.</b>	<b>56</b>
<b>Figure 36. Hand specimen of marble from Shepard pit, 1340 bench.</b>	<b>56</b>
<b>Figure 37. Photomicrographs of marble; phlogopite, calcite, and apatite. Field of view 2 mm (upper photo with plane light, lower photo with crossed Nicols).</b>	<b>57</b>
<b>Figure 38. Biotite schist, 1260 bench, Central pit. Hammer is 32" long.</b>	<b>59</b>
<b>Figure 39. Biotite schist, Shepard pit, 1340 bench. Pencil is 5.5" in length.</b>	<b>59</b>
<b>Figure 40. Biotite schist, sample 150903-1. Central pit, 1260 bench.</b>	<b>60</b>
<b>Figure 41. Photomicrograph of quartz-biotite schist. Field of view is 3.44 mm (crossed Nicols), sample 270602-1a.</b>	<b>60</b>
<b>Figure 42. Photomicrograph of biotite-amphibole-garnet schist. Field of view is 1.33 mm, crossed Nicols.</b>	<b>61</b>
<b>Figure 43. Photomicrograph of quartz-biotite-garnet schist. Field of view is 2 mm, plane light.</b>	<b>61</b>
<b>Figure 44. Graphitic schist, 1280 bench of Shepard pit, looking southeast.</b>	<b>63</b>
<b>Figure 45. Detail of graphitic biotite schist (sample 150903-3). Central pit, 1280 bench.</b>	<b>63</b>
<b>Figure 46. Graphite along foliation in graphitic biotite schist (plane light, field of view 0.85 mm, sample 180903-3a).</b>	<b>64</b>
<b>Figure 47. Graphite folded with biotite (bleached) and quartz (plane light, field of view 2 mm, sample 200703-2).</b>	<b>64</b>
<b>Figure 48. View looking southwest, Hindenberg pit (2002) showing orange and black coloration along oxidized faults, and alteration zones. Graphite (black) defines low- and high-angle fault zones in. Bench height is 20 feet.</b>	<b>65</b>
<b>Figure 49. Detail of fault coated with graphite in the fault zone and along the footwall (right center). Hindenberg pit, 1260 bench, hammer is 32" long.</b>	<b>65</b>
<b>Figure 50. Hand specimen of amphibolite-biotite-carbonate schist, sample 060802-4. Hindenberg pit, 1360 bench.</b>	<b>67</b>
<b>Figure 51. Photomicrograph of sample 060802-4 showing crudely aligned amphibole, biotite, and calcite. Field of view is 1.33 mm, crossed Nicols.</b>	<b>67</b>
<b>Figure 52. Map grid is one mile. See next page for explanation. Newberry et al., 1996.</b>	<b>69</b>



<b>Figure 52a. Explanation for the detail of the district map by Newberry et al., (1999). The Chatanika terrane is PDe. Note the thrust fault along the southern and western boundary of the Chatanika terrane and that it is offset by northeast-trending faults.</b>	70
<b>Figure 53a. Rootless <math>F_1</math> fold of foliation in biotite schist, pencil is 5.5" in length.</b>	71
<b>Figure 53b. Detail of folded quartz band in biotite schist.</b>	71
<b>Figure 54a. 2 mm scale fold of biotite (<math>F_1</math> ?) (plane polarized light).</b>	72
<b>Figure 54b. Centimeter scale isoclinal <math>F_1</math> folds.</b>	72
<b>Figure 54c. Meter-scale <math>F_2</math> isoclinal fold of biotite bands in quartz-biotite schist. Hindenberg pit, 1440 bench.</b>	73
<b>Figure 54d. Multi-meter scale recumbent isoclinal <math>F_2</math> fold of biotite-quartz schist with quartz core. Hindenberg 1360 bench. Hammer is 32" in length.</b>	73
<b>Figure 55a. Metamorphic quartz vein in biotite schist.</b>	78
<b>Figure 55b. Small, folded metamorphic quartz vein in biotite schist.</b>	78
<b>Figure 56a. Hydrothermal quartz vein in a high-angle fault with graphite on the footwall. Vein is in lower center of photo and extends up along side the footwall. It is 10-15 cm wide. Hindenberg, 1320 bench.</b>	79
<b>Figure 56b. Hydrothermal quartz vein within a low angle fault. It has been brecciated by later fault movement. Hindenberg pit, 1340 bench. 32" tall hammer in center of photo.</b>	79
<b>Figure 57a. Low angle fault system. Hindenberg, 1480 bench. Faults are defined by graphite. 20' bench height.</b>	80
<b>Figure 57b. Closer look at low-angle fault-vein system. Same outcrop. Pencil for scale.</b>	80
<b>Figure 58a. Shepard pit showing the traces of faults defined by graphite. The blue normal fault offsets the red, mineralized, fault. Bench height is 20', looking southwest.</b>	82
<b>Figure 58b. Detail of the fault zone (right side of 49a), showing a quartz vein in fault damage zone. Hammer is 32" tall.</b>	82
<b>Figure 60a. Outcrop photo of crosscutting carbonate veins in biotite schist.</b>	83
<b>Figure 60b. Detail of older ankerite-dolomite veins cut by late white calcite.</b>	83
<b>Figure 61a. Late stage calcite growing in open fractures.</b>	85
<b>Figure 61b. Late calcite, fine dog-tooth spar from an open fracture.</b>	85
<b>Figure 62. Paragenetic diagram for True North veins. Note that the area in red does not represent separate stages, vein phases vs. alteration halo phases are in separate columns for clarity.</b>	86
<b>Figure 63a-b. Gold in arsenopyrite; textures indicate that the gold is replacing the arsenopyrite.</b>	87
<b>Figure 63c. SEM backscatter image of arsenopyrite crystal containing two grains of gold.</b>	88
<b>Figure 64a. Several larger fluid inclusions, Hindenberg 1300 vein.</b>	91

<b>Figure 64b. Two planes with secondary inclusions, Hindenberg 1280 vein.</b>	<b>91</b>
<b>Figure 65. Histograms of homogenization temperatures. Top histogram is the entire data set, middle histogram is the two Hindenberg veins, and the lower histogram is the Shepard vein. Shows the population distribution and that there are two separate populations, one in Hindenberg, and one in Shepard.</b>	<b>93</b>
<b>Figure 66. Salinity data for all veins.</b>	<b>94</b>
<b>Figure 67. Salinity vs. temperature plots for Hindenberg veins (upper graph) and Shepard vein (lower graph).</b>	<b>94</b>
<b>Figure 68a. Hand specimen of fuchsite-ankerite alteration. All that remains of the original texture (graphitic mica schist) is a weak schistosity. Fresh sample from Hindenberg 1300 bench.</b>	<b>98</b>
<b>Figure 68b. Bright green fuchsite in a mildly weathered sample. Only remanent schistosity remains of the original biotite schist. Sample is from Hindenberg 1340 bench.</b>	<b>98</b>
<b>Figure 69. Partly altered biotite schist.</b>	<b>99</b>
<b>Figure 70. Edge view of sample in Figure 61, centimeter scale at top.</b>	<b>99</b>
<b>Figure 71a. Silica-carbonate alteration, early stages. Photo field of view 2 mm, plane light.</b>	<b>101</b>
<b>Figure 71b. Biotite with fuchsite growing within and around it. Photo field of view is 0.85 mm.</b>	<b>101</b>
<b>Figure 72a. Almost complete destruction of texture in schist. Original schistosity was sub-parallel to the long axis of the photo (see lower right corner).</b>	<b>102</b>
<b>Figure 72b. Complete textural destruction. Field of view 1.33 mm.</b>	<b>102</b>
<b>Figure 73a. View of north wall of the mine 1320 bench to 1480 bench (and low-grade stockpiles at skyline), 20' bench height.</b>	<b>103</b>
<b>Figure 73b. Closer view of strongly weathered, altered schist, Hindenberg 1340 bench.</b>	<b>103</b>
<b>Figure 74. Hindenberg pit, bench 1460 showing shaded contoured gold values from blast-hole assay values. The darker the shade the higher the grade (black is the highest grade). Alignment of the high-grade zones indicates high-angle structures, broad lower-grade zones are low-angle structures. Geologic interpretation by K. Campbell, on Kinross contoured blast-hole data (Unpublished internal report).</b>	<b>105</b>
<b>Figure 75. Hindenberg pit, bench 1380 showing shaded contoured blast-hole assay values. The darker the shade the higher the grade (black is the highest grade). Alignment of the high-grade zones indicates high-angle structures, broad lower-grade zones are low-angle structures. Geologic interpretation by K. Campbell, on Kinross contoured blast-hole data (Unpublished internal report).</b>	<b>106</b>
<b>Figure 76. Carbon and oxygen isotope plot for the True North carbonates. Explanation on next page.</b>	<b>108</b>
<b>Figure 76a. Explanation for carbon and oxygen isotope plot (previous page).</b>	<b>109</b>

<b>Figure 77. Calculated water oxygen isotope values from carbonates. Stars are late stage carbonates, diamonds are intermediate stage carbonates, and the X's are early stage carbonates.</b>	<b>114</b>
<b>Figure 78. Carbon isotope plot for graphite from schist, slate, faults that cut schist and slate, and the Birch Hill slate.</b>	<b>116</b>
<b>Figure 79. Sulfur isotope values for sulfides and whole rock samples.</b>	<b>118</b>
<b>Figure 80. Fuchsite age spectra for True North (From Jenson, personal communication).</b>	<b>120</b>
<b>Figure 81. Fuchsite and plagioclase age spectra for samples from True North and Pedro Dome.</b>	<b>122</b>
<b>Figure 82. Gold versus bismuth. Data from Kinross drill hole geochemical database.</b>	<b>125</b>
<b>Figure 83. Gold versus mercury. Data from Kinross drill hole geochemical database.</b>	<b>126</b>
<b>Figure 84. Gold versus arsenic. Data from Kinross drill hole geochemical database.</b>	<b>128</b>
<b>Figure 85. Gold versus antimony. Data from Kinross drill hole geochemical database.</b>	<b>129</b>
<b>Figure 86. Correspondence Analysis plot of elemental data, factors 1 and 2, from the Kinross multi-element drill hole database. Elements that plot in the same space are not plotted, for clarity. Chromium plots with Mn and Na in the center group.</b>	<b>131</b>
<b>Figure 87. Correspondence Analysis plot of elemental data, factors 2 and 3, from the Kinross multi-element drill hole database. Elements that plot in the same space are not plotted, for clarity. Chromium plots with Mn and Na in the upper group.</b>	<b>132</b>
<b>Figure 88. Correspondence Analysis plot of elemental data, factors 1 and 2, with high tungsten samples removed. From the Kinross multi-element drill hole database. Elements that plot in the same space are not plotted, for clarity. Chromium plots with Mn and Na in the center group.</b>	<b>134</b>
<b>Figure 89. Correspondence Analysis plot of elemental data, factors 2 and 3, with samples with high tungsten values removed. From the Kinross multi-element drill hole database. Elements that plot in the same space are not plotted, for clarity. Chromium plots with Mn and Na in the center group.</b>	<b>135</b>
<b>Figure 90. Correspondence Analysis plot of samples, factors 1 and 2, from the Kinross multi-element drill hole database. Samples that plot in the same space are not plotted for clarity.</b>	<b>136</b>
<b>Figure 91. Correspondence Analysis plot of samples, factors 2 and 3, from the Kinross multi-element drill hole database. Samples that plot in the same space are not plotted for clarity.</b>	<b>137</b>

- Figure 92. Correspondence Analysis plot of samples, factors 1 and 2, samples with high tungsten values have been removed. From the Kinross multi-element drill hole database. Samples that plot in the same space are not plotted for clarity.** 139
- Figure 93. Correspondence Analysis plot of samples, factors 2 and 3, samples with high tungsten values have been removed. From the Kinross multi-element drill hole database. Samples that plot in the same space are not plotted for clarity.** 140
- Figure 94. Paleogeographic reconstructions for YTT and related terranes. A) Devonian-Early Mississippian (ca. 356 Ma). B) Schematic cross-section, Late Devonian-Early Mississippian. C) Mid-Permian (ca. 270). D) Permo-Triassic reconstruction. From Nelson, 2006.** 144

## INTRODUCTION

The True North gold deposit is interesting and unique in several aspects. It is a gold deposit hosted in amphibolite to eclogite grade metasedimentary rocks of the Chatanika terrane, (Fig. 1) about 28 kilometers northeast of Fairbanks, Alaska (Swainbank, 1971). Although quartz-stibnite veins, with and without gold, were known to crop out at the surface (Prindle, 1913) exploration and development drilling indicated a confusing array of high- and low-angle faults in complexly deformed metamorphic rocks and revealed little evidence of a vein system that could account for the deposit (Bakke et al., 2000). In 2001 mining started at True North and as the open pit mine was developed, an bewildering array of features representing ductile (metamorphic) and brittle (faulting) deformation, hydrothermal alteration, and weathering was observed.

As this project got underway in 2002, a number of significant questions remained to be answered. Among those were; the character of the deposit, vein or disseminated mineralization; its geochemical and isotopic character; age of the deposit; setting at the time of mineralization, was this part of the Chatanika terrane mineralized as a part of the eclogite grade metamorphism, or at mesothermal crustal levels, or shallower; alteration, hydrothermal vs. supergene; relationship between brittle and ductile deformation and the gold deposit; and the connection, if any, between the deposit and a nearby diorite intrusion.

The study of any ore deposit begins with an assessment of the regional and local geologic setting and the significance of the host rocks within this setting. From there, the specifics of the host rock interaction with the mineralizing fluids can be developed,

leading to an understanding of the alteration, geochemistry, and isotopic variation in the ore deposit. From there the deposit may be characterized and modeled.

## TECTONIC SETTING

### Physical Setting

The Chatanika terrane consists of two klippen of blueschist to eclogite facies rocks resting upon the Fairbanks schist (Fig. 1, Dusel-Bacon et al., 2006). The Fairbanks schist includes amphibolite facies pelitic schist, quartzite, marble, and amphibolite (Dusel-Bacon et al., 2006; Newberry et al., 1996a). About 28 kilometers to the south of the Chatanika terrane, just north of Fairbanks and roughly parallel to the Chena River (Fig. 1), a low-angle fault separates the Fairbanks schist from greenschist facies slate, marble, stretched-pebble conglomerate, and Upper Devonian to Lower Mississippian felsic units (Dusel-Bacon et al., 2006). To the north and east of the Chatanika terrane, on the south side of the Kaltag fault system, are a series of sediments, meta-basalts, and chert, the Wickersham grit unit (Fig. 1), which is separated from the Fairbanks schist by thrust faults (Dover, 1996). The Wickersham grit unit together with the Chatanika terrane has been interpreted as an oceanic terrane of unknown age and affinity (Patton et al., 1996). Northeast of the Tintina fault (Fig. 1, east of the Chatanika terrane), are the weakly metamorphosed units of the McKenzie fold and thrust belt and the Selwyn basin, all deposits of the North American passive margin (Windermere Supergroup) (Dover, 1996).

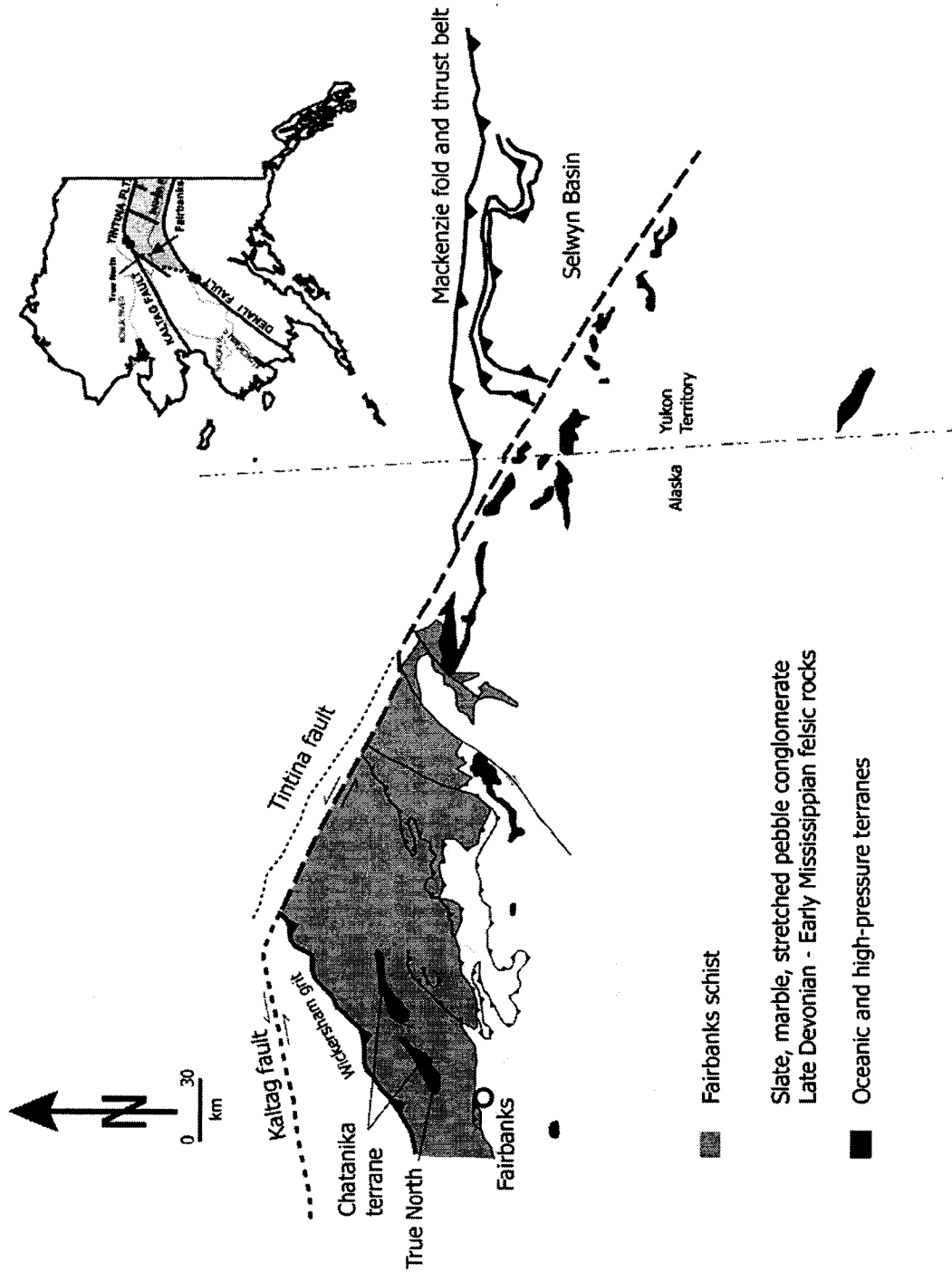


Figure 1. Location map and regional geologic map of central Alaska and part of the Yukon, showing locations of geologic units and features. After Dusel-Bacon et al. (2006).

### **The North American Continental Margin**

The continental margin of North America in the Yukon Territory and Alaska consists of Precambrian through Cretaceous sedimentary sequences and Upper Proterozoic or Lower Cambrian basaltic volcanic and volcanoclastic rocks. On Figure 1 this is the area to the north and east of the Tintina fault and extending off the map area to the north. This passive margin sequence has been folded and thrust in a northeasterly direction. In the Yukon, the fold and thrust belt is known as the Mackenzie fold and thrust belt. In Alaska, the same fold and thrust belt is known as the Charley River fold and thrust belt. Although only crudely shown on Figure 1, at about the point where the thrust belt meets the Tintina fault, a bend in the thrust belt is cut off by the Tintina fault.

A correlation between the Wickersham grit and the Windermere Supergroup, across the Tintina/Kaltag fault systems, has been proposed by a number of authors (Dusel-Bacon et al., 2006). Points of correlation though, have been difficult to establish. However, Dover (1994) established that the Wickersham grit of the Livengood area could be correlated with units in the Charley River fold and thrust belt, based on facies relationships and fold/thrust geometry (Fig. 2), in particular, matching the bend in the thrust belt. This restoration requires about 400 kilometers of offset along the Tintina fault system (Figure 3 shows the area of central Alaska to the southern Yukon border, with current positions of units. Figure 4 shows the same area with the displacement on the Tintina fault restored), which compares favorably with tectonic reconstructions farther south (Price and Carmichael, 1986). Dusel-Bacon et al. (2006) reported detrital zircon data showing that the Wickersham grit, the Fairbanks schist, and the Windermere Supergroup in the Selwyn Basin all have common sources. These reconstructions indicate



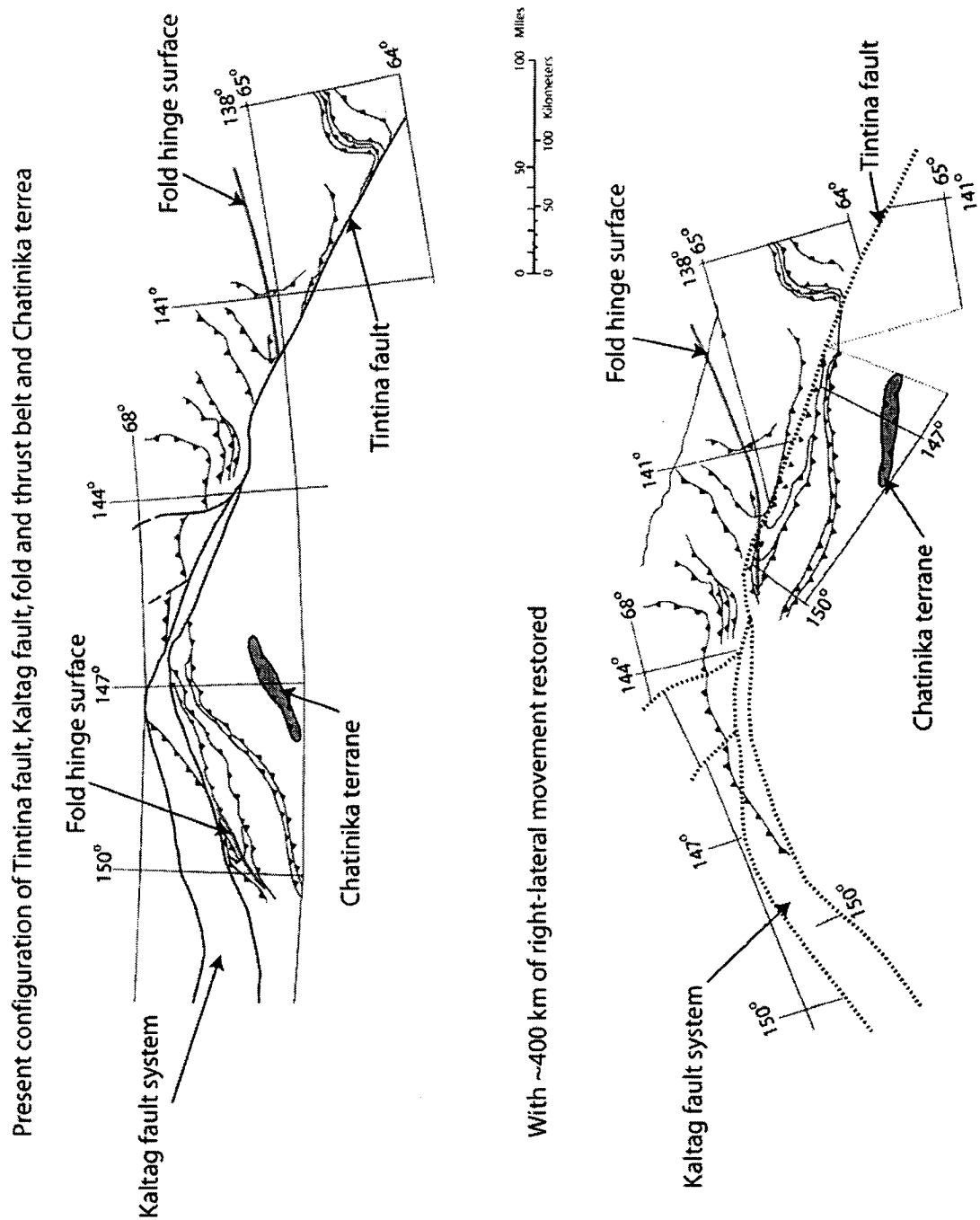
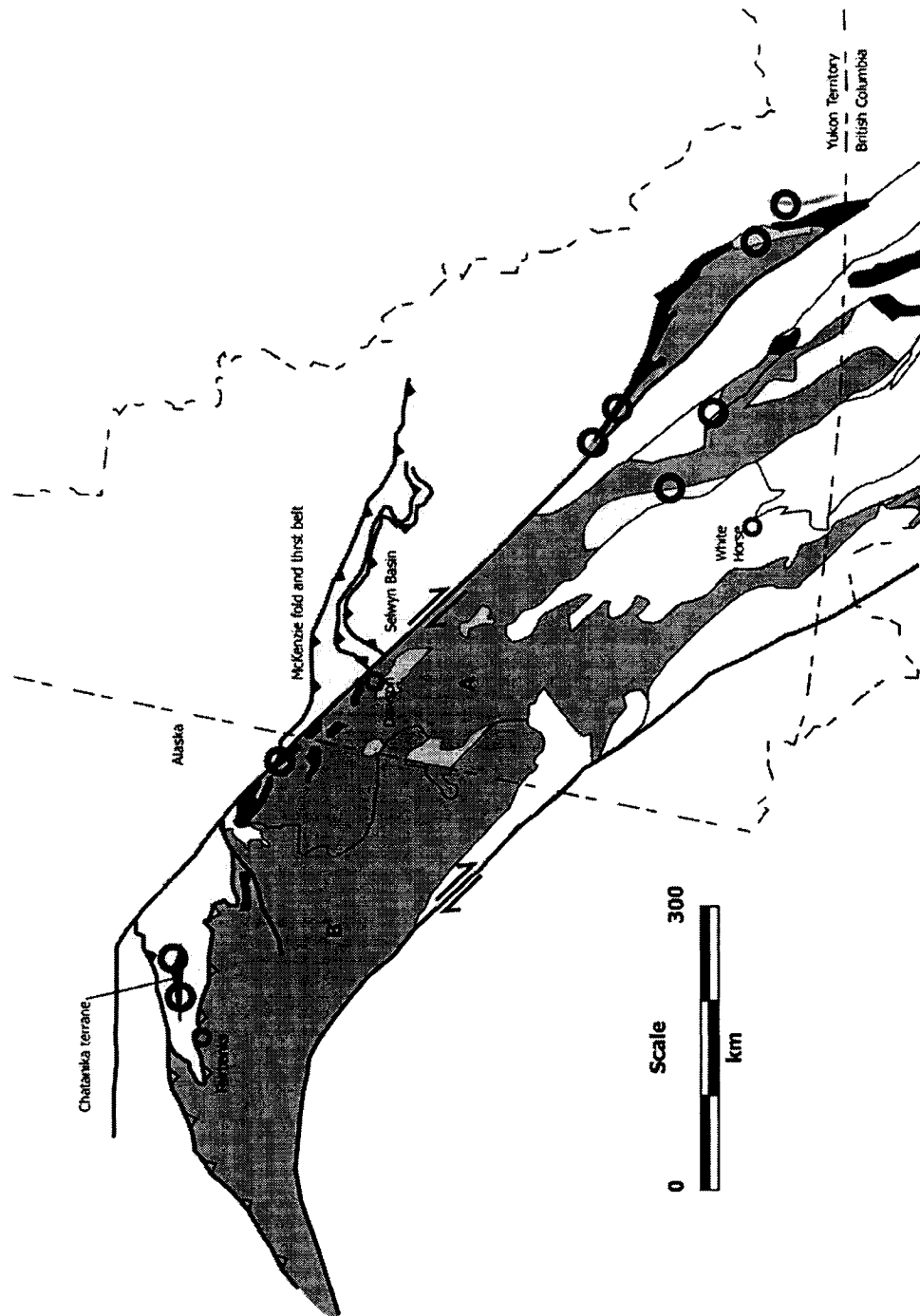


Figure 2. Reconstruction of the offset of the Charley River fold and thrust belt by the Tintina and Kaltag faults. After Dover (1994) and Foster and Keith (1994).



**Figure 3. Map of parts of Alaska, Yukon Territory, and British Columbia. Shows the Yukon-Tanana (YTT), bounding faults, assemblages within the YTT including eclogite/blueschist occurrences, and reference political boundaries and cities. The explanation is on the following page. After Nelson et al. (2006) and Dover (1994).**

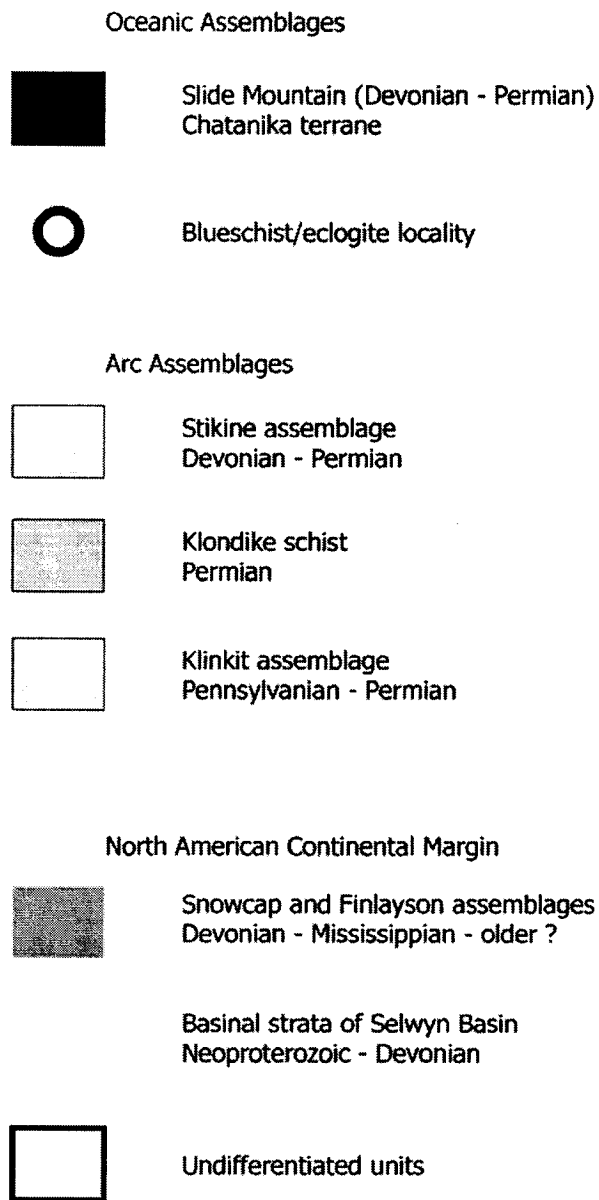
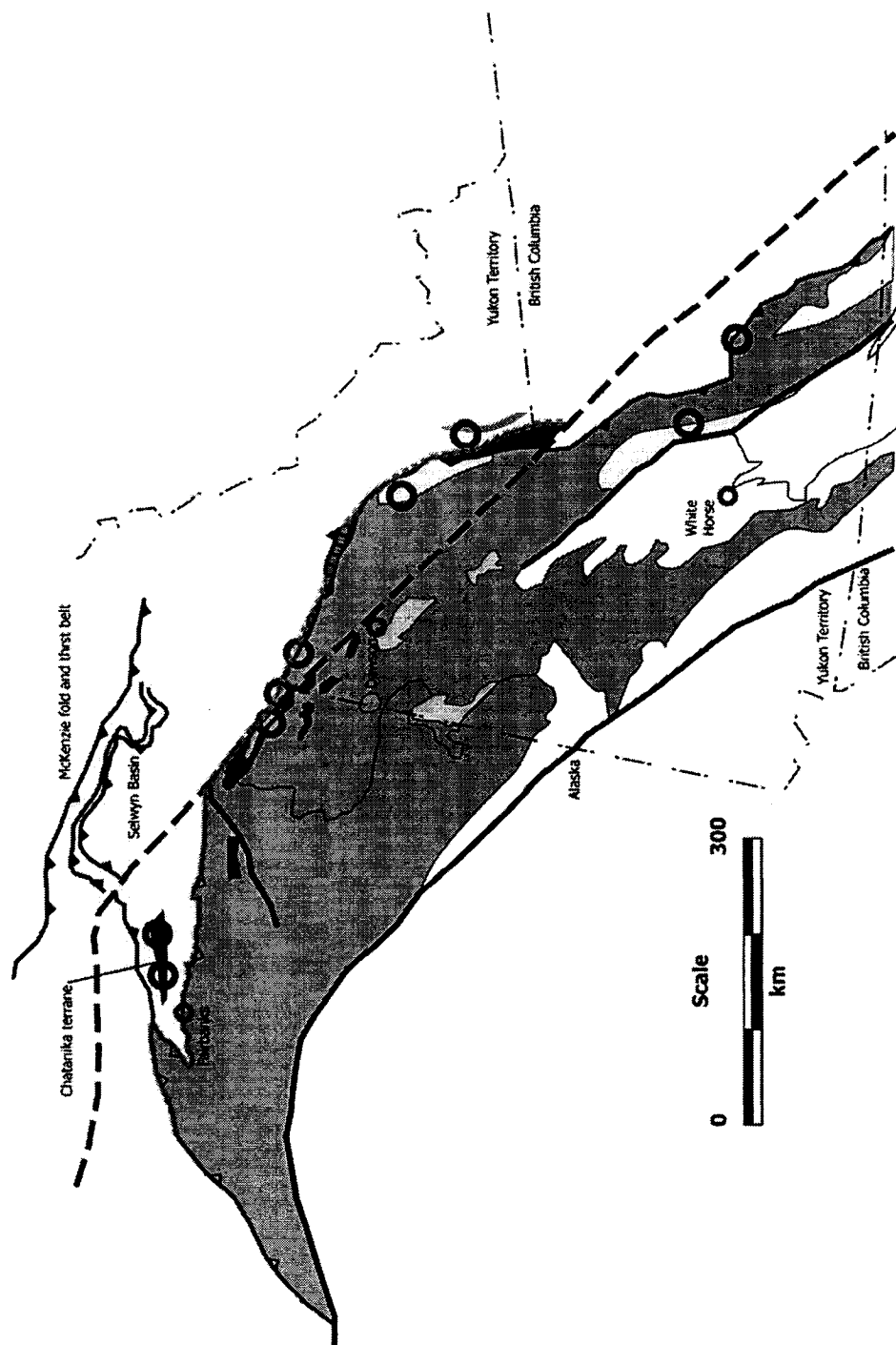


Figure 3a. Explanation for Figures 3 and 4. After Nelson et al. (2006).



**Figure 4.** Map showing the same area as Figure 3 after restoration of ~425 km of displacement on the Tintina fault. Same units as Figure 4. Dotted red line is inferred suture between N. America and YTT. After Nelson et al. (2006) and Dover (1994).

that the Fairbanks schist has affinities with the Selwyn basin and the North American passive margin, and has been displaced to the northwest by 400 km displacement on the Tintina fault.

### **The Yukon-Tanana Composite Terrane**

The Yukon-Tanana composite terrane (YTT) is a mosaic of fault-bound rock packages arranged in crudely linear belts sub-parallel to the Tintina and Denali faults, and the paleo-North American continental margin (Fig. 3). A simplistic view of the YTT is that it is made up of siliciclastic rocks that have a continental character, fragments of oceanic platforms, subduction zone remnants, and arc volcanic and intrusive suites. The YTT is bound on the north and west by two right lateral strike slip faults, the Tintina and Kaltag, and on the east by the Denali fault, also a right lateral strike-slip fault. The YTT extends, in an arc, from southwestern Alaska through central Alaska and descending into western Canada, a distance of over 1000 kilometers (Newberry et al., 1996). The siliciclastic rock packages physically and chemically resemble rocks from the North American continental margin. Oceanic rock packages range from accreted oceanic platforms to ophiolite sequences and some of these are metamorphosed to blueschist facies in subduction complexes. Locally, metamorphosed basinal sediments and interbedded volcanics are of uncertain origin. Plutons stitch together many of the terranes and provide timing constraints on the assembly of the YTT and isotopic data on the crust through which the intrusive masses traveled. Many authors narrow or expand the definition of the YTT based on age, presumed origin, sediment or magma source, and geologic history (see for example, Plafker and Berg, 1994 and Nokleberg et al., 1994).

Proposed origins of the YTT tend to be as varied as its definition. Some authors interpret it as a land mass that was closely associated with North America, but not attached until the Cache Creek Sea closed, between 210 and 180 Ma (for example, Johnston, 2001). Other interpretations are that the YTT is exotic, from parts unknown or a fragment of the Appalachian orogen that was transported around the southern edge of North America and then north to its present position, between 210 and 180 million years ago (for example, Harms, 2003). None of these hypotheses completely explains the internal structure or the origins of all elements of the YTT.

Current thoughts on the origin and construction of the YTT envision it as a segment of the North American continental margin that rifted away between 360 and 230 million years ago, forming the Slide Mountain ocean, then returning to North America between 210 and 180 Ma, closing the Slide Mountain ocean (Colpron et al., 2006).

Recent work on the YTT in Canada and Alaska has shown that the YTT includes four main assemblages (Fig. 5) representing a continental metaclastic basement and three overlying, unconformity-bound volcanic and volcanoclastic arc sequences. The basement is the Snowcap assemblage (Fig. 5), which contains pre-Late Devonian, polydeformed clastic sediments, pelitic schist, marble, and amphibolite (N-MORB to OIB). It is also intruded by Devonian to Mississippian plutons. The intercalated siliciclastic and pelitic metasediments and MORB to OIB basalts of the Snowcap assemblage are interpreted as having formed along a rifted continental margin (Colpron et al., 2006).

The three overlying arc assemblages are, from oldest to youngest; the Finlayson assemblage, the Klinkit assemblage, and the Klondike assemblage. The Finlayson assemblage (Late Devonian to Early Mississippian) contains arc and back-arc mafic to

felsic metavolcanic units, carbonaceous pelite, chert, volcanoclastic rocks, minor quartzite, and marble. The volcanic rocks in the Finlayson assemblage are coeval with the plutons in the Snowcap basement. This is interpreted as a continental arc and back-arc sequence (Colpron et al., 2006).

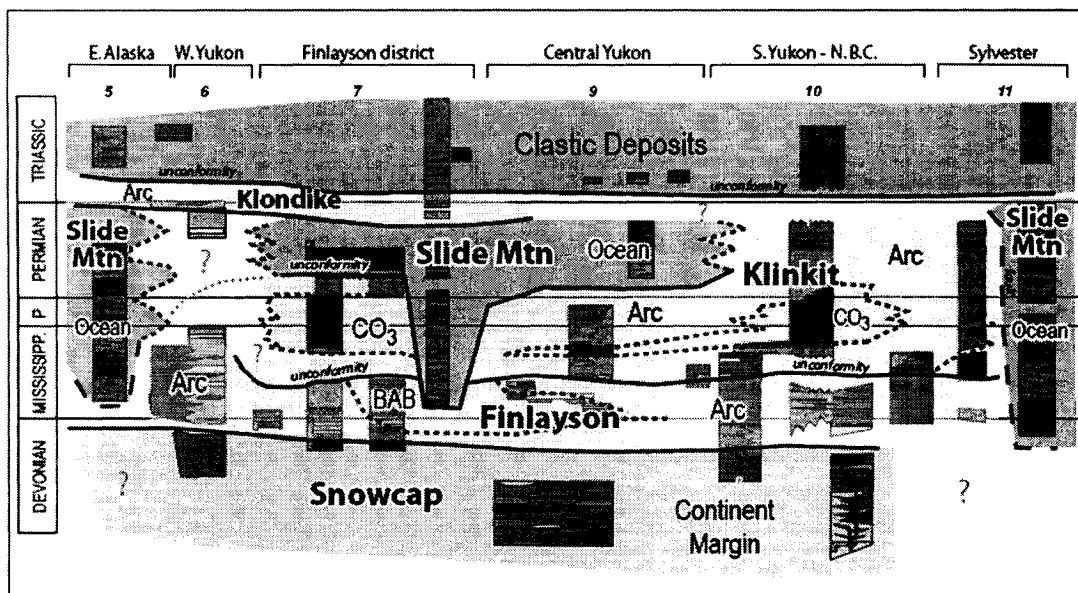


Figure 5. Tectonic assemblages for the Yukon-Tanana terrane, CO<sub>3</sub> is carbonate, BAB is Back-Arc-Basin. From Colpron et al., 2006.

The middle sequence is the Middle Mississippian to Lower Permian Klinkit assemblage, which contains intermediate to mafic calc-alkaline volcanic to volcanoclastic units with minor alkali basalt. Sedimentary rocks within the Klinkit include limestone and a basal conglomerate. The Klinkit assemblage is interpreted as an island arc sequence (Colpron et al., 2006).

The youngest sequence is the Middle to Upper Permian Klondike assemblage, which contains calc-alkaline felsic metavolcanic and minor mafic metavolcanic rocks. The Klondike assemblage has a continental arc magmatic geochemical signature and is interpreted to have been produced by subduction of the Slide Mountain oceanic lithosphere beneath the YTT (Colpron et al., 2006).

As can be seen in Figure 5, the Slide Mountain assemblage is another tectonic unit in the YTT. The Slide Mountain assemblage is a series of slices of basalt, gabbro, serpentinite, and chert. It represents the remains of an oceanic basin. Within some of these assemblages are slices of high-pressure rocks, including eclogites. These slices of high-pressure rocks occur as fault blocks in Slide Mountain units, between continental margin and YTT sequences or as klippen resting on YTT terranes or in one case on continental margin rocks (Colpron et al., 2006). The blueschist to eclogite rocks of the Chatanika terrane comprise such a slice.

Overlying clastic deposits (Figure 5) include Permian to Triassic calcareous siltstone, sandstone, argillaceous limestone, bioclastic limestone, conglomerate, with minor basalt and rhyolite (Colpron et al., 2006).

Figure 3 shows the distribution of assemblages discussed above (figure 3a is the explanation). The Yukon Tanana terrane in Alaska, Yukon Territory, and British



Columbia is divided into two units labeled A and B. Although the areas contain units broadly similar in lithology and age, unit B in Alaska, is not considered part of the YTT by some authors (Colpron et al., 2006 and Dusel-Bacon et al., 2006). Dusel-Bacon et al. (2006) assign this unit to the North American continental margin based on a number of differences from the defined YTT assemblages described above. Rocks dated from this unit have Devonian to Early Mississippian ages (missing are Middle Mississippian to Late Permian arc suites found in the Yukon). The bimodal composition, non-magmatic arc, and within plate (rift) geochemical affinities for most of the meta-igneous rocks in this area are other cited differences. The authors also interpret structural relationships that are incompatible with this region having been rifted away from North America (Dusel-Bacon et al., 2006 and Nelson et al., 2006).

For this purposes of this paper, the YTT is considered to include both units A and B as shown on Figures 3 and 4.

## DISTRICT GEOLOGY

In the Fairbanks district there, metamorphic sequences currently are recognized. These units, from oldest to youngest are: the Proterozoic Fairbanks Schist, a sequence of amphibolite facies metasedimentary and metavolcanic rocks; the Ordovician (?) to upper Devonian Birch Hill Sequence, low grade metasedimentary phyllites; the Upper Devonian Muskox Sequence that consists of amphibolite facies metavolcanic and metasedimentary rocks, and the Chatanika Terrane (Fig. 6) containing calcareous sedimentary rocks, metamorphosed to eclogite and amphibolite facies (Newberry et al., 1996; Brown and Forbes, 1986).

The Chatanika Terrane was interpreted as the highest structural block by Newberry et al. (1996) and as a lower structural block visible through a window in the upper plate of a thrust sheet by Forbes and Weber (1982) and Metz (1991).

The Fairbanks Schist, Birch Hill, and Muskox Sequences have been deformed four times. From oldest to youngest, structures include, northwest verging isoclinal folds, northeast verging isoclinal folds, and northeast trending, overturned, open to sub isoclinal folds, all with amplitudes from meters to 15 kilometers. The fourth deformation event is represented by a set of smaller scale, 1-3 meter amplitude, northeast verging, upright to overturned open folds (Hall, 1985). Folds with north-verging axial planes and northeast-trending hingelines transect the older northwest-verging folds at about a 60° angle.

The Chatanika Terrane was described by Swainbank (1971) as having southwest-verging recumbent isoclinal folds, refolded by a northwesterly trending, upright to overturned open fold set.

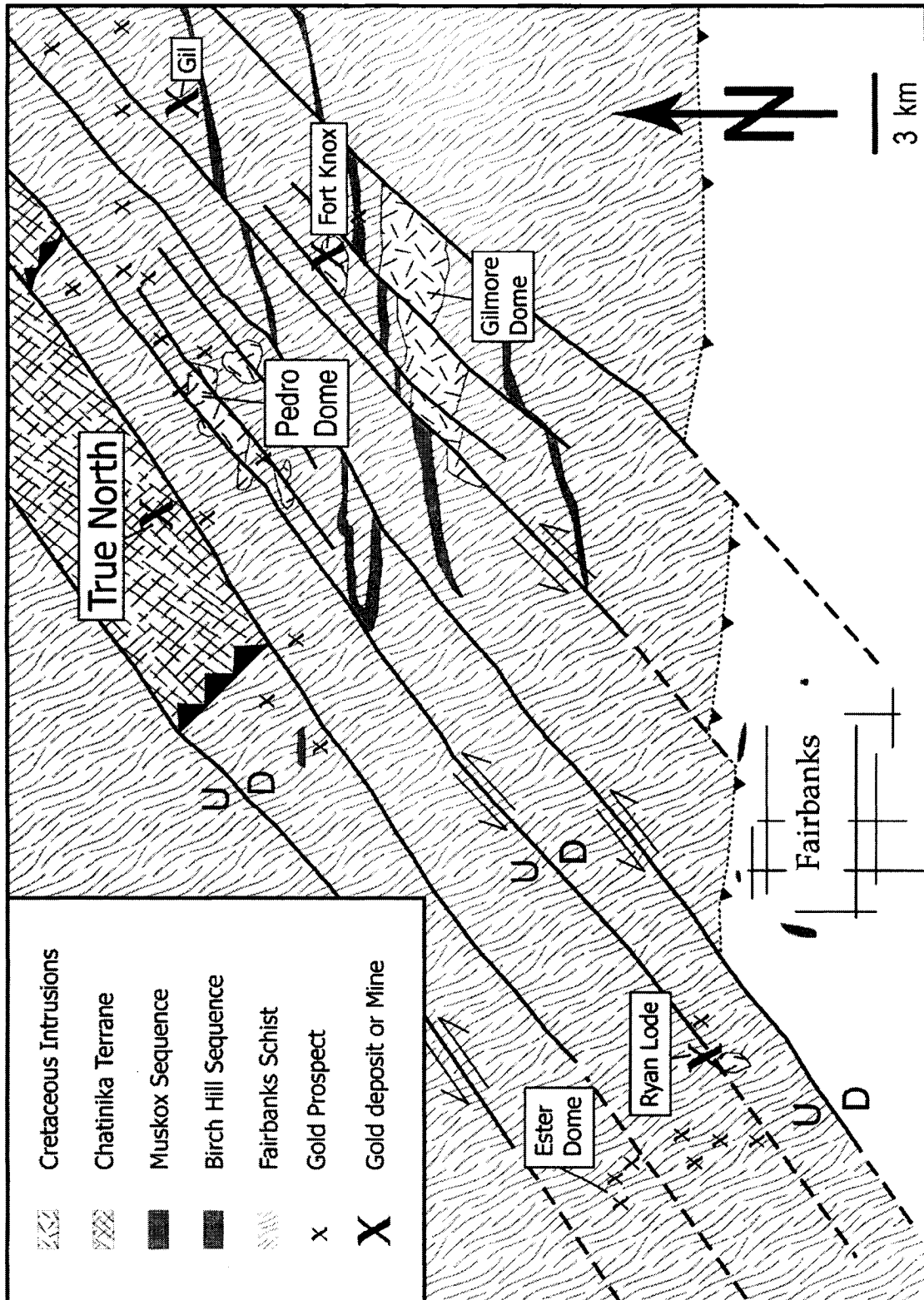


Figure 6. Geologic sketch map of part of the Fairbanks district. After Newberry et al., 1996.

A system of northeast trending, high angle, left lateral faults with apparent horizontal displacements of several meters to several kilometers is pervasive in the district (Newberry et al., 1996). These have been interpreted as related to left lateral displacement generated by the subduction of the Farallon and Kula plates beginning at 100 and 85 Ma, respectively (Flanigan et al., 2000). Within the Fairbanks district, stair-stepped offsets in of units are the manifestation of these faults.

Granitic rocks intruded the older metamorphic rocks of the district in two pulses, the first a quartz-poor intrusive event at 110 Ma and the second, a quartz-rich intrusive event between 88 to 94 Ma. Intrusive-related gold deposits are hosted in or are spatially related to the second intrusive group (88 to 94 Ma), which is interpreted to be I-type granites with a low initial oxidation state (ilmenite series) (McCoy et al., 1997). The Gilmore Dome, Fort Knox, and Pedro Dome stocks shown in Figure 6 are part of the same intrusive suite with ages of 88 to 96 Ma (Blum, 1983; McCoy et al., 1997). The Fort Knox stock hosts the Fort Knox deposit and is the most evolved stock in the suite, porphyritic biotite granite to quartz monzonite. The Pedro Dome stock, the closest known intrusive body to the True North deposit ( $\approx$  1.5 miles or 3 kilometers), is interpreted to be the least evolved, with a dioritic to granodioritic composition.

All or most of the district was buried beneath 50 to 55 Ma tholeiitic basalts and these are preserved in several areas 18 to 35 kilometers to the northeast of the True North area (Newberry et al., 1996).

### **District Exploration History**

The Fairbanks district was discovered in 1902 and has produced about 300 tons (about 8.8 million oz) of gold, almost all by placer mining (Hart et al., 2002). Historic and active placer workings are present in the major drainages to the northwest and south of the True North mine, Eldorado and Dome Creeks, respectively.

The current mines and prospects are the result of many years search for the source of the placer gold. Many of the deposits are hosted by or closely related to a series of 88 to 94 Ma felsic intrusions (Newberry et al., 1996). These deposits are sheeted veins, skarns or sulfide replacement deposits with a distinctive assemblage of elements including Au, Sn and/or W, with Bi, As, Sb, Te  $\pm$  Pb, Ag, and Mo (Hart et al., 2002). The sheeted vein deposits are the most prevalent and the largest. True North is not a sheeted vein, skarn, or sulfide replacement deposit and of the deposits in the Fairbanks district it is the least well known.

### **True North Property**

In 1909 or 1910 gold was discovered associated with quartz-stibnite-pyrite-arsenopyrite veins and shear zones at the Tolovana mine (Prindle, 1910), about 5.5 km west of True North. The discovery of gold and stibnite veins in the True North area is not well documented, but probably occurred shortly after the discovery of the Tolovana deposit. During World War I and II, at what is now True North, high grade stibnite pods and veins were mined with about 200 tons of stibnite shipped from the Ohio claims in the Hindenberg area (Fig. 7) in 1916 (Mertie, 1917) and another 16.5 tons shipped during from the Markovich property in 1942 (Joesting, 1943).

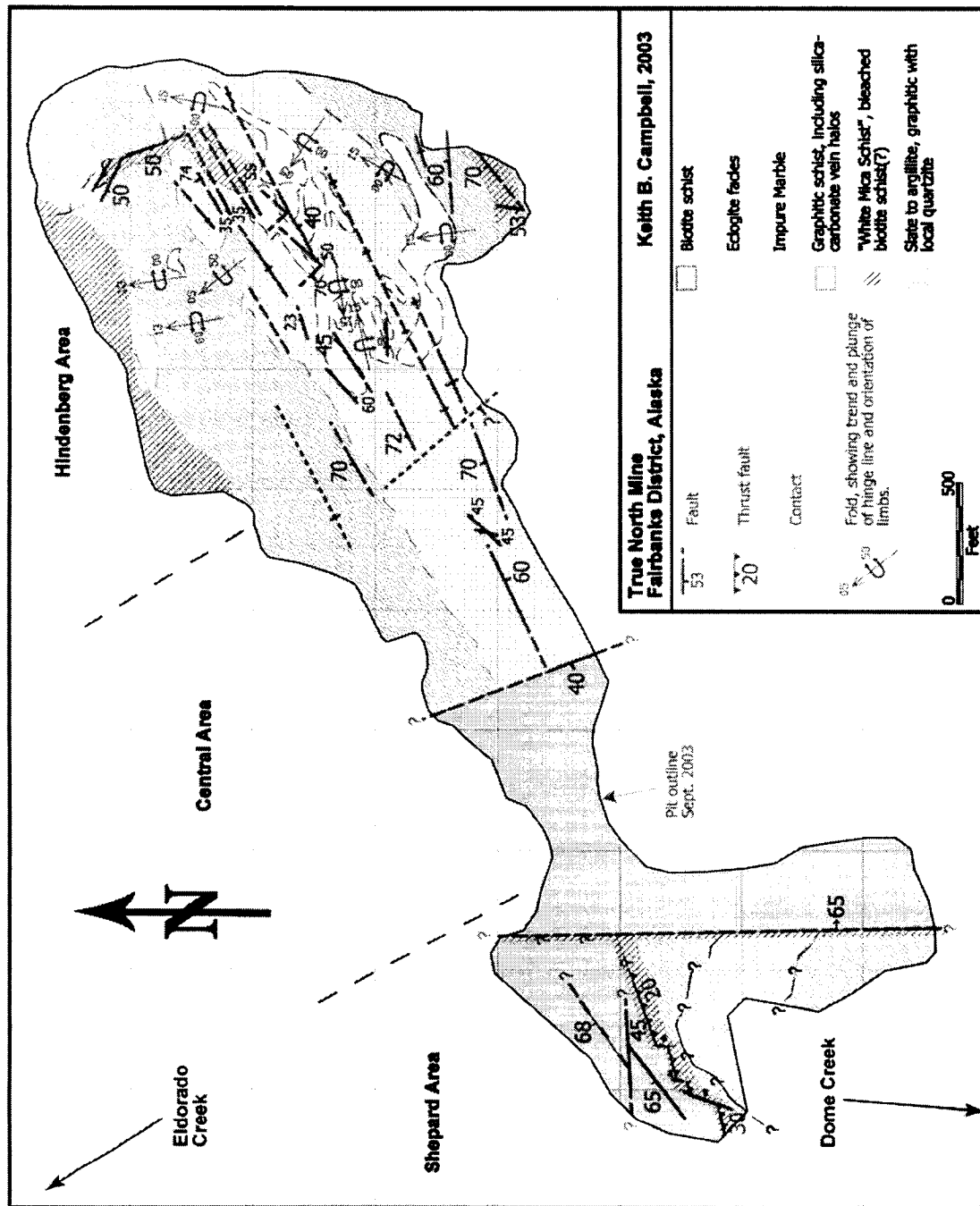


Figure 7. Map of True North showing geology, area names, and key geographic names.

In the 1960's and 1970's five mineralized zones were discovered by geochemical prospecting and some excavations were made on the Chomco claims in the Hindenberg area (Prenn et al., 1995). During this time a greater understanding of the host rocks, the Chatanika eclogite terrane, was gained through several studies. The eclogite suite of the Chatanika terrane was first noted in rubble found in Cleary, Vault, and Dome creeks, in placer spoils (Prindle, 1913). In the 1960's the extent of the eclogitic terrane was worked out and it was noted that its recumbent isoclinal folds are distinct from the more open upright folds of the Fairbanks schist. A better description of the eclogite suite itself (three distinct compositions) and preliminary work on the chemical composition of constituent minerals was all reported (Forbes et al., 1968a; Forbes et al., 1968b; Forbes et al., 1961). The 1970's saw more work done on the geochemistry and petrology of the eclogite, pressure and temperature estimates (14 -15 kilobars and 650°C), and definition of the eclogite as Type C or having as a sedimentary protolith (Swainbank, 1971; Swainbank et al., 1975).

New claims were staked at or near True North (Shepard claims) (Fig. 7) and the older claims (Ohio (?) Hindenberg/Markovich and Chomco) changed hands in the 1980's (Freeman, pers. comm.). Early exploration work (trenching) on the Shepard claims showed, or perhaps reaffirmed, that gold was present. This work coupled with observations made during the studies of the eclogite facies terrane showed that the possibility of an economic mineral deposit existed.

In mid-1990 Amax Gold exploration, which was conducting a regional exploration program in Alaska, learned that there was evidence of gold in the True North area and heard about the recent work, and went to have a look. Samples taken in the

trenches showed potential, and by year's end Amax Gold had negotiated a deal on the Chomco and Hindenberg/Markovich area. By mid-1991, four reverse-circulation holes totaling 1,000 feet were drilled. All four holes encountered the mineralized zones of 15 to 70 feet with grades between 0.025 and 0.087 opt. One holed bottomed in ore grade material. In January of 1992, Amax Gold arranged a deal to access the Shepard claims and a 16 hole reverse-circulation drilling program was planned. By about mid-year, drilling and a soil-sampling program were underway. Based on the results of the drilling, a broad gold resource of 300,000 ounces was defined. The soil geochemistry indicated that there was a much larger, untested, potential.

Amax Gold sold the property to La Teko in 1993. In 1993 and 1994, La Teko drilled a total of 233 holes, 225 reverse-circulation holes, and eight core holes. They identified a resource, measured and indicated, of 6.9 million tons at 0.065 ounces per ton (opt), or 446,000 ounces of gold using a 0.015 opt cut-off. The drilling was done on two separate zones, the Hindenberg and the Shepard. Drilling was restricted to a depth of about 225 feet, the approximate limit of oxidation.

In 1995, Newmont entered into a joint venture agreement with La Teko and acquired a 65 percent interest in the property. By the end of 1995, Newmont had located a third mineralized zone, the Zeppelin, and had confirmed that mineralization was continuous between the Hindenberg and Shepard zones, an area they called the Central zone. Work continued until 1999, when Kinross Gold Corporation acquired La Teko and purchased Newmont's 65 percent share of the True North property.

A resource of about 14.6 million tonnes at an average grade of approximately 1.69 grams per ton gold (13.7 tons at 0.046 ounces per ton) was defined and by 2001



True North ore was being shipped to the Fort Knox mill, where it was mixed with Fort Knox ore at a ratio of three parts Fort Knox ore to one part True North ore. In the early spring of 2004, mining at True North was halted due to difficult mining conditions.

## MAPPABLE LITHOLOGIC UNITS AT TRUE NORTH

### Introduction

The True North area is underlain by three distinct tectonic units; the Fairbanks schist; the Chatanika terrane, which is the host of the gold deposit; and the much lower grade argillite to slate unit. In the True North area, the Fairbanks schist consists mainly of muscovite-quartz schist which grades into micaceous (muscovite) quartzite. Biotite, chlorite, garnet, tourmaline, magnetite, carbonate, and zircon are present in minor to trace amounts (Buisseret, 1997). The Fairbanks schist is not exposed in the pit at True North. The argillite to slate unit crops out in a limited area on the mine site and has not been described elsewhere in the Chatanika terrane. The Chatanika Terrane has been described as consisting of conformable bands and lenses of eclogite intercalated with amphibolite, impure marble and schist (mica schist and pelitic schist) (Swainbank et al., 1975).

Chip and core logging, and geologic mapping at True North were hampered by the complex structural relationships in the folded and faulted rocks of the Chatanika terrane. Comparing mine outcrops and the Kinross lithologic units (Fig.8), it is clear that the lithologic units defined for core and chip logging did not constitute mappable units in the mine. The lithologic scheme used by Kinross at True North was based on field observations (surface samples, drill cuttings, and core), and reports by several authors (Buisseret, 1997; Swainbank, 1975; Amax Gold, Newmont, and Kinross internal reports). The units in the mine area were divided into thirty-two separate lithologic units in three basic divisions, Fairbanks schist, Chatanika terrane, and igneous (Fig. 8). Under this scheme, rocks at True North were divided by mine geologists into six groups comprising

STRAT NAME	LITH	DEFINITION
Overburden	OVB	Overburden (soil)
Fairbanks Schist	QMSC QZT MSC GQSC GMSC GQZT	quartz-mica schist quartzite muscovite schist graphitic quartz-mica schist graphitic muscovite schist graphitic quartzite
Tectonic Unit (Chatanika Terrane)	CBX CBXM	carbonaceous, calcareous CBX texture CBX w/ significant amounts of chl or biot
Felsic Schist (Chatanika Terrane)	QMSC QZT MSC CBXF	quartz-mica schist quartzite muscovite schist non-carbonaceous CBX texture
Graphitic Metased Unit (Chatanika Terrane)	GQSC GMSC GQZT GBND CBXG	graphitic quartz-mica schist graphitic muscovite schist graphitic quartzite Banded graphitic and non-carbonaceous metaseds (flysch or turbidites) non-calcareous CBX texture
Mafic Unit (Chatanika Terrane)	MFSC ECLOG AMPH MBL ARG	chlorite or biotite schist eclogite amphibolite marble argillite (formerly mylonite)
Magnetic Unit (Chatanika Terrane)	MGMB MGEC MGQT MGSC	magnetic marble magnetic eclogite magnetic quartzite magnetic schist
Slate Unit (Chatanika Terrane)	SLT PHY QZT ARG	slate phyllite quartzite argillite (formerly mylonite)
Igneous	FGI	fine grained (intermediate to felsic) intrusive rock

Figure 8. Kinross (2002) lithologic units and descriptions (Note: CBX= calcareous breccia).

twenty-four separate lithologic units. With the opening of the mine, this lithologic scheme was used in mine mapping.

In this study, mine outcrops were examined for obvious broad divisions and mappable units. Duplications in the lithologic scheme were also eliminated. For example, CBX or the carbonaceous, calcareous breccia, is better mapped as a lithologic unit, slate-argillite.

Within the mine exposures obvious divisions include, high- vs. low- grade metamorphic units and within the high-grade metamorphic units, foliated vs. non-foliated units. The slate-argillite unit, which is clearly of lower metamorphic grade than the schists, amphibolites, marbles, and eclogites, constitutes a mappable unit. Marble and eclogite exposed in the mine are massive to poorly foliated, in clear contrast to strongly foliated mica schists and amphibolites. Although marble and eclogite are distinctive enough to be mapped, they locally grade into one another and are difficult to distinguish in hand samples. Amphibolite proved to be not continuous enough to map alone; it is included with biotite (mafic) schist. Kinross' divisions within the schists, felsic- (muscovite), mafic- (biotite), and graphitic- (muscovite or biotite with strong graphite) were retained, since the majority of the orebody occurs in these units.

Six basic units were mapped in the first field season of this study: 1) slate-argillite, 2) eclogite, 3) marble, 4) felsic schist, 5) mafic schist, and 6) graphitic schist, all with descriptive prefixes as necessary. Amphibolite, where identified, was mapped together with the mafic schists. A seventh unit, a coarse-grained 'white mica schist', was also included on the map. This unit, which occurs near the pre-mine surface and locally along faults, is important because it is unstable in the mine high walls.

However, the mica schists proved to be impossible to map accurately. Outcrops, such as the one in Figure 9, illustrate the problem. Individual schist units are discontinuous; felsic schists appear to grade into mafic schists and visa versa. In mine exposures this appears to be a weathering phenomenon. To examine the problem in detail, samples were taken of a variety of mica schists, biotite and muscovite, and all were analyzed using x-ray diffraction to identify specific mica types, and an examination of the literature on biotite weathering was examined to determine whether schists at True North are similar to published examples.

### **The Physical and Mineralogical Aspects of Biotite Weathering**

Early studies on weathered biotite noted that the weathering of biotite caused a color change from dark-brown or black, to silver or white, passing through golden-yellow. Weathering also causes an increase in the optic axial angle, a decrease in specific gravity, a decrease in the refractive index, and the disappearance of pleochroism. It was also noted that there was a loss of iron (preceded by the oxidation of ferrous to ferric iron), magnesium, and sodium, and a gain in water (Walker, 1949). The final product, kaolinite was also observed, under both weathering and hydrothermal conditions, and that a variety of intermediate products including vermiculite, chlorite, and hydrobiotite were possible. The study of biotite from a single 100 centimeter thick soil profile near Glen Buchat, Scotland, included x-ray and optical (petrographic) investigations and concluded that biotite weathering proceeds by the replacement of potassium ions with water, slightly increasing the spacing of the basal planes, seen as a broadening of the  $10\text{\AA}$  x-ray peak. Within the silicate layers oxidation of iron occurs, along with the substitution of hydroxyl



**Figure 6. Sample site for the XRD samples. On the right is unweathered biotite schist, center and to the left, is variably weathered biotite schist (Hindenberg Pit 1340 bench).**

for oxygen and the loss of magnesium, to balance the lattice charges. As the interlayer attractive forces are reduced by the further replacement of iron in the interior of the silicate layers and the complete removal of potassium, double layers of water build up and the structure becomes that of vermiculite. At this point the biotite is a mixed layer biotite-vermiculite. This process continues until the biotite is converted completely to vermiculite. The x-ray patterns of these samples show a distinctive vermiculite peak at about  $14\text{\AA}$  (Walker, 1949). In the discussion Walker (1949) notes that this weathering occurs in well-drained soils and that in wetter or less well-drained soils the process might proceed directly to montmorillonite, which has a structure and x-ray pattern similar to vermiculite.

In another study in the same area Wilson (1966) also looked at biotite from the soils. In this study the parent rock is identified as "a biotite-rich quartz gabbro", and in addition to x-ray and optical techniques, chemical, differential thermal, and infrared studies were performed. The samples in this case came from three widely spaced sites. X-ray diffraction patterns from these samples showed peaks between  $13.8$  and  $14.6\text{\AA}$ , about where vermiculite peaks should be, but furthering testing by heating (to  $300^{\circ}\text{C}$ ) and saturating the samples with a potassium-rich solution did not show the expected collapse to  $10\text{\AA}$ , indicative of vermiculite. After treating these samples with  $\text{Na}_2\text{CO}_3$  to remove any amorphous alumina and silica the samples reacted as interlayered biotite-vermiculite. Analysis of the material removed showed it to be  $2.58 - 5.4\%$   $\text{Al}_2\text{O}_3$  and  $2.92 - 4.67\%$   $\text{SiO}_2$ . The differential thermal and infrared studies of some samples identified kaolinite and gibbsite as the minerals interlayered with the biotite. Thin sections made from epoxy impregnated soil blocks show biotite interlayered with what appear to be clays. Wilson

suggests that these samples are further along in the weathering process than the samples studied by Walker (1949) and based on work from this study proposed the sequence for weathering of biotite in Table 1.

Weathering Stage	
I	II
Biotite →	Vermiculite
	Interlayered with chlorite →
	Vermiculite-Chlorite with
	Kaolinite and
	Gibbsite interlayers →
	Kaolinite
	Gibbsite
Youngest or least weathered	→ → → → → → Oldest or most weathered

**Table 1. Weathering Stages of Biotite to Kaolinite or Gibbsite (from Wilson, 1966).**

Development of vermiculite opens the biotite structure, exposing fresh material for further weathering and helps provide the pathways for material movement. Samples from this study had a complex mixture of aluminum-rich -vermiculite-chlorite with zones of kaolinite and gibbsite. This weathering occurred in well-drained soils in a northern temperate climate.

Cation budgets for the various stages of weathering have been calculated (Banfield and Eggleton, 1988). In one to one replacement of biotite by vermiculite, Si, Mg, and Fe need to be added, with Ti and K lost (Figs. 10 – 12). Presumably, the extra



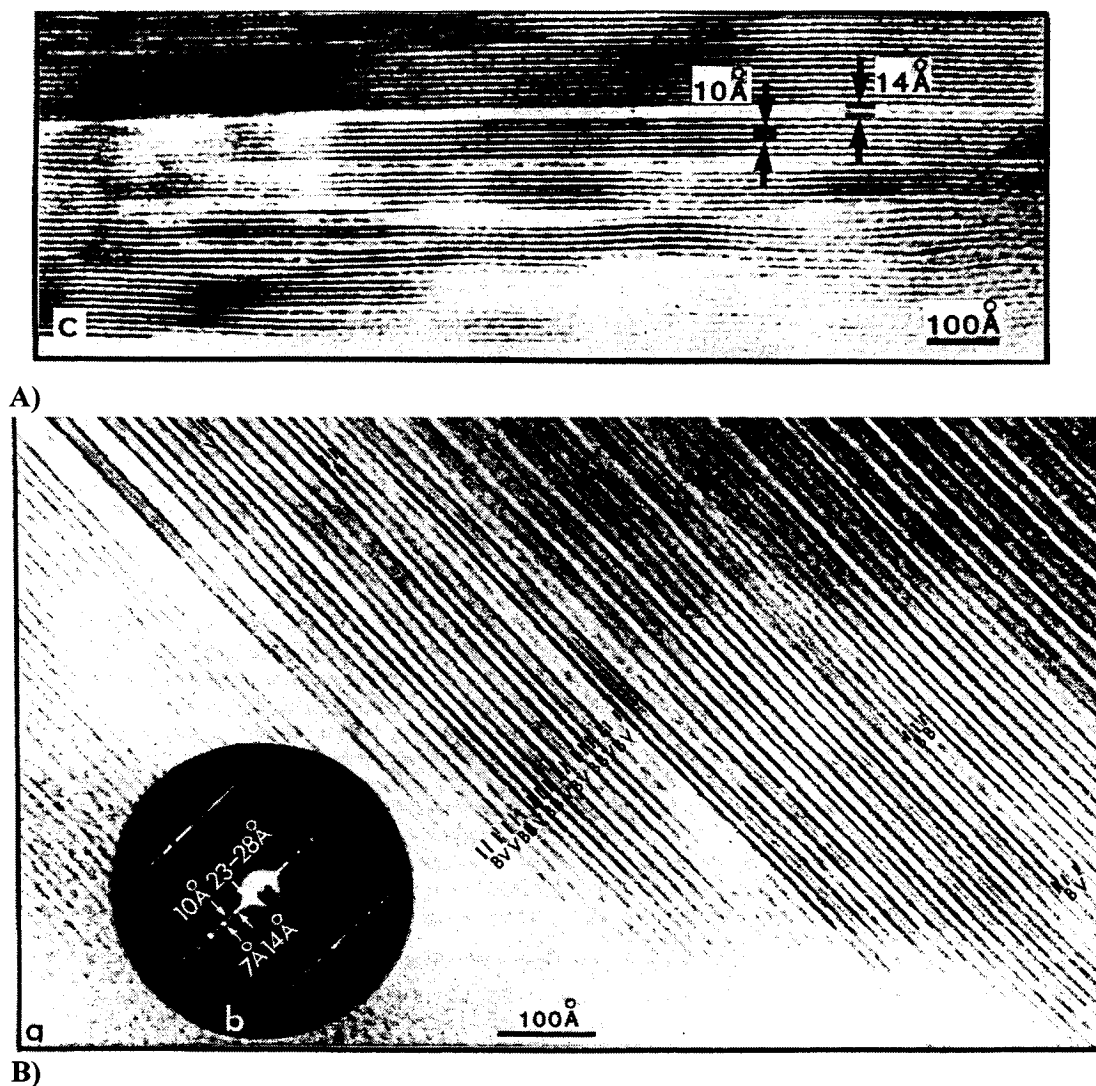


**Figure 10. TEM images of biotite-vermiculite. A) Showing the layer spacing.  $10\text{\AA}$  layers are biotite,  $14\text{\AA}$  layers are vermiculite. B) Showing the interlayering of biotite and vermiculite. B= biotite, V= vermiculite (from Banfield and Eggleton, 1988).**

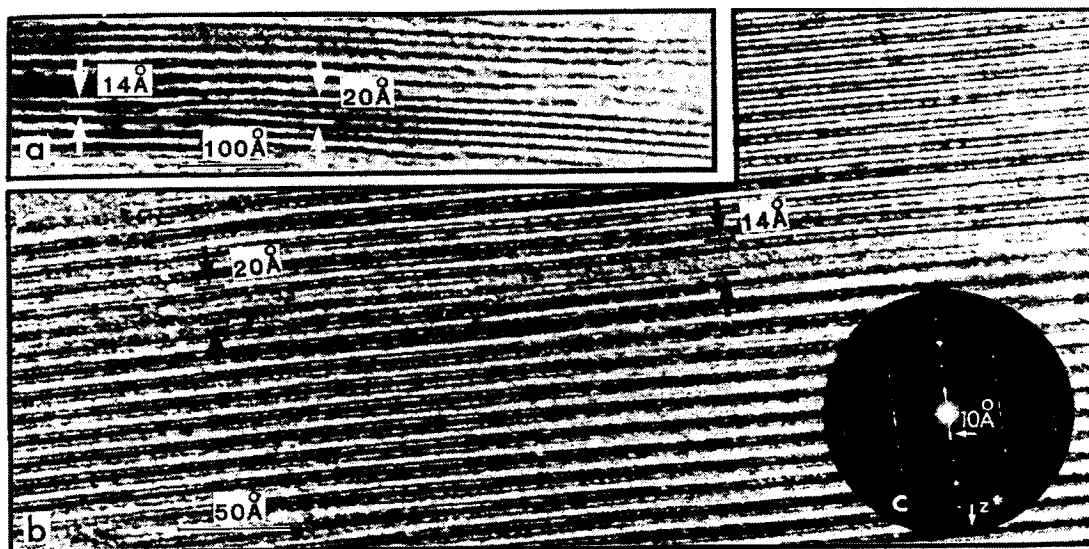


Figure 11. TEM image showing gradual change from biotite, left, to vermiculite, right. The layer spacing changes from 10Å to 14Å as biotite converts to vermiculite. (from Banfield and Eggleton, 1988).

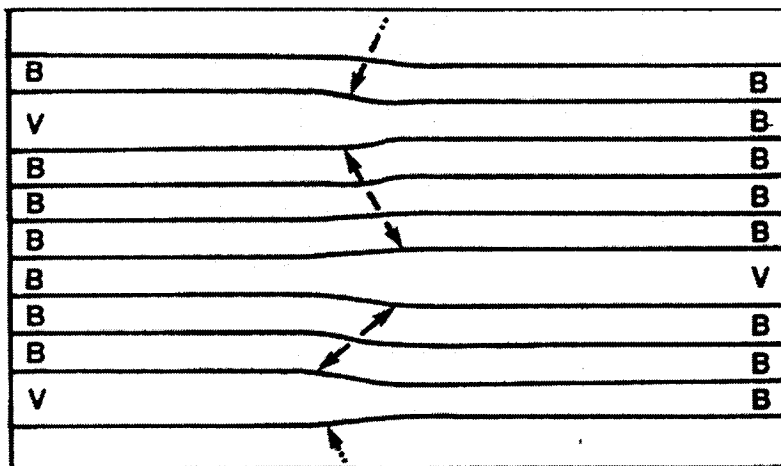


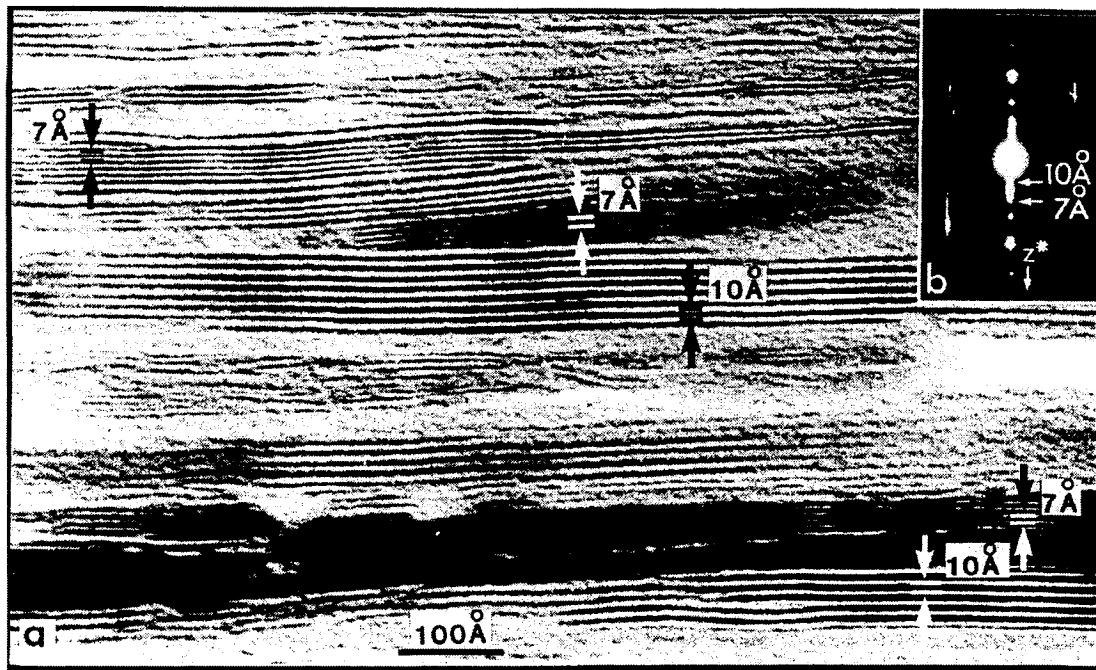
Figure 12. Diagrammatic illustration of biotite converting to vermiculite, showing relationship between fronts of vermiculite and the biotite being replaced, B= biotite, V= vermiculite. (from Banfield and Eggleton, 1988).

cations are coming from adjacent areas where dissolution is taking place. In the two to one replacement of biotite by vermiculite there is a net loss of all cations. The same is true for the next step, to kaolinite and goethite (Fig. 13). A net volume loss from biotite to kaolinite and goethite was shown.

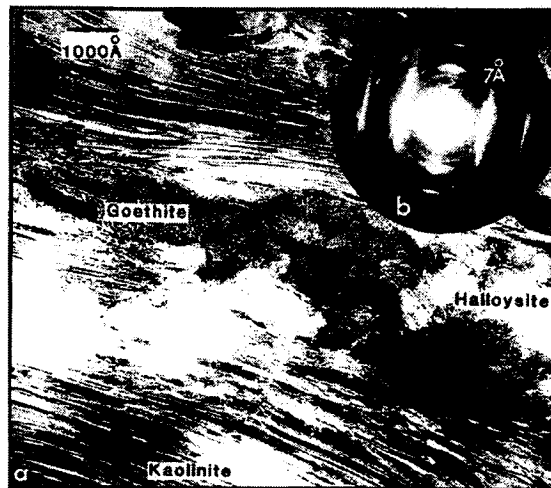
This pattern of weathering, biotite altering to interlayered biotite-vermiculite, and then to kaolinite, with or without goethite, is well studied and established in the literature. Generally speaking, as biotite weathers cations are removed and/or replaced and the mica structure is altered. On the other hand, muscovite is relatively stable under weathering conditions and can be found in sediments and sedimentary rocks (Fleet, 2003). The X-ray patterns from True North then can be examined with this in mind to see if the “felsic schists” are muscovite or weathered biotite.

#### **Characterization of Biotite Weathering at True North**

Twenty-one samples were selected from mica-quartz schists that exhibited color variations from dark-brown to black (biotite), to mottled brown, yellow-brown to silver-white (weathered biotite?), to pure silver-white (muscovite?) for x-ray diffraction (XRD) analysis. These included samples that would be identified in outcrop as biotite-schist (dark-brown micas), weathered biotite-schist (medium-brown to yellow-brown micas), probable weathered biotite (golden-brown to silvery micas), and ‘White Mica Schist’ or muscovite-schist/felsic schist (silvery to white micas). All of the weathered samples and the muscovite-schist samples have considerable quantities of iron-oxides and -hydroxides in them. Samples were also of a variety of mica grain sizes, including fine-grained biotite schist, fine-grained muscovite-quartz schist (felsic schist), fine-grained muscovite-



A)



B)

Figure 13. A) TEM image of packets of 7Å kaolinite sheets parallel to biotite layers. B) Showing Goethite, halloysite, and kaolinite from biotite (from Banfield and Eggleton, 1988).

graphite-quartz schist (graphitic schist), coarse-grained biotite schist (mafic schist), and coarse-grained muscovite schist ('White Mica Schist'). Figure 9 shows an outcrop photo of one sample area that shows dark-brown to yellow-brown to silvery micas. Samples that most resembled muscovite and the "White Mica Schist" were a particular emphasis.

Interpretation of the XRD data was done using Jade version 6.5 peak identification and matching software. All of the patterns were handled in the same manner, automatic background fitting, and removal; search and match for mineral identification was done for extreme preferred orientation of the sample. The selection of the best fit was done by progressively removing the peaks of identified minerals and then searching for minerals to fit the remaining peaks. Quartz was present in the samples analyzed or added to provide reference peaks (as a standard).

The XRD analyses turned out to be more complicated to interpret than anticipated. As anticipated, little to no muscovite was identified in the samples analyzed, but simple end-member biotite was also absent from all samples. In light of the x-ray data, a closer look at the protoliths of the Chatanika terrane is merited. Swainbank (1971), Swainbank and Forbes (1975), and Brown and Forbes (1986) indicated that the bulk geochemistry of the eclogite rocks resembles a marl rather than the mafic igneous protolith of most eclogites. Impure limestone, dolomite, and limy pelitic sediments metamorphosed to eclogite facies would likely produce the impure marble and calcareous eclogite of the Chatanika terrane. Calcareous eclogite retrograded to amphibolite facies could produce some of the biotite schist that mantles the eclogite (Swainbank, 1971). Biotite produced by the metamorphism of marl would be Mg-rich, relatively Fe-poor, and at the phlogopite end of the solid solution series. A second complication is that alteration

in and around the mineralized area of True North consists of carbonate (ankerite-dolomite) flooding and alteration of biotite to sericite or fuchsite (depending on the availability of chromium to form fuchsite). In x-ray patterns, altered mica is similar to the vanadium-barium muscovite 2M1 (the Jade version available does not have powder diffraction files for chromium micas). Alteration will be discussed in greater detail in the section on alteration.

Appendix A contains all of the x-ray data and reference powder diffraction patterns for a number of micas including phlogopites, muscovites, and biotite showing the differences (and similarities) between these micas. The quartz standard is plotted on each mica pattern for reference.

As described above, a number of samples of mica schist from several locations in the mine were examined and all of them contain phlogopite or weathered phlogopite. The freshest samples resemble and have X-ray powder diffraction patterns like sample 200703-2, which is fine-grained quartz-biotite (phlogopite) schist (Fig. 14). Figure 15 the powder diffraction pattern (x-ray pattern) for sample 200703-2 shows three phases, quartz, phlogopite, and apatite. A weakly weathered sample (200703-1) from the same outcrop (Figs. 16 and 17) shows that along with quartz, two types of phlogopite occur. The next pair, banded phlogopite schist is the only sample that contains vermiculite (Figs. 18 and 19). As can be seen in the x-ray pattern, this sample is a complex mixture of weathered phlogopite and chlorite, with kaolinite, albite, and vermiculite. Figures 20 and 21 show muscovite or felsic schist, x-ray pattern and hand sample. Although the mica is yellow to silver the x-ray pattern shows that there is phlogopite types, halloysite and vanadium-barium muscovite that is probably hydrothermal mica (fuchsite?). The 'white

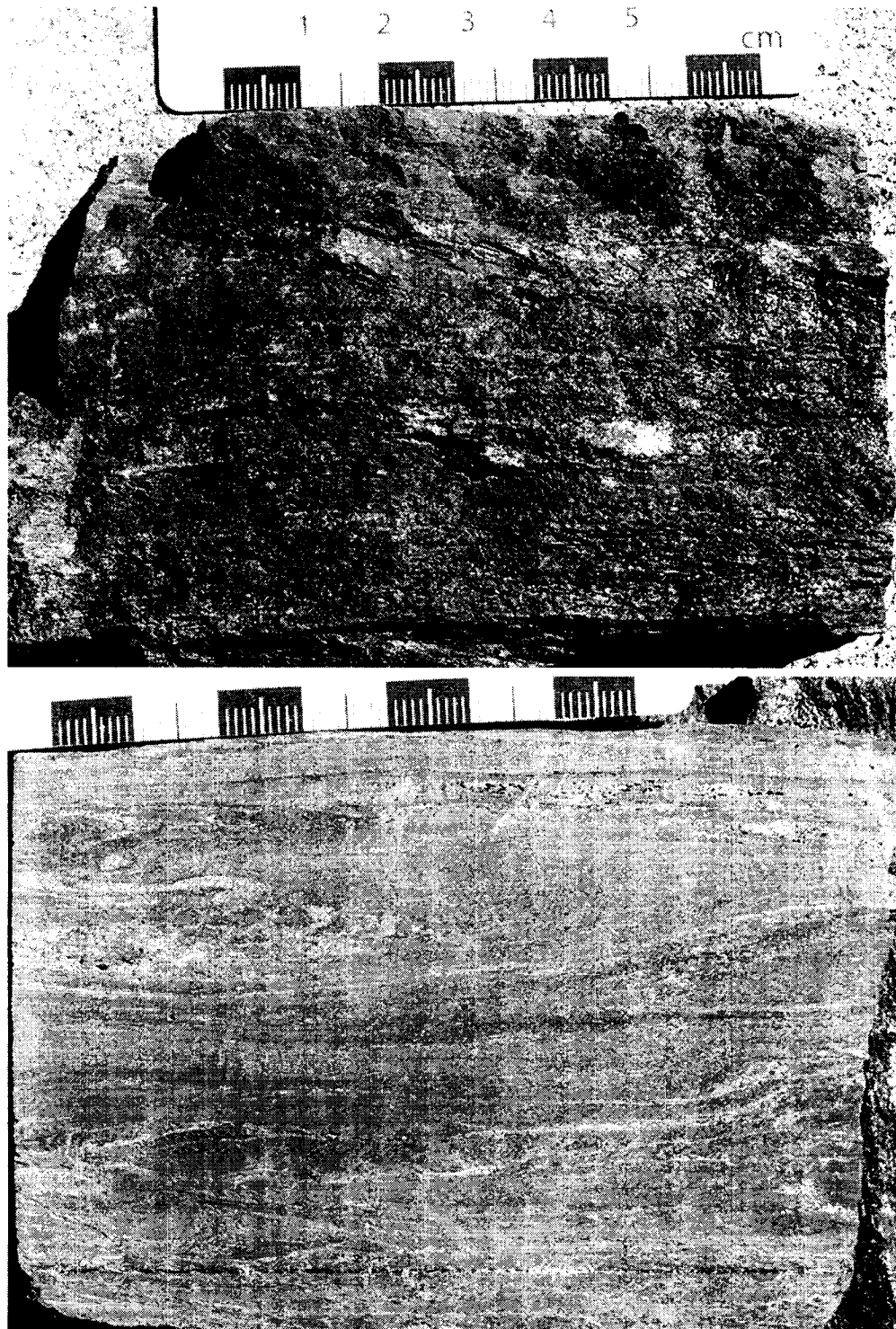


**Figure 14. Fresh, fine-grained biotite (phlogopite)-quartz schist. Top photo is natural surface, lower photo is sawed surface.**

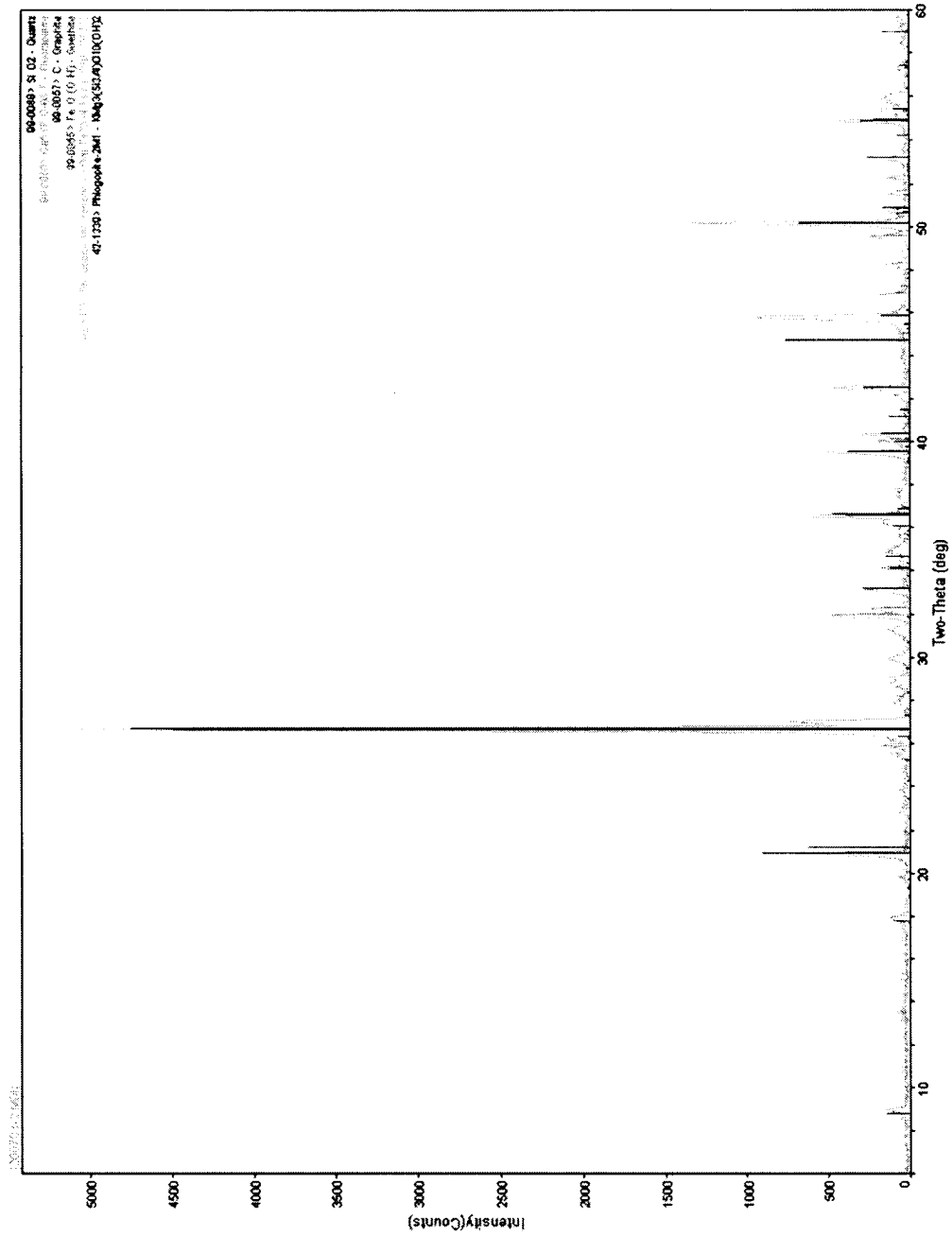
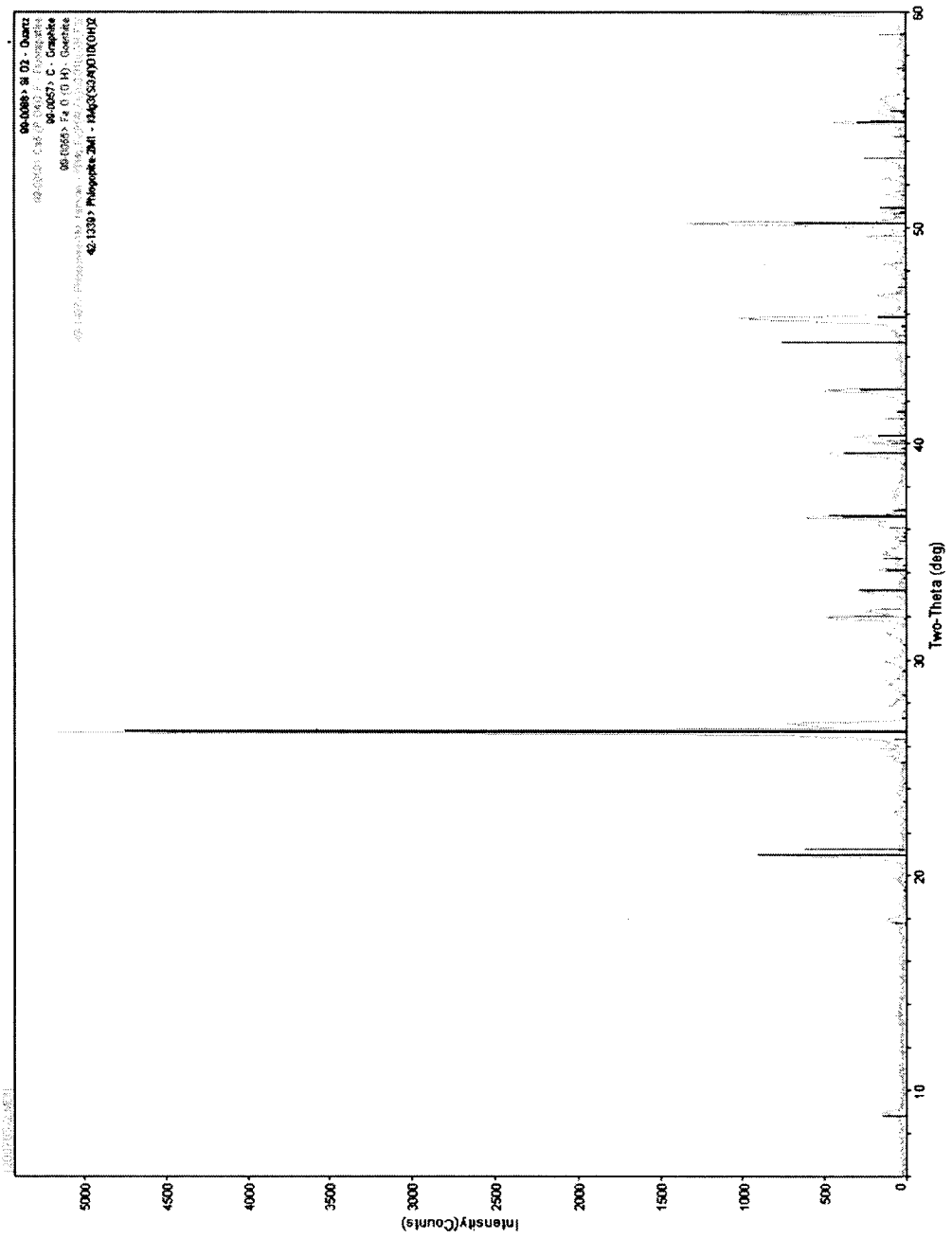


Figure 15. Powder diffraction pattern for sample 200703-2, unweathered biotite schist.





PROJ:kwh\1\Documents and Settings\kwh\1\Campbell\Monday, Sep 25, 2006 07:51p (MJDJUANES)

MSESE

Figure 16. X-ray powder diffraction pattern for sample 200703-1, weakly weathered biotite schist.

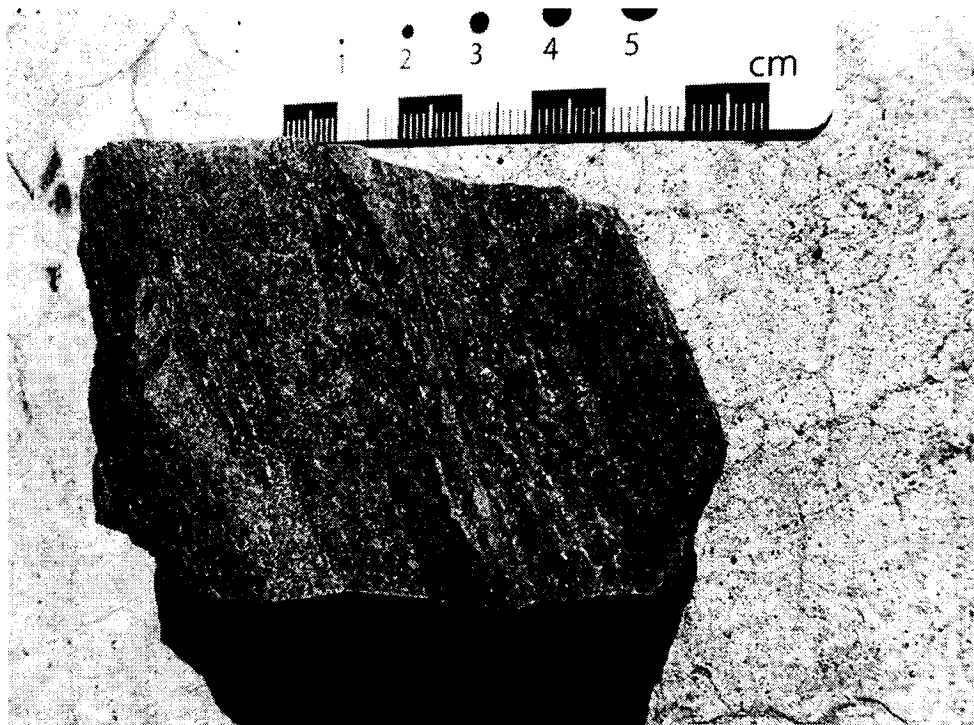


**Figure 17. Weakly weathered biotite schist, sample 200703-1.**

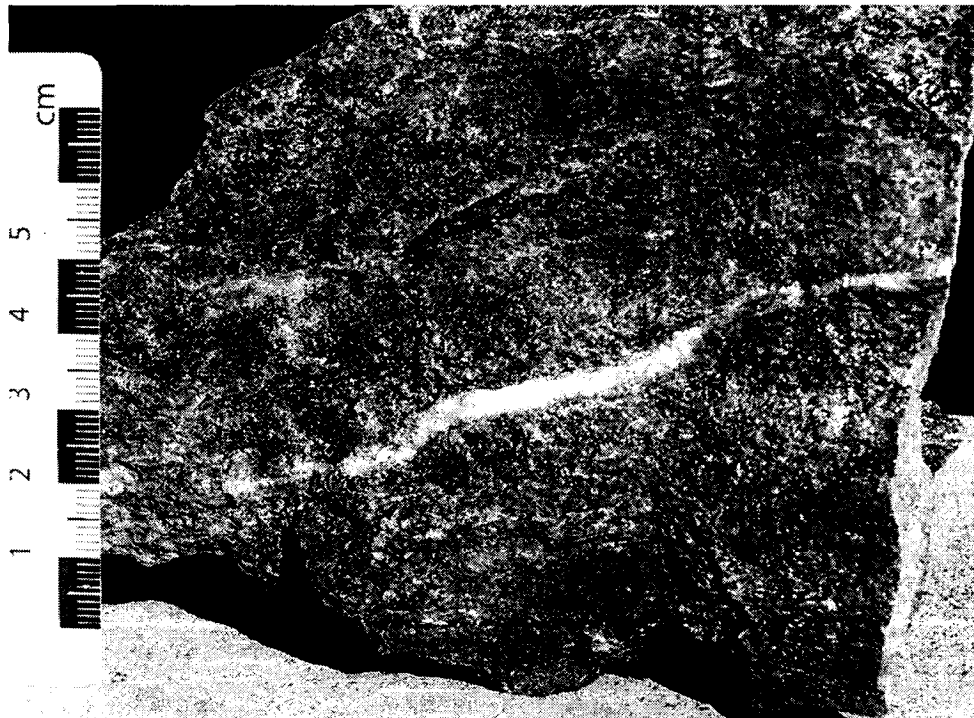


**Figure 18. Weakly weathered biotite schist, with vermiculite. Sample 040903-3**

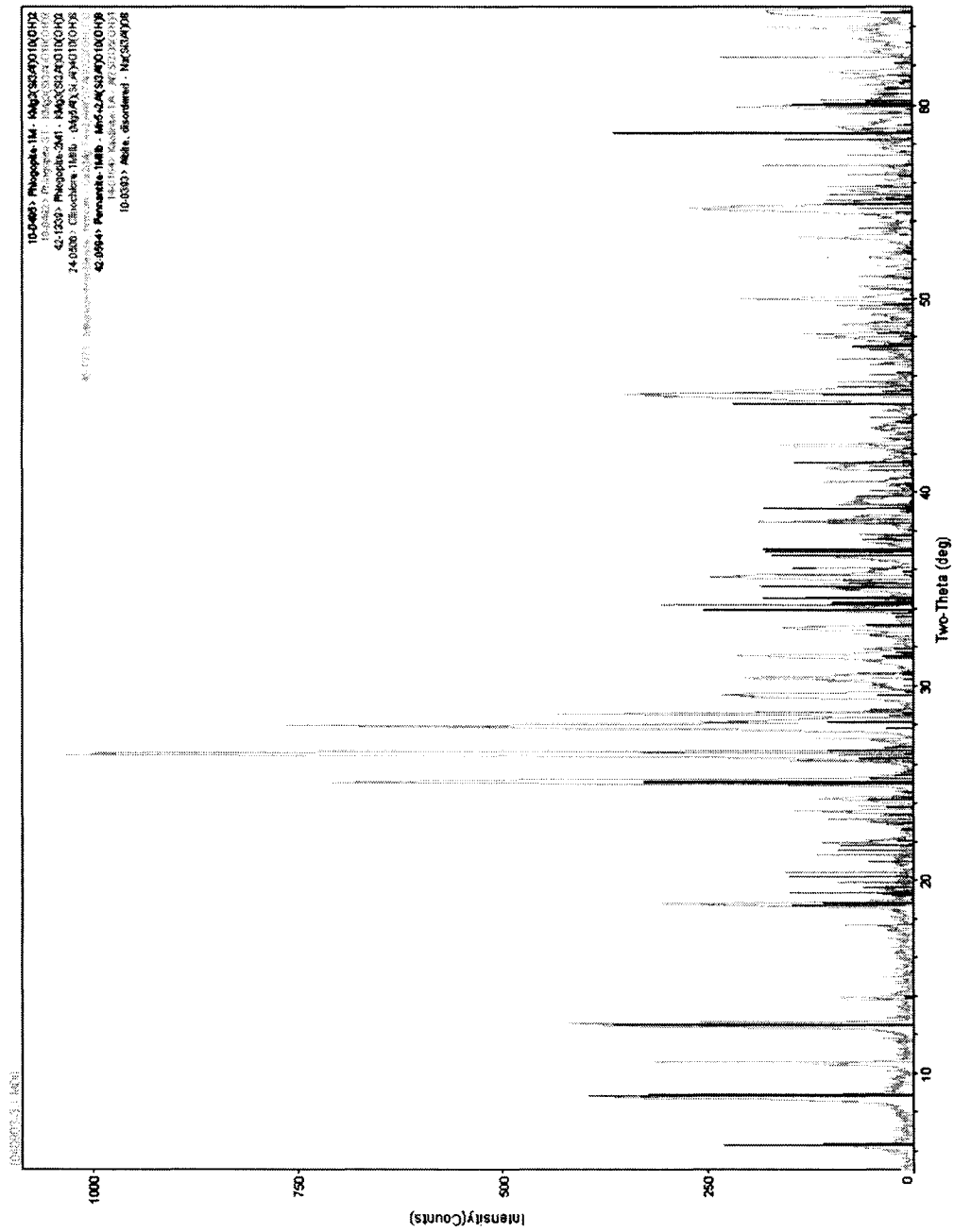
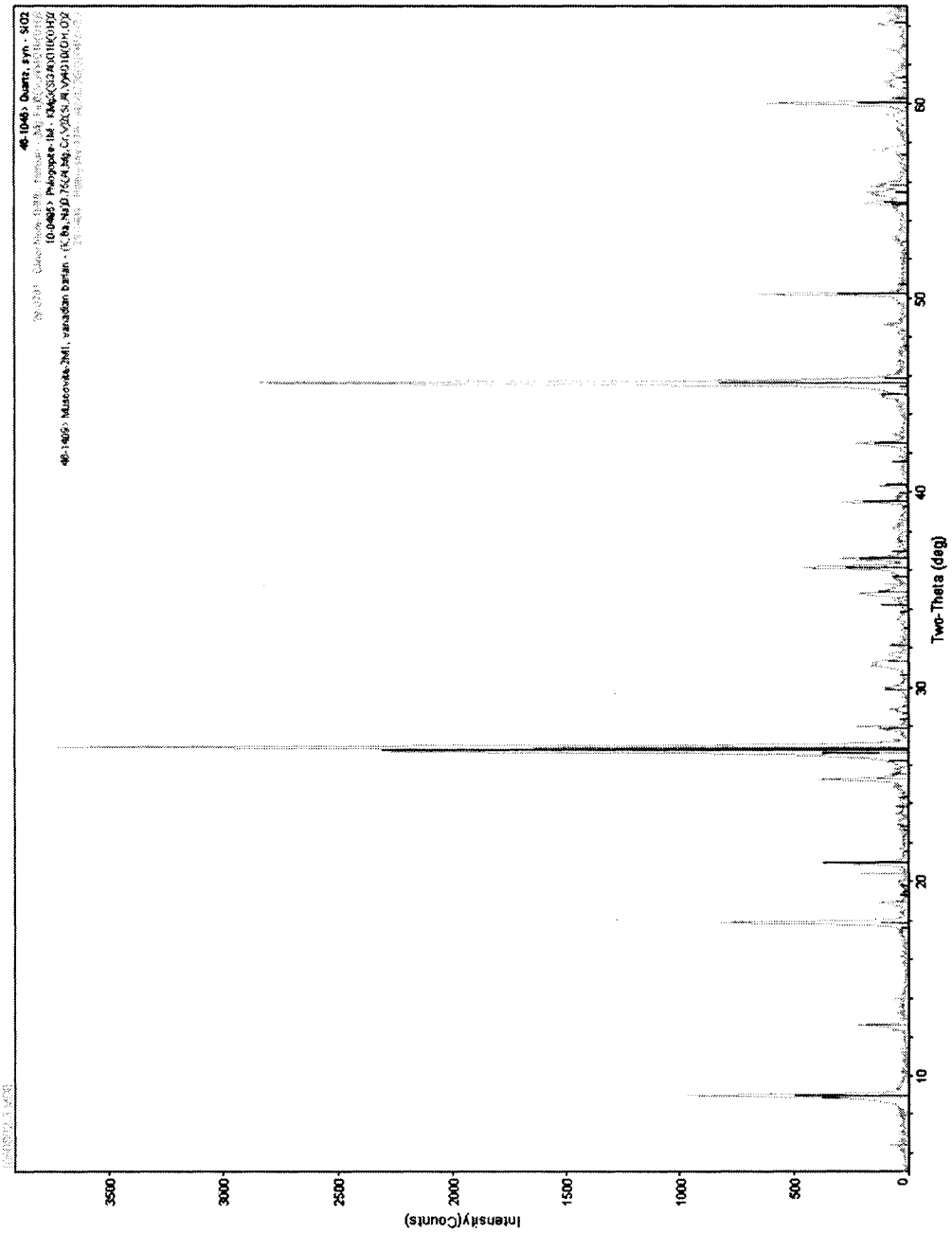


Figure 19. X-ray powder diffraction pattern for sample 040903-3, weakly weathered biotite schist with vermiculite.



DRD:\mhj\c:\Documents and Settings\mhj\CompLab\Wednesday, Sep 20, 2006 05:45p (481046.D)

.INSESE

Figure 20. X-ray powder diffraction pattern for sample 060802-3, muscovite schist.

mica schist' (250802-1) x-ray pattern shows several phlogopite types and no muscovite (Fig. 22-23).

In general x-ray patterns of micas at True North show several phlogopite species, chlorite, kaolinite group minerals (kaolinite or halloysite), and in one case, vermiculite, all of which suggests that none of the 'white' mica at True North is muscovite. Photomicrographs (Fig 24) of altered phlogopite schist demonstrate that altered phlogopite is non-pleochroic, has little to no color and iron oxides are clearly visible between micaceous layers. Viewed in thin section, samples from True North contain very little unaltered phlogopite. Most "fresh" phlogopite has been bleached and is no longer pleochroic. Thin sections of felsic schist mica occurrences also exhibit similar layers of iron oxides between micaceous layers (Fig. 25).

### **Summary of Schists and Definition of Map Units**

X-ray data on mica schist indicate no muscovite, leading to the conclusion that the light-colored micas are actually weathered or bleached biotite (phlogopite). Although dark micas are from the phlogopite end of the annite-phlogopite solid solution series, they will be referred to as biotite in this paper.

Based on the analysis of the mica schists, a new division of lithologic units at True North is proposed; 1) slate-argillite, 2) eclogite, 3) marble, 4) biotite schist, and 5) graphitic schist, all with descriptive prefixes as needed. Graphite in graphitic schist and slate-argillite samples was identified by XRD (without quartz) and all samples had a strong graphite peak. Unit seven, the 'white mica schist' is coarse-grained, strongly

weathered biotite schist that is noted for ground control purposes. These units are described in detail below. Petrographic details are in Appendix B.

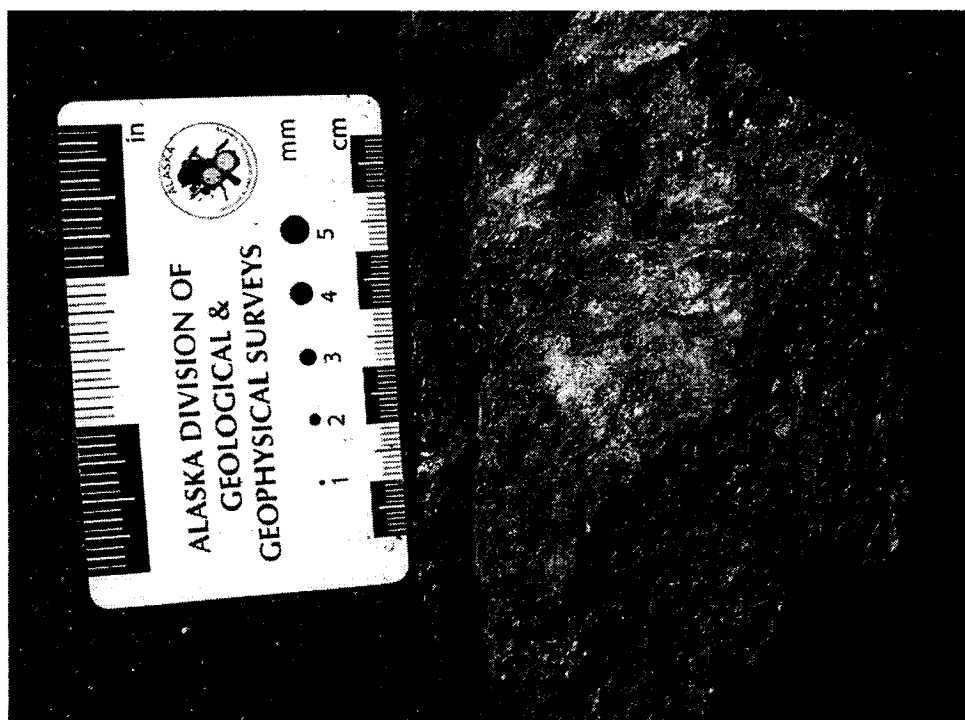


Figure 21. Muscovite schist, sample 060802-3.

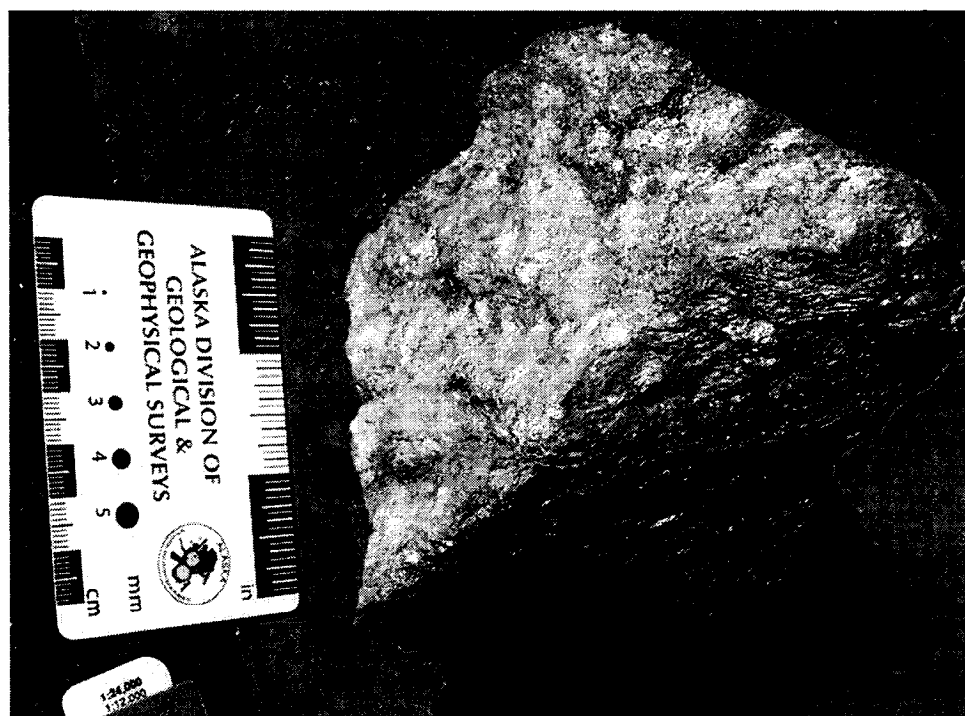
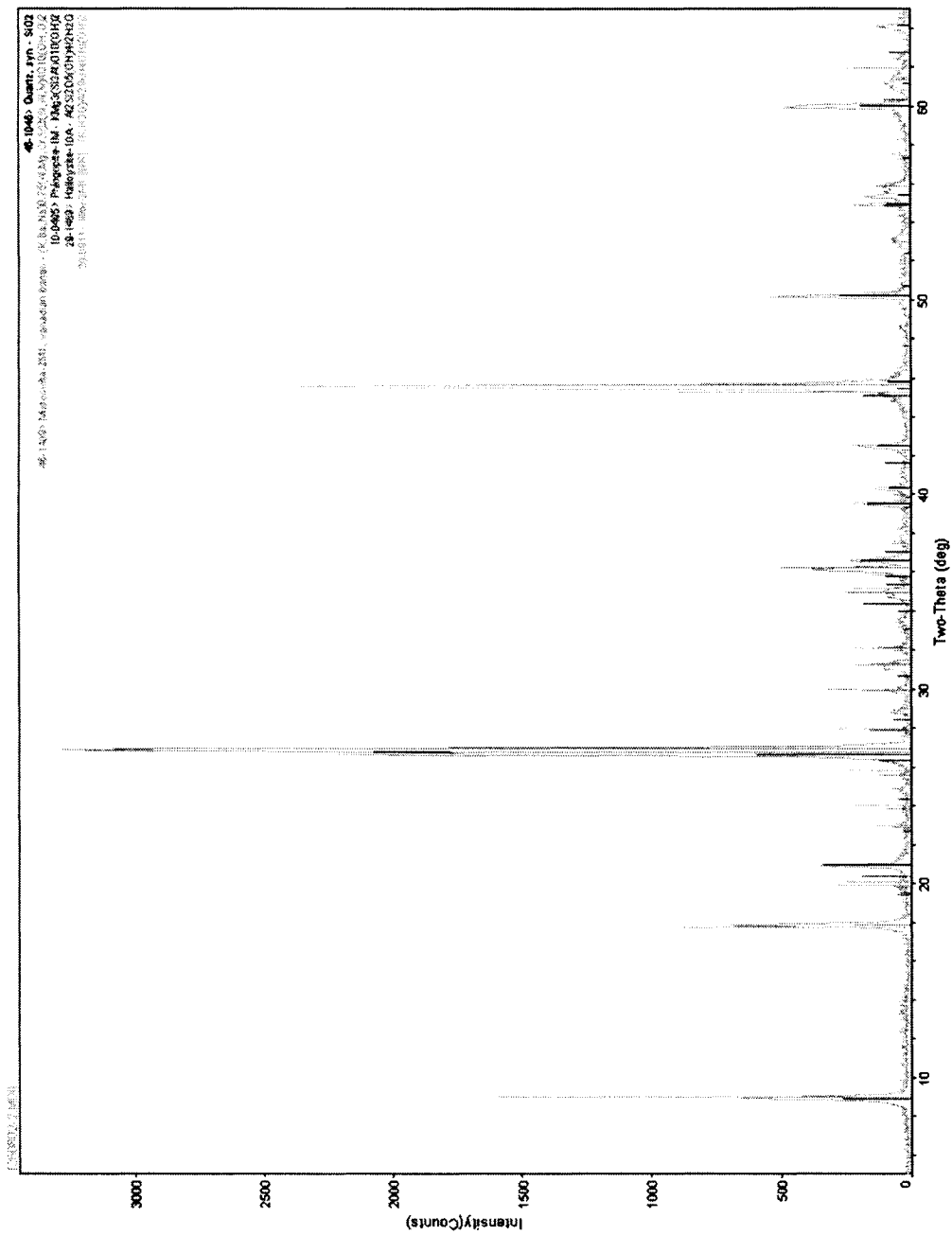


Figure 22. Coarse-grained muscovite schist (white mica schist), sample 260802-2

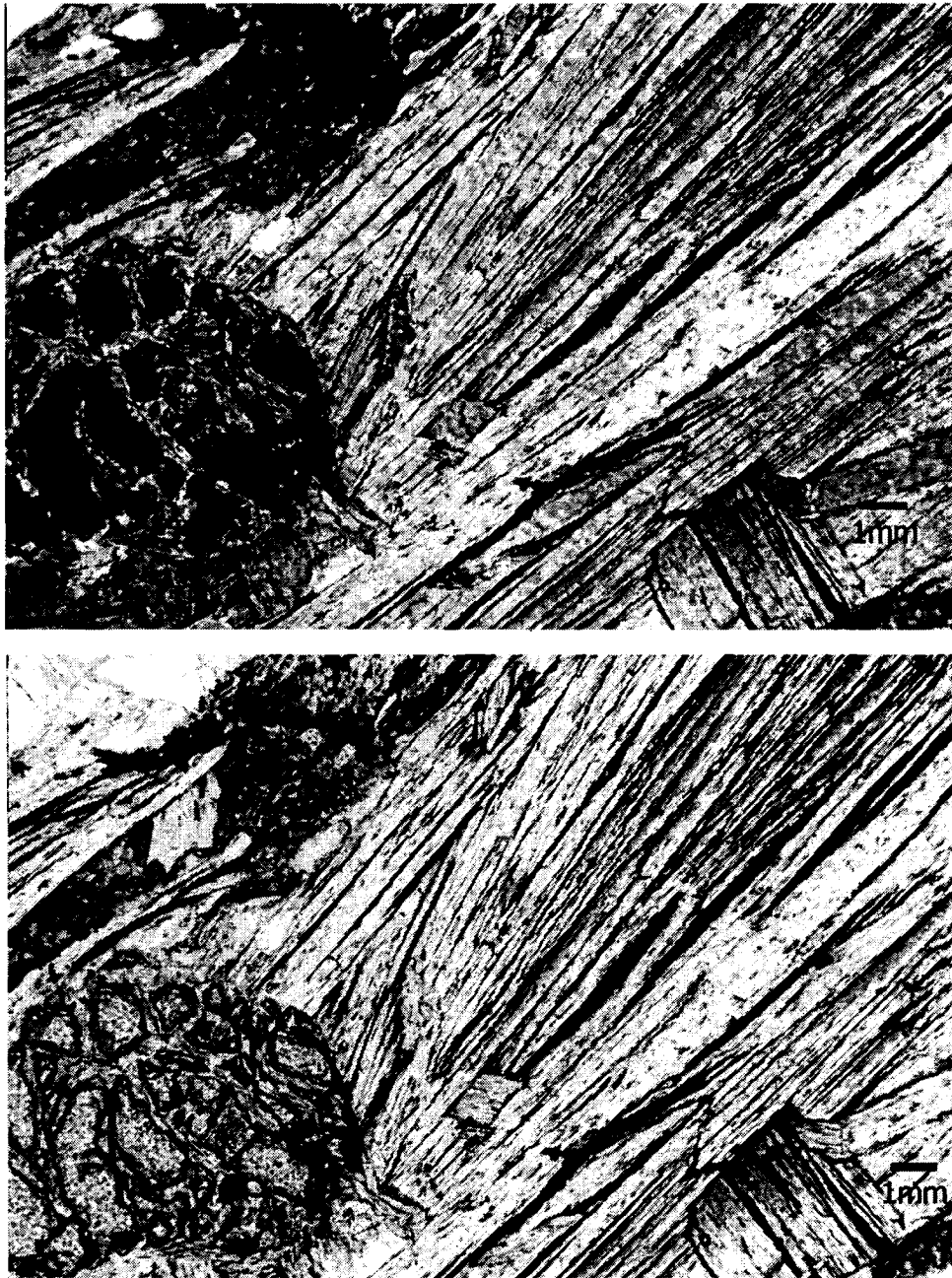


[PRD\kath] \c:\Documents and Settings\kath\Cambos - Wednesday, Sep 20, 2006 08:14p (MCI\JAD\B)

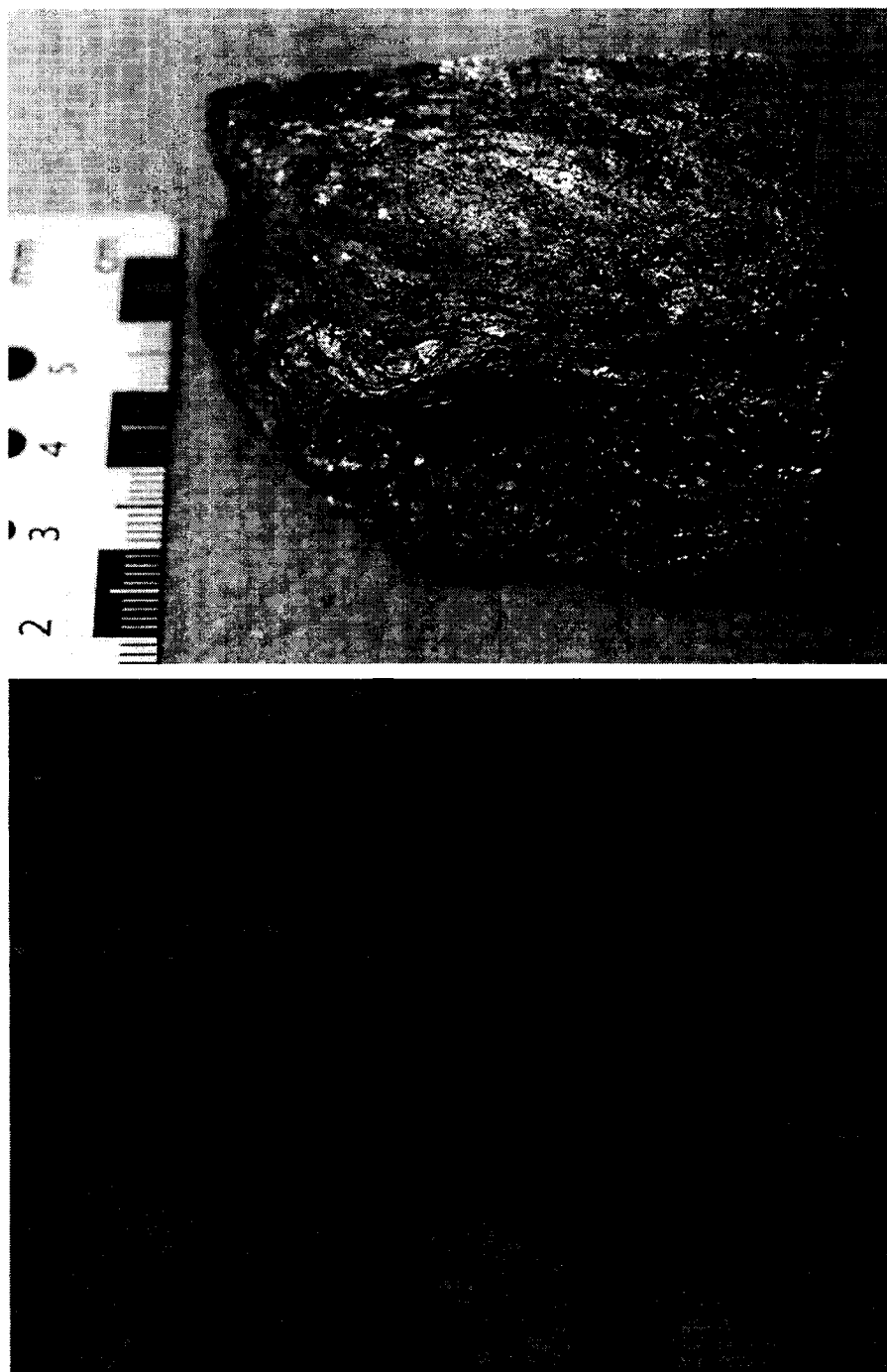
MSESE

Figure 23. X-ray powder diffraction pattern for sample 260802-2 coarse-grained muscovite schist (white mica schist).





**Figure 24. Photomicrograph of biotite-garnet schist sample 270802-2a. Top photo is crossed polars. Bottom is plane polarized light. Field of view is 1.33 mm. At lower left is a fragmented garnet. The phlogopite is non-pleochroic, and almost colorless.**



**Figure 25. 'white mica schist' (260802-1) Top photo is hand specimen. Lower is a photomicrograph in plane light, field of view of 2mm, showing the lack of color and iron-oxides/hydroxides between mica layers.**

## DESCRIPTIONS OF MAP UNITS

### **Lithologic Units**

Within the mine area, the various lithologic units show very little continuity, due to compositional variation, folds, and later faults. Most contacts between units are faults. Where contacts are exposed, eclogite grades into both amphibolite and marble, both of which may contain garnet, amphibolite or garnet-rich amphibolite grades into biotite-quartz-amphibole  $\pm$  garnet schist, which in turn, with increasing quartz, grades into quartzite. Amphibolite (actinolite schist) is also developed along faults (shear zones?) within eclogite bodies. These zones are truncated by all other faults in the mine exposures.

### **Slate-argillite Unit**

The slate to argillite unit occurs in the Shepard pit. It is dark grey to black, fine-grained, graphite-rich, with biotite-quartz lamellae and grades into quartzite with biotite lamellae (Figs. 26, 27, 28). It has a well-developed foliation and locally has poorly developed slaty cleavage. In thin sections of (Fig. 29) the slate-argillite, fine bands of chlorite or biotite alternate with quartz. The presence of chlorite and biotite in these units suggests that the maximum metamorphic grade is greenschist. Pyrite and iron oxides are present in many samples (Fig. 29). At the exposed base of the unit, along a fault contact with underlying biotite schist, carbonate flooding has occurred (Plate 1). The slate to argillite unit is of a distinctly lower metamorphic grade than the other rocks at True North and in the Shepard pit appears to have been tectonically imbricated with biotite schist.



**Figure 26. Shepard pit, 1300 bench: photo of slate-argillite, looking west. Bench height is 20'.**



**Figure 27. Detail of slate-argillite, 1300 bench, Shepard pit. Hammer is 32" tall.**

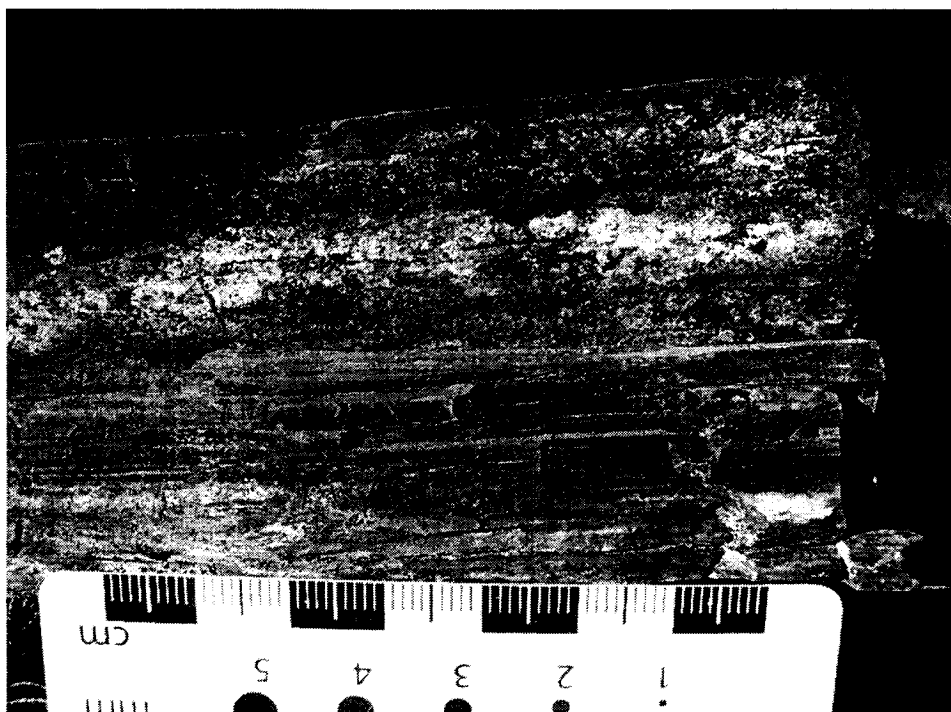


Figure 28. Slate-argillite hand specimen.

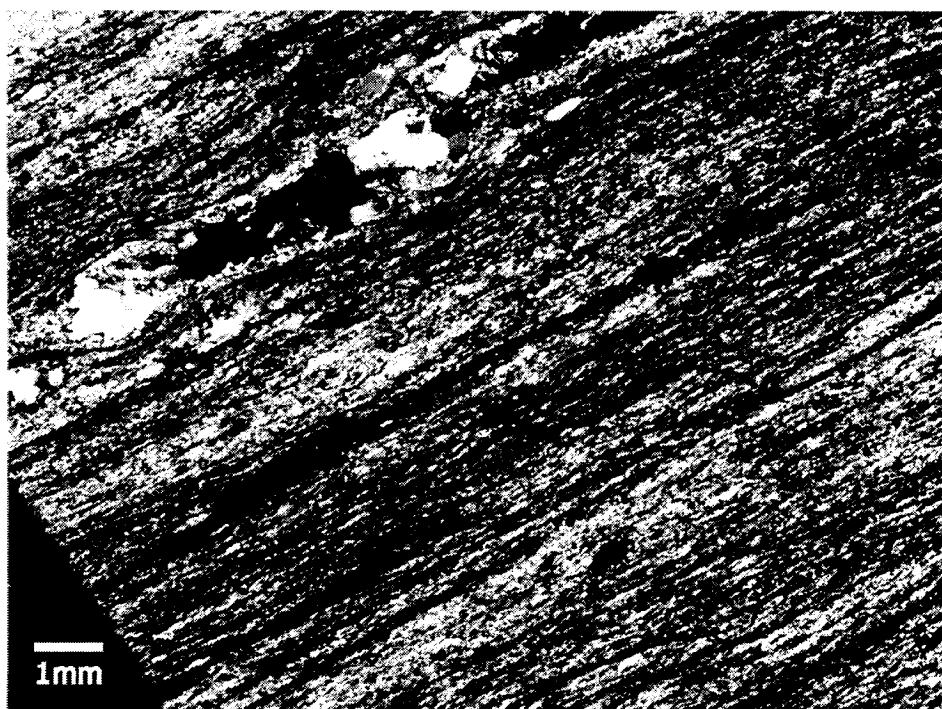


Figure 29. Photomicrograph of slate-argillite, plane light, 2mm field of view.

This unit resembles and is probably correlative with the Birch Hill sequence that crops out near the city of Fairbanks (Fig. 6, p.15). It is here excluded from the Chatanika terrane.

### **Eclogite**

Eclogitic rocks are garnet-rich with fine-grained pyroxene, and contain widely varying amounts of quartz, plagioclase (albite), amphibole, muscovite, biotite, chlorite, epidote, and rutile (Figs. 30, 31, 32). The eclogitic rocks also contain considerable calcite and may contain pyrite. All of the units of the Chatanika Terrane have undergone retrograde metamorphism to amphibolite and perhaps again to upper greenschist facies (Swainbank and Forbes, 1975). In thin section, eclogite contains garnet, amphibole, pyroxene relicts, albite, calcite, quartz. Chlorite, iron oxides, and trace amounts of sphene, apatite, graphite, magnetite, and tourmaline were also noted.

Compositions of garnets in six eclogite samples were obtained by scanning electron microscope, energy dispersive x-ray analysis (SEM-EDX). Along with oxygen, aluminum, and silicon the, garnets contain calcium, magnesium, iron, and titanium. This is in general agreement with the results of Swainbank (1971) who found silicon, aluminum, and in decreasing order of abundance, iron, calcium, magnesium, titanium, and manganese. Garnets in eclogite of the Chatanika terrane were defined as almandine to grossular, with 4 – 11% pyrope (Swainbank, 1971).

Due to the relatively low garnet and omphacite content, less than 75 percent combined garnet and omphacite by volume, and the presence of plagioclase, the “eclogite” rocks at True North are not true eclogites by IUGS classification

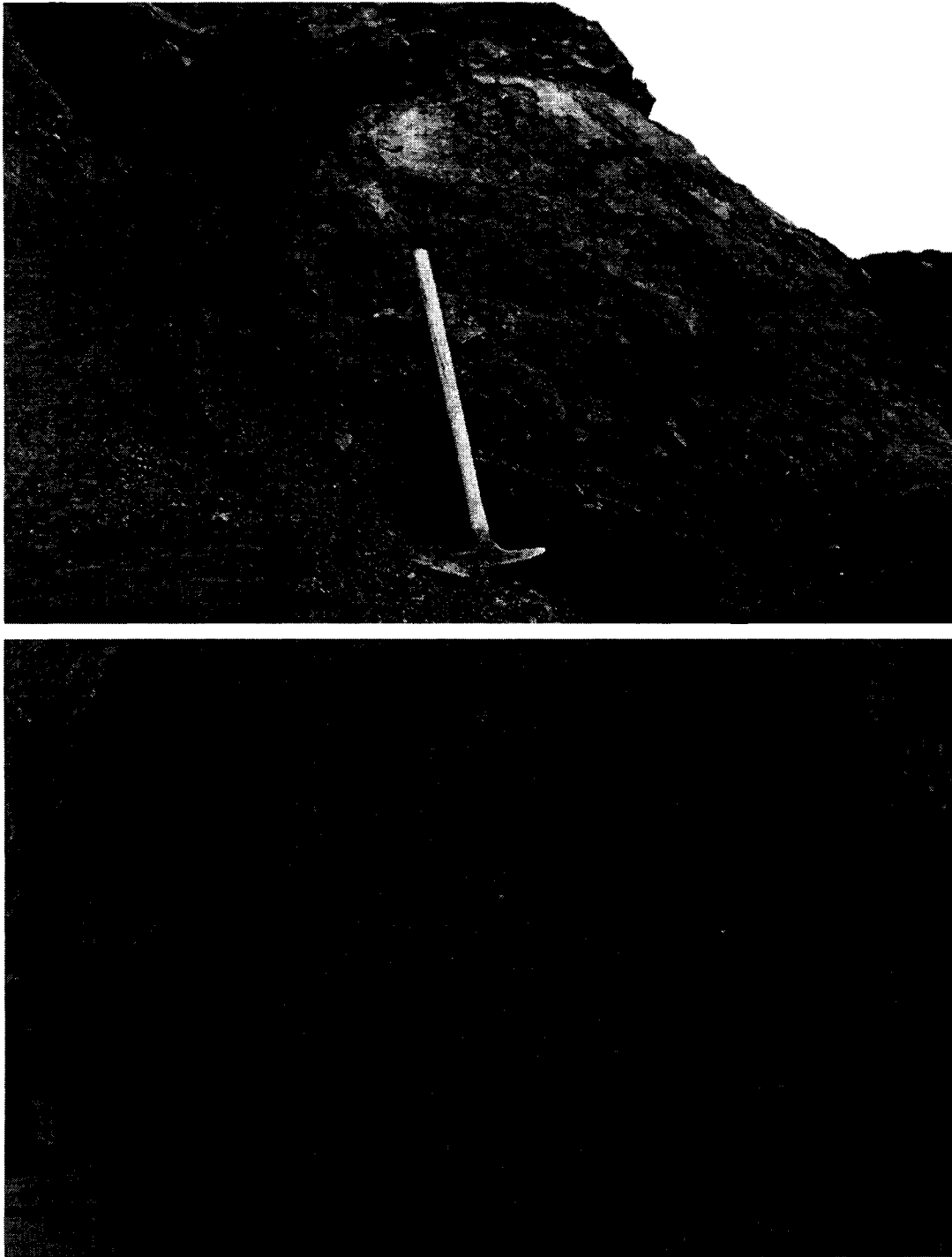


**Figure 30. Eclogite, Hindenberg 1420 bench looking north. Top shows eclogite pod in core of recumbent isoclinal fold, hammer is 32" in length. Lower photo shows detail of surface textures.**

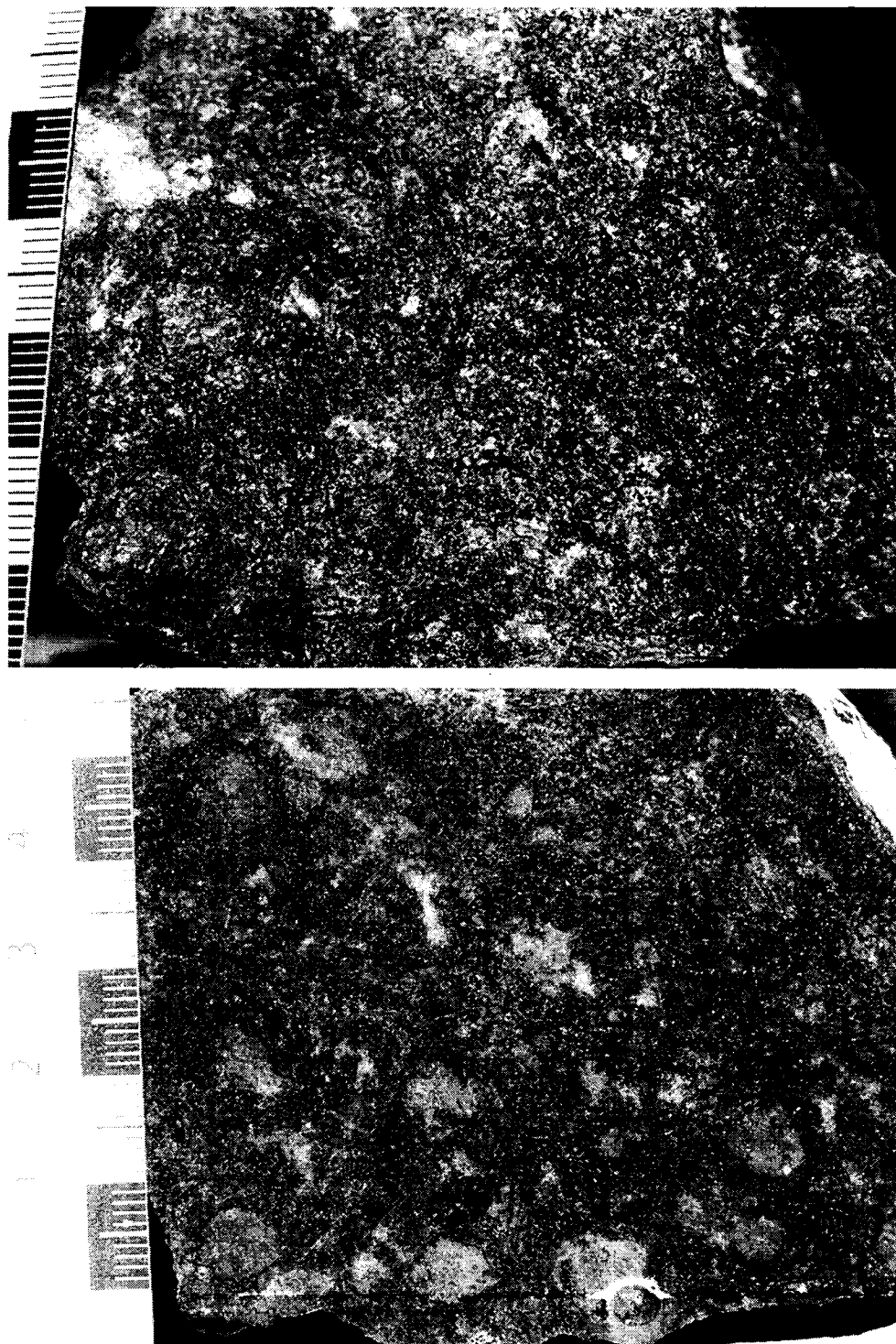


**Figure 31. Hand specimen of eclogite. Top photo is broken surface, lower photo shows sawed surface showing large pink garnets and groundmass of chlorite, pyroxene, amphibole, calcite, and albite.**



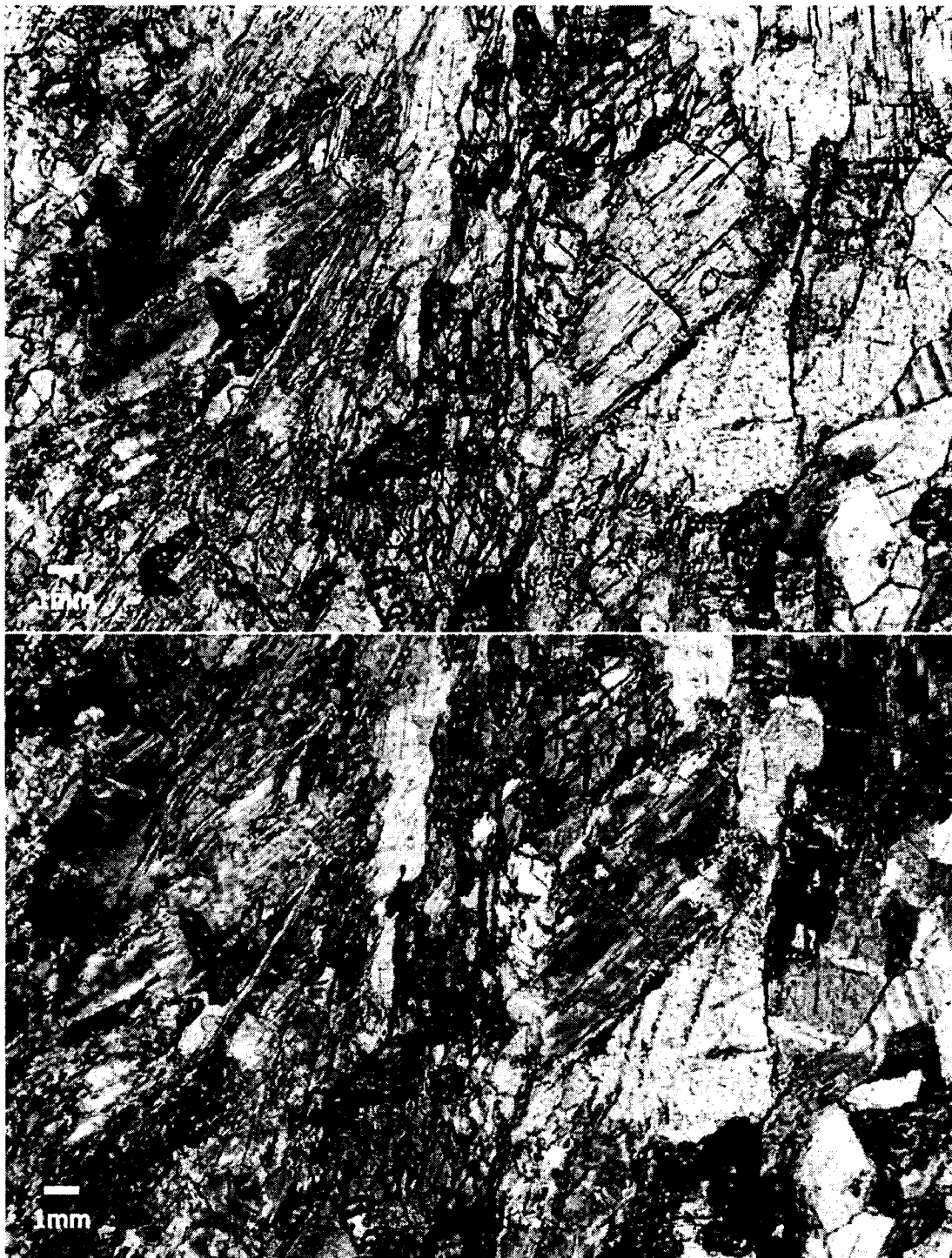


**Figure 32. Photomicrographs of sample EG-1 (same as previous figure). Shows garnet, amphibole, calcite, mica, and iron oxides. Field of view is 1.33 mm. Upper photo in crossed Nicols, lower photo in plane light.**

(Desmons and Smulikowski, 2004); rather, they are better described as “eclogite facies”. The term eclogite is used here as a mine unit name and is used to describe a generally massive eclogite facies metasedimentary rock that contains considerable calcite. Distinguishing eclogite from impure marble (also eclogite facies) is problematic in the field. While most of the units in the Chatanika terrane are thought to have been at eclogite facies temperature and pressure before retrograde metamorphism, only the massive units at True North are called “eclogite” (Forbes et al., 1968b; Swainbank, 1971; Swainbank and Forbes, 1975; Brown, 1986).

### **Actinolite Schist**

Shear zones containing strongly foliated actinolite schist (Figs. 33 and 34) occur exclusively within the relatively calcite-poor eclogite. Actinolite is aligned parallel to the shear direction and crosscuts eclogite textures. These zones are crosscut by brittle faults. Due to faults and weathering, pit exposures of these zones are difficult to identify or to trace for more than a meter or two.

### **Marble**

Marble is mottled medium to dark gray (Figs. 35 and 36) and contains relict pyroxene, amphibole, garnet, quartz, biotite, chlorite, magnetite, and pyrite in amounts from trace to several percent (Fig. 37), is massive to weakly foliated and locally contains sufficient magnetite to deflect a compass needle. Where present, foliation in marble is defined by aligned, sub- to euhedral phlogopite bands separated by zones of



**Figure 33. Actinolite schist, sample 230903-5.**



**Figure 34. Photomicrograph of actinolite schist showing fine-grained actinolite and carbonate, crossed Nicols, 2 mm field of view. Same sample as above.**



**Figure 35. Marble, 1340 bench, Shepard pit. 20' bench height. The marble is the blocky material cropping out on the left side of the photo.**

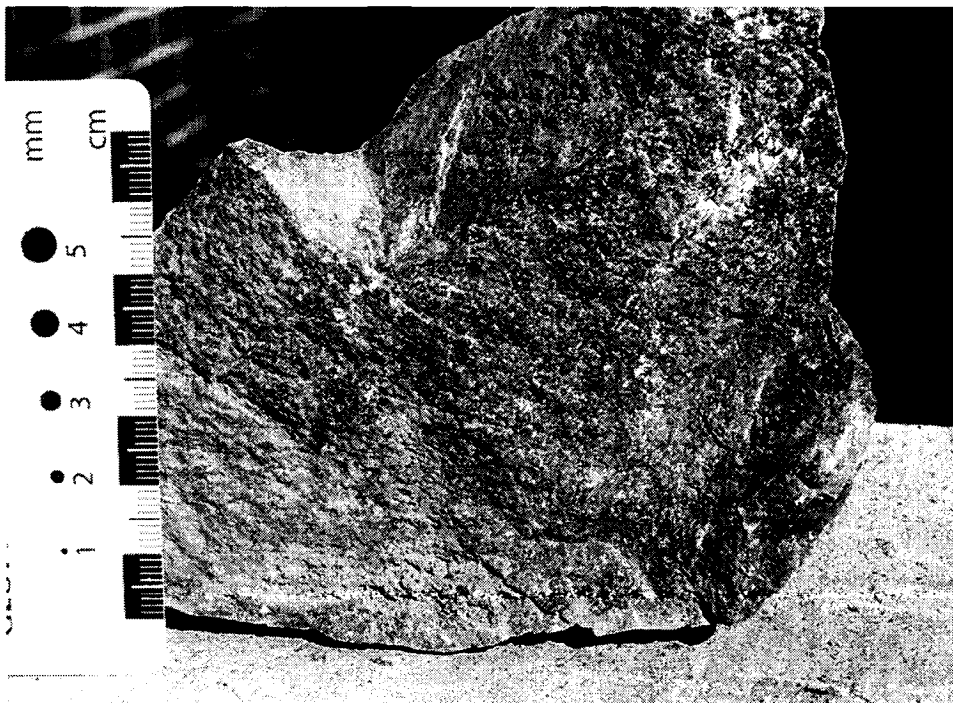


**Figure 36. Hand specimen of marble from Shepard pit, 1340 bench.**

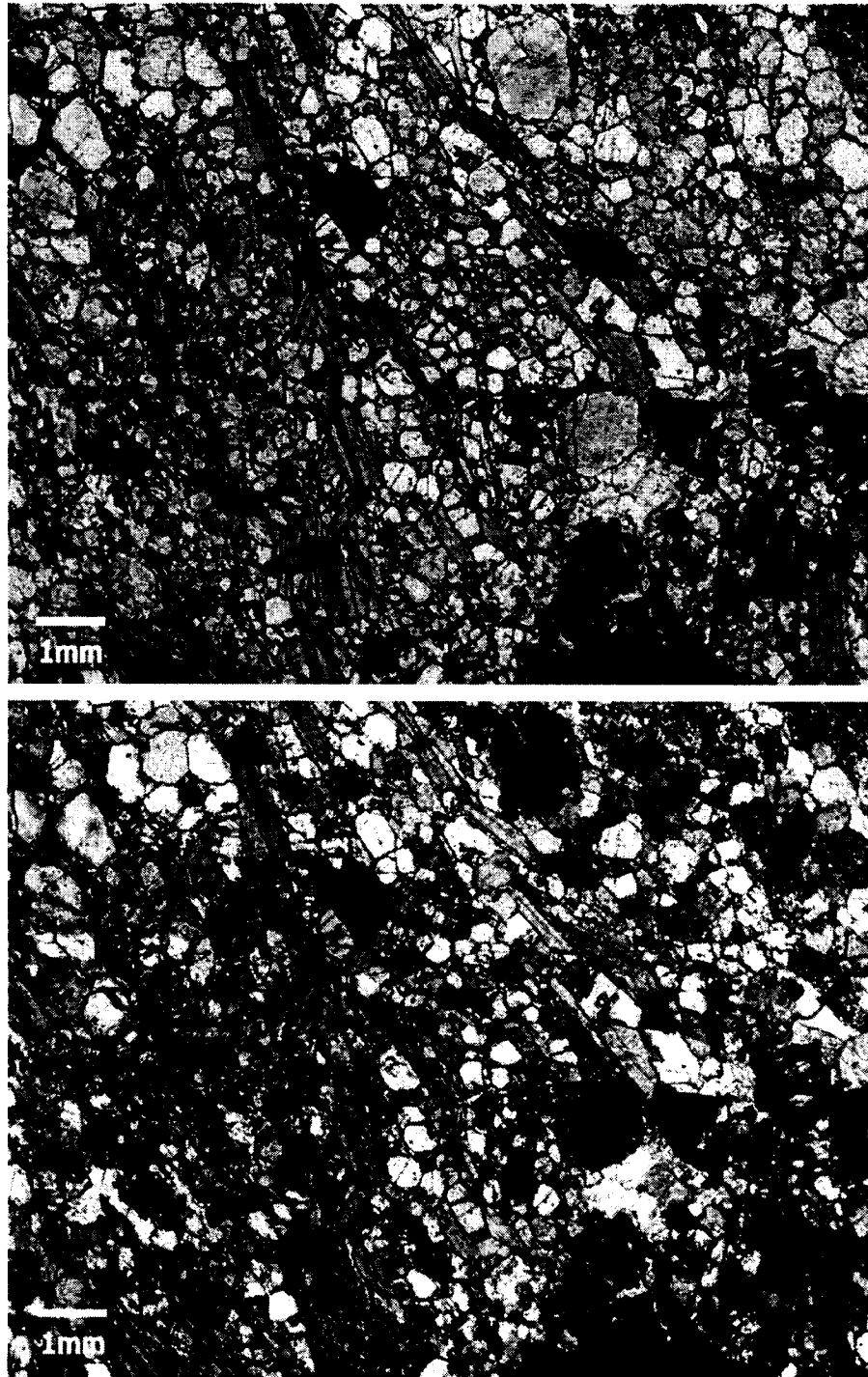


**Figure 37. Photomicrographs of marble; phlogopite, calcite, and apatite. Field of view 2 mm (upper photo with plane light, lower photo with crossed Nicols).**

recrystallized massive calcite. The impure marble tends to be only locally and weakly weathered.

### **Biotite Schist**

Biotite and biotite-graphite schists range in composition from nearly pure quartzite to biotite-graphite-amphibole-garnet-quartz-carbonate schist. The bulk of the exposures at True North are biotite schist.

Biotite-quartz schist and quartz-biotite schist have quartz contents ranging from less than 10 percent to nearly 100 percent (quartzite) and form a continuous series. The schists are strongly foliated, and interlayered quartz and biotite are the most visible minerals. Amphibole, graphite, plagioclase, garnet, pyrite, chlorite, and carbonate are present in minor amounts (Figs. 38-41). Local variations include biotite-amphibole schist (Fig. 42) and biotite-garnet schists that contain garnets as large as one centimeter in diameter (Fig. 43). Biotite schist in mine exposures is strongly weathered, with chlorite replacing garnet and amphibole.

In thin section, foliation in biotite schist is defined by aligned, subhedral biotite alternating with ribbons of recrystallized quartz (Fig. 41). Aligned biotite in biotite-amphibole schist crosscuts more massive amphibolite, suggesting that the foliation and biotite formed during retrograde metamorphism. Quartz-garnet-biotite schist has foliation defined by biotite-garnet bands, alternating with ribbons of recrystallized quartz (Fig. 43). Locally, in quartz-garnet-quartz schist, garnet appears to have been replaced by later, finer grained biotite, suggesting retrograde metamorphism.



**Figure 38. Biotite schist, 1260 bench, Central pit. Hammer is 32" long.**



**Figure 39. Biotite schist, Shepard pit, 1340 bench. Pencil is 5.5" in length.**



Figure 40. Biotite schist, sample 150903-1. Central pit, 1260 bench.

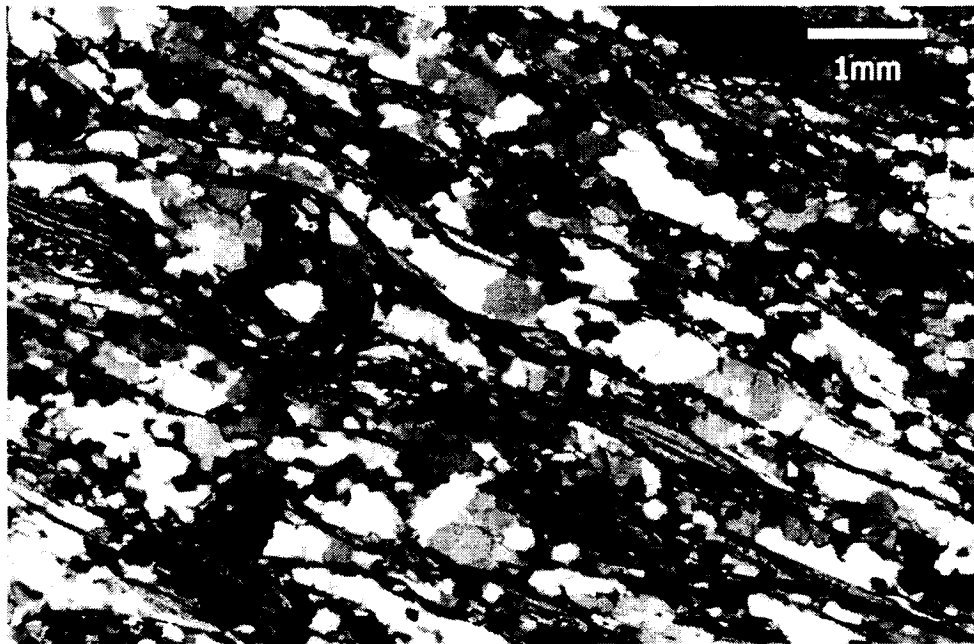
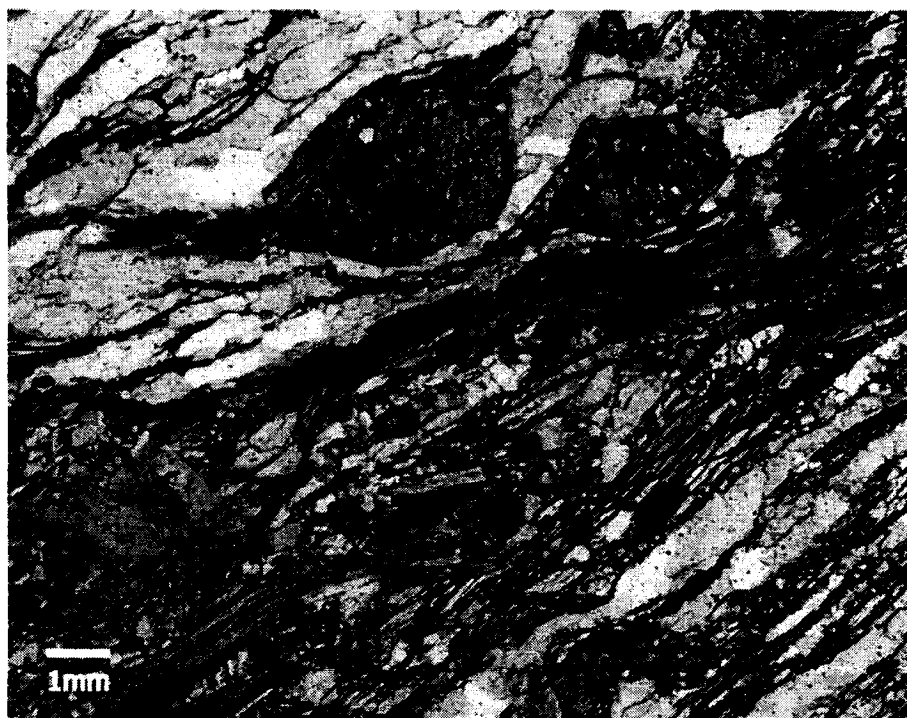


Figure 41. Photomicrograph of quartz-biotite schist. Field of view is 3.44 mm (crossed Nicols), sample 270602-1a.





**Figure 42. Photomicrograph of biotite-amphibole-garnet schist. Field of view is 1.33 mm, crossed Nicols.**



**Figure 43. Photomicrograph of quartz-biotite-garnet schist. Field of view is 2 mm, plane light.**

### **Graphitic Biotite Schist**

Graphite rich biotite-quartz  $\pm$  garnet interlayered with local quartzite is a sub-unit of biotite-quartz or quartz-biotite schist. Graphite rich schist forms a more or less continuous appearing mass near the center of the deposit, although it is most likely interlayered and folded with eclogite and biotite schist. Graphitic biotite schist occurs in the approximate center of the deposit (Plate 1) (Figs. 44 and 45). Because graphitic schist contains ore fluid feeder structures, discussion between Kinross geology staff and visiting mining industry and research geologists focused on whether graphite was formed from the hydrothermal fluids that generated the gold deposit. However, petrographic examination of samples of graphitic biotite schists shows that fine lamellae of graphite occur along foliation planes, with subhedral biotite and recrystallized quartz, that developed during metamorphism and before hydrothermal alteration (Figs. 46-47). Figure 46 also shows that the foliation in graphitic schist is finer, without distinct ribbons of recrystallized quartz and that it is cut by a crenulation cleavage, at a high angle to the older foliation (Fig. 46). Graphite that has been remobilized from this unit coats faults and fractures that have been mineralized in the Hindenberg Pit (Figs. 48-49).

### **White Mica Schist**

A second sub-unit of the biotite-quartz schist, the white-mica schist, has been mapped because of its importance in ground control efforts at True North. This unit is extremely incompetent, and several failures have occurred along the faults that bound this unit. White-mica schist is restricted to areas near major faults and/or close to the pre-

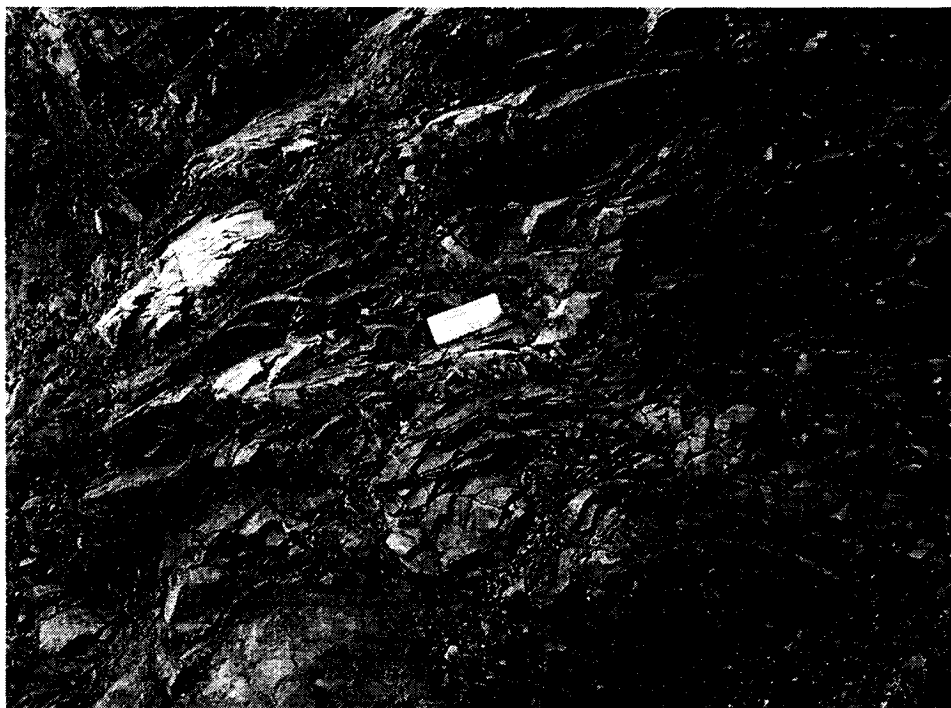


**Figure 44. Graphitic schist, 1280 bench of Shepard pit, looking southeast.**

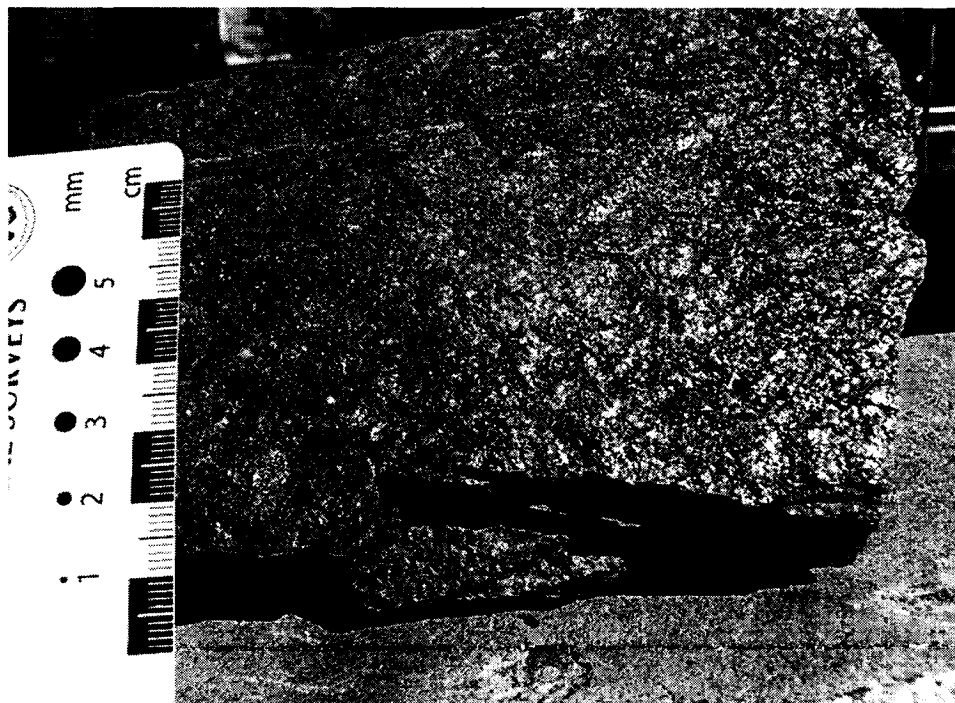


**Figure 45. Detail of graphitic biotite schist (sample 150903-3). Central pit, 1280 bench.**

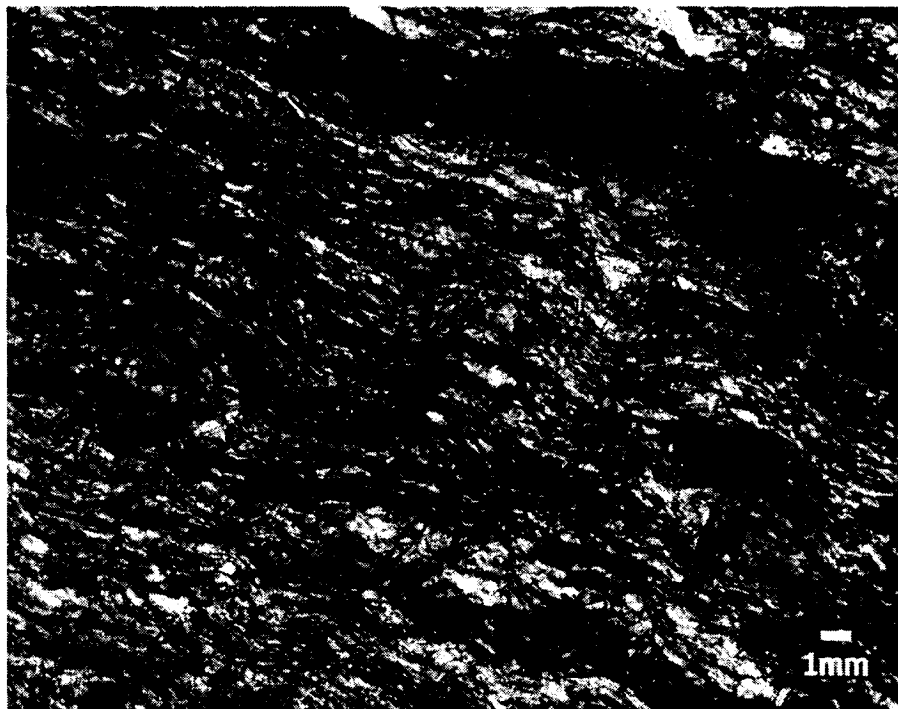


**Figure 46.** Graphite along foliation in graphitic biotite schist (plane light, field of view 0.85 mm, sample 180903-3a).



**Figure 47.** Graphite folded with biotite (bleached) and quartz (plane light, field of view 2 mm, sample 200703-2).



**Figure 48. View looking southwest, Hindenberg pit (2002), showing orange and black coloration along oxidized faults, and alteration zones. Graphite (black) defines low- and high-angle fault zones. Bench height is 20 feet.**

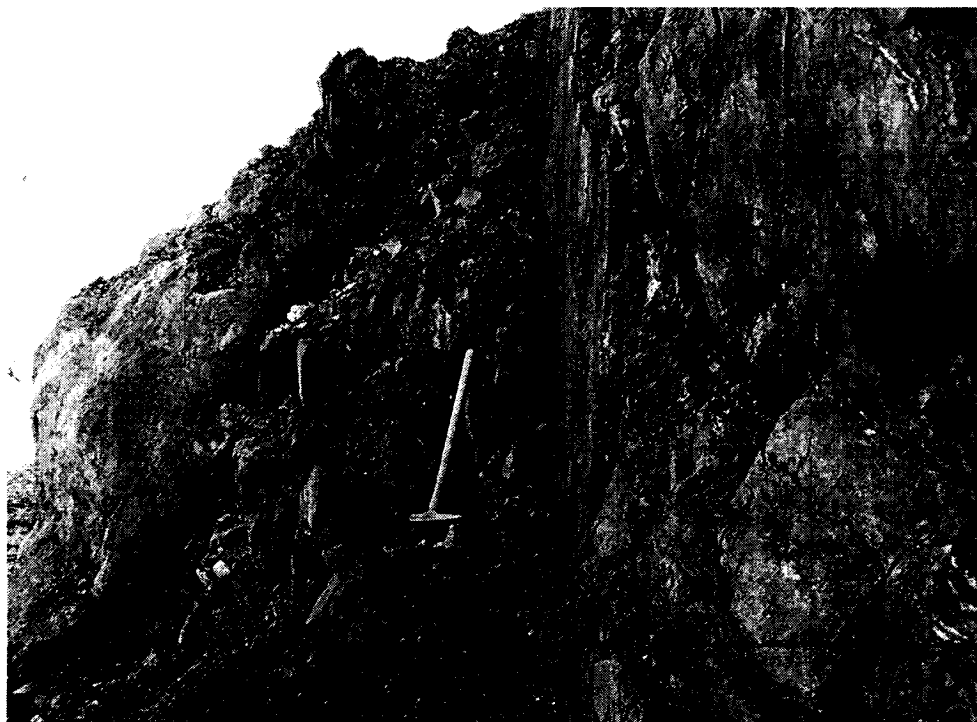


**Figure 49. Detail of fault coated with graphite in the fault zone and along the footwall (right center). Hindenberg pit, 1260 bench, hammer is 32" long.**

mine surface (Plate 1). Whit mica schist is relatively coarse-grained, strongly iron-stained mica schist.

#### **Amphibolite (Amphibole Biotite Schist)**

Amphibolite is a mine unit name used to describe an amphibole rich subunit of biotite schist, made up of hornblende, biotite, plagioclase, quartz, epidote, and chlorite with trace amounts of pyrite, and garnet (Figs. 50-51). Amphibolite is much less common than mica schist and does not constitute a mappable unit. As mentioned previously, foliation defined by subhedral biotite cuts massive to poorly foliated amphibolite, suggesting that the biotite and foliation represents retrograde effects. Most outcrops are strongly weathered, with chlorite replacing most of the hornblende.

#### **Distribution of Units**

The general distribution of units in the mine exposures is shown on the geologic map of the True North mine (Plate 1). This map is based on the dominant lithologic units in each area. Due to the considerable variation within each unit in addition to folds and faults, the units described are complexly interleaved. Overprinting by hydrothermal alteration and later by weathering further obscures the relationships between units. The actual outcrop patterns and contacts are considerably more complex than is shown at this scale.

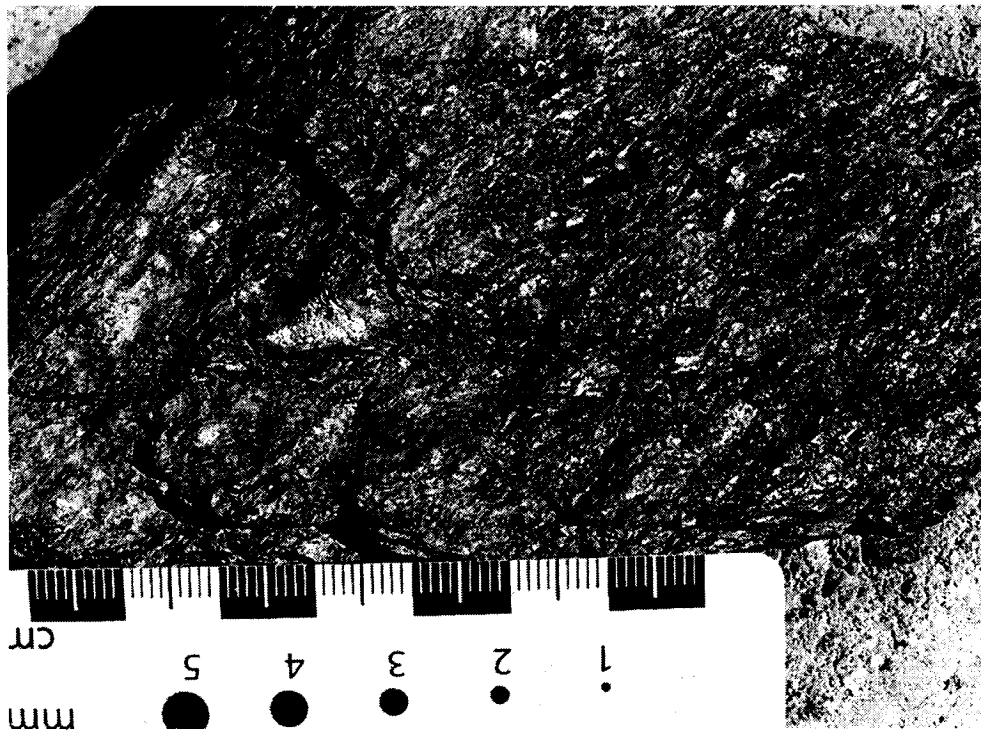


Figure 50. Hand specimen of amphibolite-biotite-carbonate schist, sample 060802-4. Hindenberg pit, 1360 bench.



Figure 51. Photomicrograph of sample 060802-4 showing crudely aligned hornblende, biotite, and calcite. Field of view is 1.33 mm, crossed Nicols.

## STRUCTURE

The contact between the Chatanika Terrane and the Fairbanks schist to the south and west is a west-northwest trending thrust fault that has been offset by northeast-trending high angle faults (Fig. 52). The high angle fault segment near the True North mine is the Eldorado fault (Plate 1).

### Metamorphic Foliation and Folds

Rootless folds and lack of sedimentary features (graded bedding, cross bedding, or soft sediment deformation features) indicate that compositional layering in the pit exposures is metamorphic foliation, not bedding (Fig. 53). This is the earliest foliation ( $S_1$ ) identified at True North. In thin section,  $S_1$  foliation in biotite schist is defined by aligned, subhedral biotite alternating with ribbons of recrystallized quartz (Fig. 41). Garnet-rich biotite schist (Fig. 42) has similar biotite and quartz foliation, with biotite wrapping around garnets.  $S_1$  foliation and  $F_1$  folds formed during peak metamorphism. Figure 53 illustrates a possible  $F_1$  fold, with highly thinned limbs and considerable thickening in the hinge.

The fabrics described above are folded into recumbent isoclinal folds ( $F_2$ ) that have northwest and northeast trending hinge lines; isoclinal folds are visible at scales from centimeters to tens of meters (Fig. 54). Isoclinal  $F_2$  folds are defined by folding of  $S_1$  foliation and are post peak metamorphism.  $S_2$  foliation is weak to nonexistent. The  $F_2$  isoclinal folds are refolded by upright open folds ( $F_3$ ) that generally have northeast trending hinge lines, and are locally visible in pit exposures. A locally developed crenulation cleavage ( $S_3$  ?) crosscuts  $S_1$  foliation (Fig. 46).





Figure 52. Map grid is one mile. See next page for explanation. Newberry et al., 1996.

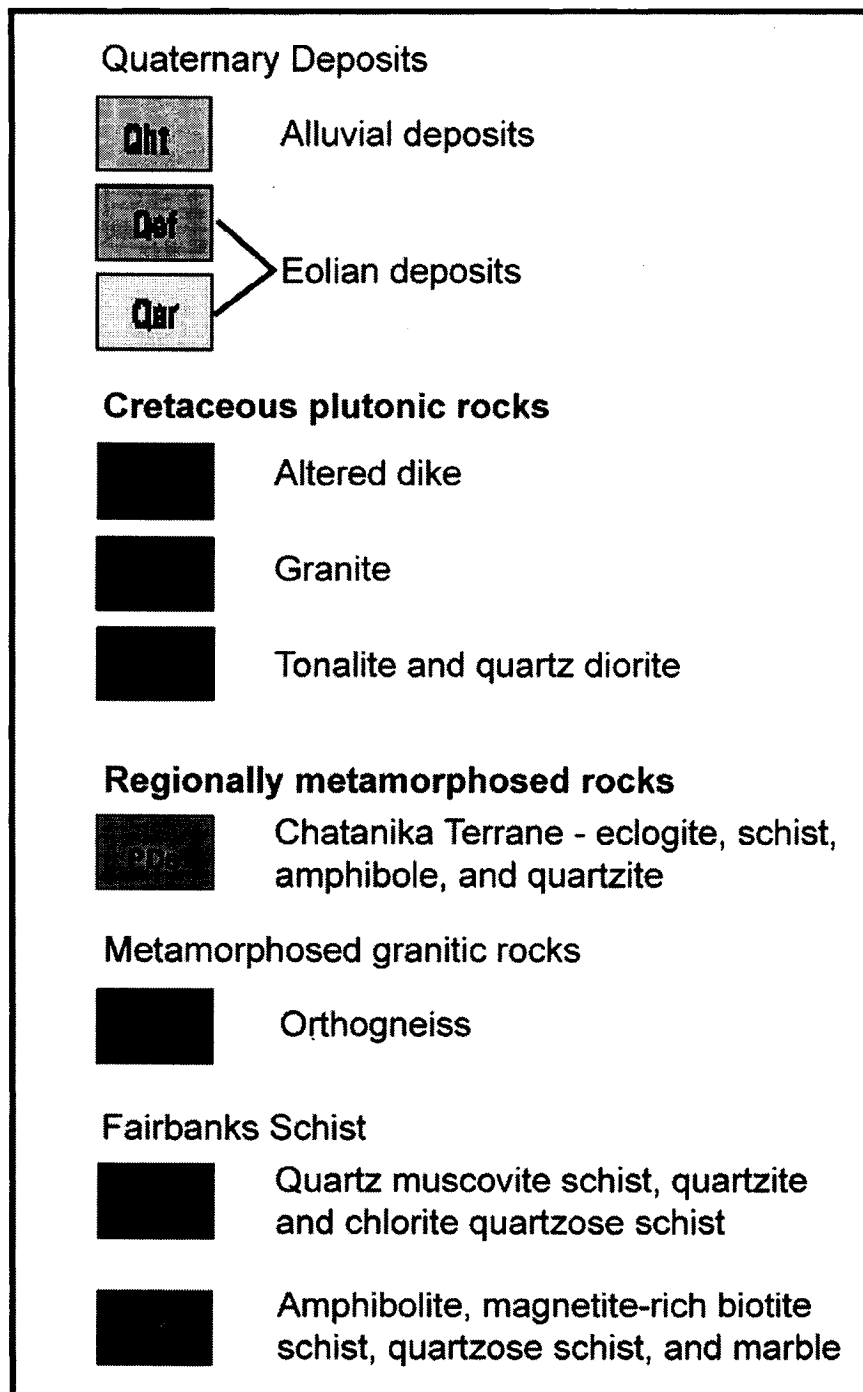


Figure 52a. Explanation for the detail of the district map by Newberry et al., (1999). The Chatanika terrane is PDe. Note the thrust fault along the southern and western boundary of the Chatanika terrane and that it is offset by northeast-trending faults.

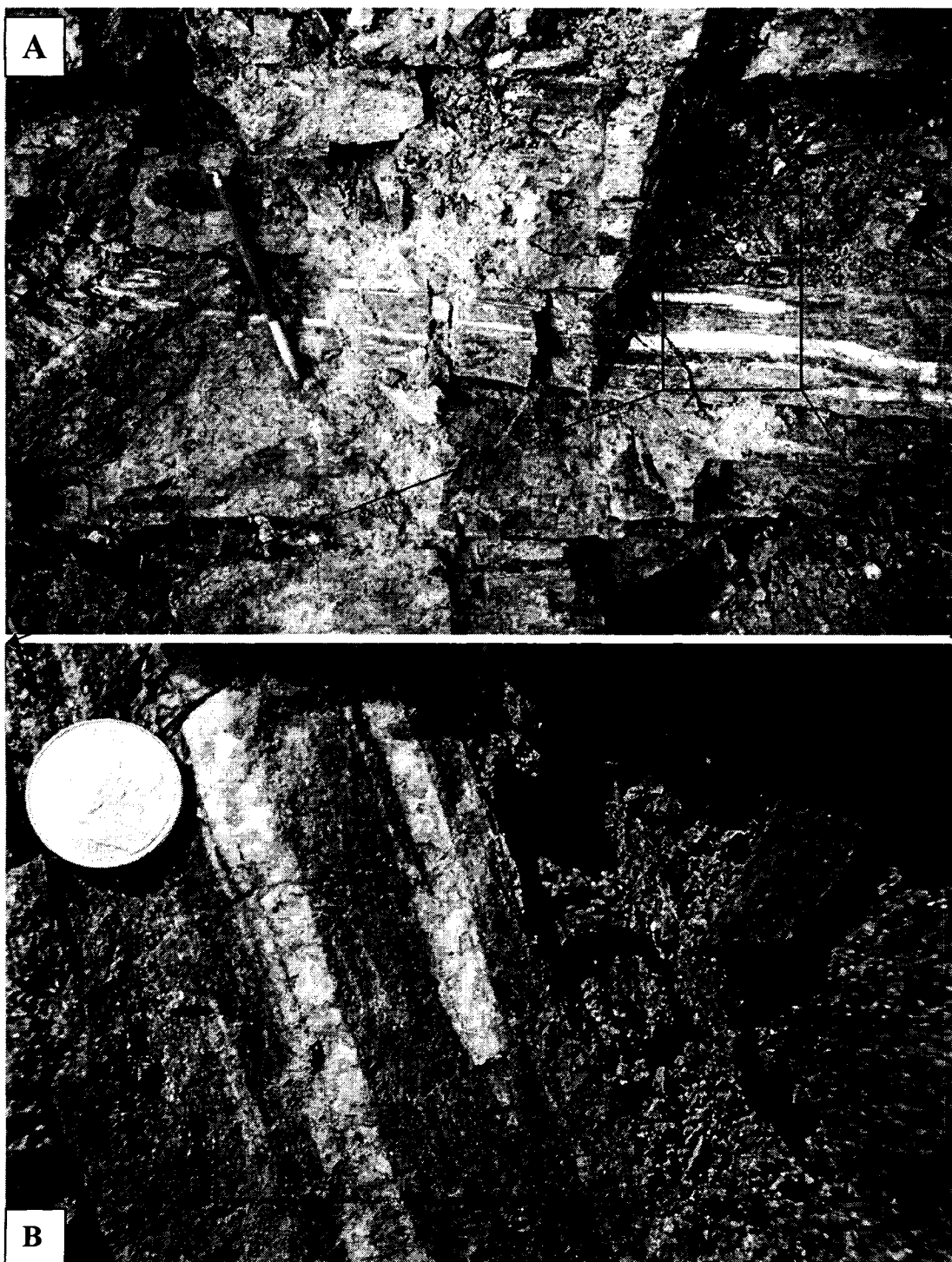


Figure 53a. Rootless  $F_1$  fold in biotite schist, pencil is 5.5" in length.

Figure 53b. Detail of folded quartz band in biotite schist.



**Figure 54a. 2 mm scale fold of biotite ( $F_1$  ?) (plane polarized light).**



**Figure 54b. Centimeter scale isoclinal  $F_1$  folds.**



**Figure 54c. Meter-scale  $F_2$  isoclinal fold of biotite bands in quartz-biotite schist. Hindenberg pit, 1440 bench.**



**Figure 54d. Multi-meter scale recumbent isoclinal  $F_2$  fold of biotite-quartz schist with quartz core. Hindenberg 1360 bench. Hammer is 32" in length.**

During  $F_2$  folding, the eclogite behaved in a rigid manner and is present as boudins, lenses and pods, or locally in the cores of folds. However, in most of the eclogite exposures, the combination of complex foliation patterns, faults, and weathering make it difficult to tell if the eclogite is the cores of folds or is present as lenses within a metamorphic fabric.

### **Faults**

Three sets of faults cross-cut the folds. These include a low-angle fault set and two sets of high-angle faults, one northeast trending and the other north-northeast to northwest trending (Plate 1 and Plate 3). Low-angle faults are the earliest, and are cut by both high-angle fault sets. Northeast-striking high-angle faults are cut by the north-northeast to northwest-striking faults. Low-angle faults are extremely variable in strike and dip, with undulating fault surfaces. Northeast striking faults have more consistent strikes and dips. North-northeast to northwest striking faults are highly variable in both strike and dip.

In the Hindenberg and Central Pits, low angle faults generally have northwest strikes and northeasterly dips, although they are highly variable due to the tendency of fault surfaces to follow foliation and deflect around lenses of eclogite and quartzite. In pit exposures these faults occur in sets of sub-parallel faults connected by higher angle ramps (Fig. 48). Most of these faults are zones of graphitic gouge, tens of centimeters to several meters wide, coalescing, and bifurcating to form complex anastomosing patterns. Local zones of brecciation lay just outboard of the central gouge zone, or between fault zones. The gouge is clay-sized material that is half a meter to several meters thick and

exhibits a strong laminar fabric much like schistosity. Low-angle fault zones both parallel and crosscut foliation. Many low-angle faults in the Hindenberg and Central Pits are mineralized. In the Shepard Pit, a single prominent, mineralized, low-angle fault separates biotite schist/eclogite units from slate-argillite (Plates 1 and 3).

Within the damage zones of low-angle faults, kinematic indicators suggest varied slip directions. The presence of gouge and breccia, and the width of the damage zones suggest that the low-angle faults are brittle features, had repeated periods of movement, and that considerable fluid flow occurred along the faults. The low-angle faults at True North are interpreted to be sub-parallel to and related to thrust faults that initially placed the Chatanika terrane over the Fairbanks schist, but they may have subsequently been reactivated as low-angle normal faults.

Low angle faults in the Hindenberg and Central pits are crosscut by a set of northeast-striking, nearly vertical faults that tend to be localized in the center of the Hindenburg pit. These faults also truncate foliation at a high angle

Northeast-striking high-angle faults together form a zone of between one hundred feet wide in the Hindenberg Pit to less than twenty feet wide in the Central Pit. Individual faults contain centimeters to one meter of breccia and gouge, and many are marked by graphitic zones (Plate 1 and Fig. 49). Within this zone, little to no foliation and folds are preserved; however, several segments of graphitic low angle faults can be seen. Northeast-striking high-angle faults are mineralized and the central part of the Hindenberg and Central pits, where the high-angle faults are closely spaced, is the richest part of the True North deposit. The central part of the Hindenberg and Central pits is also very strongly weathered.

Northeast-striking high-angle faults are sub parallel to and are interpreted to be related to the district scale, northeast left-lateral oblique faults shown on Figure 52, although movement on these faults is complex. Locally graphite coated fault surfaces have lineations (grooves) indicating three stages of movement; dip-slip, hanging wall up to the northeast 20 degrees and hanging wall down to the northeast 35 degrees, all within twenty meters.

North-northeast to northwest striking faults are relatively clean fractures, with little gouge, and open spaces along them are locally filled with transparent calcite crystals. This group of faults crosscuts the first two fault sets.

In the Hindenberg and Central pits, northeast-striking faults offset mineralized faults a few centimeters to a meter. In the Central Pit, biotite schist is truncated by a northeast striking, 40° west-dipping reverse fault (Plate 1). This fault juxtaposes slate-argillite against biotite schist, contains no gouge, and is post mineral.

In the Shepard Pit, one of the three mineralized faults is a north-south striking reverse fault that dips 65° to the east (Plate 1). In the southern part of the Shepard Pit, this fault puts biotite schist, eclogite, and marble over slate-argillite. It also truncates the mineralized low-angle fault in the center of the Shepard Pit (Plate 1). The third mineralized fault in the Shepard Pit is an east-northeast striking, 65° northwest dipping fault, offset by a post mineral normal fault, entirely within argillite-slate (Plate 1 and Fig. 48). Mineralization is restricted to a breccia zone that is one or two meters wide and centered on the fault.



## VEINS

Two general types of veins are present in the mine exposures at True North, quartz veins and carbonate veins. The quartz veins can be divided into two types, those related to metamorphism and those related to the mineralizing events.

Metamorphic quartz 'veins', actually thin quartz bands or lenses parallel to foliation, tend to be randomly scattered through the area and are composed of massive white to grey quartz, tens of centimeters to tens of meters in length; they are locally folded (Fig. 55).

Quartz veins associated with the mineralizing events lie along or are parallel to the low-angle faults, or lie within or parallel to the northeast striking high-angle faults (Plate 1 and Fig 56).

Quartz in hydrothermal quartz veins is transparent to pale white in color, has open-space filling textures, may be vuggy, and locally contains sulfides, dominantly stibnite, and arsenopyrite. There are a number of generations of quartz veins in the fault sets, with earlier ones broken and dismembered by later fault movement. Most quartz veins contain graphite in or along them.

A typical vein in the oxidized portion of the Hindenberg pit consists of small quartz fragments in a graphitic, orange colored, oxidized mass of loose fragments in the larger damage zone of a fault (Fig. 57). Limited arsenopyrite with gold is disseminated in the altered schist around or between vein sets.

In the Shepard pit, the host rock is the slate/argillite unit, which is both less reactive to the ore fluids and has much lower porosity and permeability. There, the veins are restricted to the narrow damage zones of faults and show little alteration and no



**Figure 55a. Metamorphic quartz vein in biotite schist.**



**Figure 55b. Small, folded metamorphic quartz vein in biotite schist.**



**Figure 56a. Hydrothermal quartz vein along a high-angle fault with graphite on the footwall. Vein is in lower center of photo and extends up along side the footwall. It is 10-15 cm wide. Hindenberg, 1320 bench.**



**Figure 56b. Hydrothermal quartz vein within a low angle fault. It has been brecciated by later fault movement. Hindenberg pit, 1340 bench. 32" tall hammer in center of photo.**



**Figure 57a. Low angle fault system. Hindenberg, 1480 bench. Faults are defined by graphite seams. 20' bench height.**



**Figure 57b. Closer look at low-angle fault-vein system. Same outcrop. Pencil for scale.**

disseminated mineralization (Fig. 58). In common with the Hindenberg pit, veins in the Shepard pit have been shattered and dismembered by later fault movements.

### **Paragenesis**

The paragenesis of productive quartz veins is as follows. The quartz is the earliest stage forming euhedral crystals that grow out into the center of the vein. Early (?) veins are more massive and lack well-formed euhedral quartz crystals but contain arsenopyrite, pyrite, and stibnite. In later (?) veins stibnite fills in around euhedral quartz crystals, and arsenopyrite and pyrite are found in the alteration halos that surround the veins (Fig. 59).

Carbonate veins, as with the quartz veins, consist of a number of generations. The observed types are massive translucent, massive white, banded white, pale brown and yellowish carbonate. In outcrop the massive translucent calcite veins are the oldest, crosscut by the banded veins and by at least three generations of brown to yellow weathering dolomite-ankerite veins (Fig. 60) these are in turn crosscut by massive white calcite veins. In the banded veins coloration tends to be due to the composition and the degree of weathering. Dolomite and ankerite weather cream to yellowish brown with increasing time. Calcite yellows somewhat with weathering. In hand specimen, staining with alizarin red S and potassium ferricyanide (Hitzman, 1999), indicates that at least at a local scale the earliest veins are very fine calcite, followed by massive white dolomite, then by banded ankerite. The last stage, ankerite, cuts both earlier veins (including quartz-sulfide) and the silica-carbonate alteration halo (Fig. 59a). Isolated instances suggest that later calcite veining crosscuts the dolomite and ankerite veins. On a mine



**Figure 58a.** Shepard pit showing the traces of faults defined by graphite. The blue normal fault offsets the red, mineralized, fault. Bench height is 20', looking southwest.

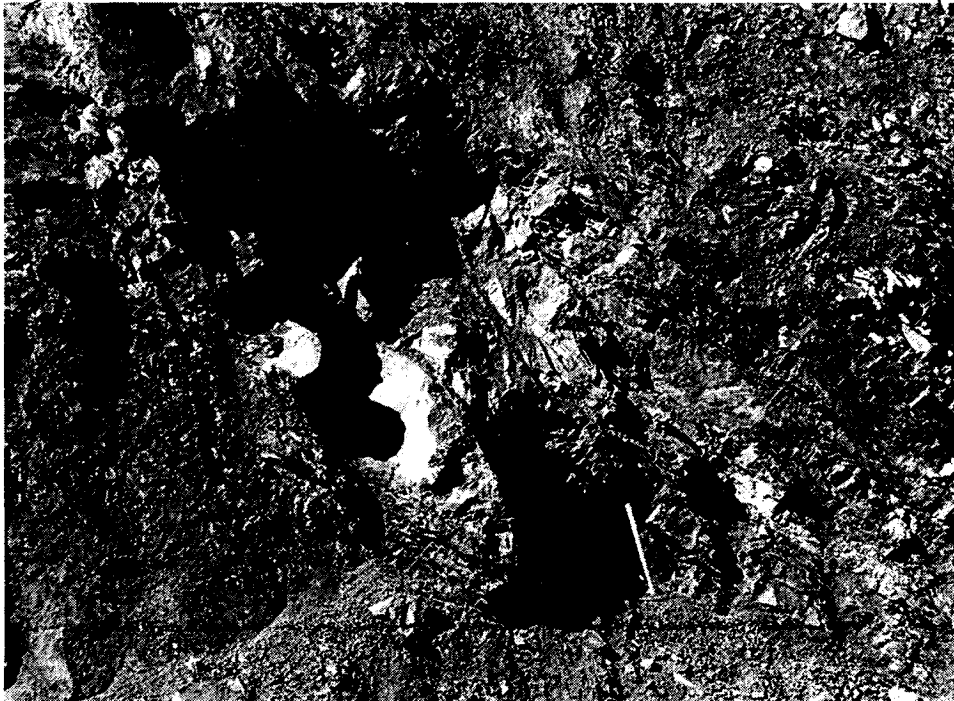


**Figure 58b.** Detail of the fault zone (right side of 49a), showing a quartz vein in fault damage zone. Hammer is 32" tall.

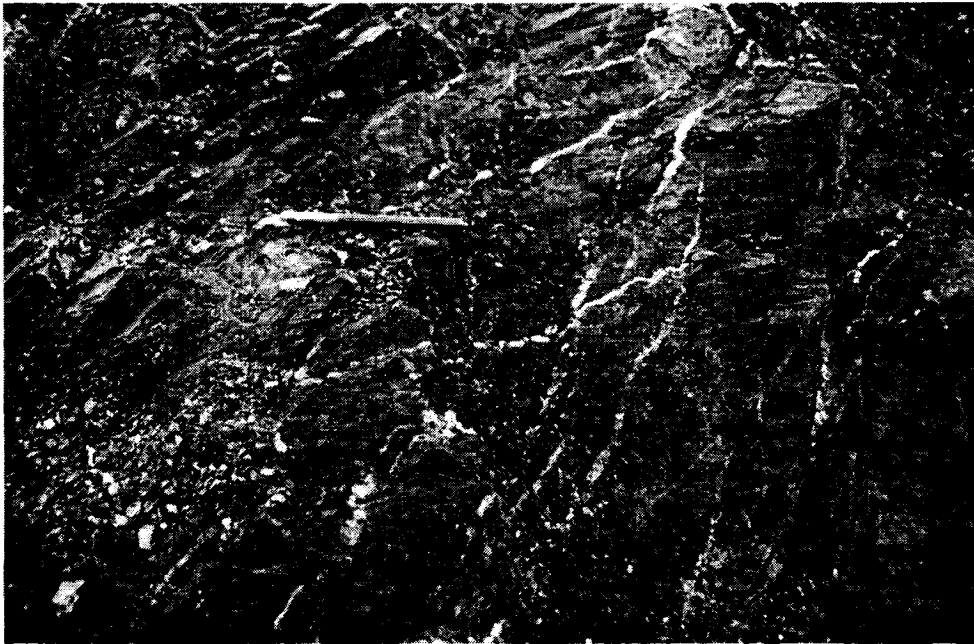


**Figure 60a. Outcrop photo of crosscutting carbonate veins in biotite schist.**



**Figure 60b. Detail of older ankerite-dolomite veins cut by late vein with white calcite.**

scale at least three generations of ankerite veins and isolated massive calcite veins sub-parallel to quartz veins are the most common veins types observed (Fig. 60).

The youngest vein events observed in the mine workings are open fracture fillings and coatings by calcite, locally euhedral crystals filling fractures (Fig. 61). These crystals either tend to be of the dogtooth spar variety or flattened tabular crystals. Fracture fillings occur mostly in the later north-northeast to northwest striking joints and faults or in irregular fractures.

### **Quartz-Sulfide Vein Paragenesis**

Although intact quartz veins are a rarity, enough were found to put together a vein paragenesis. Figure 62 shows the sequence of mineral deposition within veins and relative sequence of deposition between vein types. In quartz veins euhedral, open-space filling quartz is the first stage, followed by medial arsenopyrite, pyrite, and stibnite, precipitating between or within quartz crystals. Arsenopyrite and pyrite are the earliest sulfides, with stibnite late. Arsenopyrite and pyrite are also found disseminated in the alteration halo surrounding the veins.

Gold is found replacing arsenopyrite, within arsenopyrite grains or crystals (Fig. 63). The maximum size observed is 0.1 mm (100  $\mu\text{m}$ ). Also contained within arsenopyrite are extremely small (sub-micron) grains of galena, observed while obtaining the backscatter images of the gold. A single microprobe data point indicates that True North gold contains approximately 10% silver (Richard Trotman, personal communication). An earlier study noted that gold was found with both pyrite and stibnite,





**Figure 61a. Late stage calcite growing in open fractures.**



**Figure 61b. Late calcite, fine dog-tooth spar from an open fracture.**

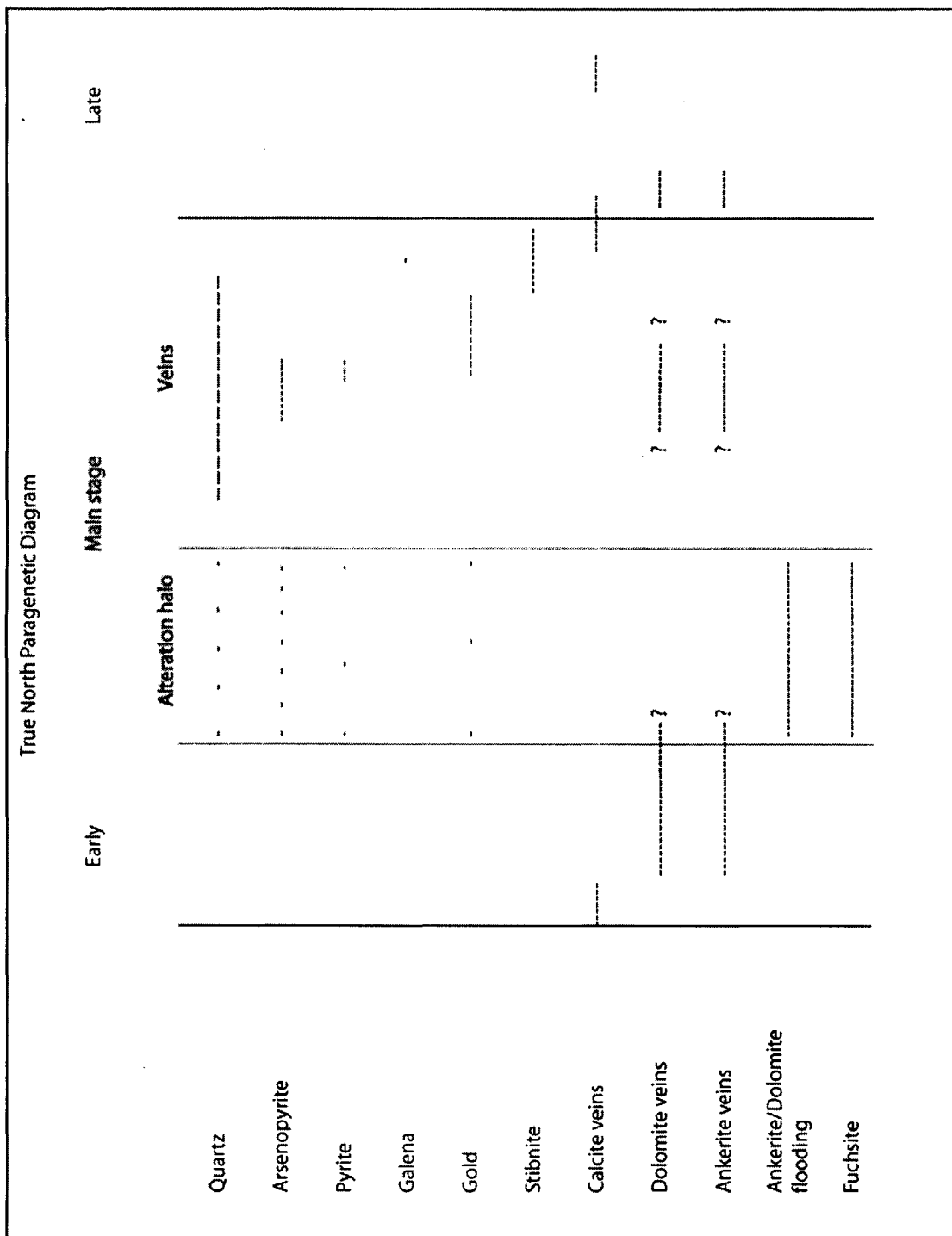
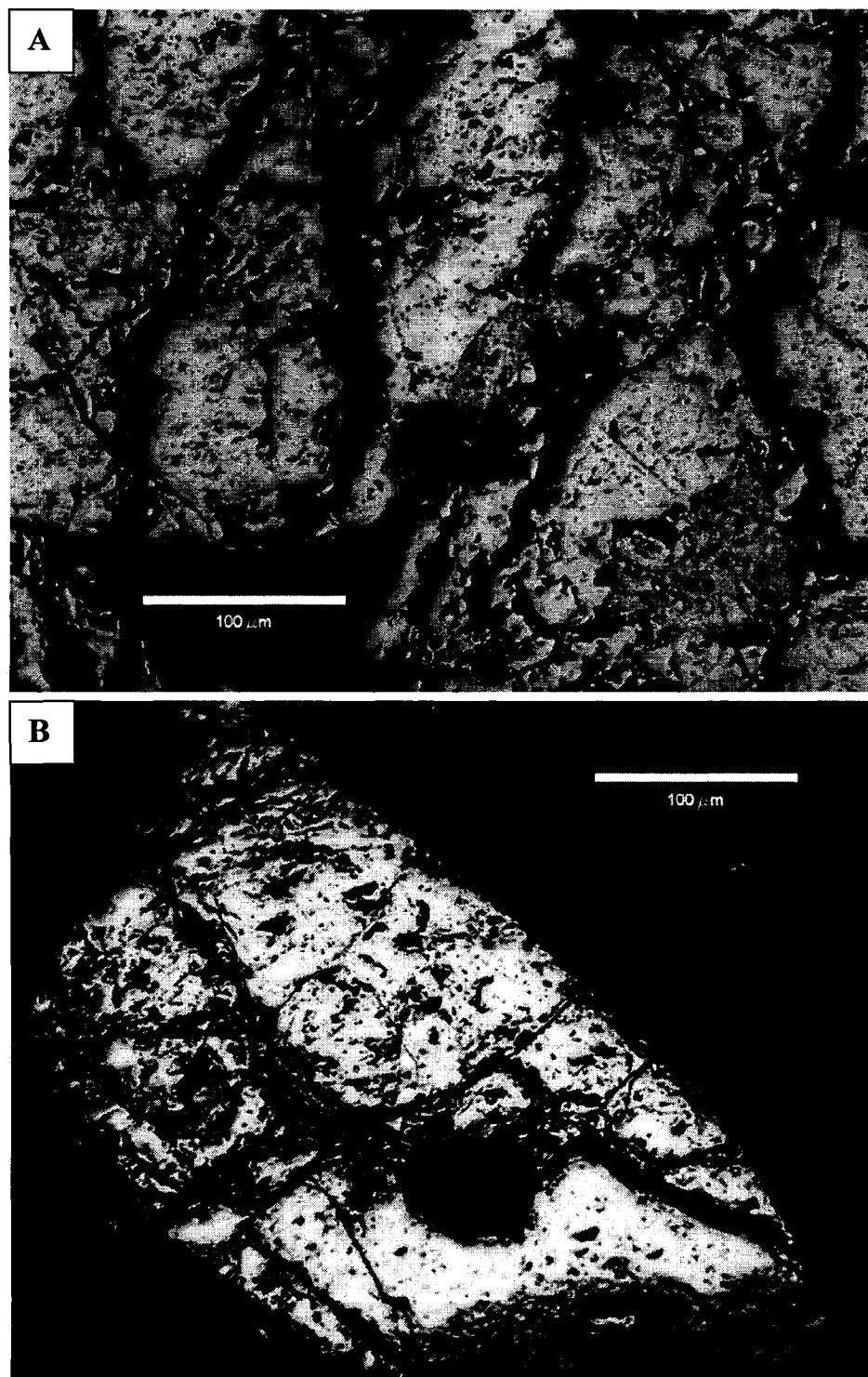
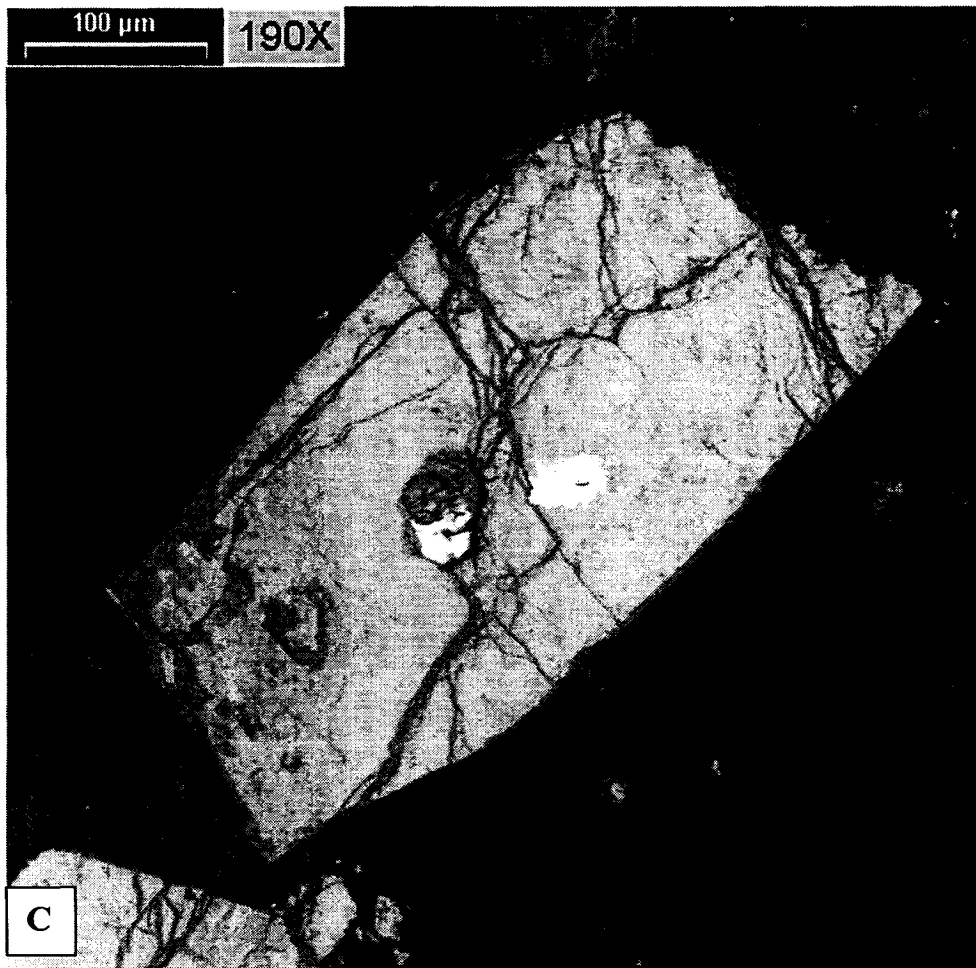


Figure 62. Paragenetic diagram for True North veins. Note that the area in red does not represent separate stages, vein phases vs. alteration halo phases are in separate columns for clarity.



**Figure 63a-b. Gold in arsenopyrite; textures indicate that the gold is replacing the arsenopyrite.**



**Figure 63c. SEM backscatter image of arsenopyrite crystal containing two grains of gold.**

and that the pyrite was arsenic-rich (arsenian pyrite) and that gold was detected in the high arsenic areas and not in the low arsenic areas (McCoy, 2000).

Precise relationships between arsenopyrite, pyrite, and stibnite were not observed. Large intact stibnite veins and pods, with and without quartz were found in several locations within the mine, suggesting that at least some of the stibnite was deposited late. The amount of crushed quartz in fault damage zones suggests that there were a number of generations of veining; however no banded veins have been noted.

The relationships between the various carbonate veins and the quartz-sulfide veins can be seen in Figure 62. It is important to remember that the events listed in the “Alteration” and “Veins” columns are occurring simultaneously, but are separated for clarity.

### **Fluid Inclusions**

All veins at True North are within faults and all of the faults have had numerous episodes of movement; thus most veins are dismembered to highly brecciated. Four veins were identified as having quartz vein material suitable for preserving fluid inclusions. Of the four veins sampled, three contained usable fluid inclusions and were analyzed. The three veins are: (see Plate 2)

- H1300, a low-angle (045 25S) quartz-stibnite vein (0.08 opt gold) from the Hindenberg pit, 1300 bench, south wall. Analyses are from whole euhedral quartz crystals and doubly polished plates.

- H1280, a high-angle (050 60S) quartz to quartz-arsenopyrite vein (0.90 opt gold, with visible gold after arsenopyrite) from the Hindenberg pit, 1280 bench, south wall. Analyses are from doubly polished plates.
- S1340, a high-angle (055 40S) quartz vein (0.06 opt) from the Shepard pit, 1340 bench, west wall, from the footwall of the main mineralized fault, north of the offsetting fault. Analyses are from doubly polished plates.

A total of 128 inclusions were measured to obtain homogenization temperatures from the three veins, 80 from H1300, 26 from S1340, and 22 from H1280. Of these a total of 21 were suitable for determining salinity, 14 from H1300, 2 from H1280, and 5 from S1340. The majority of the inclusions analyzed from the H1300 vein were in small whole euhedral quartz crystals that had grown into a vein cavity, these crystals were put on the fluid inclusion stage intact. The rest of the H1300 and all of the H1280 and S1340 vein inclusions are from doubly polished plates. Inclusions chosen for analysis were primary inclusions, isolated or in small groups, and averaged  $9.0\mu$  measured along the long axis (Fig. 64a). The smallest analyzed inclusion was  $2.2\mu$  and the largest  $51.6\mu$ . All of the samples contained numerous sealed fractures containing very small secondary inclusions (Fig. 64b). These and any primary or pseudosecondary inclusions that could not be clearly identified as such were not used for these analyses. Inclusions analyzed for salinity (freezing) were larger,  $12.0\mu$  as compared to  $9.0\mu$ , due to difficulties in seeing ice crystals.

A Fluid Inc. modified U.S.G.S. gas-flow heating/freezing stage mounted on an Olympus binocular microscope was used for all analyses. The system is calibrated to



**Figure 64a. Several larger fluid inclusions, Hindenberg 1300 vein.**

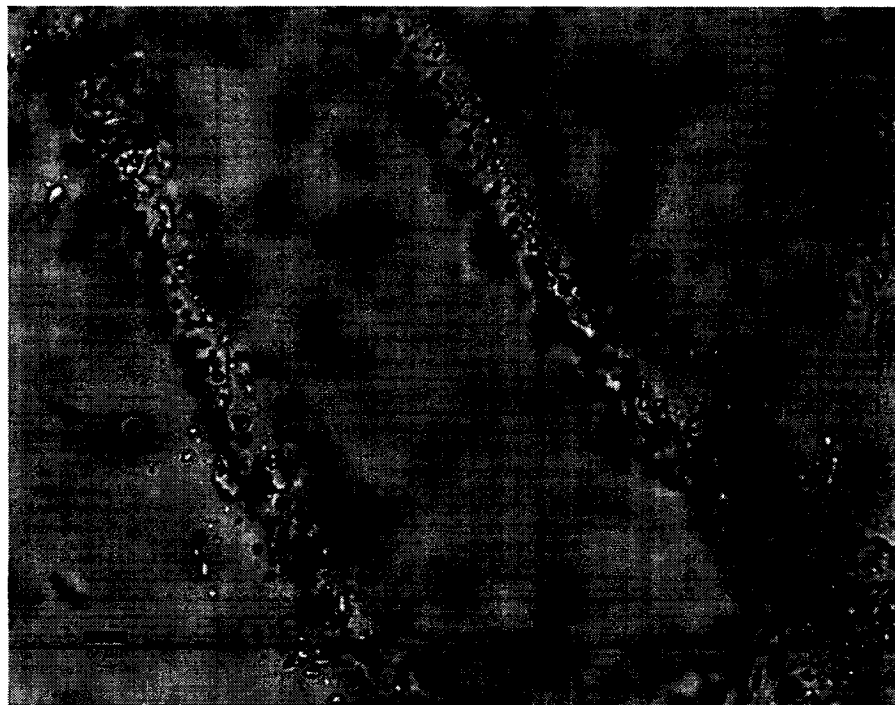


**Figure 64b. Two planes with secondary inclusions, Hindenberg 1280 vein.**

$\pm 0.1^{\circ}\text{C}$  for both heating and freezing. Replicate analyses performed during this study indicate reproducibility of  $\pm 0.1^{\circ}\text{C}$  for heating runs and  $\pm 0.2^{\circ}\text{C}$  for freezing runs.

Figure 65 shows the distribution and frequency of the homogenization temperatures for the whole data set, the two Hindenberg veins, and each vein separately. The range of temperatures measured is between  $173.4$  and  $309.0^{\circ}\text{C}$ . The mean of the whole data set is  $242.8^{\circ}\text{C}$ . The histogram for minimum homogenization temperatures shows that the mean ( $242.8^{\circ}\text{C}$ ) and the mode (the frequency peak,  $240.0^{\circ}\text{C}$ ) are only about two degrees apart. This indicates that the data set is statistically 'normal' or that it represents a sampling of a normal population. Despite this, it is clear that there are two populations. The histogram shows that the Shepard vein (S1340) population has a separate peak at about  $285.2^{\circ}\text{C}$  and a mean of  $273.3^{\circ}\text{C}$ , while the Hindenberg veins (H1280 and H1300) have a mean at about  $236^{\circ}\text{C}$ , very close to the mode of  $231.4^{\circ}\text{C}$ . Inspection of Plate 1 shows that the Hindenberg and Shepard portions of the deposit are about 2500 feet apart; the Hindenberg veins are within eclogite or retrograded eclogite facies (biotite schists to amphibolite) units, while the Shepard vein is in the slate/argillite unit. The approximately  $40^{\circ}\text{C}$  temperature difference may explain why stibnite is lacking in the Shepard pit and it may reflect a more focused fluid flow in a less porous host. It may also be possible that the Shepard is a deeper level of the deposit faulted into contact with the Hindenberg, a conclusion that is supported by the presence of the Slate/argillite unit, the low-angle fault seen in the Shepard pit, faulting between the Shepard and Central pits, and the fault in the Central pit.

Figure 66 shows the distribution and frequency of the weight percent NaCl equivalent (wt percent NaCl equiv) for the three veins. The range of salinities calculated



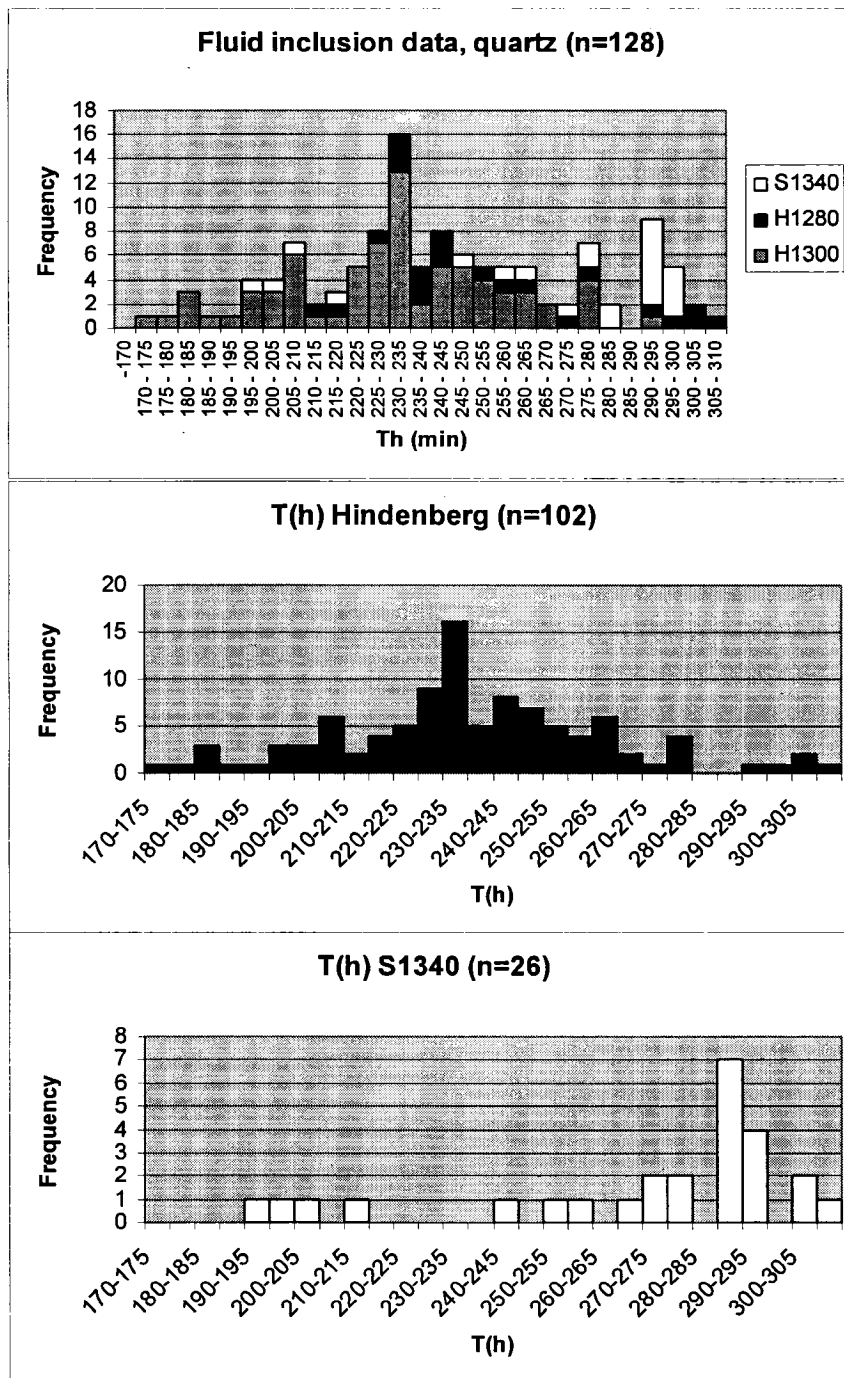


Figure 65. Histograms of homogenization temperatures. Top histogram is the entire data set, middle histogram is the two Hindenberg veins, and the lower histogram is the Shepard vein. Shows the population distribution and that there are two separate populations, one in Hindenberg, and one in Shepard.

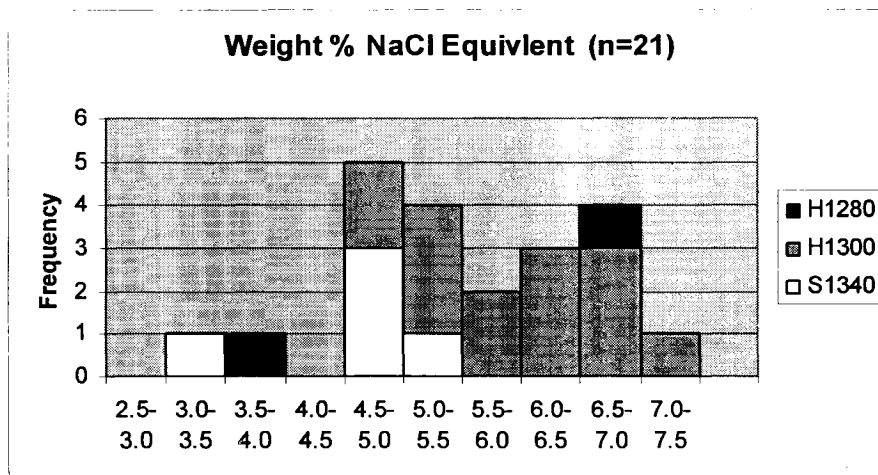


Figure 66. Salinity data for all veins.

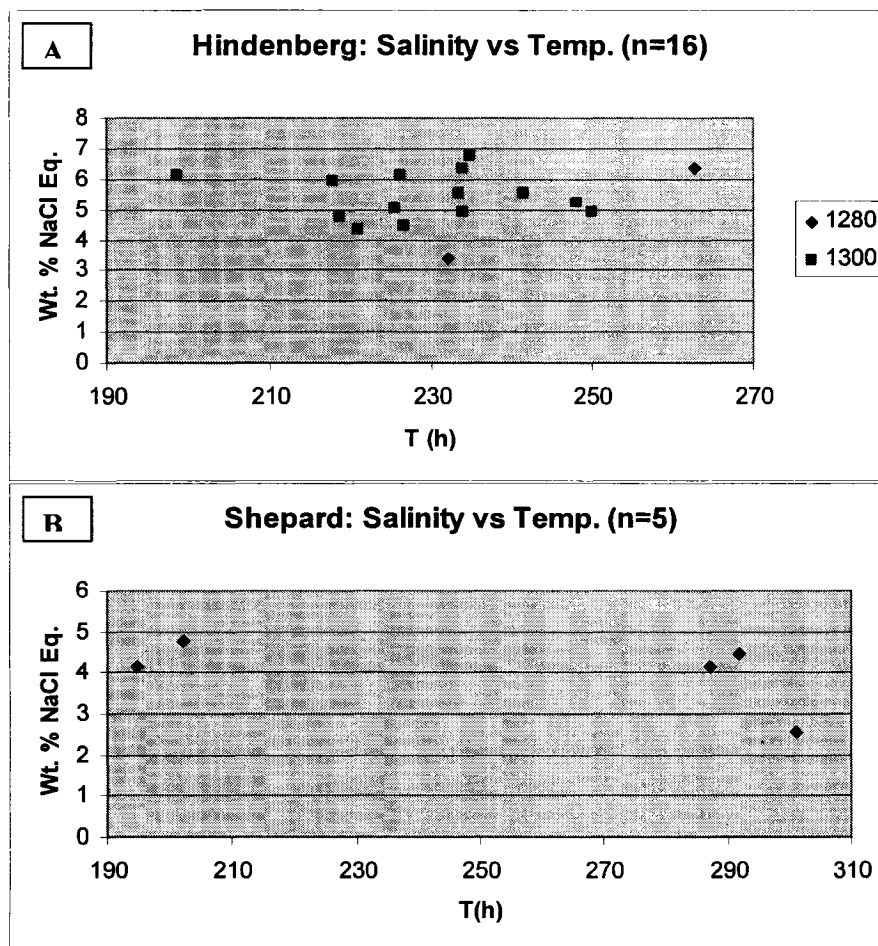


Figure 67. Salinity vs. temperature plots for Hindenberg veins (upper graph) and Shepard vein (lower graph).

is between 2.56 wt percent NaCl equiv and 6.78 wt percent NaCl equiv. The mean salinity is 5.11 wt percent NaCl equiv. There appears to be no significant difference in salinity between the Hindenberg and Shepard veins, although the sample population is a bit small for definitive conclusions. Figures 67a and 67b are salinity vs. temperature plots for the Hindenberg and Shepard veins. Neither shows a discernible trend of increasing or decreasing salinity with temperature. Although no inclusions exhibited double menisci, during freezing runs two developed gas hydrates or clathrates. Crushing tests showed that most primary inclusions have a positive internal pressure, suggesting that CO<sub>2</sub> is present. An aqueous solution can contain about 3 mole % CO<sub>2</sub> in solution at room temperature before developing a double meniscus and due to the water contained in the gas hydrate structure it can cause an apparent increase in salinity of about 25% (Collins, 1979). This equates to about 1 weight percent NaCl equivalent, shifting the average salinity from 5 weight percent NaCl equivalent to 4 weight percent NaCl equivalent assuming all inclusions contained equal amounts of CO<sub>2</sub>.

## ALTERATION

Observed alteration types in mine exposures are bleaching of biotite-rich schists (weathering), the silica-carbonate (hydrothermal fuchsite-ankerite) alteration of amphibolite to biotite schist, graphitic biotite schist, and possibly eclogite, and graphite along the low-angle and northeast striking high-angle faults (remobilized during fault movement).

In pit exposures and hand specimens, it is possible to see a progression from biotite to silver-white mica within the same band. In thin sections this is seen as colorless, non-pleochroic mica with iron oxides between layers. X-ray diffraction analysis, discussed earlier, shows that weathering of biotite (phlogopite) from outside the principal ore zones produces a mixture of vermiculite, altered phlogopite (with peaks that resemble but don't quite match any phlogopite polytype or variation), and kaolinite group clays (usually halloysite). An extreme version of this type of alteration is the 'White Mica Schist', found along major structures and close to the pre-mine surface (Plate 1).

Newmont XRD and XRF analysis in metallurgical reports, with data derived from samples taken from the ore zones in what is now the Hindenberg pit, show an inverse relationship between biotite and sericite, as biotite decreases, sericite increases (Baker, 1996). Sericite per se was not identified during the X-ray work for this study, however a number of samples have peaks that are not explainable by any phlogopite pattern. The best fit to these peaks is a muscovite variety (muscovite 2M1 vanadium-barium or rarely muscovite 2M2 barium). Since no muscovite polytype or variety should be formed by weathering of biotite or phlogopite another explanation is needed. It is possible that the pattern represents muscovite in the host rocks, but if so why the imperfect fit to an odd

variety. Muscovite is remarkably stable in the supergene environment and even manages to survive transport to be deposited in sedimentary basins (Ehlers, 1982).

For comparison purposes several samples of the fuchsite-carbonate alteration suite were X-rayed. Samples were chosen that contain chromium micas (fuchsite) visible in hand specimen. The resulting patterns show less phlogopite than the weathered mica schist samples and all have a vanadium-barium (V-Ba) muscovite-like pattern.

These samples also contain the alteration minerals ankerite, dolomite, magnesite, and arsenopyrite. Several of these samples are shown in Figure 68. The corresponding X-ray patterns are in Appendix A. The presence of hydrothermal mica indicates that much of the area mapped as biotite schist has been altered to some degree. Although these schists have no visible alteration and little carbonate the presence of hydrothermal mica does argue that they have been altered. The lack of carbonate may be due to carbonate dissolution during weathering. Some samples have both the V-Ba muscovite and another muscovite polytype. The second muscovite variety is interpreted to be sericite, which is not found in the Jade powder diffraction file database. Based on these analyses the alteration package can be described as fuchsite-sericite, ankerite-dolomite-magnesite  $\pm$  arsenopyrite, and pyrite. The controlling factor on the development of fuchsite over sericite would be the availability of chromium. Controlling the development of ankerite, dolomite, and magnesite would be the amounts of iron and magnesium present.

Hydrothermal fluids migrated along foliation in schist, altering the biotite as it went. Figure 69 shows the upper surface of partially altered biotite schist. The dark areas are relatively unaltered biotite; the light colored areas are altered. The brownish veins are ankerite-dolomite. Figure 70 is an end view of the same sample showing the variable

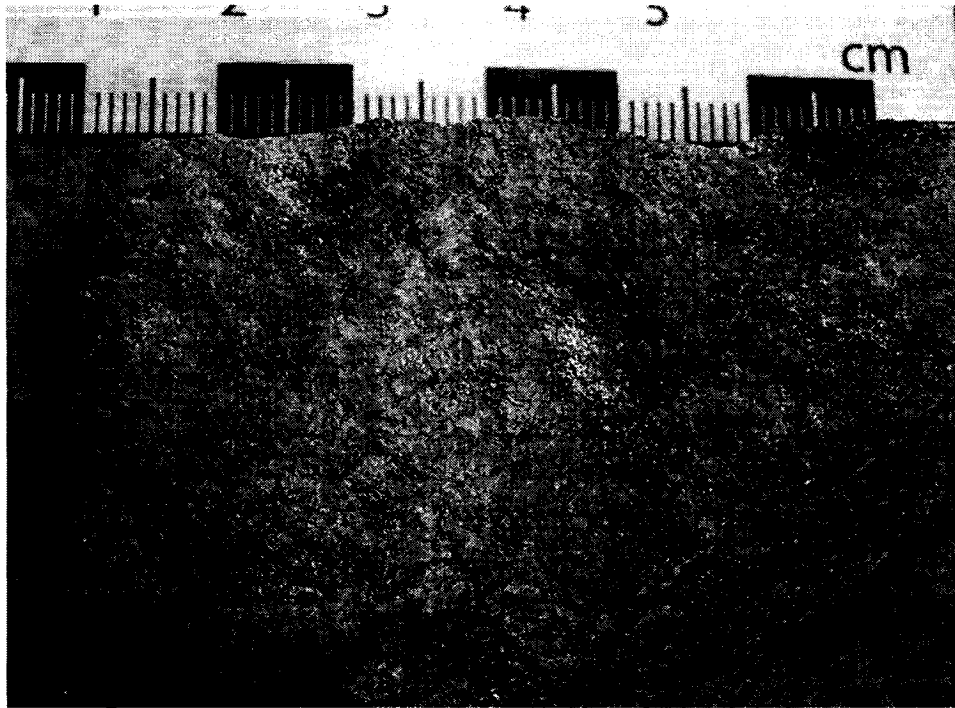


**Figure 68a. Hand specimen of fuchsite-ankerite alteration. All that remains of the original texture (graphitic mica schist) is a weak schistosity. Fresh sample from Hindenberg 1300 bench.**

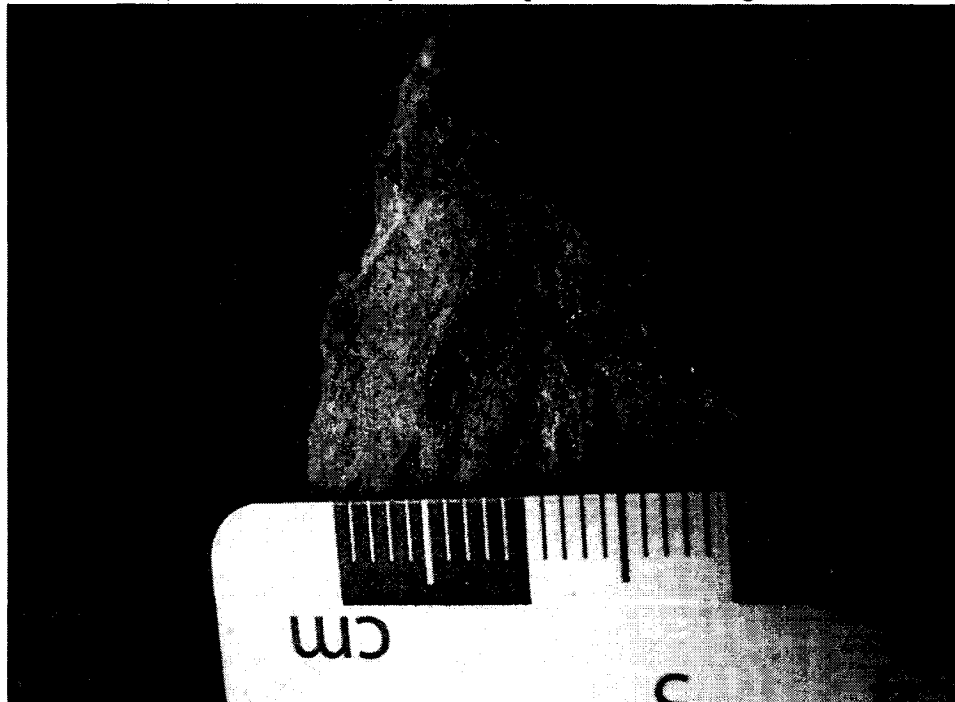


**Figure 68b. Bright green fuchsite in a mildly weathered sample. Only remanent schistosity remains of the original biotite schist. Sample is from Hindenberg 1340 bench.**

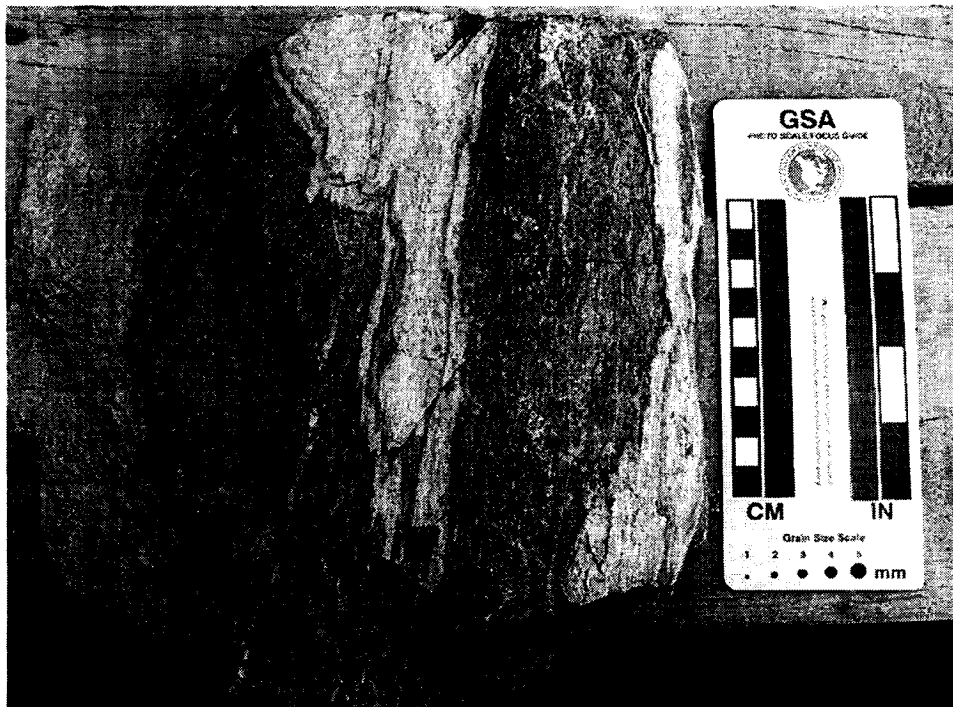


**Figure 69. Partly altered biotite schist.**



**Figure 70. Edge view of sample in Figure 61, centimeter scale at top**

alteration along foliation. In thin section the hydrothermal alteration of biotite is seen as the opening of the biotite structure and growth of hydrothermal mica (sericite or fuchsite). In Figure 71 there is some recognizable biotite remaining with its structure opened by fuchsite-carbonate growth. In the center of the frame the biotite is completely replaced by fuchsite-ankerite. Alteration continues with the growth of mats of finer-grained micas (fuchsite-sericite) (Fig. 72). Unlike weathering, which seems to leave the original mica structure mostly intact, at least in True North samples, hydrothermal alteration of biotite to fuchsite-sericite is a texturally destructive process. This may in part explain the lack of visible metamorphic textures (foliation) in the most highly altered parts of the deposit, the center of the deposit (the center of the Hindenberg pit northeast highwall, for example).

The silica-carbonate alteration (the approximate limit of alteration is shown on Plate 1) is best developed in the graphitic schist zone. It turns the normally dark brown to black rocks to pale green with local concentrations of the bright green mica, fuchsite, in fresh samples (Fig. 68a), or to medium brown or buff, where moderately weathered (Fig. 68b). In highly weathered areas this alteration is burnt orange with fragments of quartz and locally high concentrations of graphite (Fig. 73). This style of alteration is most prevalent between vein/fault set in the low-angle fault sets or between the low-angle and northeast striking high-angle vein/fault sets. Where intact veins are present the silica-carbonate alteration is observed as a selvage to the veins. In fresh outcrop the silica-carbonate alteration contains as much as 5% fine arsenopyrite and trace pyrite.

Graphite along faults was one of the most striking features of the True North pit as mining progressed into the Hindenberg pit (Fig. 48 (p 29-30)). Graphite is found along





Figure 71a. Silica-carbonate alteration, early stages. Photo field of view 2 mm, plane light.

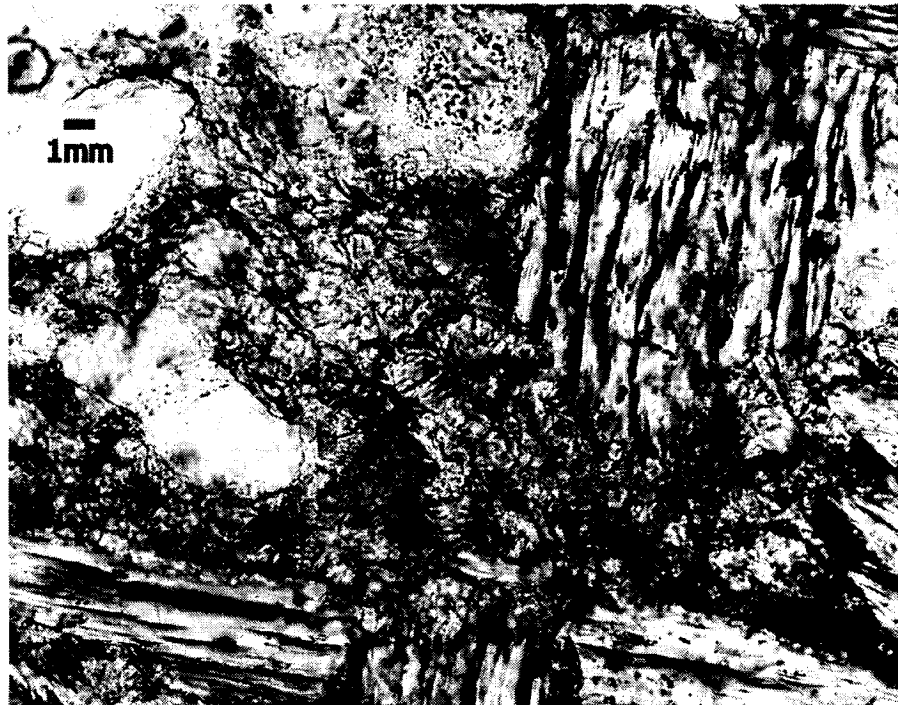
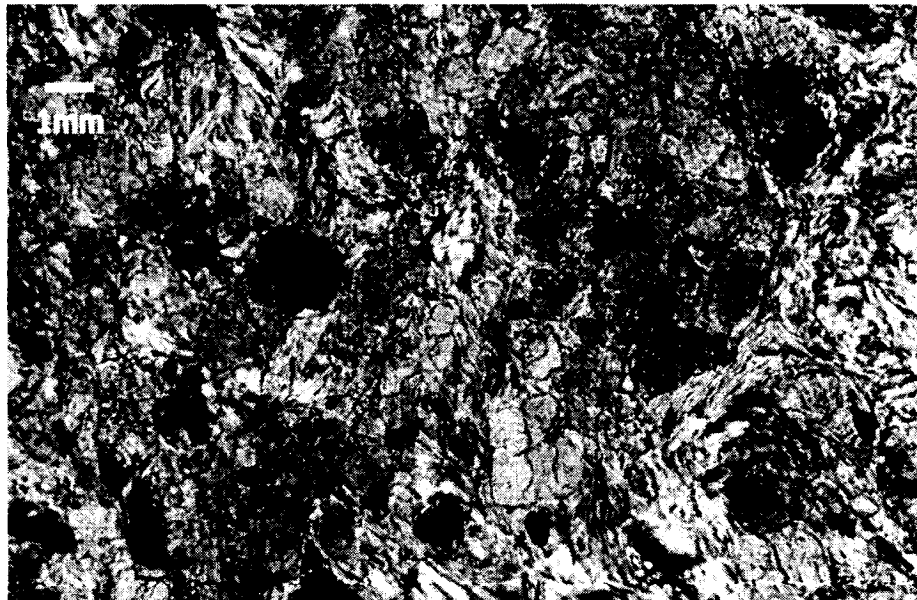


Figure 71b. Biotite with fuchsite growing within and around it. Photo field of view is 0.85 mm.



**Figure 72a.** Almost complete destruction of texture in schist. Original schistosity was sub-parallel to the long axis of the photo (see lower right corner).



**Figure 72b.** Complete textural destruction. Field of view 1.33 mm.

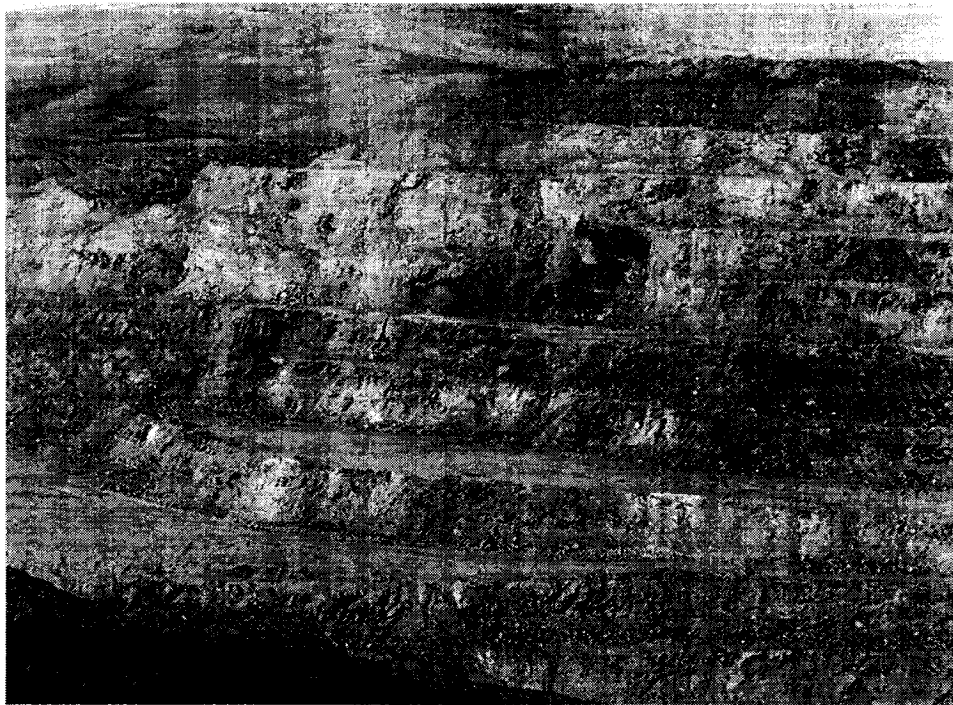


**Figure 73a. View of north wall of the mine 1320 bench to 1480 bench (and low-grade stockpiles at skyline), 20' bench height.**



**Figure 73b. Closer view of strongly weathered, altered schist, Hindenberg 1340 bench.**

or in most of the low-angle faults and many of northeast striking high-angle faults as surface coatings along discrete fault plans and as 1 – 2 meter wide halos along faults. Graphitic schist (mica-quartz, graphite, ± amphibole schist) is locally present in and around the areas of the low-angle and northeast striking fault zones, in the core of the deposit (Plate 1). The slate-argillite section in the Shepard pit is also strongly graphitic and graphite is remobilized along faults there as well. These graphitic units are the most likely source for the graphite in the faults. For further discussion of this, see the section on isotopic data.

### **STRUCTURE, VEINING AND GOLD GRADES**

Blast-hole gold grades contoured and overlain on a structure and vein map for the 1460 and 1380 elevation benches in the Hindenburg Pit demonstrate the relationship between the structure, veins, and gold values (Fig. 74 and 75). The contour maps clearly show that the gold values tend to be somewhat erratic, however the structural grain that the veins follow shows up very well. Strings of gold highs tend to be aligned parallel to the northeast and northwest to north-northeast trends of the high-angle faults and gold grade tends to be more erratically distributed along the broader trends of the low-angle faults. The central part of Figure 74 (1460 bench) is the best example of the latter. A string of dark gray to black, medium to high grade zones extend in a southwest-northeast trend and a larger area extends north-northeast. This zone has a fairly distinct eastern edge, a high angle fault, and extends off to the east along a low angle structure forming an ore zone perhaps 100 ft wide by 250 ft long (Fig. 74).

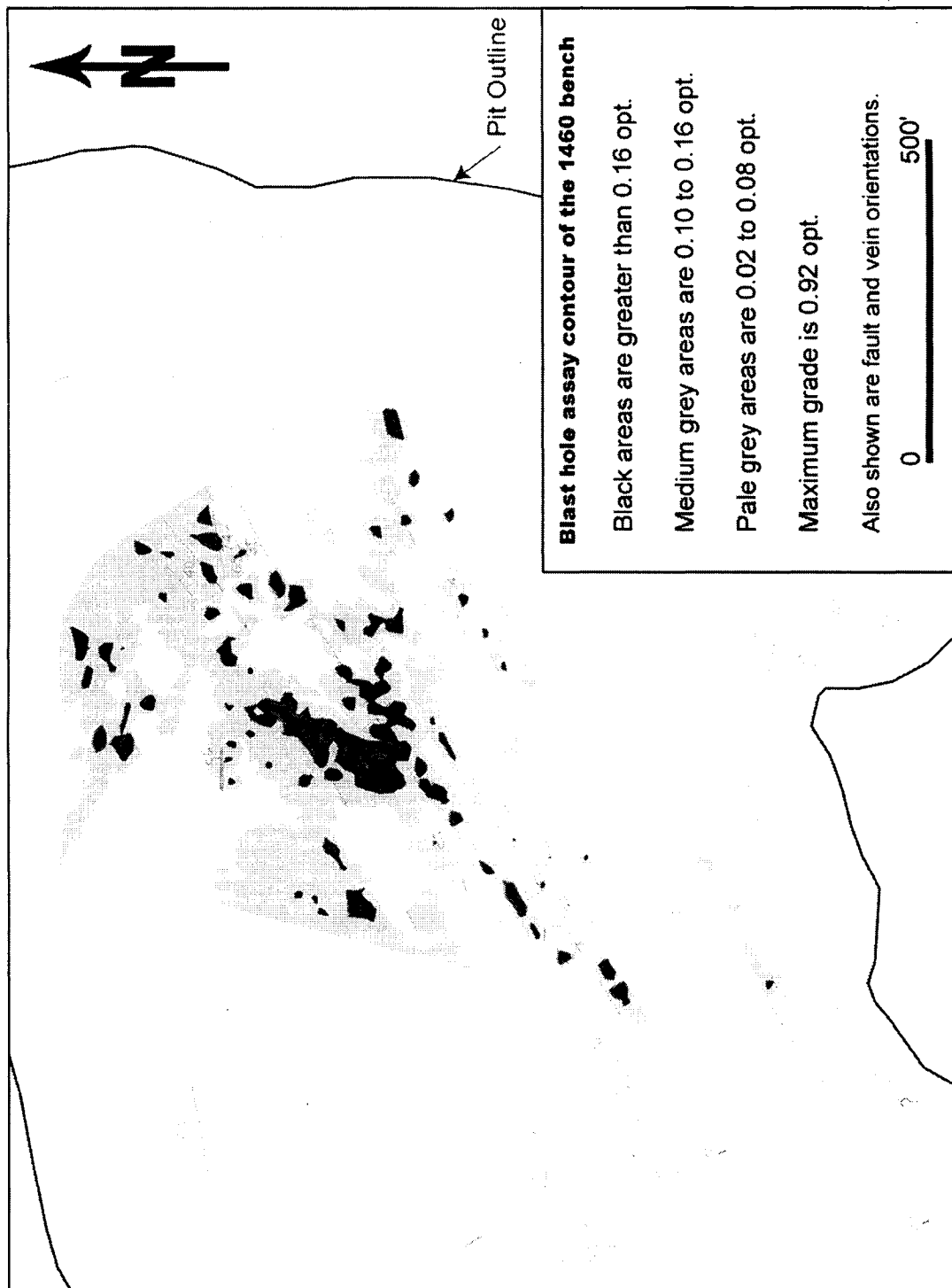


**Figure 74. Hindenberg pit, bench 1460 showing shaded contoured gold values from blast-hole assay values. The darker the shade the higher the grade (black is the highest grade). Alignment of the high-grade zones indicates high-angle structures, broad lower-grade zones are low-angle structures. Geologic interpretation by K. Campbell, on Kinross contoured blast-hole data (Unpublished internal report).**

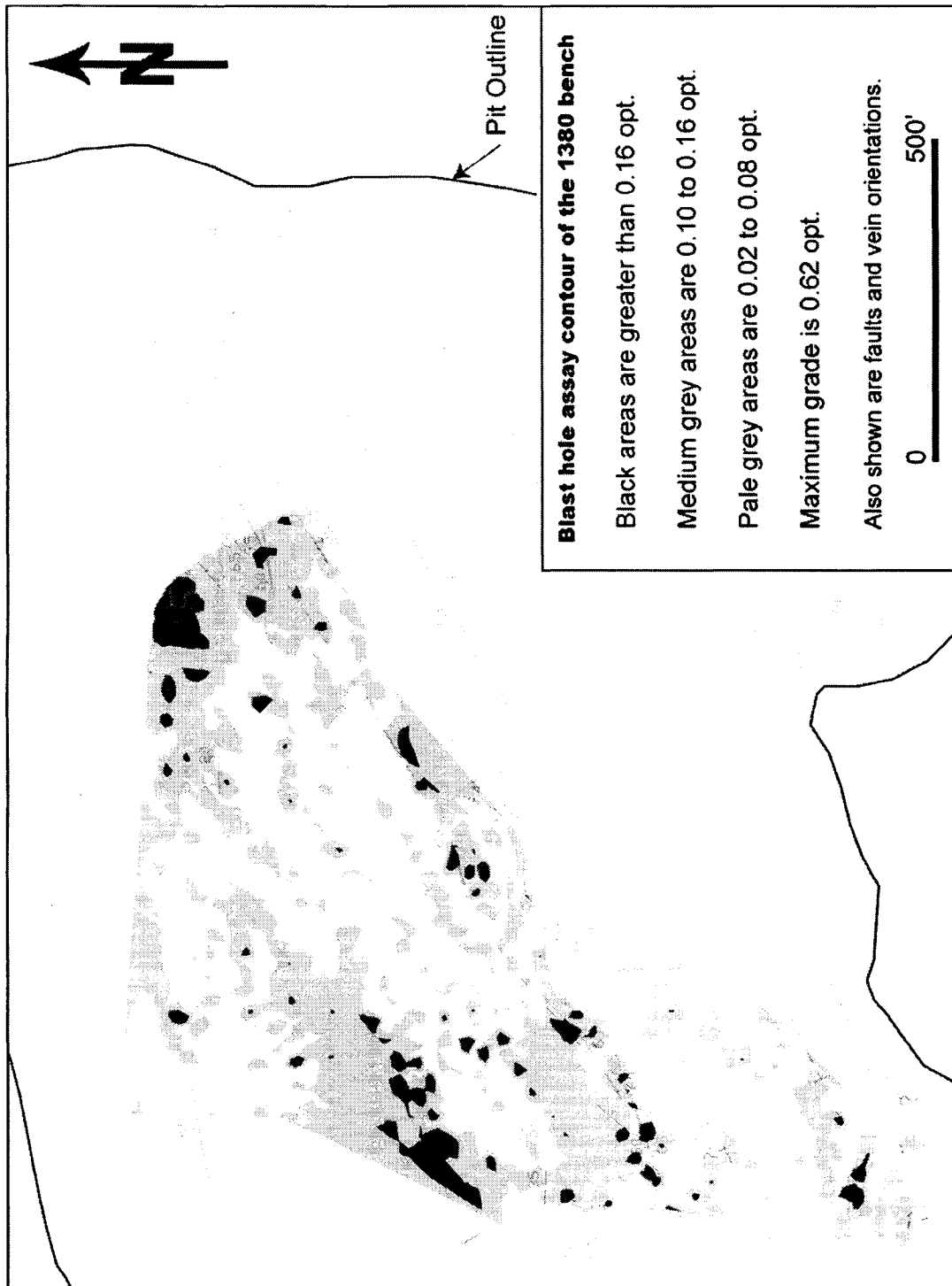


**Figure 75. Hindenberg pit, bench 1380 showing shaded contoured blast-hole assay values. The darker the shade the higher the grade (black is the highest grade). Alignment of the high-grade zones indicates high-angle structures, broad lower-grade zones are low-angle structures. Geologic interpretation by K. Campbell, on Kinross contoured blast-hole data (Unpublished internal report).**

## STABLE ISOTOPE DATA

### Carbonate $\delta^{13}\text{C}$ and $\delta^{18}\text{O}$ Values

The carbonate  $\delta^{13}\text{C}$  and  $\delta^{18}\text{O}$  isotopic ratios were analyzed in 20 samples to attempt to clarify the relationships between vein stages, the silica-carbonate alteration halos around veins, and the carbonate present in the host rocks. Samples were chosen that allowed analysis a) of cross-cutting relationships between carbonate veins, b) silica-carbonate alteration, c) veins with no clear cross-cutting relationships (isolated veins), and d) carbonate from the eclogite, marble, and calcite flooding(?) along a fault between the argillite-slate unit and the biotite and graphitic schists in the Central area in the mine (Plate 1). Figure 76 displays the data generated.

Three labeled triangles (ST1, ST2, and ST3 in red) are crosscutting ankerite veins from a single sample in biotite schist that is not visibly altered. ST1 is the oldest (crosscut by the two younger stages), ST2 is intermediate (crosscut by ST-3 and crosscuts ST1) and, ST3 is the youngest (crosscuts both ST1 and ST2). This suite of three samples establishes fractionation trend for carbonate veining at True North. Each successive generation has slightly heavier  $\delta^{13}\text{C}$  values and lighter  $\delta^{18}\text{O}$  values. This same trend is observed in the two sample set ST1A and ST2A (labeled medium blue triangles). The remaining four triangles are two ankerite samples from silica-carbonate alteration zones (the two unlabeled green triangles below the 'Calcite- $\text{HCO}_3$ ' line) and two ankerite veins that crosscut silica-carbonate alteration (the two unlabeled blue-green triangles above the 'Calcite-  $\text{HCO}_3$ ' line).

Based on the ST1-ST3 and ST1A and ST2A series the samples in Figure 76 may be subdivided in to early, intermediate, and late (indicated by three circled areas). The

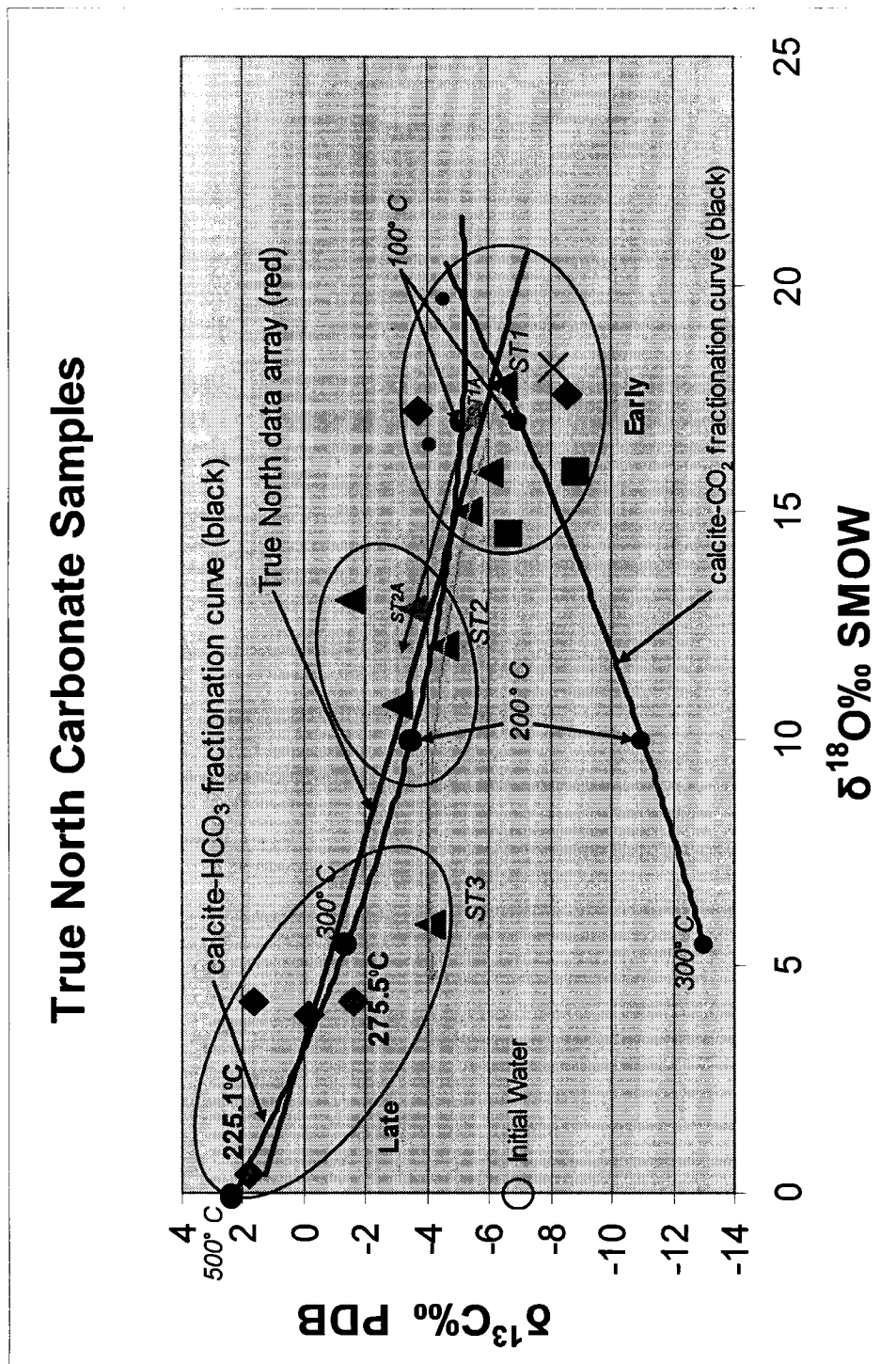


Figure 76. Carbon and oxygen isotope plot for the True North carbonates. Explanation on next page.



### Explanation for Carbon and Oxygen Isotope Plot

- ◆ Calcite veins with no visible cross-cutting relationships
- ▲ Ankerite veins with no visible cross-cutting relationships
- ▲ Alteration carbonate
- ▲ Ankerite vein with cross-cutting relations to other veins, stages shown
- ▲ Ankerite vein with cross-cutting relations to other veins, stages shown
- Calculated point (temperature) on fractionation curve, with temperature shown
- ◆ Calcite vein used for calcite-graphite geothermometry calculation, temperature shown
- Eclogite
- Marble
- × Calcite flooding along slate-schist contact in the Cental Pit

**Figure 76a. Explanation for carbon and oxygen isotope plot (previous page).**

early stage includes all the pre-mineralization stages, eclogite, marble, and the calcite flooding along the Central pit fault, plus early stage veins, the ankerite in the silica-carbonate alteration zones, and one isolated calcite vein. The intermediate stage includes second and third stage ankerite veins, and zones. Late stages are all calcite veins found along the same faults that contain the quartz veins, but with no clear crosscutting relationships visible between them and any other vein set. These calcite veins tend to be encased in graphitic gouge and/or contain graphite lamellae within the vein.

### **Interpretation**

In order to gain insight into the fluid chemistry and evolution at True North two theoretical fractionation curves were calculated and plotted on Figure 76, the calcite-HCO<sub>3</sub> curve and the calcite-CO<sub>2</sub> curve. Both curves use initial water with a  $\delta^{13}\text{C}$  value of -7 per mil and a  $\delta^{18}\text{O}$  value of 0 per mil. This initial water value was chosen only because it places the two curves into the same ranges of values as the True North data. The calcite-HCO<sub>3</sub> curve is calculated for calcite in equilibrium with an aqueous solution where HCO<sub>3</sub> is the dominant carbon bearing species (Bottinga, 1968; Mook et al., 1974). The calcite-CO<sub>2</sub> curve is calculated for calcite in equilibrium with an aqueous fluid where CO<sub>2</sub> is the dominant carbon species (O'Neil et al., 1969). On both curves temperatures are labeled that encompass the values observed from fluid inclusions in quartz from True North (100-300°C). The purpose of the curves is to compare calculated fractionation curves with the data array from True North.

If the fluid responsible for the calcite at True North contained significant CO<sub>2</sub> and CO<sub>2</sub> was the dominant carbon species then it would be expected that the data array from

True North would be at least crudely parallel to the calculated curve for CO<sub>2</sub> dominant water (for example see John et al., 2003). It would seem reasonable that CO<sub>2</sub> would be important at True North due to the quantity of silica-carbonate alteration and that fluid inclusions containing sufficient CO<sub>2</sub> to display a double meniscus and/or develop a clathrate when frozen have been observed (Jenson, personal communication, this study). However, based on the observation that the True North data array and in particular the vein series ST1-ST3 and ST1A-ST2A cross the calcite-CO<sub>2</sub> curve it would seem that based on this technique, CO<sub>2</sub> was not the dominant carbon species. The calcite-HCO<sub>3</sub> curve appears to provide a better fit, at least the trend of the True North data and the calcite-HCO<sub>3</sub> curve are roughly parallel. It is interesting however, to note that for both curves the 'normal' temperature evolution expected in a vein system is from left to right on Figure 76, from high to low temperature, and that the evolution in the True North data set is the opposite, right to left.

There are several possible explanations for this apparent reversal of the expected cooling trend. The first is that perhaps the hydrothermal system at True North was prograde or increased in temperature with time. Although it would seem difficult to preserve the signature of a system that increased in temperature as it evolved, the retrograde solubility of carbonates would allow the deposition of calcite during the prograde development of the system and prevent it from being dissolved during the retrograde or cooling. The temperatures spanned by the True North data on the calcite-HCO<sub>3</sub> curve, from below 100°C to 500°C and some 200°C hotter than the maximum quartz fluid inclusion temperatures, don't seem particularly reasonable. Another possibility is that the early stage veins and alteration at True North were formed by a

fluid that interacted continuously with the wallrock as it traveled, and was exchanged isotopically, to something close to that of the wallrock signature. With time and increasing fluid movement the conduit was altered isotopically to something closer to the fluid itself, until by the late stage the isotopic signature is much closer to or entirely that of the fluid. A potential difficulty with this possibility is that the wallrocks containing both of the vein series ST1-ST4 and ST1A-ST2A are not visibly altered and contain no carbonate whereas, in areas surrounding the quartz veining this same unit (biotite- to biotite-quartz-amphibole schist) is strongly altered to silica-carbonate.

A third possibility is that it was not the carbon species in the fluid that controlled the isotopic fractionation of carbon at True North. Two of the lithologic units at True North contain graphite, the argillite-slate unit and the graphitic schist, and this graphite has been remobilized along many of the faults, including those that contain both quartz and calcite veins. This graphite may have buffered the carbon fractionation, effectively decoupling the oxygen and carbon fractionation for the carbonates deposited at True North.

### **Calcite-Graphite Geothermometer**

To test the third possibility the calcite-graphite geothermometer was used. The calcite-graphite geothermometer is an isotopic thermometric technique that uses the difference between the  $\delta^{13}\text{C}$  values of co-existing calcite and graphite to calculate the temperature at the time of isotopic exchange between co-existing calcite and graphite in metamorphic events (Dunn and Valley, 1992), or the temperature of precipitation of calcite formed from a fluid in contact with pre-existing graphite. If the fluid from which

the calcite precipitated should have been in equilibrium with the pre-existing graphite, temperatures calculated should be the temperature of precipitation. The calculated temperatures should also be close to the temperatures measured in fluid inclusions.

Two samples from True North met the conditions of calcite in physical contact with graphite. The calculated temperatures are 225.1 and 275.5°C, shown on Figure 76 as blue diamonds with red interiors and annotated with the appropriate temperature. These temperatures are well within the range of measured fluid inclusion temperatures (173.4 to 309°C), showing that the carbon isotope fractionation could have been controlled by graphite and not by dissolved carbon species in the fluid and that the fractionation curves on Figure 76 have nothing to do with the fluid isotopic evolution at True North.

#### **Oxygen Isotope Values for Carbonate Precipitating Waters**

The oxygen isotope data from the carbonates was also used to calculate the oxygen isotopic composition for the water from which the carbonates precipitated. The results are on Figure 77. Also plotted are  $\delta^{18}\text{O}$  values for the metamorphic and igneous water boxes (Taylor, 1997). The trend is from igneous or metamorphic dominated to an increasing meteoric component in the fluid, an indication that the mineralizing fluid started off dominantly igneous, or groundwater isotopically in equilibrium with the host rocks, and as the system cooled, an increasing amount of meteoric water was incorporated.

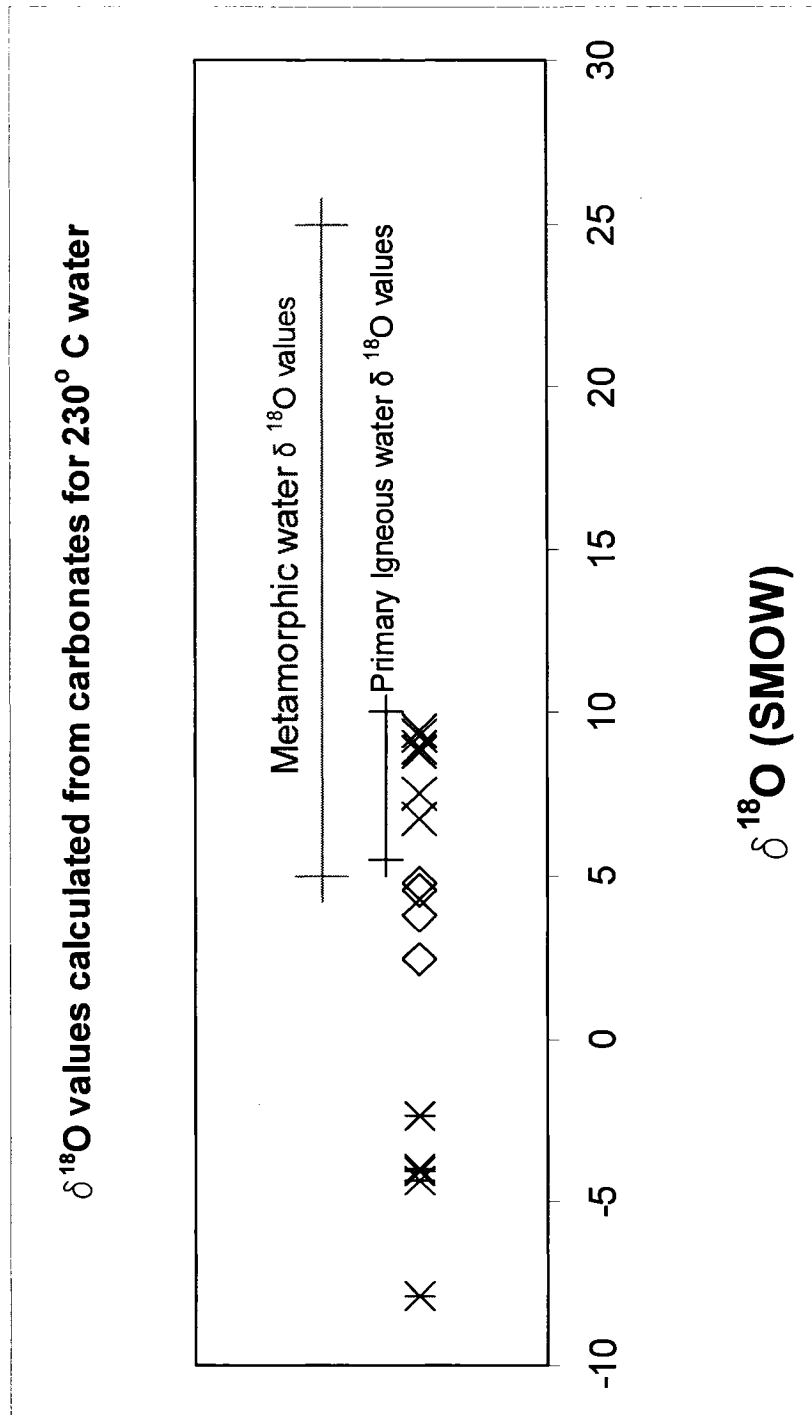


Figure 77. Calculated water oxygen isotope values from carbonates. Stars are late stage carbonates, diamonds are intermediate stage carbonates, and the X's are early stage carbonates.

### Carbon Isotopes of Graphite

Carbon isotopes of graphite in the schist and slate-argillite were analyzed to attempt to trace the origin of the graphite in the fault/vein zones. There are two lines of evidence to indicate that the graphite was present in the host rocks and faults prior to the precipitation of the veins, petrographic and isotopic. Petrographic evidence is in the form of graphite folded along with the other minerals in the schists. Isotopic evidence is the calcite-graphite geothermometer that calculates temperatures of calcite vein precipitation that fit well with observed fluid inclusion temperatures. The calcite-graphite geothermometer is based on the assumption that the calcite precipitated in equilibrium with the graphite, which would imply that the graphite was present prior to the precipitation of the calcite. One remaining question is whether or not the graphite is metamorphic or formed during a hydrothermal event. The petrographic evidence suggests that the graphite was in the rock prior to the last metamorphic event, and thus metamorphic. Carbon isotope values for host rocks (graphitic schist and slate-argillite) are presented in Figure 78. Samples from each unit and their respective faults are plotted on the same line. Hindenberg schist and faults within the schist are plotted on the lowest level. Shepard slate-argillite and faults that cut it are in the middle. The upper value is from the Birch Hill slate a unit that crops out south of Fairbanks and appears to be very similar to the slate-argillite exposed at True North.

In both sets of host rock vs. contained faults the faults have slightly heavier  $\delta^{13}\text{C}$  values than the respective host rock, suggesting that the graphite was remobilized from the host rock and that there was a small, consistent fractionation during remobilization.

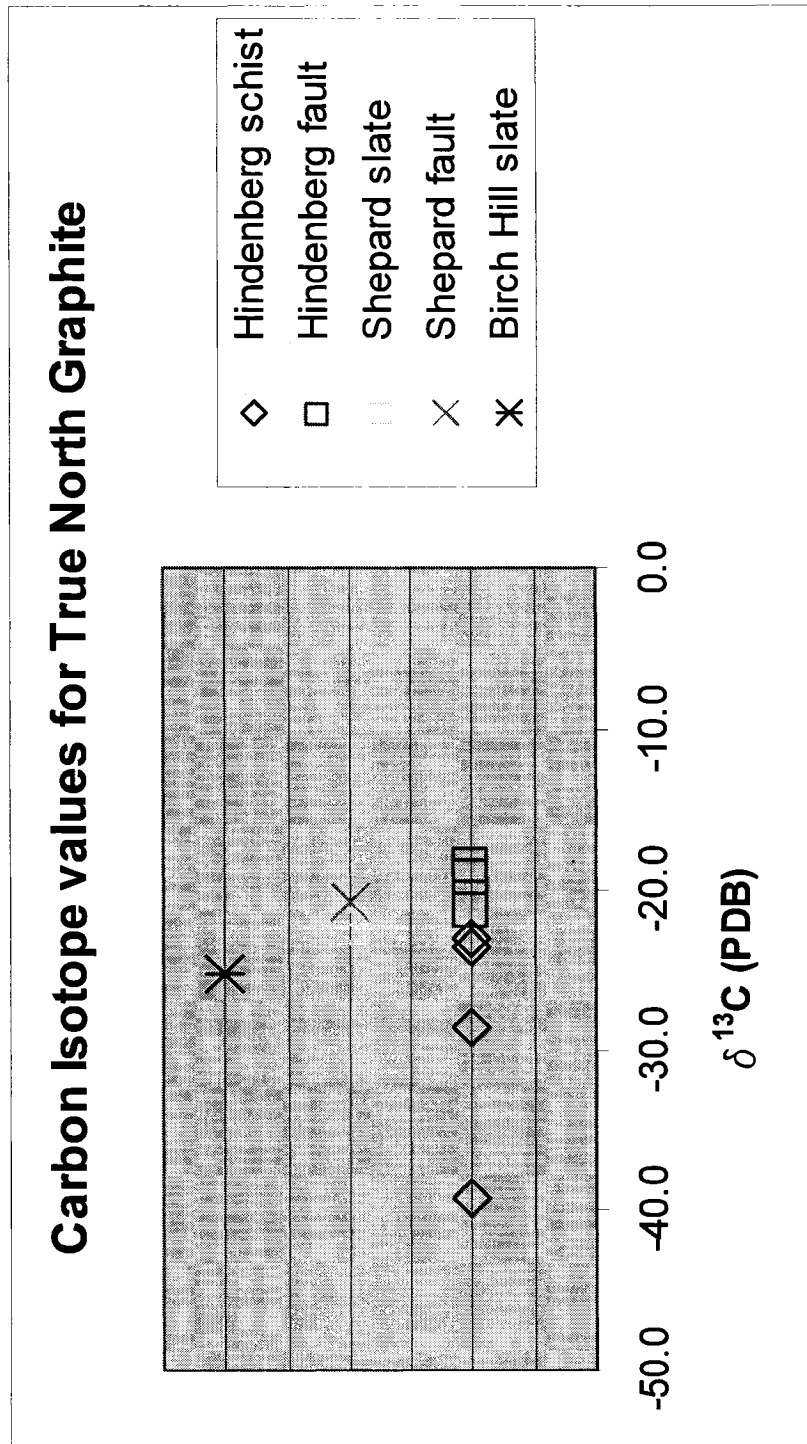


Figure 78. Carbon isotope plot for graphite from schist, slate, faults that cut schist and slate, and the Birch Hill slate.



It is interesting to note that the Birch Hill slate value is very close to that of the slate-argillite values from True North, which might suggest a relationship between the two units.

### **Sulfur Isotopes**

Sulfides (pyrite, arsenopyrite, and stibnite) from veins and alteration halos were analyzed for their sulfur isotopic ratios. The results are a clustering of data points between +2‰ and -2‰ (VCDT) (Fig.79). These values do not permit unambiguous source identification for the sulfur at True North. There are two potential sources; the first is magmatic sulfur from the Pedro Dome intrusion, the second is groundwater isotopically equilibrated with the metamorphic host rocks. Pedro Dome whole rock sulfur value is plotted as solid circle and the eclogite facies host whole rock as X's.

## **GEOCHRONOLOGY**

### **Review of Data Available From Previous Work**

An integral part of most geologic studies is timing. At True North understanding the timing of the various events, documented or interpreted, is crucial to the understanding of the formation of the deposit. Important timing questions include: the ages of protoliths and metamorphism of the Fairbanks schist and the Chatanika eclogite facies rocks, the age of the thrusting of the Chatanika rocks over the Fairbanks schist, the ages of the other generations of faults in the True North area, the age of intrusion of the Pedro and Gilmore Dome stocks, and the age of the True North deposit itself.

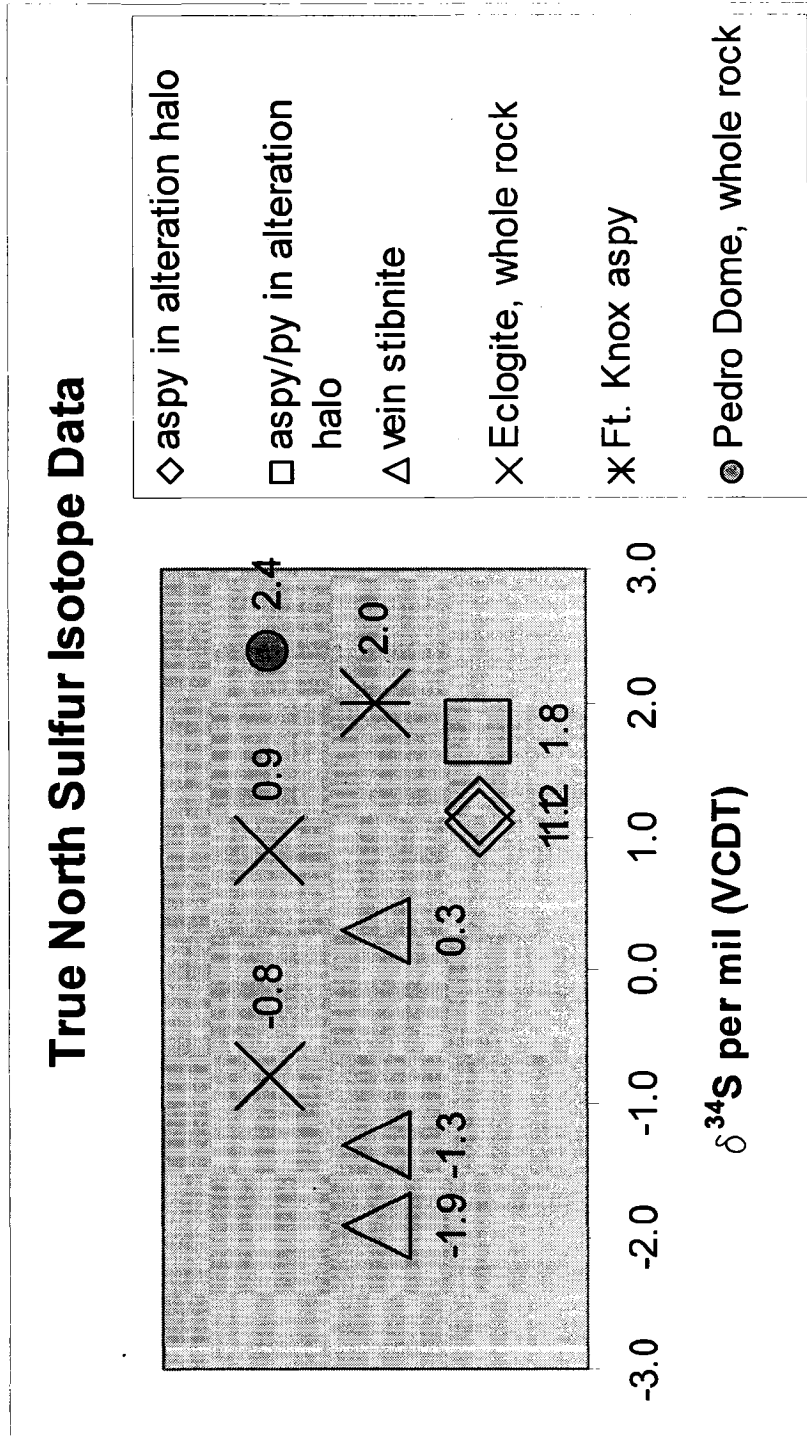


Figure 79. Sulfur isotope values for sulfides and whole rock samples.

Proterozoic zircons have been recovered from the Fairbanks schist (Aleinikoff and Nokleberg, 1989) indicating that it is Proterozoic or younger and a  $^{40}\text{K}/^{40}\text{Ar}$  mineral age from a hornblende in the Chatanika Terrane yielded an age of 470 Ma (Swainbank and Forbes, 1975). Peak amphibolite metamorphism for the Fairbanks schist at approximately 196 Ma, with a minimum age of  $\sim 175$  Ma for the cooling, to  $\sim 300^\circ\text{C}$ , from eclogite facies metamorphism for the Chatanika Terrane; a 140-115 Ma age range for the thrust event that placed the Chatanika over the Fairbanks schist; and an age of  $\sim 92$  Ma for the hydrothermal event in the area around the Chatanika Terrane have been reported (Douglas et al., 2002). An age of  $\sim 92$  Ma for the Gilmore and Pedro Domes was reported (Blum, 1985). An age of  $\sim 88$  Ma was determined for the Fort Knox stock (McCoy, 2000), and Jenson (personal communication) obtained two ages on fuchsite from the 1340 bench of the Hindenberg pit, True North mine, indicating an age for the alteration of  $\sim 92$  Ma (Fig. 80). The youngest ages reported for the area are 56-50 Ma for basalt flows (Roe and Stone, 1993), the scattered remains of which are found near Fairbanks and to the north and east of True North in a graben between two of the northeast striking district scale faults.

### **Dates Generated in This Study**

For this study three samples were submitted for  $^{39}\text{Ar}/^{40}\text{Ar}$  dating, two samples of fuchsite from vein alteration halos at True North, and a sample of the Pedro Dome granodiorite. As the incremental heating age spectra show (Fig. 81) the most recent samples from True North and Pedro Dome produced complex spectra that are not easily

interpreted. Both of the fuchsite samples, 280802-15 (Fig. 81A) and 070703-5 (Fig. 81B) have spectra with rising ages from the initial steps to the last. Sample 280802-15 rises

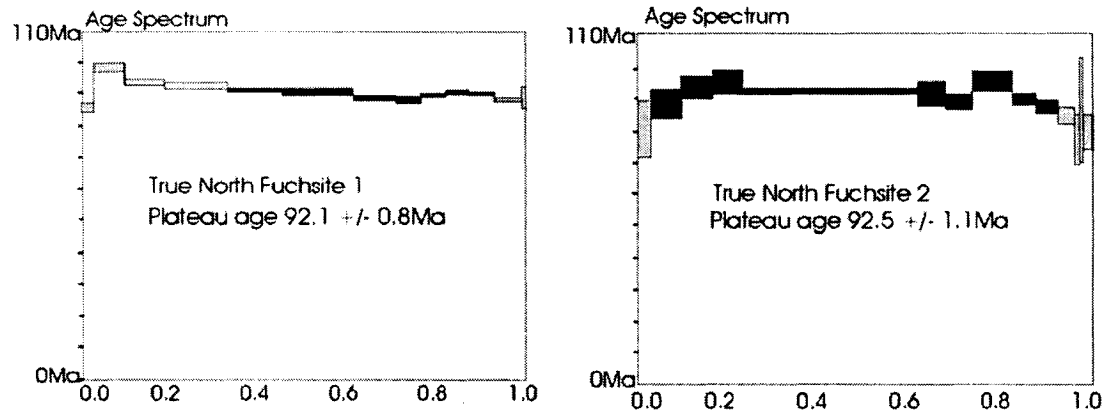


**Figure 80. Fuchsite age spectra for True North (From Jenson, personal communication).**

from 0 Ma to a maximum of ~90 Ma. Sample 070703-5 has a similar pattern, rising from an initial step of ~17 Ma to ~77-80 Ma for the last 50 percent of the gas released. Neither sample has a plateau nor an isochron age. Both samples may be interpreted as having indications of open system behavior. In this case original crystallization was probably prior to ~80 Ma and thermal event in the Tertiary caused argon loss.

Sample 'PD plagioclase' is a plagioclase separate from the Pedro Dome granodiorite. The age spectra (Fig. 81C) show a 'classic' U-shape, indicating excess argon in the sample. This sample may be interpreted as indicating an age of ~66.8 Ma, in contrast to the ages reported by Blum (1985) of ~92 Ma for the Pedro Dome stock.

### **Interpretation**

The peak metamorphism in the Proterozoic or younger Fairbanks schist was at ~196 Ma and by ~175 Ma the Ordovician Chatanika Terrane had cooled from eclogite temperatures. Between 140 and 115 Ma the Chatanika Terrane was thrust over the Fairbanks schist. The Gilmore Dome complex (Pedro Dome, Gilmore Dome and the Fort Knox stock) intruded between 88 and 92 Ma. True North and Chatanika hydrothermal alteration was at ~92 Ma, as indicated by fuchsite and resets of older minerals. Based on argon loss from minerals in and around True North and the Chatanika Terrane the youngest dated event is the 56-50 Ma basalt, which apparently covered the area.

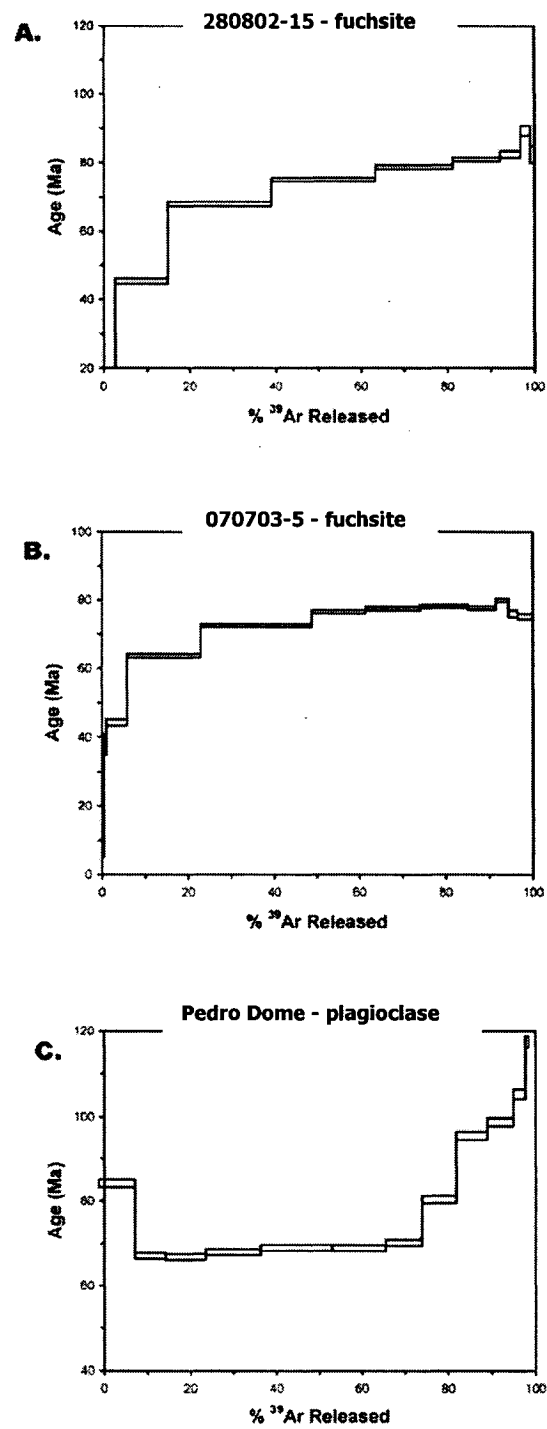


Figure 81. Fuchsite and plagioclase age spectra for samples from True North and Pedro Dome.

## MULTI-ELEMENT GEOCHEMISTRY

More than three thousand (3258) geochemical samples were taken from drill cuttings from 65 reverse-circulation rotary exploration and development drill holes. An additional 93 samples were taken of pit outcrops to characterize specific lithologic or vein types (Appendix E contains the pit data). These samples were analyzed for 35 or 36 elements. This work was done over a five-year period, with several changes in laboratories and/or sample preparation facilities. Mercury was part of the analytical suite for some analyses and not for others. It is not always clear when it was part of the analytical package, but not detected or whether no analysis was done. There is some question as to whether or not tellurium and bismuth were a part of the analytical package every year; certainly detection limits varied between the various laboratories. As a result, a rigorous analysis of the data is not possible. Nevertheless a number of observations about specific elements are possible based on the data available. Unfortunately, no three-dimensional presentation is possible for the entire database. Appendix E-1 is the correlation diagram for the drill-hole geochemical database.

Elements of interest include bismuth, tellurium, mercury, chromium, and tungsten. Bismuth (Bi) is present in the combined database (drill-hole and pit) in 265 samples; its range is 51 to 1 ppm with an average value of 3.55 ppm. Average crustal abundance of Bi is about 1 ppm. Tellurium (Te) is present in 16 samples; its range is 30 to 10 ppm with an average value of 13.88 ppm, with an average crustal abundance of 0.002 ppm. Mercury (Hg) is found in 2034 samples; and an average value of 0.06 ppm and a range of 2.25 to 0.011 ppm compared to an average crustal abundance of 0.02 ppm. Chromium (Cr) (Cr is in fuchsite at True North, but it is odd for metamorphosed marl to

contain much) has an average crustal abundance of 100 ppm and is present in all lithologies at True North in amount ranging from 7 ppm to 1426 ppm and an average of 171.77 ppm. Tungsten (W) (found in only 12 samples) has a range of 10 to 1070 and an average of 168.42 ppm. Average crustal values are from Rose et al. (1979).

The elements just detailed were chosen specifically for what they can tell about the True North deposit. Bismuth is closely associated with intrusions and intrusive hosted or related gold deposits (McCoy, 2000). While bismuth levels at True North are above average crustal levels, the levels are not at the levels of intrusion hosted or related deposits. Fort Knox, for example has native bismuth in some veins (McCoy, 2000). Tellurium and mercury are commonly associated with epithermal deposits. True North has elevated levels of both elements with tellurium significantly above average crustal levels. Chromium was chosen because of its association with the alteration mineral fuchsite, which is fairly common at True North. Chromium is not an element that would normally be associated with pelitic to limey sedimentary rocks, so its presence in the host rocks is an anomaly. The fact that chromium is present in all rocks at True North (Appendix E), both altered and unaltered, leads to two possibilities: the first is that it was present in the host rocks prior to the hydrothermal event; the second is that it is part of the suite of elements introduced by the hydrothermal event.

The relationship between gold and various elements is of interest as well. Since rocks at True North are enriched in bismuth and mercury, Figures 82 and 83 show gold plotted against bismuth and mercury. Neither shows a strong correlation. The correlation coefficient (Appendix E) for gold and bismuth is 0.1366 while that for gold and mercury is 0.4152, which might indicate neither a traditional epithermal nor intrusion association.



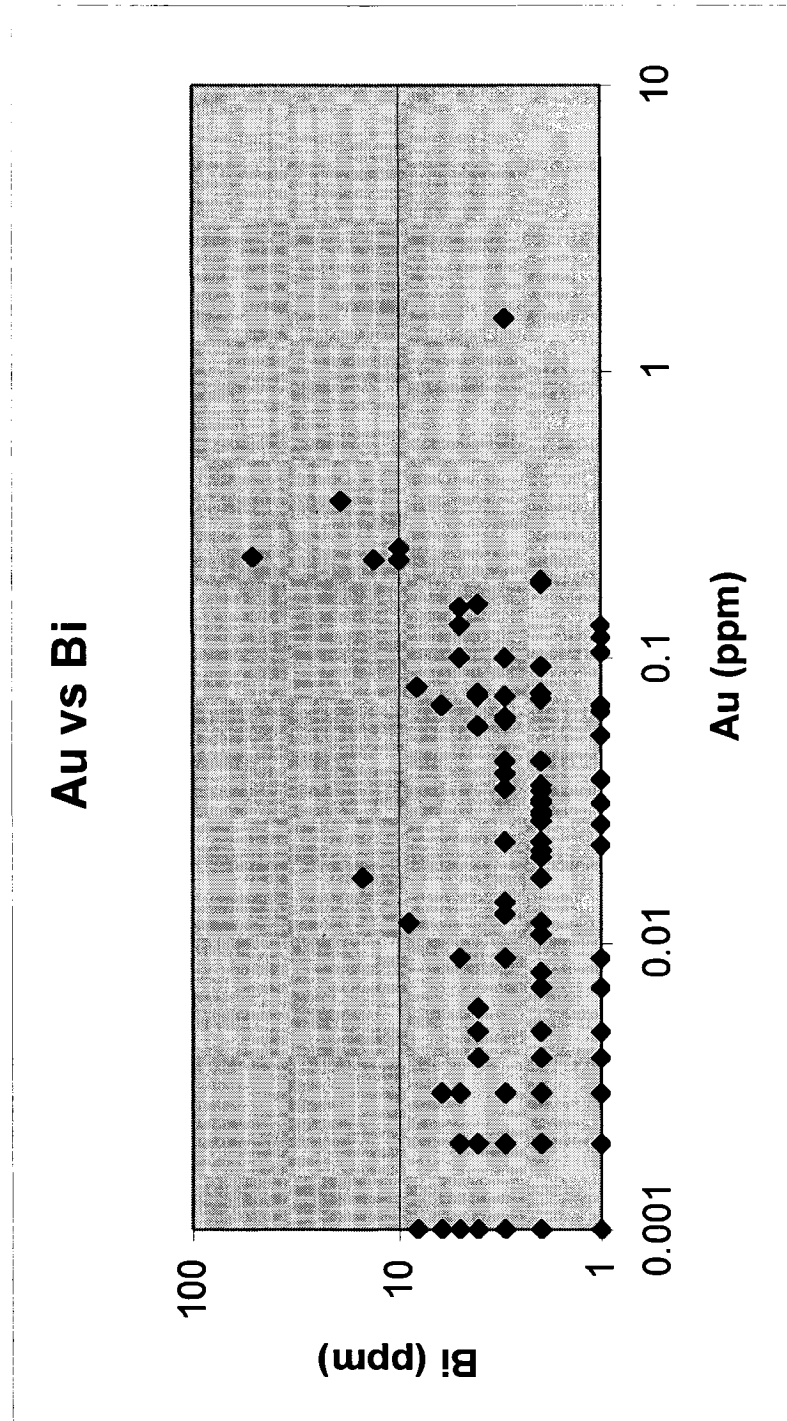


Figure 82. Gold versus bismuth. Data from Kinross drill hole geochemical database.

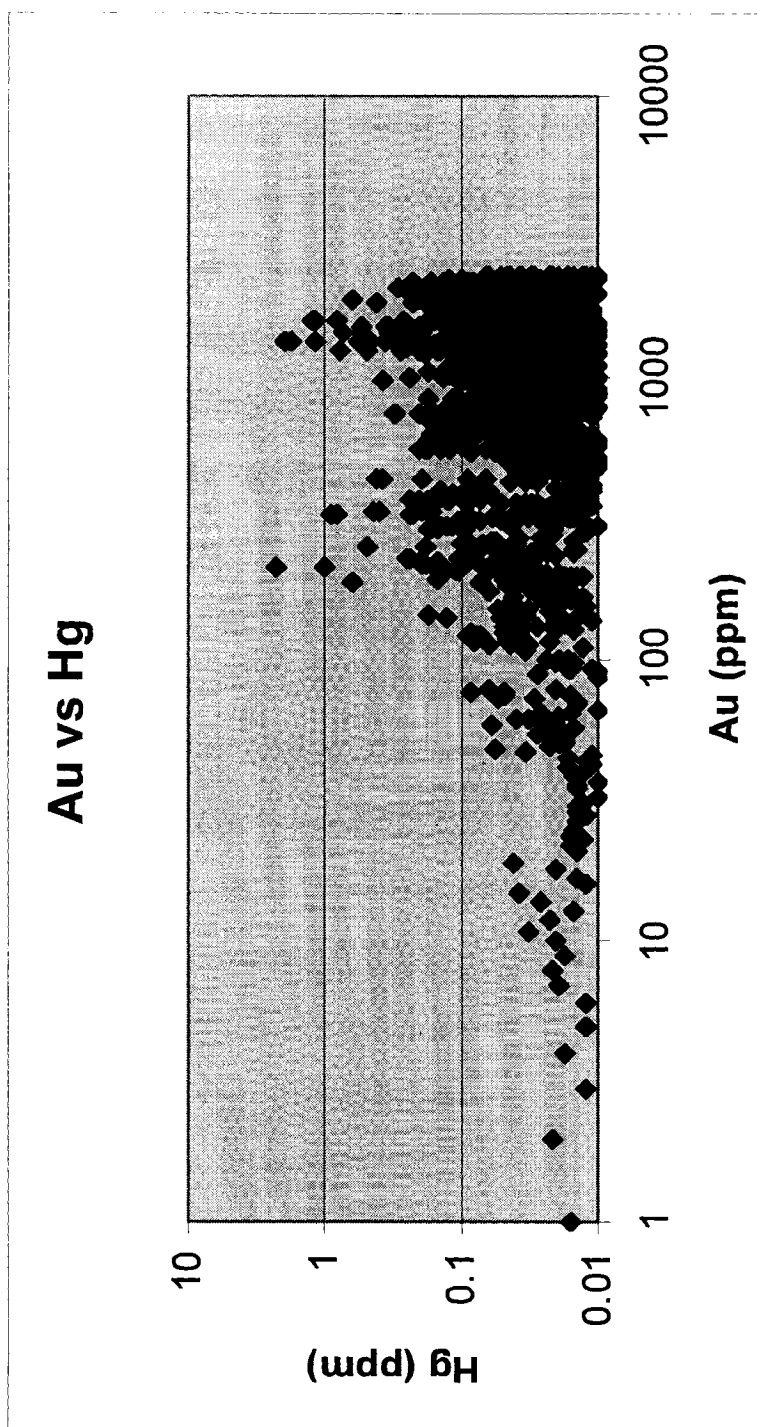


Figure 83. Gold versus mercury. Data from Kinross drill hole geochemical database.

Following up with elements that are commonly associated with gold and have an association at True North, arsenic, found in arsenopyrite with gold, (Fig. 84) exhibits a positive correlation (0.6008 from Appendix E). Stibnite is found in the same veins; Figure 85 shows gold versus antimony, yielding a low correlation (0.1089 from Appendix E). This indicates that the association between gold and stibnite is likely only a spatial coincidence. The correlation diagram in Appendix E shows that there is only one good gold correlation, gold-arsenic.

As useful as it may be to look at the absolute concentrations of individual elements and plots of one element against another, it is just as important to look at how the various elements relate to each other. Doing this one element at a time, or even using a correlation diagram is tedious and it is difficult to see relationships clearly. One technique for visualizing the relationships between data points is correspondence analysis, which looks for relationships (correspondence) between data points and displays them in graphical format. Correspondence analysis is a form of principal components analysis, a technique in which the idea is to represent multivariate data visually on an X-Y plot. This is accomplished by calculating a new X-Y data set, of perfectly independent data (to avoid data distortion) from the original multivariate database. This process involves creating a matrix of correlation coefficients (the data similarity matrix) and using eigendecomposition to calculate eigenvectors and eigenvalues. The X-Y plot is generated by plotting the eigenvalues and using the eigenvectors as axes (see Carr (2002) for a complete explanation). Correspondence analysis differs from other forms of principal components analysis by using the chi-square distance between each data entry and its expected value to calculate the similarity matrix, from which the plot is created

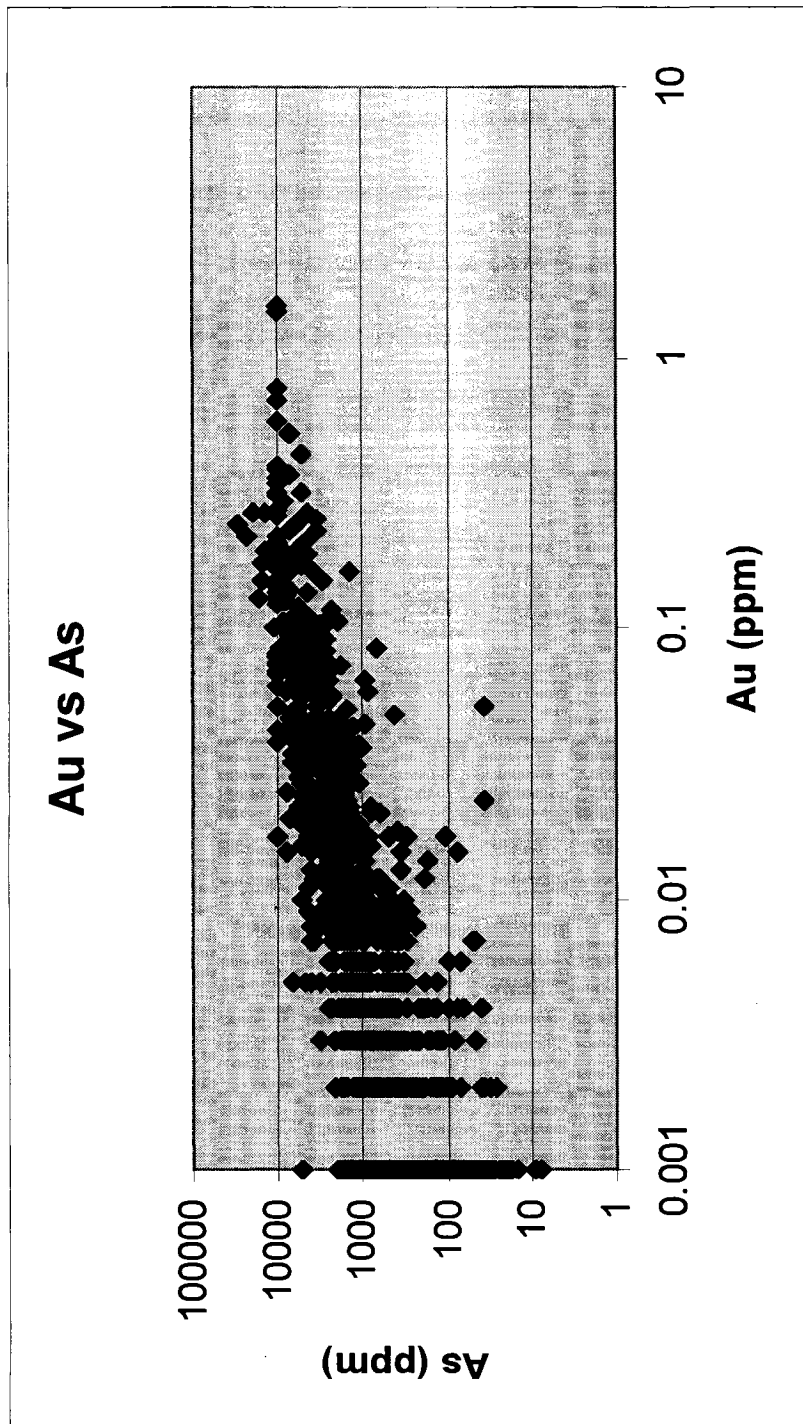


Figure 84. Gold versus arsenic. Data from Kinross drill hole geochemical database.

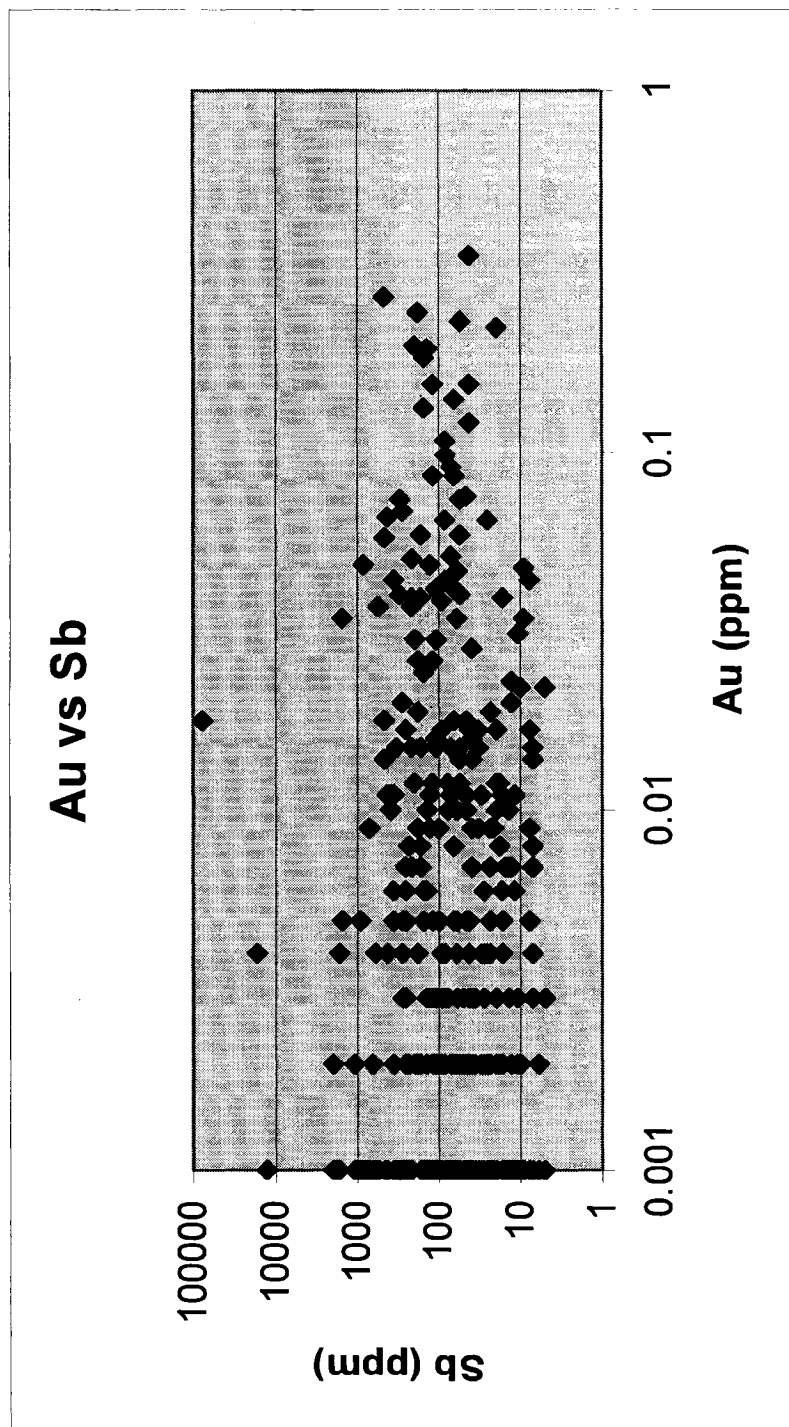


Figure 85. Gold versus antimony. Data from Kinross drill hole geochemical database.

(Carr, 2002). Figure 86 is a correspondence analysis plot of the drill-hole multi-element data set, with variables (elements) plotted. All of the plots presented here were generated using a specially modified version of the Visual Data program (Carr, 2002). Factors (eigenvalues) 1 and 2 are plotted and together they represent 55% of the data set. The plot has a horizontal row of elements across the top with tellurium on the left and gold on the right, with a grouping of elements left of center. Tungsten sits, alone on the lower margin of the page. This plot shows several things, many of the elements that are likely to have been introduced by the ore-forming system are grouped to the left (Te, Ba) and right (Bi, Ag, Hg, Pb, Cd, Sb, As, Au) of a central group of elements (everything else, except W). Elements that plot directly on top of another are not plotted, to increase legibility. The program produces a list of variables that plot in the same position so that interpretations can be made. Starting with tungsten, its position alone and below indicates that although it is physically present it bears virtually no relation to any of the other elements, as if it were part of an entirely different system. Tellurium and barium are as far away from gold as is possible, suggesting that they should have negative correlations with gold, which they do (Appendix E). On the right side are all elements that would reasonably be added by a hydrothermal system. Arsenic is closest to gold, showing that it has the strongest correlation. Left of center, titanium through sodium, are the elements that make up the host units, including chromium. Figure 87 exhibits factors 2 and 3 (33% of the data set) with similar results. The line of elements is now vertical and W is still off to one side. This confirms that W is not related to anything else. On this plot gold and antimony are on opposite ends and most everything else grouped together.

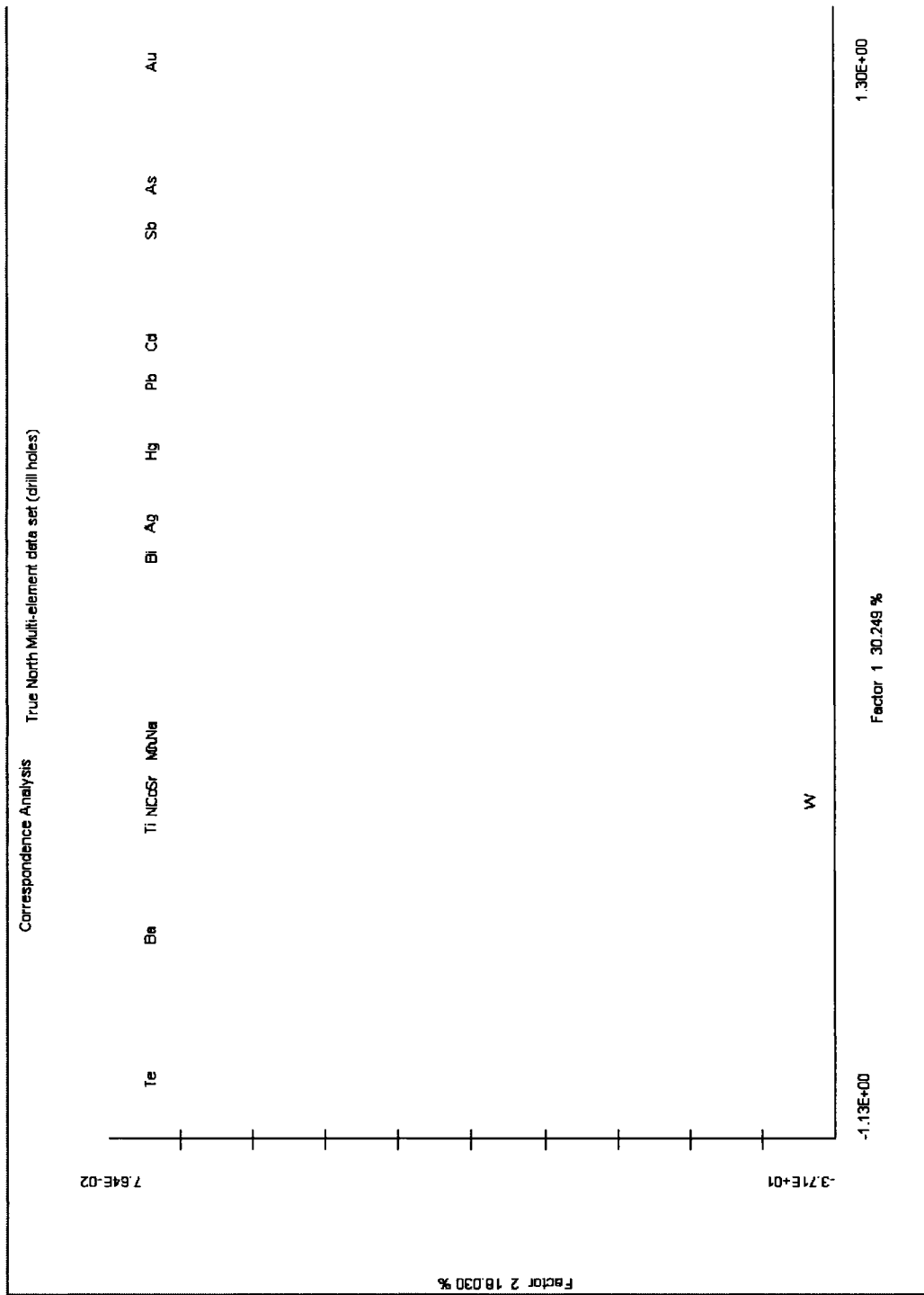
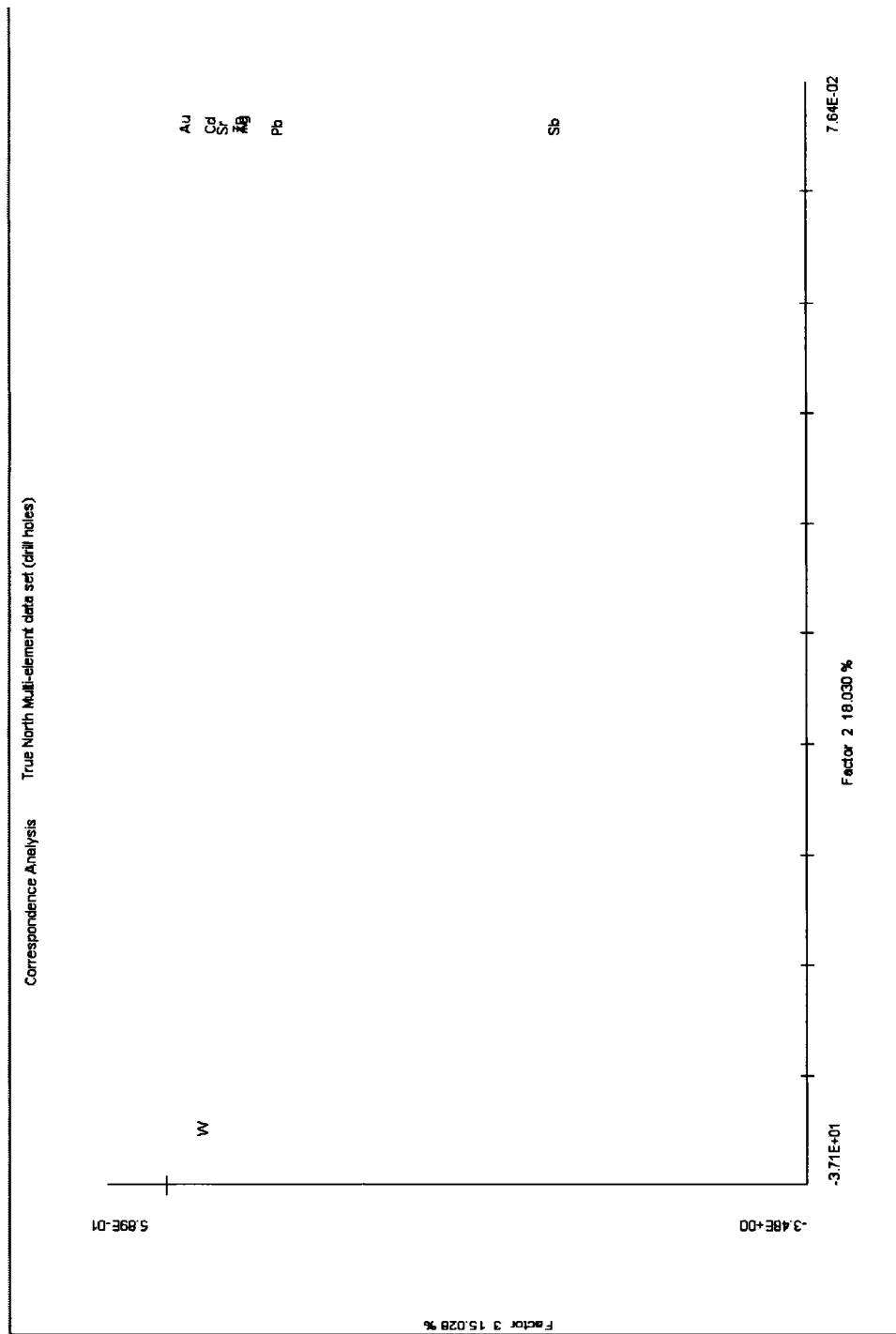


Figure 86. Correspondence Analysis plot of elemental data, factors 1 and 2, from the Kinross multi-element drill hole database. Elements that plot in the same space are not plotted, for clarity. Chromium plots with Mn and Na in the center group.



**Figure 87. Correspondence Analysis plot of elemental data, factors 2 and 3, from the Kinross multi-element drill hole database. Elements that plot in the same space are not plotted, for clarity. Chromium plots with Mn and Na in the upper group.**



One of the weaknesses of this method is that in this situation where one element is clearly not related to the others, it forces all of the other variables into a tighter group and it is not possible to see the variation within this group. To see how the tightly grouped elements relate to one another, the database was modified, removing the samples that contain tungsten. The rest of the data re-plots as seen in Figure 88. The basic structure is not greatly modified, but more detail is visible. Antimony now falls below the rest of the elements, suggesting more strongly that the link between stibnite and gold is spatial only. Tellurium and barium still show their negative correlation, but now the 'hydrothermal suit' shows a little spread, both horizontal and vertical. Gold and arsenic are together, off to one side, with Cd, Pb, Hg, Ag, and Bi grouped together. This may indicate that the elements of this 'base metal suite' are related and perhaps are from a different pulse or stage than gold. Figure 89, the factor 2 and 3 plot, supports the relationships seen in Figure 88. Antimony is still alone. Now Te and Sr show a strong negative correlation, Au and As are still grouped, Cd and Hg are together, with Pb on the left indicating less of a correlation with the groups on the right side (Cd/Hg and Au/As).

The same technique was applied to the individual samples within the data set (Fig. 90, factors 1 and 2). Samples were plotted with each sample assigned a number (1 to 3246), indicating its position in the data set. Obviously many samples plot one on top of the other along the upper horizontal group. Note the string of samples that trail off to the bottom of the plot; these are the high tungsten samples. The amount of tungsten increases away from the main group. The left side of the plot is made up of mainly eclogite samples. Samples 43 and 2978 (indicated) just to the right of the tungsten group are slate-argillite, and the right side is mostly graphitic-quartz-mica schist. Figure 91 shows factors

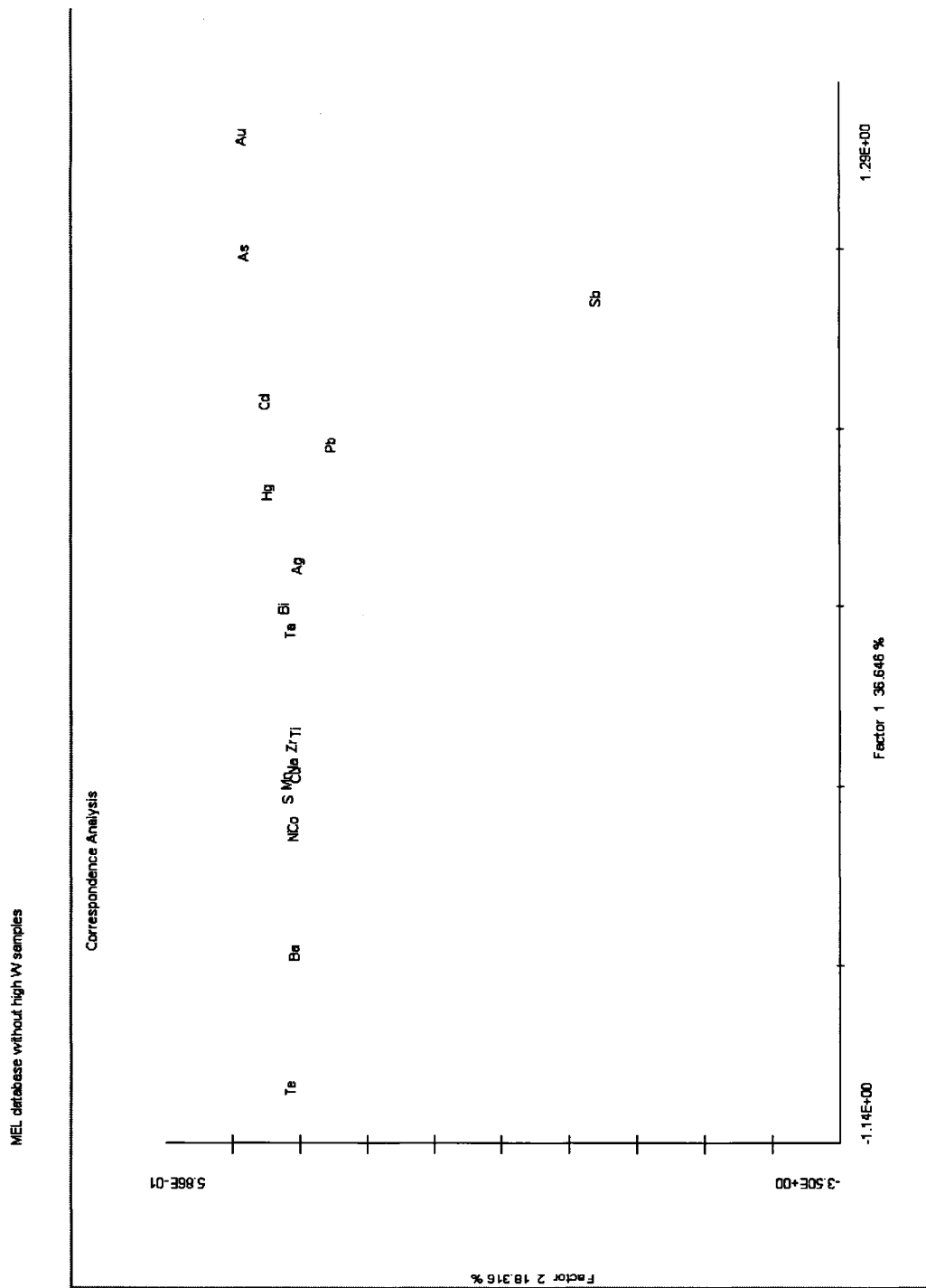


**Figure 88. Correspondence Analysis plot of elemental data, factors 1 and 2, with high tungsten samples removed. From the Kinross multi-element drill hole database. Elements that plot in the same space are not plotted, for clarity. Chromium plots with Mn and Na in the center group.**

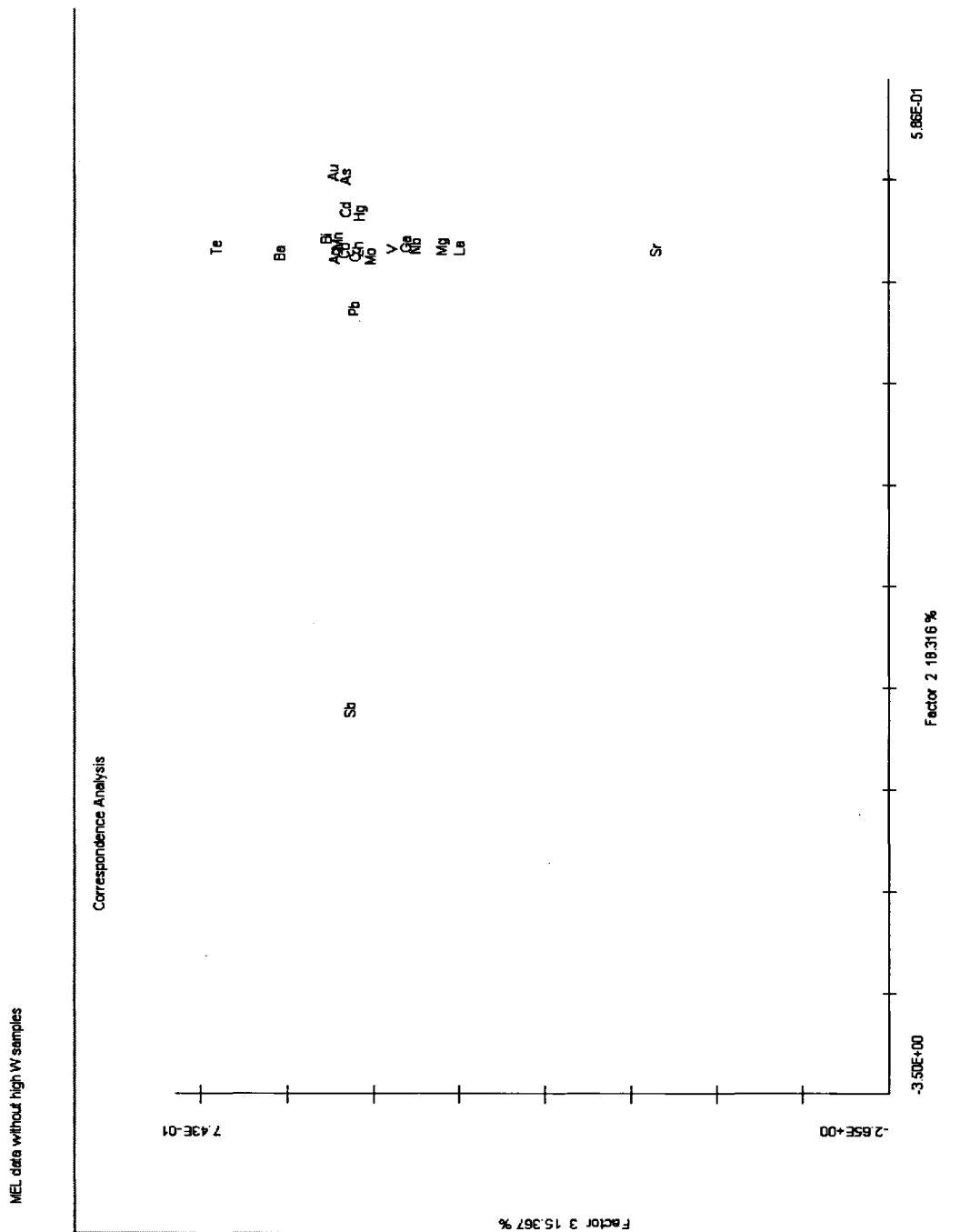


**Figure 89. Correspondence Analysis plot of elemental data, factors 2 and 3, with samples with high tungsten values removed. From the Kinross multi-element drill hole database. Elements that plot in the same space are not plotted, for clarity. Chromium plots with Mn and Na in the center group.**

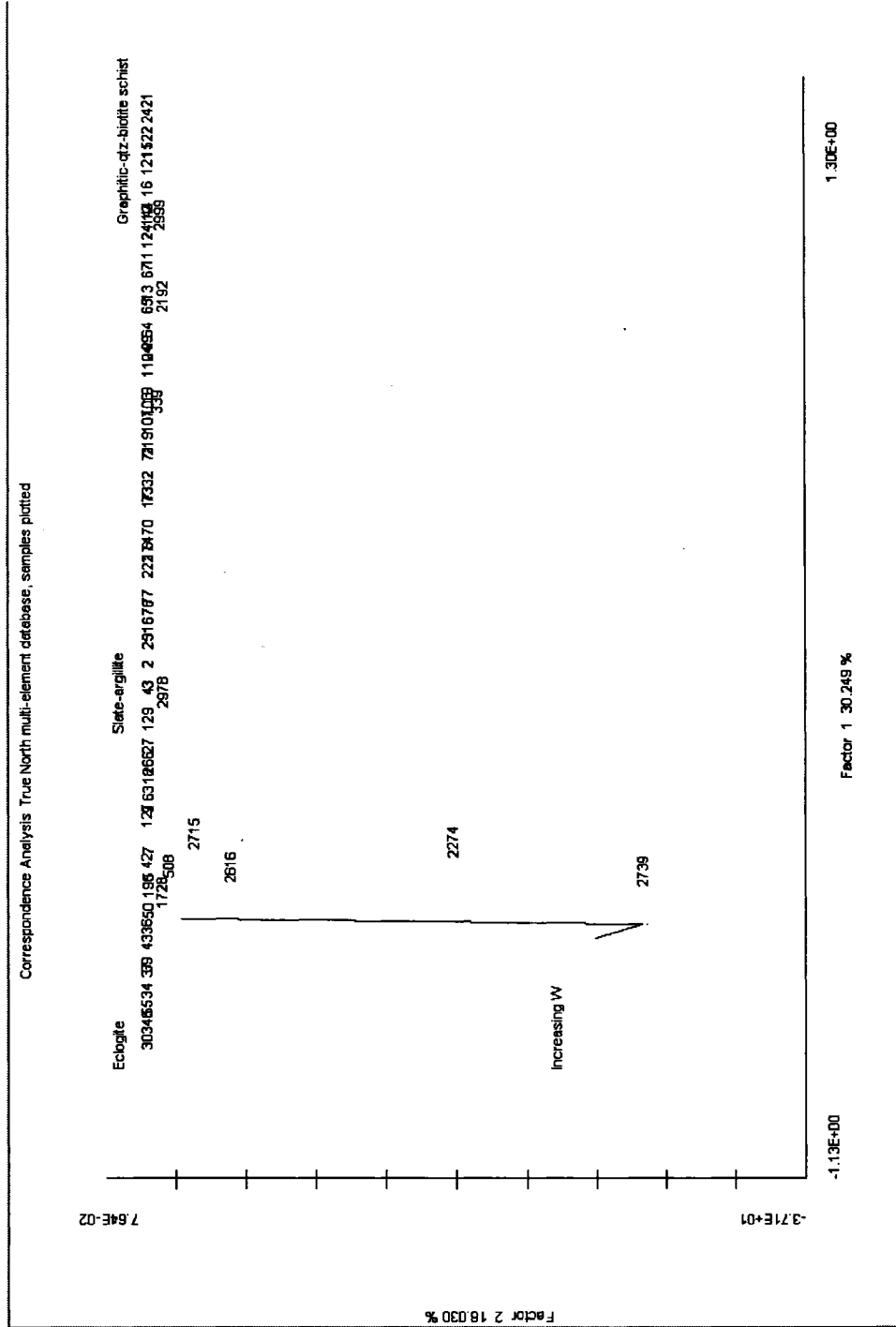


Figure 90. Correspondence Analysis plot of samples, factors 1 and 2, from the Kinross multi-element drill hole database. Samples that plot in the same space are not plotted for clarity.

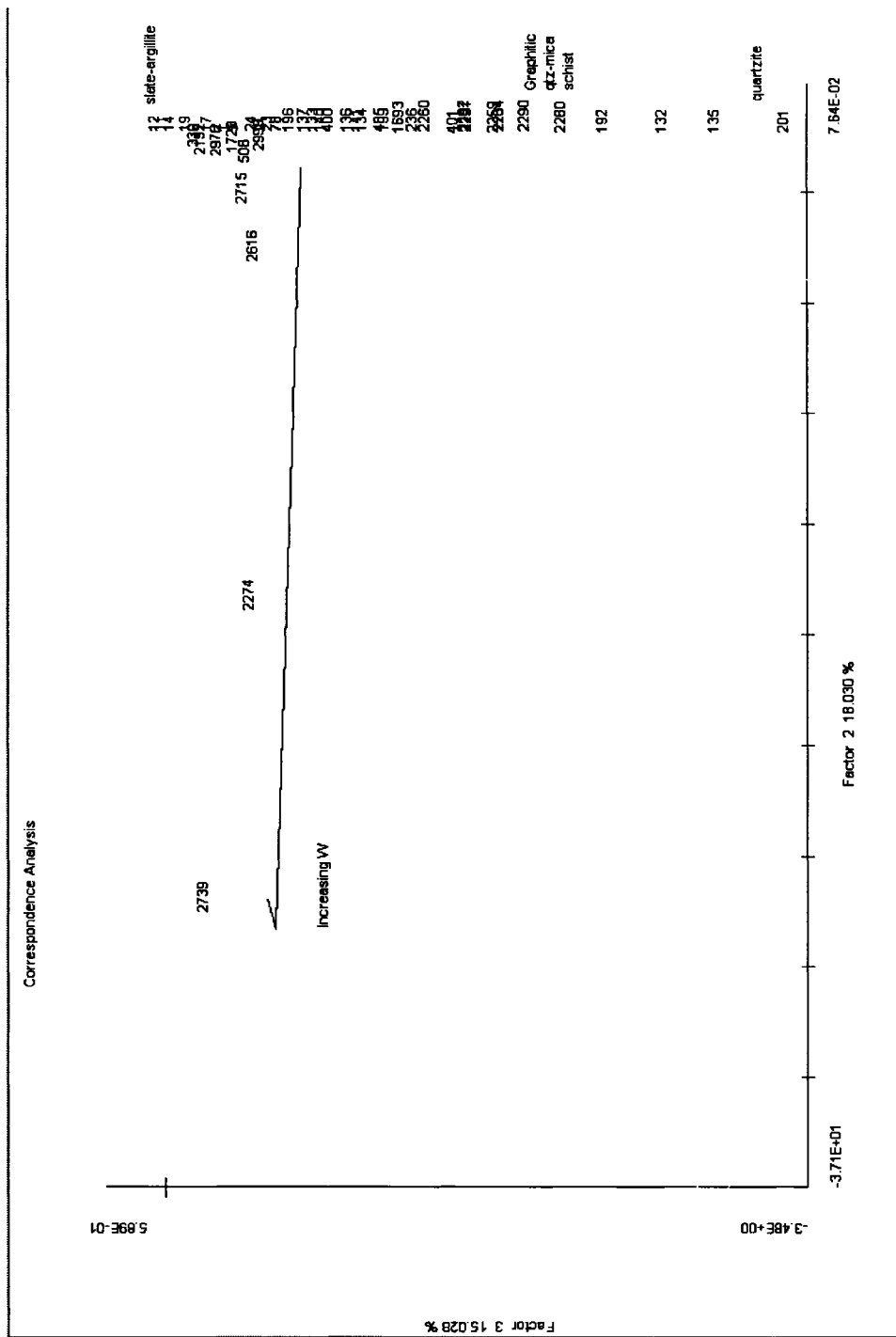


Figure 91. Correspondence Analysis plot of samples, factors 2 and 3, from the Kinross multi-element drill hole database. Samples that plot in the same space are not plotted for clarity.

2 and 3 plotted. The high tungsten group now extends out to the left, slate-argillite plot to the top, graphitic-quartz-mica schist lower center, and quartzite at the bottom. These plots were reproduced using the data set without the high tungsten samples (Figs. 92 and 93). Although the samples spread more, these plots are difficult to interpret. The downward tail on the Factor 1 and 2 plots may indicate variation due to weathering; since many of the samples that plot in that region are probably weathered (the logged lithographic units for those sample numbers are generally felsic schist or muscovite schist). The factor 2 and 3 plot now exhibits two tails; one below and one to the left, both may be related to weathering, although there is no clear pattern. Neither plot allows the separation of samples by rock type, nor do sample alteration or mineralized samples stand out. Perhaps subsets of the data could be plotted to show more detail; unfortunately drill-hole geologic coding isn't setup to allow weathering, alteration, or mineralization to stand out. It is possible that dividing the dataset by lithology would allow alteration and/or mineralization to be differentiated, but there are more efficient ways of doing this (petrographic analysis or sorting the database by gold values).

These plots give a visual means of identifying patterns in data. Some of these patterns are fairly obvious; Au, As, Cd, Sb, Hg, Ag, Bi, Ta, Te, and Ba have been added to system. Less obvious is the meaning of the relative positions of elements on the plots. Using Figure 88 as an example; As and Au plot close together suggesting a close relationship. The elements Ta, Bi, Ag, Hg, Pb, Cd plot between As/Au and the host rock cluster in the center, along the same axis, suggesting that the elements are related, but perhaps differ in timing or means of transport. Antimony plots off axis and below arsenic







suggesting that it is related spatially, but not temporally. Tellurium and barium plot on the same axis as gold and arsenic, but as far from them as is possible on this plot, suggesting that there is a negative relationship between the elements. Tellurium and barium have been introduced to these rocks, but are not spatially or temporally related to gold and arsenic. On Figure 86 tungsten plots off axis and below the host rock central cluster, perhaps suggesting an earlier tungsten event in this area.

Chromium plots in the center with the elements that make up the host rock suite, suggesting that it was added to the host rocks prior to the hydrothermal event, perhaps during the eclogite facies metamorphism when it could have come into contact with fluids derived from mafic or ultramafic rocks. It is clear from these plots that the chromium was not introduced with the elements of the ore forming system.

## CONCLUSIONS

### **Summary and Interpretation of Regional Tectonic Setting**

The True North gold deposit is hosted in a rock package, the Chatanika terrane, which was metamorphosed to eclogite grade in a subduction zone that closed the Slide Mountain ocean and brought the Yukon-Tanana composite terrane (YTT) and North American plate back together. This eclogite klippe structurally overlies amphibolite grade metasediments, the Fairbanks schist.

The Fairbanks schist had been thought to be part of the YTT. Recently, detrital zircons have been recovered from the Fairbanks schist that are of same ages and populations as those found in passive margin strata of the Selwyn Basin (Aleinikoff and Nokleberg, 1989; Dusel-Bacon et al., 2006). Detrital zircons and reconstructions of offset stratigraphy and deformation patterns on either side of the Tintina fault demonstrate that the Fairbanks schist and Wickersham grit (north of the Fairbanks schist) are a continuation of passive margin strata on the west side of the Tintina fault (Dover, 1994; Mair et al., 2006). Redefinition of the Fairbanks schist, as former deposits of the North American passive margin, is part of a larger redefinition of the character and history of the YTT. Redefinition of Fairbanks schist and YTT units provides a framework to piece together a history of the North American passive margin, the YTT, and the Chatanika terrane host of the True North gold deposit.

North American passive margin strata of the Selwyn Basin contain Proterozoic to Cretaceous sediments, metamorphosed to between greenschist and upper amphibolite grades. In Canada (Yukon) and adjacent Alaska, passive margin strata are deformed into

fold and thrust belts. The Snowcap sequence, YTT basement, comprises continentally derived clastic sequences. These rocks are unconformably overlain and intruded by Late Devonian-Early Mississippian continental arc/back arc rocks (Colpron et al., 2006), the Finlayson arc assemblage, which corresponds to an earlier interpretation of the beginning of east dipping subduction at ~340 Ma (Erdmer et al., 1998). The Slide Mountain ocean began to open at about this time (back arc sequences) rifting the YTT away from North America (Nelson et al., 2006). The Middle Mississippian to Early Permian Klinkit island arc assemblage volcanic and volcanoclastic rocks unconformably overlie Finlayson arc rocks (Colpron et al., 2006). Mid to Late Permian, Klondike arc assemblage, volcanic and volcanoclastic rocks unconformably overlay Klinkit assemblage units and mark the beginning of west-dipping subduction of Slide Mountain oceanic lithosphere under the YTT (Colpron et al., 2006). In Permo-Triassic time, the Yukon-Tanana docked with North America.

Paleogeographic reconstructions, based on the framework above, are shown on Figure 94, relating the relative positions of arcs, continents, and oceans at several points in time. Also shown is a schematic cross-section at Late Devonian to Early Mississippian time.

Based on this timeline, the sediments that were subducted to form the Chatanika terrane (mud and limy mud to limestone) would have probably been deposited in the Mississippian (?) in order to have been subducted and metamorphosed by the time the Slide Mountain ocean basin was closed in the Permian to Triassic, during which time they were thrust over the passive margin strata of North America.

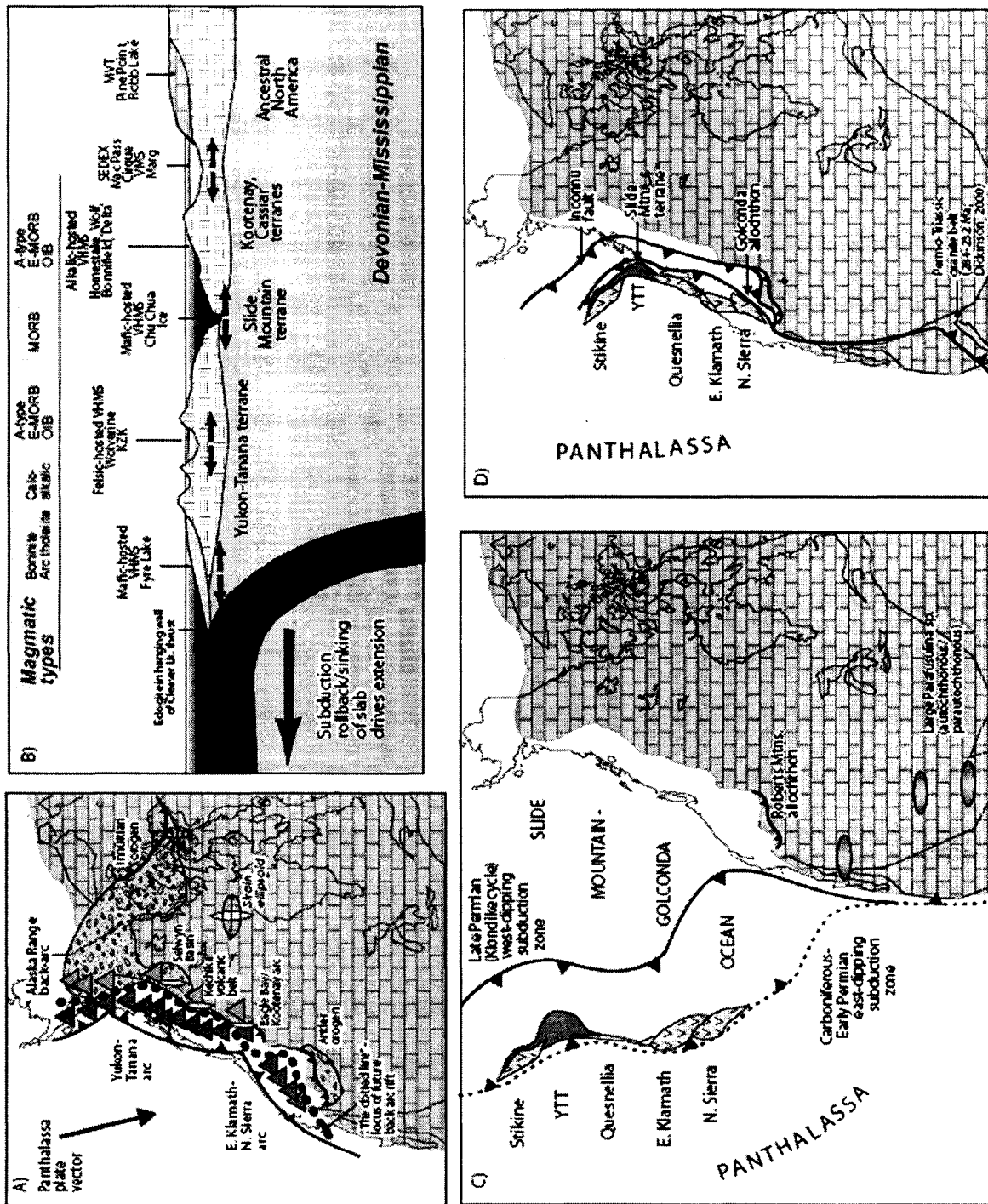


Figure 94. Paleogeographic reconstructions for YTT and related terranes. A) Devonian-Early Mississippian (ca. 356 Ma). B) Schematic cross-section, Late Devonian-Early Mississippian. C) Mid-Permian (ca. 270Ma). D) Permo-Triassic reconstruction. From Nelson, 2006.

Apparently contradicting the timing suggested by the YTT arc assemblages described above, are dates of ~196 Ma, for peak metamorphism in Fairbanks schist and a ~175 Ma for cooling to ~300°C from eclogite temperature and pressure (Chatanika terrane), and ~125 Ma for thrusting over the Chatanika terrane over the Fairbanks schist, reported by Douglas et al. (2002).

Other important events in the region include a 120-105 Ma, NW-SE extensional event in the Yukon-Tanana uplands (centered southeast of Fairbanks in the area of gneiss domes in Salcha River to southeastern Lake George areas) with exhumation of deep levels, exposing higher grade metamorphic units (like the Fairbanks schist?)(Mair et al., 2006). This extensional event may explain the ~125(±) Ma date (Douglas, et al., 2002) from the thrust fault between the Chatanika terrane and the Fairbanks schist. The fault contact between Chatanika rocks and the Fairbanks schist may have been reactivated as a low-angle normal fault during extension.

At about ~100 Ma, deformation in foreland fold and thrust belts and Selwyn Basin ended (Mair et al., 2006 and Dover, 1996), the Canada basin began to open (66° counterclockwise rotation) (Plafker and Berg, 1994), and Fallon plate subduction began (Newberry et al., 1996). Newberry et al. (1996) suggested that the district scale left-lateral oblique faults in the Fairbanks district are a result of Fallon plate subduction.

From an ore deposits standpoint, 93 Ma was important, with the intrusion the Tombstone-Tungsten magmatic belt across the Selwyn Basin (Mair et al., 2006) and intrusion of the Gilmore Dome complex and formation of the True North and Fort Knox gold deposits (McCoy, 2000; Jenson, pers. comm.; Blum, 1983; this study). Gilmore Dome complex granite and diorite are offset by left-lateral faults (Newberry et al., 1996).

At ~85 Ma, subduction of Kula plate began and between ~85 and 66 Ma most of the right lateral movement occurred on the Tintina fault (Plafker and Berg, 1994; Mair et al., 2006). This movement offset the Fairbanks schist, Wickersham grit, and ore deposits and hosts rocks in the Finlayson area of the Yukon, between 400 and 450 km northeast.

### **Summary and Interpretation of the True North Gold Deposit**

Mineralization occurred at about 92 Ma and was associated with the intrusion of the Pedro Dome (part of the Gilmore Dome intrusive complex) granodiorite. The Fort Knox deposit is the same age (93-92 Ma) and hosted in the Gilmore Dome intrusive complex. Quartz-arsenopyrite-pyrite-gold and carbonate veins filled open graphite lined faults and fractures in the host rocks. The graphite is metamorphic and was remobilized by fault movement. The fluid (from minimum homogenization temperatures in quartz fluid inclusions) was in the epithermal temperature range (173 and 309°C), dilute (~ 4 weight percent NaCl equivalent), contained as much as 3 mole % CO<sub>2</sub>, and was probably derived at least in part from a magmatic source. Meteoric water input would have occurred as the hydrothermal system began to collapse. Isotopic data indicate that the mineralizing veins formed in graphite-coated fractures along faults. The graphite controlled carbon isotopic fractionation in carbonate veins.

Hydrothermal alteration in the Hindenberg and Central pits occurs as sericite-fuchsite growth at the expense of biotite (phlogopite) and carbonate flooding (dolomite-ankerite) as vein halos in schist. Arsenopyrite, pyrite, trace gold are present in the alteration halos. Hydrothermal alteration changed the color of altered biotite schist from dark brown to buff, with a greenish cast (fuchsite). Orientation of foliation affected the

strength of alteration and size of the alteration halo. Where hydrothermal fluids gained access to foliation and/or where veins are closely spaced, large areas are altered (+100' across the northeast end of Hindenberg Pit). In Shepard Pit, veins hosted by slate-argillite have sericite alteration only and limited to the damage zone of the fault which is between two and three meters wide.

Supergene alteration converted the fuchsite-ankerite alteration into a burnt orange colored, friable mass of mica and iron oxides and hydroxides. Ore control geologists at True North used the coincidence of this distinctive burnt orange color, with black (graphite), and angular quartz fragments, as an accurate guide to high-grade ore.

The True North deposit formed at a depth of less than 1 km, based on the close correspondence between fluid inclusion homogenization and isotopic temperatures for quartz (173 and 309°C) and calcite veins (225.1 and 275.5°C). This would place True North approximately 2 km above Pedro Dome at the time of formation (Blum, 1983). Based on a maximum depth of formation of 1 km, a maximum temperature correction for depth of formation (pressure) would be 10°C (Potter, 1977). Thus, temperatures of deposition for vein quartz of 240°C for Hindenberg veins and 280°C for Shepard veins are obtained. Temperatures, salinities, and CO<sub>2</sub> are all characteristic of epithermal systems. The lack of 'normal' epithermal banded vein textures and the lack of multiple visible veins is likely due to frequent temporally closely spaced fault movements that sealed off vein sets and prevented the development of banded vein textures and pulverized earlier veins.

Host rock fracture characteristics and structural preparation were key factors to the development of a gold deposit at True North. Suitability of these rocks as a host for

an epithermal style gold deposit was due to the fact that they formed and retained open fractures while the majority of the surrounding rocks did not. Structural preparation involved two important sets of faults: 1) Low-angle faults that form the contact between the Chatanika rocks and the Fairbanks schist, and a series of sub-parallel low-angle faults documented in the Hindenberg and Central pits. These faults probably originated as thrusts during the Permian–Triassic (?) closure of the Slide Mountain ocean basin and may have been reactivated as low-angle normal faults during a later extensional event. 2) Left-lateral oblique faults, introduced above, that are observed district wide and are particularly important in the Hindenberg and Central pits where they are closely spaced. Both of these fault sets exhibit evidence of multiple episodes of movement and are mineralized.

Shepard Pit mineralization also occurs in low and high angle faults. The single low-angle fault in the Shepard Pit is of the same type as low-angle faults in the Hindenberg and Central pits and it is mineralized. At Shepard Pit the low-angle fault forms the contact between biotite schist/eclogite (hanging wall) and slate-argillite (footwall). The mineralized high angle faults in Shepard Pit strike north-south and northeast. The northeast-striking high angle fault may be related to the left-lateral oblique faults; but it has a slightly more northerly strike and occurs as a single fault, which may be due to different host rocks, slate-argillite vs. biotite schist. The mineralized north-south reverse fault is anomalous at True North. Other faults of similar orientation, such as the reverse fault in the Central Pit, are post mineral and offset mineralized faults.

Based on observed fault relationships in the Shepard and Central pits that include: a low-angle fault contact between slate-argillite and biotite schist/eclogite; a mineralized



reverse fault that puts slate argillite against biotite schist and eclogite and terminates a low-angle fault; and a reverse fault placing slate-argillite in contact with biotite schist and terminating mineralized fault-veins, it appears that the Shepard area and the slate-argillite have been faulted up from a deeper structural level. This interpretation is supported by fluid inclusion homogenization temperatures. Minimum homogenization temperatures from quartz inclusions from Shepard vein quartz are 40°C hotter than quartz vein inclusion minimum homogenization temperatures in Hindenberg. The low-angle (thrust) fault in Shepard Pit, with slate-argillite in the footwall suggests that the slate-argillite was either present above the Fairbanks schist when the Chatanika terrane was thrust over it, or that the slate-argillite was imbricated with the Chatanika rocks as it was transported to its present location.

There are no known occurrences of slate-argillite in other parts of the Chatanika terrane, nor are any other occurrences of slate-argillite mapped in the northern part of the Fairbanks district. In the southern part of the district near the city of Fairbanks, there are a number of small outcroppings of slate, locally known as the Birch Hill slate. These are shown (Newberry et al., 1996) as thrust over the Fairbanks schist. Slate is also part of the sequence to the south of the Fairbanks schist. This sequence is slate, marble, stretched pebble conglomerate, and Devonian to Mississippian felsic igneous rocks, also mapped as thrust over the Fairbanks schist (Dusel-Bacon et al., 2006). It seems reasonable to suggest that the Birch Hill slate and the slate mapped southeast of the city of Fairbanks is the same unit and that it became imbricated with Chatanika rocks as the Chatanika terrane was transported to its current position.

All but the most recent faults have been reactivated on numerous occasions making interpretation of initial movement impossible. The last stages of displacement occurred on the normal and reverse faults visible in the Central and Shepard pits.

Contoured gold assays from blast holes, in the Hindenberg Pit, show that while the overall gold values are erratic, both the low-angle faults and high-angle (northeast striking) faults are mineralized. Limited sampling between low-angle faults, in silica-carbonate altered units, indicates that some of the altered material between faults has anomalous gold values.

### **Deposit Model**

Structural preparation began with thrusting of Chatanika rocks over Fairbanks schist units (Permo-Triassic?) and development of low-angle fault sets. Low-angle fault sets may have been reactivated later (at ~100 Ma?) as normal faults. A later (~100 Ma?) high angle left-lateral oblique fault system finishes setting the structural stage. All fault sets had enough episodes of movement to develop considerable amounts of gouge and move graphite around. The amount of gouge suggests considerable volumes of fluid were present during fault movement; indicating that perhaps the host section was water saturated. Gilmore Dome complex, including Pedro Dome diorite was emplaced (93-92 Ma) and a hydrothermal circulation system began. Veins formed and with repeated fault movements, were sealed off from further fluids. Earliest veins are carbonate. Main stage veins were quartz-gold-sulfide (aspy-py), but carbonate veins continued to form and some cross-cut mineralized quartz veins. Late, post-gold, veins used the same conduits, but have stibnite filling open spaces in the quartz. Stibnite deposition may be related to

the cooling of the system. Youngest veins are calcite. Alteration of wall rock is contemporaneous with quartz veining. As the hydrothermal system collapsed meteoric water overwhelmed the system.

### **Suggestions for Further Work**

Regionally, more mapping, geochemical, and isotopic work needs to be done in east-central Alaska, to resolve or solidify the differences between the YTT as it is defined in Canada, and the rocks in Alaska.

Much has been made of the intrusion-hosted or intrusion-related gold deposits in Alaska and Yukon. Perhaps looking at Cretaceous plutons and extensional faults could focus the search for the next Fort Knox?

How does graphite affect a mineralizing fluid? Does it help, hinder, or is it neutral with regard to gold transport and deposition? Graphite is present at many gold deposits. Is there a connection?

Several additional studies may add to the understanding of True North. First, oxygen and deuterium isotopic analysis of fuchsite may pinpoint the fluid source. Second, a Re/Os date on True North arsenopyrite may confirm timing of deposit formation and allow comparison with other deposits in Alaska and the Yukon that have been dated by this technique. Third, district scale geophysics, or compilation of existing geophysical surveys may help define structural connections, if any, between deposits.

## REFERENCES CITED

- Aleinikoff, J.N., and Nokleberg, W.J., 1989, Age of deposition and provenance of the Cleary Sequence of the Fairbanks Schist Unit, Yukon-Tanana Terrane, east-central Alaska: *in* Dover, J. H. and Galloway, J. P., ed. U. S. Geological Survey Bulletin, Report: B 1903, pp.75-83.
- Baker, E.D., 1996, Newmont internal Memorandum.
- Bakke, A., Morrell, B., Odden, J., Bergstrom, T., and Woodman, J., 2000, Kinross Gold USA's activities in the Fairbanks mining district, K2K *in* The Tintina Gold Belt: Concepts, Exploration, and Discoveries, British Columbia Chamber of Mines, Special volume 2, p. 89-98.
- Banfield, J.F., and Eggleton, R. A., 1988, Transmission electron microscope study of biotite weathering: *Clays and Clay Minerals*, v. 36, p. 47-60.
- Blum, J.D., 1983, Petrology, Geochemistry and Isotope Geochronology of the Gilmore Dome and Pedro Dome Pluton, Fairbanks Mining District, Alaska: Alaska Report of Investigations, 59 p.
- Blum, J.D., 1985, A petrologic and Rb-Sr isotopic study of intrusive rocks near Fairbanks, Alaska: *Canadian Journal of Earth Sciences*, v. 22, pp. 1314-1321.
- Bottinga, Y., 1968, Calculation of fractionation factors for carbon and oxygen exchange in the system calcite-carbon dioxide-water: *Journal of Physical Chemistry*, v. 72, p. 800-808.
- Brown, E.H. and Forbes, R. B., 1986, Phase petrology of eclogitic rocks in the Fairbanks District, Alaska: *in* Evans, B. W., and Brown, E. H., eds., *Blueschists and Eclogites*, vol.164. Memoir - Geological Society of America: Bellingham, WA, United States, Geological Society of America, p. 155-167.
- Buisseret, P., 1997, Petrology of the Chatanika Terrane and the Fairbanks Schist at the True North Gold Project, Alaska, U.S.A.: Queen's University Honors Thesis, 46 p.
- Carr, J.R., 2002, *Data Visualization in the Geological Sciences*: Upper Saddle River, NJ, Prentice Hall, 267 p.
- Collins, P.L.F., 1979, Gas hydrates in CO<sub>2</sub> -bearing fluid inclusions and the use of freezing data for estimation of salinity: *Economic Geology*, v. 74, p. 1435-1444.

- Colpron, M., Nelson, J.L., and Murphy, D.C., 2006, A tectonostratigraphic framework for the pericratonic terranes of the northern Canadian Cordillera: *in* Colpron, M. a. N., J.L., ed., *Paleozoic Evolution and Metallogeny of Pericratonic Terranes at the Ancient Pacific Margin of North America, Canadian and Alaskan Cordillera*, Special Paper 45, Geological Association of Canada, p. 1-45.
- Desmons, J. and Smulikowski, W, 2004, 4. High P/T metamorphic rocks; A systematic nomenclature for metamorphic rocks Recommendations, web version of 01.05.2004., IUGS Subcommittee on the Systematics of Metamorphic Rocks.
- Douglas, T.A., Layer, P.W., Newberry, R.J., and Keskinen, M.J., 2002, Geochronologic and thermobarometric constraints on the metamorphic history of the Fairbanks mining district, western Yukon-Tanana Terrane, Alaska: *Canadian Journal of Earth Sciences*, v. 39, p. 1107-1126.
- Dover, James H., 1994, Geology of part of East-Central Alaska: *in* Plafker, G. and Berg, H.C., eds., *The Geology of Alaska*, G-1. *The geology of North America*: Boulder, CO, Geological Society of America, Boulder, CO, pp. 153-204.
- Dunn, S.R., and Valley, J.W., 1992, Calcite-graphite isotope thermometry: a test for polymetamorphism in marble, Tudor gabbro aureole, Ontario, Canada: *Journal of Metamorphic Geology*, v. 10, p. 487-501.
- Dusel-Bacon, C., Hopkins, M.J., Mortensen, J.K., Dashevsky, S.S., Bressler, J.R. and Day, W.C., 2006, Paleozoic tectonic and metallogenic evolution of the pericratonic rocks of east-central Alaska and adjacent Yukon: *in* Colpron, M. a. N., J.L., ed., *Paleozoic Evolution and Metallogeny of Pericratonic Terranes at the Ancient Pacific Margin of North America, Canadian and Alaskan Cordillera*, Special Paper 45, Geological Association of Canada, p. 25-74.
- Ehlers, E. G. and Blatt, H., 1982, *Petrology*: Freeman, 722 p.
- Erdmer, P., Ghent, E.D., Archibald, D.A., and Stout, M.Z., 1998, Paleozoic and Mesozoic high-pressure metamorphism at the margin of ancestral North America in central Yukon: *Geological Society of America Bulletin*, v. 110, p. 615-629.
- Flanigan, B., Freeman, C., McCoy, D., Newberry, R.J., Hart, C.J.R., Tucker, T.L., and Smith, M.T., 2000, Paleo-reconstruction of the Tintina gold belt; implications for mineral exploration: Cordilleran exploration roundup 2000; *The Tintina Gold Belt: Concepts, Exploration, and Discoveries*, Special Volume 2, British Columbia and Yukon Chamber of Mines, Vancouver, BC, Canada, p. 35-48.
- Fleet, M.E., 2003, *Muscovite and Phengite, Sheet silicates: Micas*, 3A. *Rock-Forming Minerals*: London, The Geological Society, p. 758.

- Forbes, R.B., Matsumoto, H., Haramura, H., 1968a, Eclogitic rocks in the Fairbanks district, Alaska: Special Paper - Geological Society of America, pp.71, 1968, p. 71.
- Forbes, R.B., Swainbank, R.C., and Burrell, D.C., 1968b, Structural setting and petrology of eclogite-bearing terrane near Fairbanks, Alaska: Transactions - American Geophysical Union, v. vol.49, 345 p.
- Forbes, R.B. and Weber, F.R., 1982, Bedrock geologic map of the Fairbanks mining district, Alaska: Alaska Open-File Report, vol.170, 2 sheets.
- Foster, H.L., Keith, T.E.C., Menzie, W.D, 1994, Geology of the Yukon-Tanana area of East-Central Alaska: *in* Plafker, G. and Berg, H.C., eds., The Geology of Alaska, G-1. The geology of North America: Boulder, CO, Geological Society of America, Boulder, CO, p. 205-240
- Hall, M.H., 1985, Structural geology of the Fairbanks mining district, central Alaska: Alaska Division of Geological Geophysical Surveys. Public-data File 85-61, 67 p.
- Harms, T.A., 2003, An Alternate Hypothesis for the Origin of Paleozoic Pericratonic Terranes of the Cordillera: abstract, GAC-MAC Vancouver 2003, Vancouver, BC, Canada, Geological Association of Canada, p. SS23.
- Hart, C.J.R., McCoy, D.T., Goldfarb, R.J., Smith, M., Roberts, P., Hulstein, R., Bakke, A.A., and Bundtzen, T.K., 2002, Geology, exploration, and discovery in the Tintina gold province, Alaska and Yukon: *in* Goldfarb, R. J., and Nielsen, R. L., eds., SEG Special Publication: vol.9, p. 241-274.
- Joesting, H.R., 1943, Strategic mineral occurrences in interior Alaska: Alaska Territorial Department of Mines, 26 p.
- John, D. A., Hofstra, A. H., Fleck, R. J., Brummer, J. E., and Saderholm, E. C., 2003, Geologic setting and genesis of the Mule Canyon low-sulfidation epithermal gold-silver deposit, North-Central Nevada: Economic Geology, vol. 98, n. 2, pp. 425-463.
- Johnston, Stephen T., 2001, The great Alaskan terrane wreck; reconciliation of paleomagnetic and geological data in the northern Cordillera: Earth and Planetary Science Letters, v. 193, n. 3-4, p. 259-272.
- Mair, J. L., Hart, C.J.R., and Stephens, J.R., 2006, Deformation history of the northwestern Selwyn Basin, Yukon, Canada: Implications for orogen evolution and mid-Cretaceous magmatism: Geological Society of America Bulletin, v. 118, p. 304-323.

- Mertie, John Beaver, Jr., 1918, Lode mining in the Fairbanks District, Alaska: *in* Brooks, A.H., ed., Mineral Resources of Alaska, Report on Progress of Investigations in 1916, USGS Bulletin 0662-H, p. 403-424.
- Metz, Paul A., 1991, Metallogeny of the Fairbanks Mining District, Alaska and Adjacent Areas: Mineral Industry Research Laboratory Report Number 90, Mineral Industry Research Laboratory, 370 p.
- McCoy, D., Newberry, R.J., Layer, P.W., DiMarchi, J.J., Bakke, A.A., Masterman, J.S., and Minehane, D.L., 1997, Plutonic-related gold deposits of interior Alaska: Economic Geology Monographs, v. 9, p. 191-241.
- McCoy, D.T., 2000, Mid-Cretaceous pluton-related gold deposits of interior Alaska; characteristics, metallogenesis, gold-associative mineralogy and geochronology: Unpub. Doctoral thesis, University of Alaska, 177 p.
- Mook, W.G., Bommerson, J.C., and Stavermen, W.H., 1974, Carbon isotope fractionation between dissolved bicarbonate and gaseous carbon dioxide: Earth and Planetary Science Letters, v. 22, p. 169-176.
- Moore, D.M. and Reynolds, R.C. Jr., 1997, X-ray diffraction and the identification and analysis of clay minerals: Oxford University Press, 378 p.
- Nelson, J. L., Colpron, M., Piercey, S.J., Dusel-Bacon, C., Murphy, D.C. and Roots, C.F., 2006, Paleozoic tectonic and metallogenic evolution of the pericratonic terranes in Yukon, northern British Columbia and eastern Alaska: *in* Colpron, M. a. N., J.L., ed., Paleozoic Evolution and Metallogeny of Pericratonic Terranes at the Ancient Pacific Margin of North America, Canadian and Alaskan Cordillera, Special Paper 45, Geological Association of Canada, p. 323-360.
- Newberry, R.J., Bundtzen, T.K., Clautice, K.H., Combllick, T.D., Laird, G.M., Liss, S.A., Pinney, D.S., Reifentuhl, R.R, Solie, D.N., 1996, Preliminary geologic map of the Fairbanks Mining District: Alaska, Alaska Division of Geological and Geophysical Surveys.
- Newberry, R.J., Layer, P.W., Burleigh, R.E., and Solie, D.N., 1996, New (super 40) Ar/ (super 39) Ar dates for intrusions and mineral prospects in the eastern Yukon-Tanana Terrane, Alaska; regional patterns and significance: *in* Gray, J. E., Riehle, J. R., ed., Geologic studies in Alaska by the U.S. Geological Survey, 1996 U. S. Geological Survey Professional Paper, Report: P 1595, pp.131-159.

- Nokleberg, W.J.P., Leonid M., Monger, James W.H., Baranov, Boris V., Byalobzhesky, Stanislav G., Bundtzen, Thomas K., Feeney, Tracey D., Fujita, Kazuya, Gordey, Steven P., Grantz, Arthur; Khanchuk, Alexander I., Natal'in, Boris A., Natapov, Lev M., Ian O., Norton, Patton, Jr., William W., Plafker, George, Scholl, David W., Sokolov, Sergei D., Sosunov, Gleb M., Stone, David B., Tabor, Rowland W., Tsukanov, Nickolai V., Vallier, Tracy L., Wakita, and Koji, 1994, Circum-North Pacific Tectonostratigraphic Terrane Map: Open-File Report 94-714, USGS Open File Report, p. 126.
- O'Neil, J.R., Clayton, R.N., and Mayeda, T.K., 1969, Oxygen isotope fractionation in divalent metal carbonates: *The Journal of Chemical Physics*, v. 51, p. 5547-5558.
- Patton, W.W. Jr, Box, S.E., and Grybeck, D.J., 1994, Ophiolites and other mafic-ultramafic complexes in Alaska, *in* Plafker, G., and Berg, H.C., eds., *The geology of Alaska, G-1. The geology of North America: Boulder, CO, Geological Society of America, Boulder, CO, p.671-686.*
- Plafker, G., and Berg, H.C., 1994, Overview of the geology and tectonic evolution of Alaska, *in* Plafker, G., and Berg, H.C., eds., *The geology of Alaska, G-1. The geology of North America: Boulder, CO, Geological Society of America, Boulder, CO, p. 989-1021.*
- Potter, R. W., 1977, Pressure corrections for fluid-inclusion homogenization temperatures based on the volumetric properties of the system NaCl-H<sub>2</sub>O: *Jour. Research U.S. Geological Survey*, v. 5, n. 6, pp. 603-607.
- Prenn, N., Coulthard, John, and Ristorcelli, Steve, 1995, Resources and Reserves for the True North Project: Reno, NV, Mine Development Associates, 50 p.
- Price, R.A., and Carmichael, D.M., 1986, Geometric test for Late Cretaceous-Paleogene intracontinental transform faulting in the Canadian Cordillera: *Geology*, v. 14, p. 468-471.
- Prindle, L.M., 1913, A geologic reconnaissance of the Circle quadrangle, Alaska: *USGS Bulletin 538*, p. 261.
- Reiners, P.W., Spell, T.L., Nicolescu, S., and Zanetti, K.A., 2004, Zircon (U-Th)/He thermochronometry: He diffusion and intercalibration with <sup>40</sup>Ar/<sup>39</sup>Ar dating: *Geochemica et Cosmochemica Acta*, v. 68, p. 1857-1887.
- Roe, R.A. and, Stone, D.B., 1993, Paleomagnetism of the Fairbanks basalts, interior Alaska: *Alaska Division of Geological and Geophysical Surveys*, p. 61-70.



- Rose, A.W., Hawkes, H.E., and Webb, J.S., 1979, *Geochemistry in Mineral Exploration*: Orlando, Florida, Academic Press, 657 p.
- Spell, T.L., Smith, E.I., Sanford, A. and Zanetti, K.A., 2001, Systematics of xenocrystic contamination: Preservation of discrete feldspar populations at McCullough Pass Caldera revealed by  $^{40}\text{Ar}/^{39}\text{Ar}$  dating, *Earth and Planetary Science Letters*. v. 190/3-4, p. 153-165.
- Swainbank, R.C., 1971, *Geochemistry and petrology of eclogitic rocks in the Fairbanks area, Alaska*: Unpub. Doctoral thesis, University of Alaska. 130 p.
- Swainbank, R.C. and Forbes, R.B., 1975, Petrology of eclogitic rocks from the Fairbanks District, Alaska: *in* Forbes, R.B., ed, *Contributions geol. Bering Sea Basin and adjacent regions*, Special Paper no.151- Geological Society of America, p.77-123.
- Taylor, H. P., 1997, Oxygen and hydrogen isotopic relationships in hydrothermal mineral deposits; *in* Barnes, L. B., ed., *Geochemistry of Hydrothermal Ore Deposits*, p. 229-302.
- Wilson, M. J., 1966, The weathering of biotite in some Aberdeenshire soils: *Mineralogical Magazine*, v. 35, p. 1080-1093.

## Appendix A

### **X-ray data**

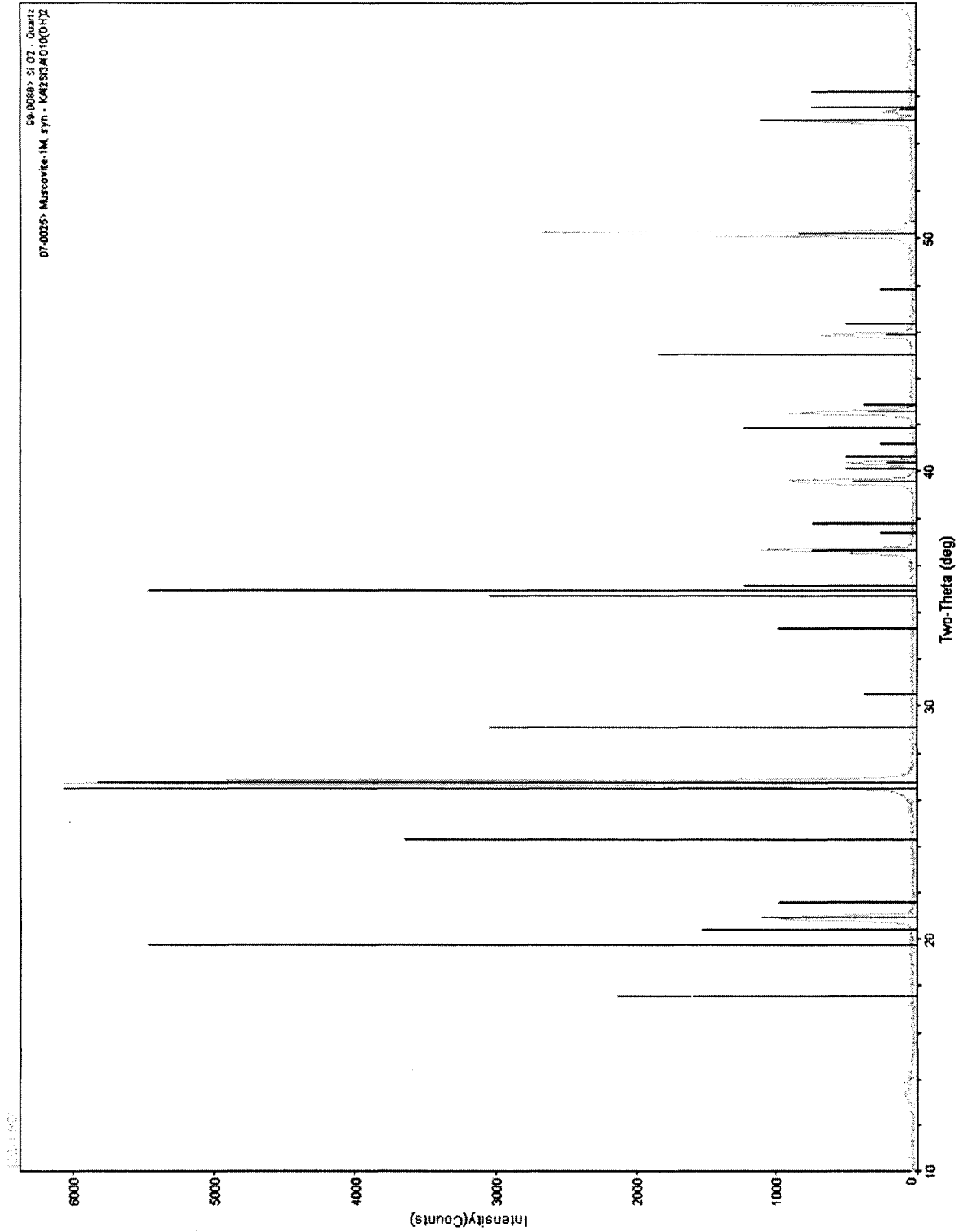
X-ray analysis for this study was performed using a Phillips 3100 Diffractometer, copper tube, 40KV and 30mA, set to 'Routine Scan'.

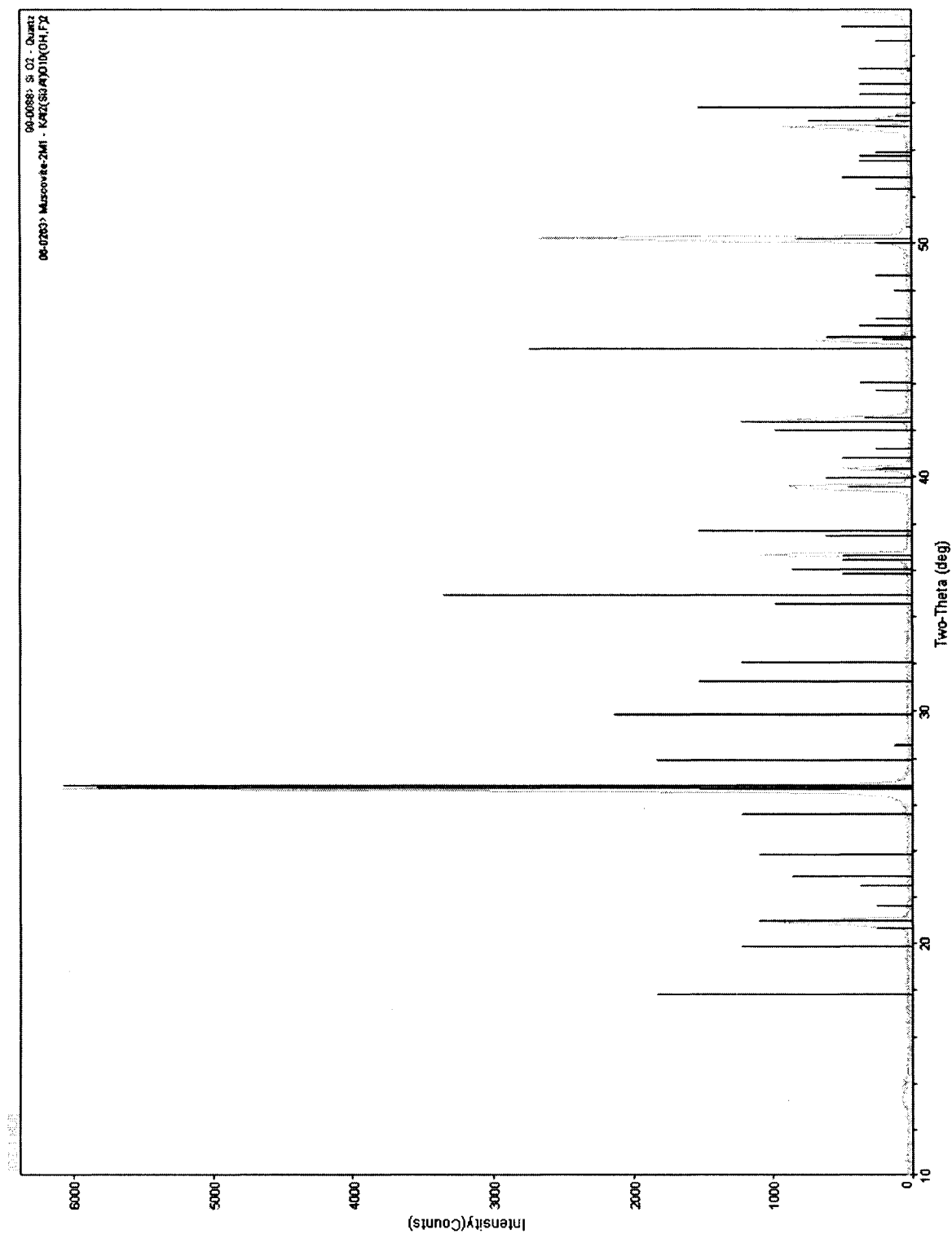
Interpretation of the XRD data was done using Jade version 6.5 peak identification and matching software. The selection of the best fit was done by progressively removing the peaks of identified minerals and then searching for minerals to fit the remaining peaks. Quartz was present in the samples analyzed or added to provide reference peaks (as a standard).

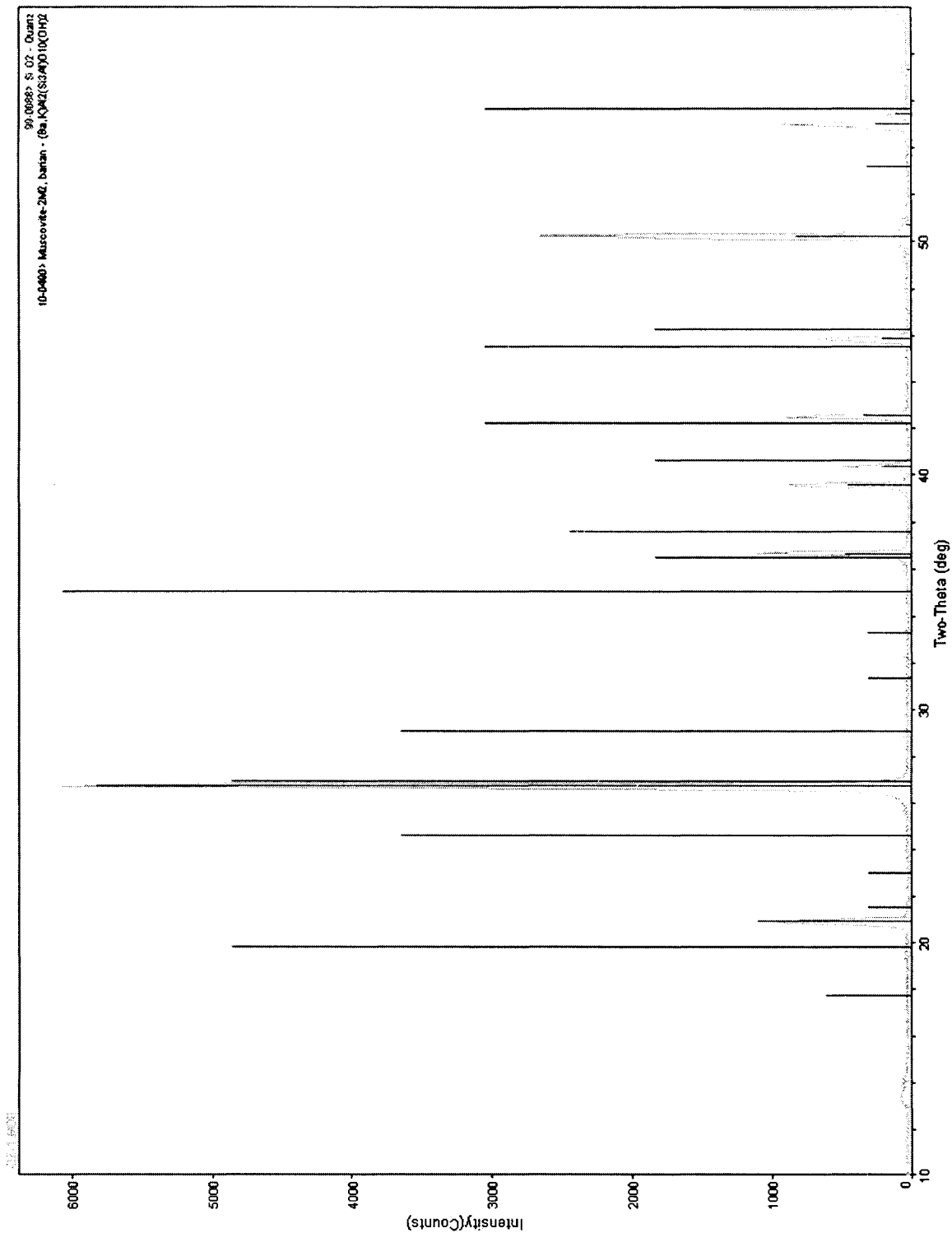
For a complete discussion of this subject see Moore and Reynolds (1997).

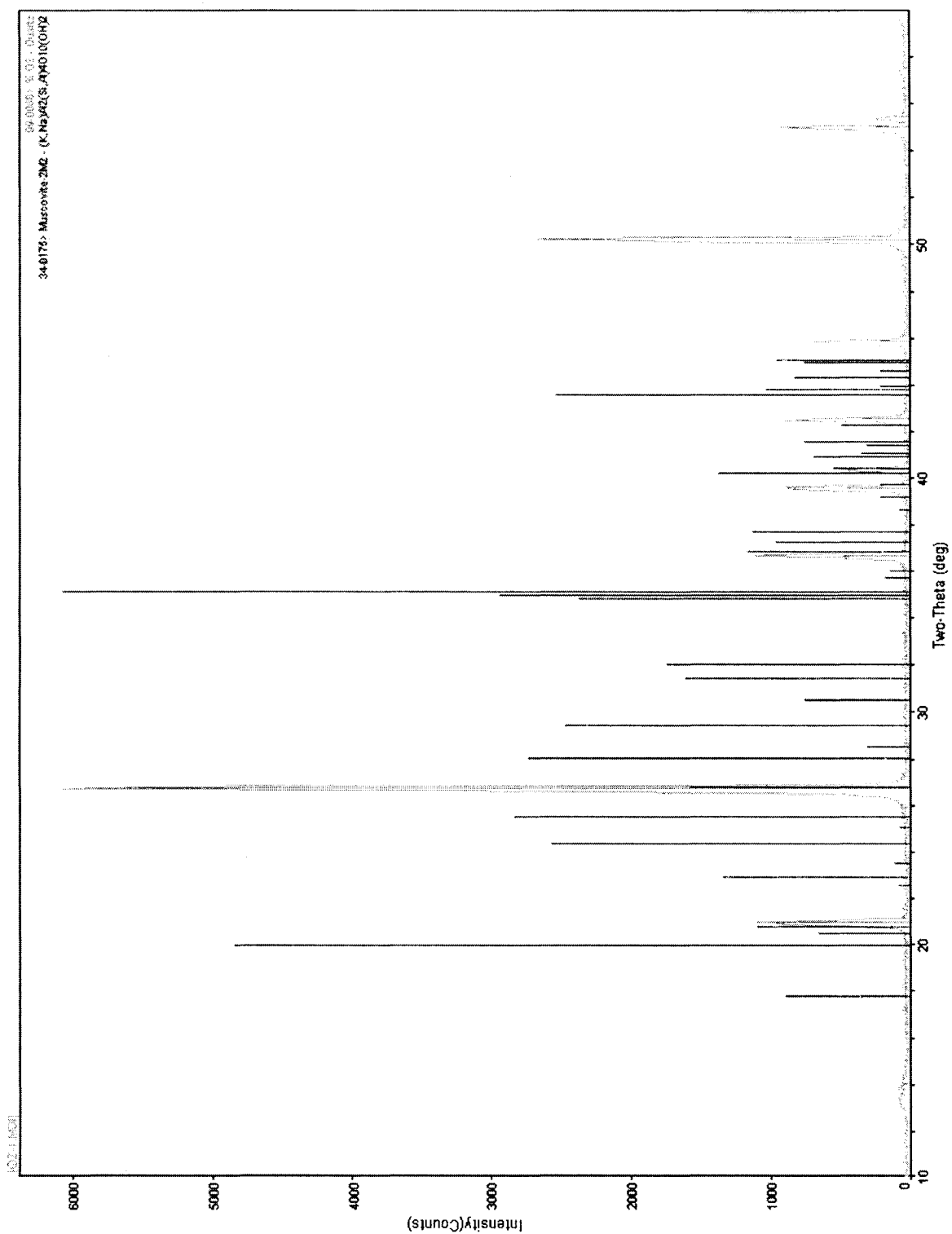
### Appendices

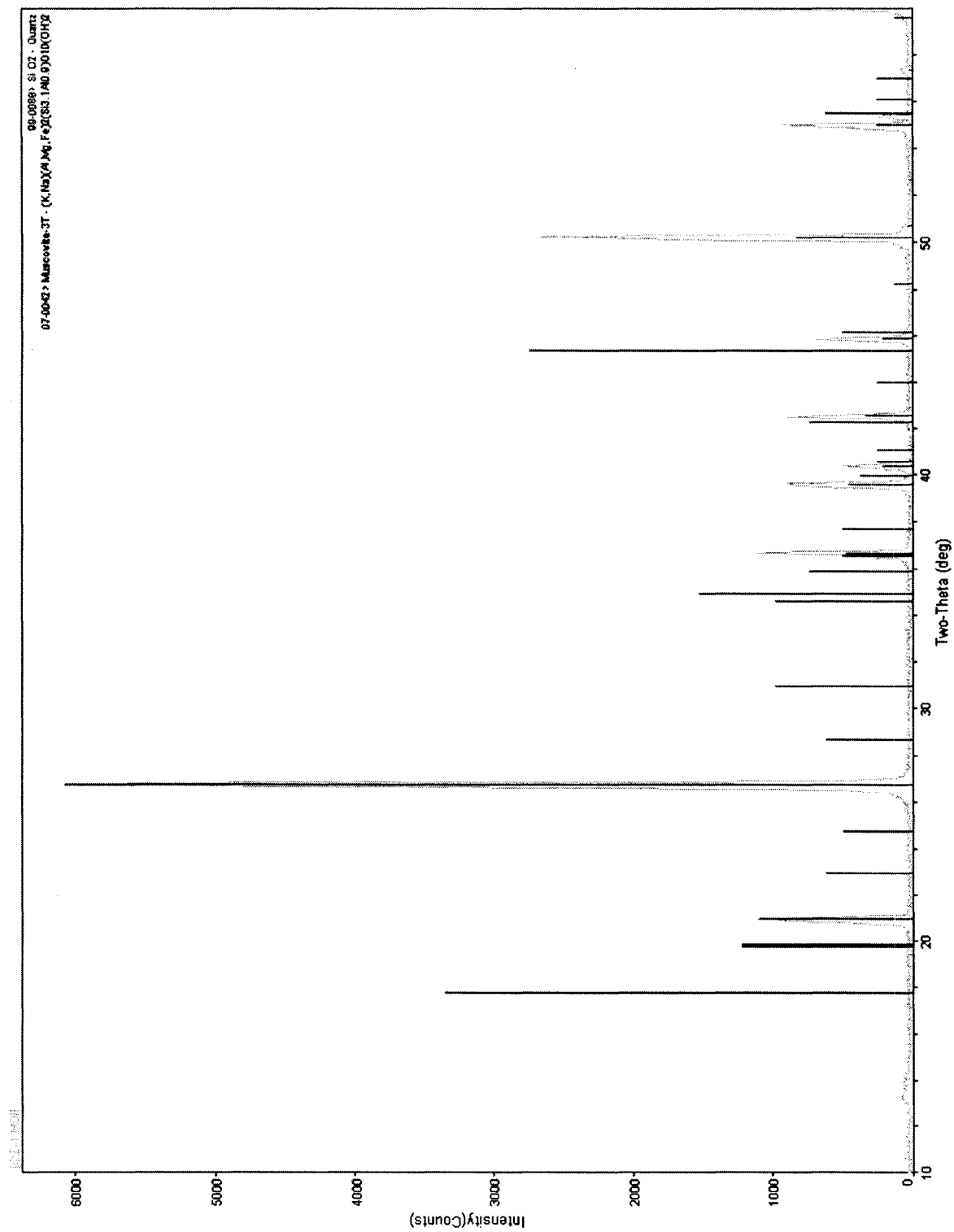
**Appendix A: Part 1.**  
**Comparison Patterns**



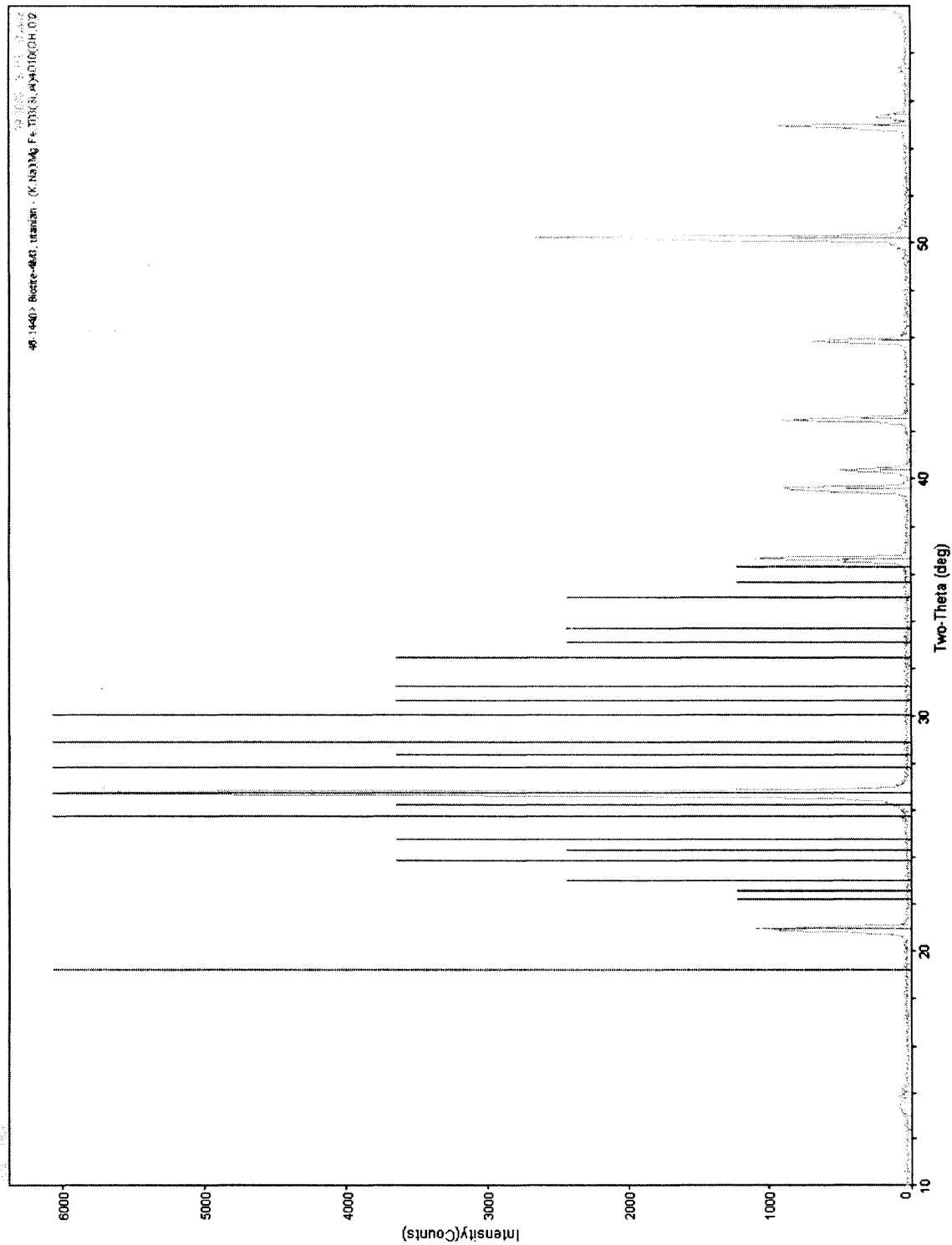


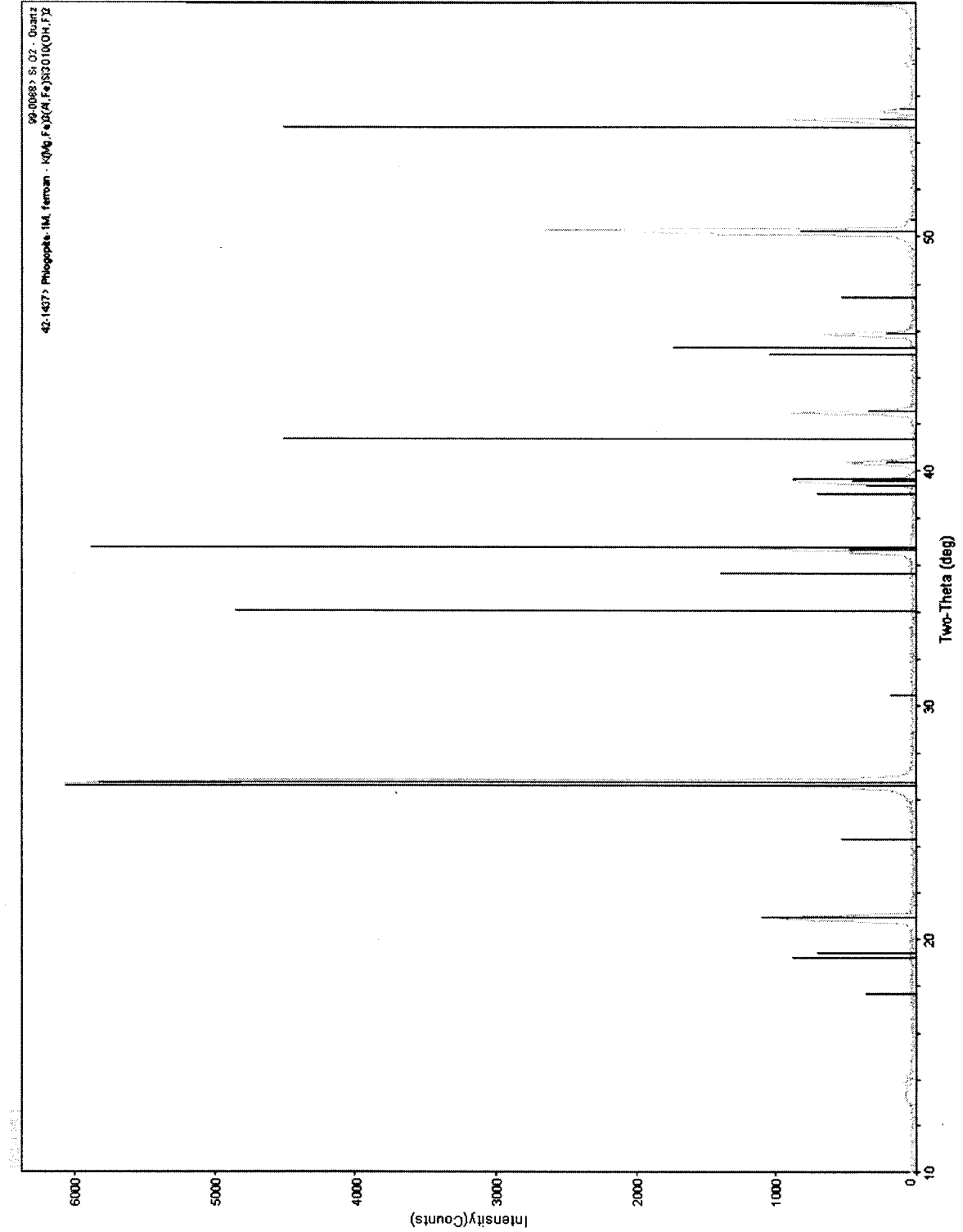


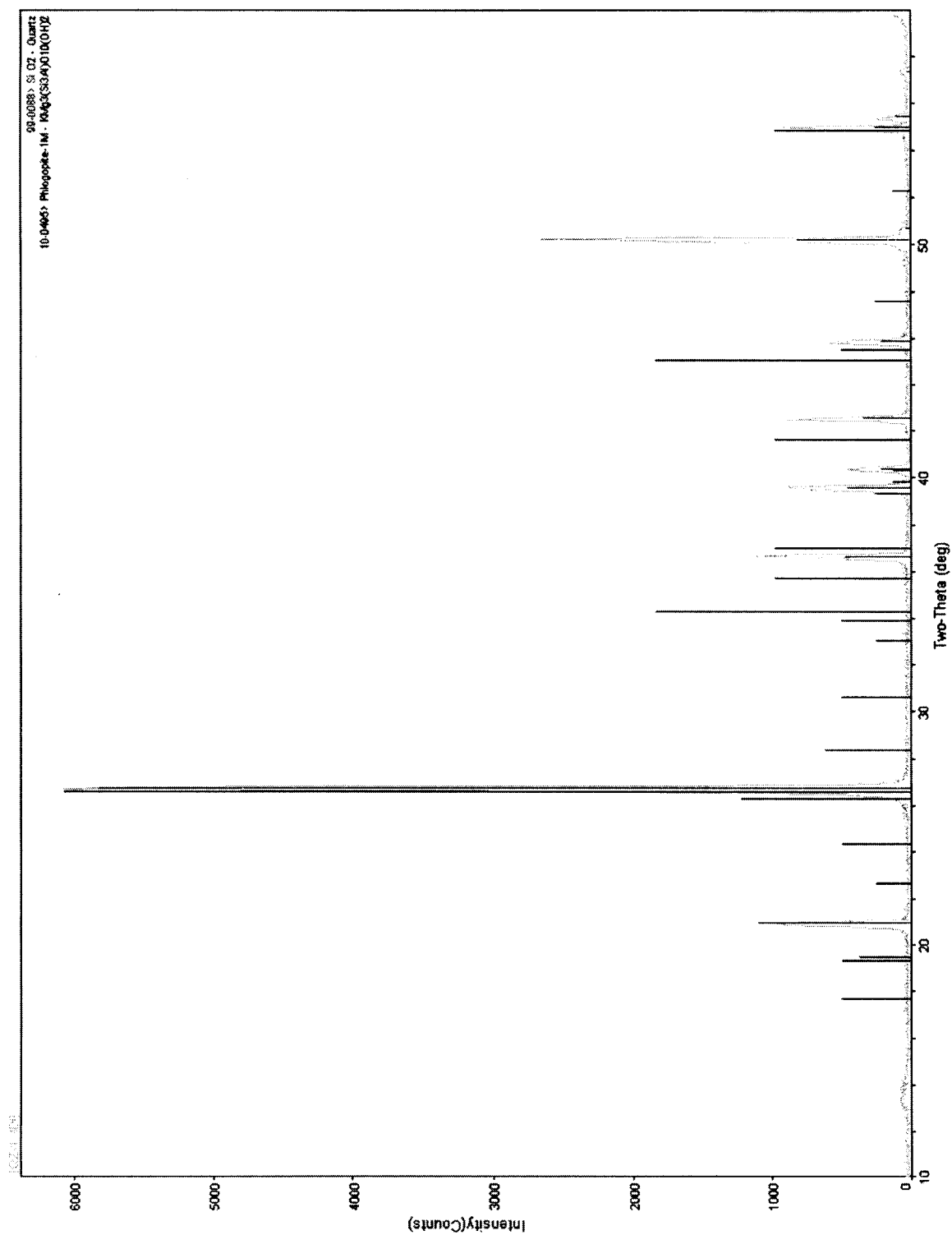


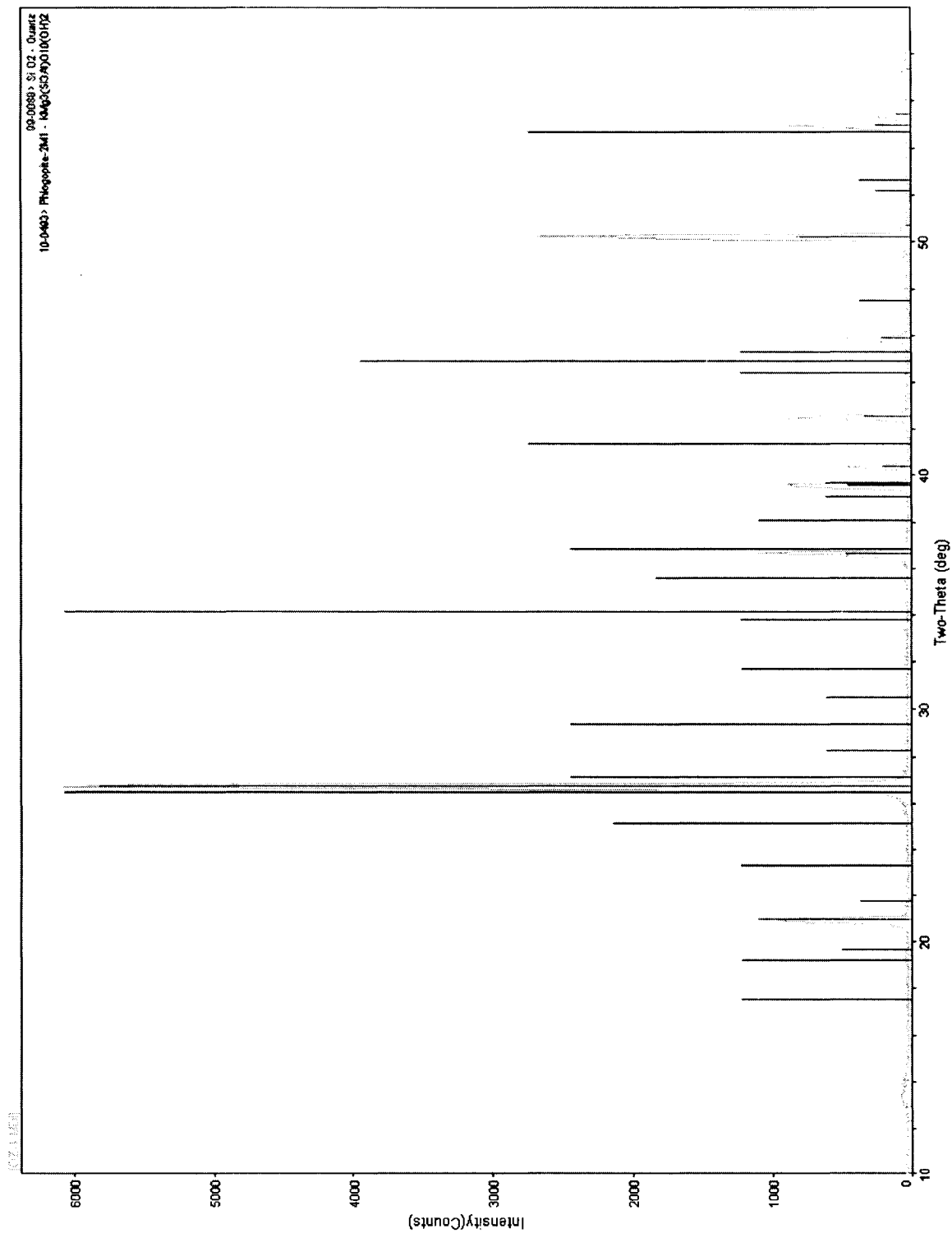


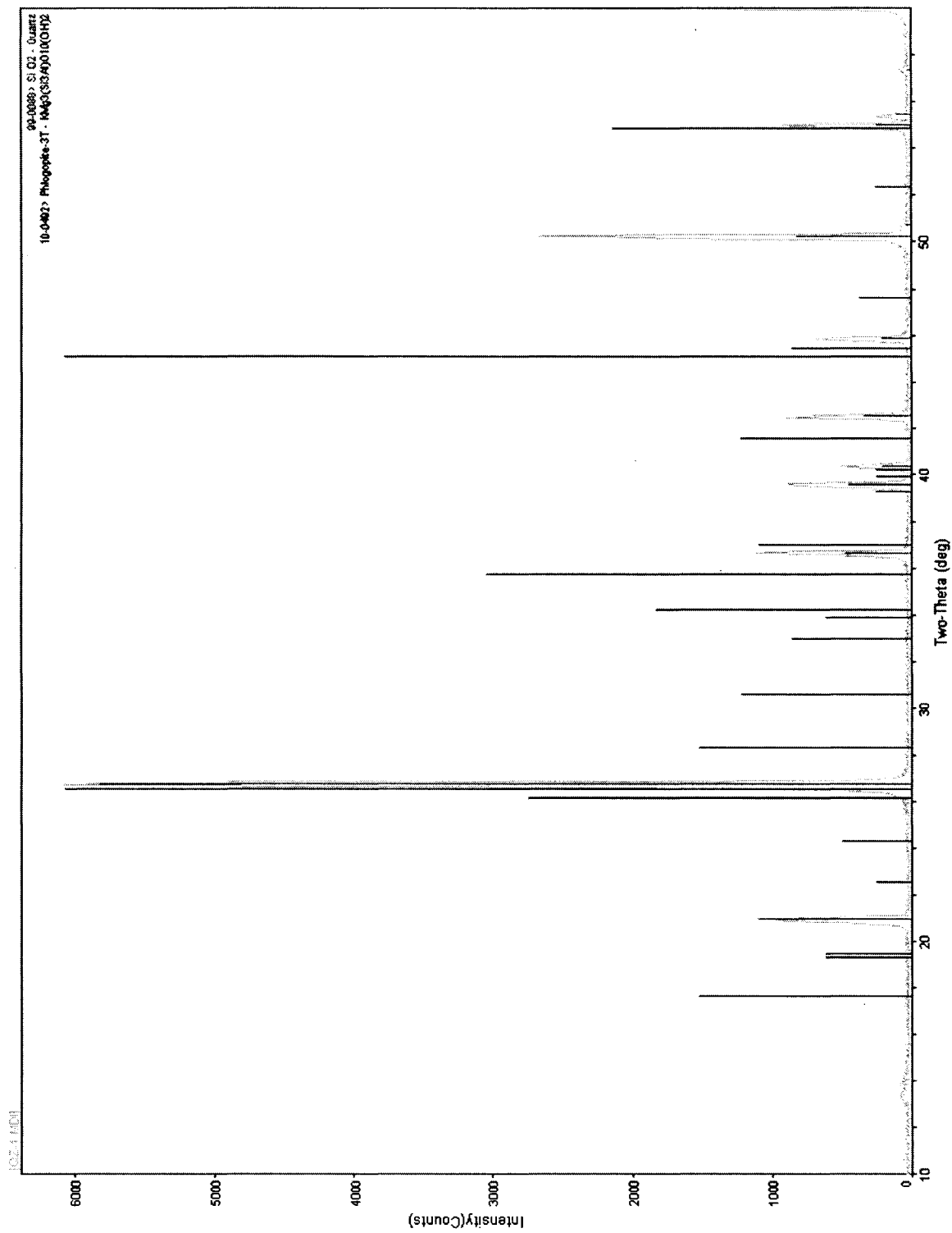


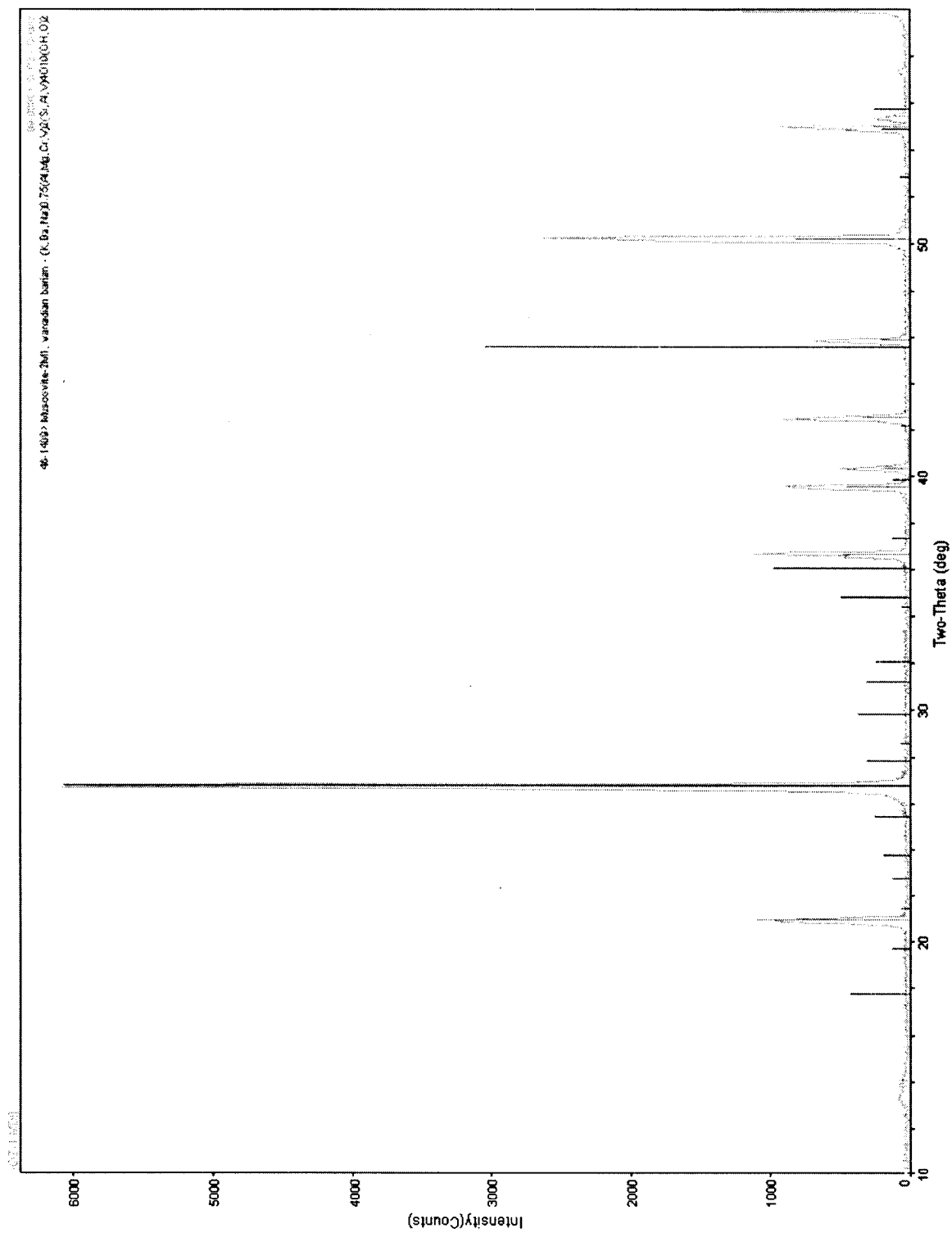


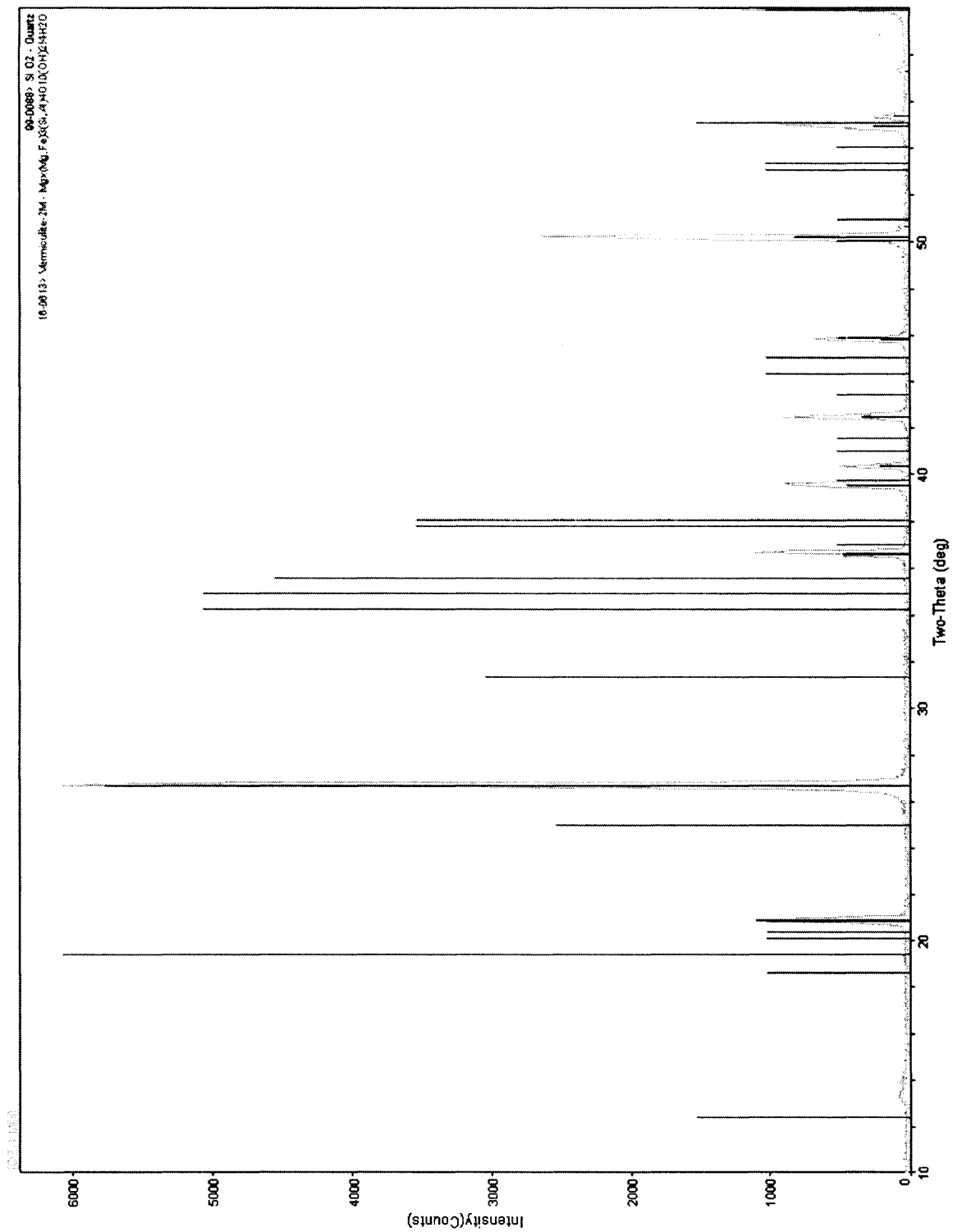






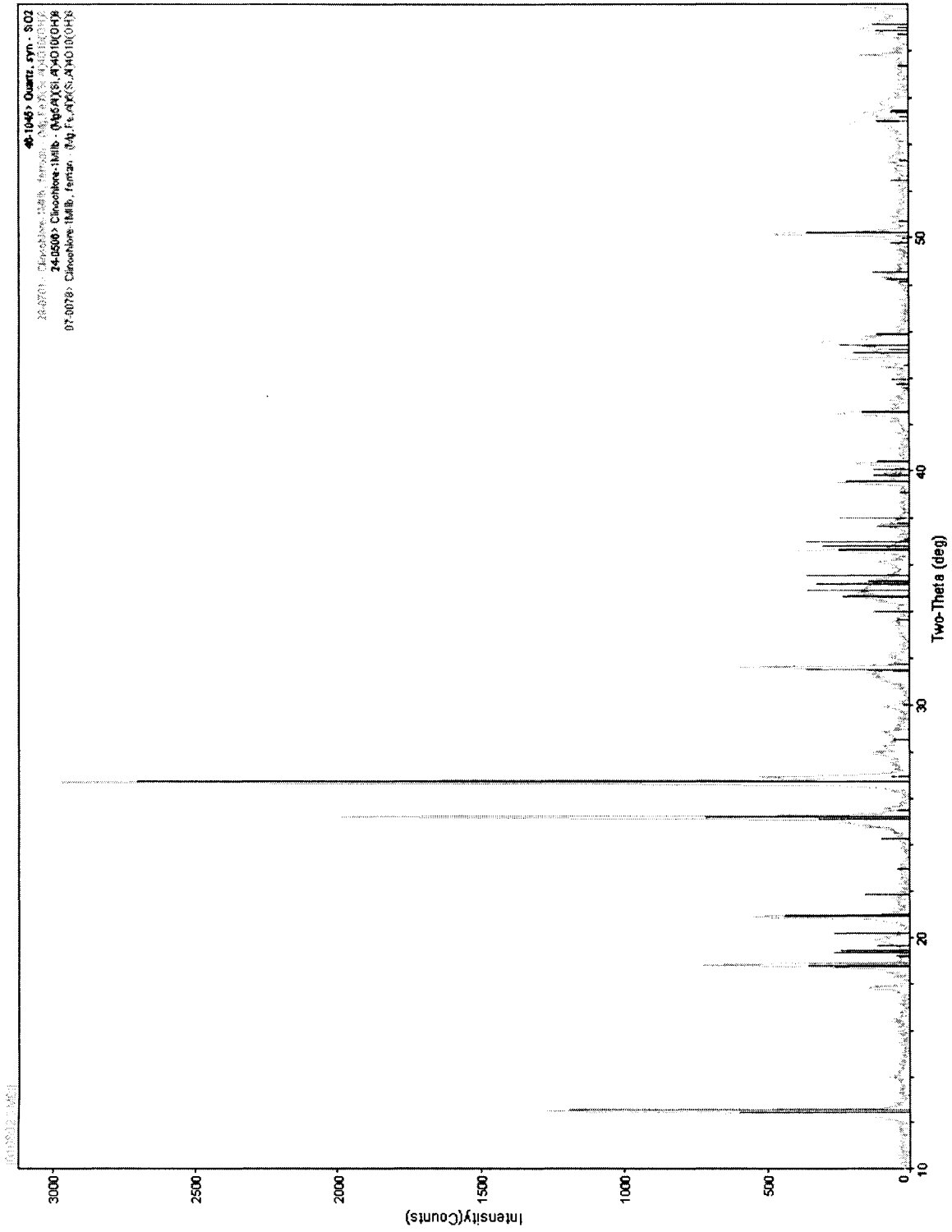


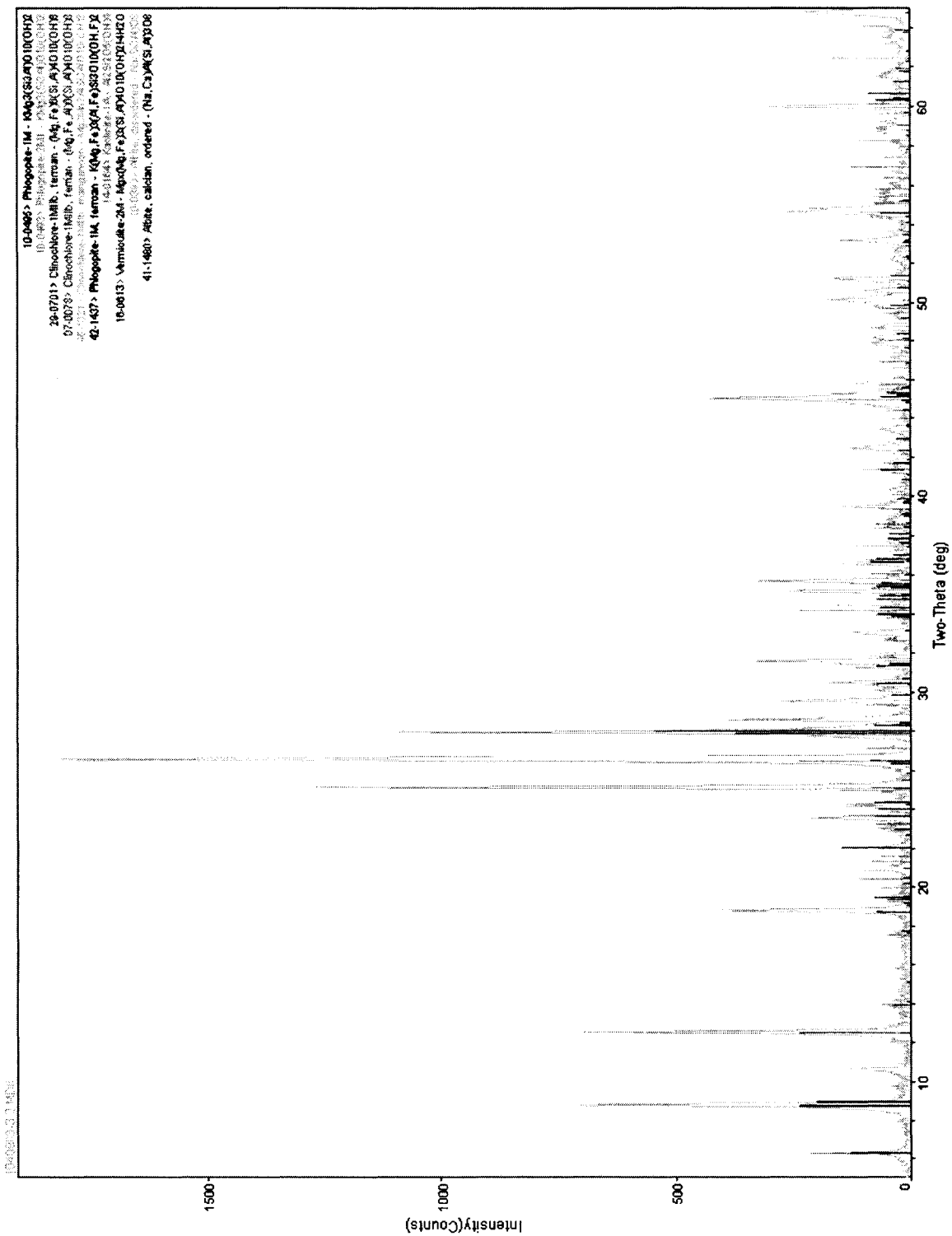


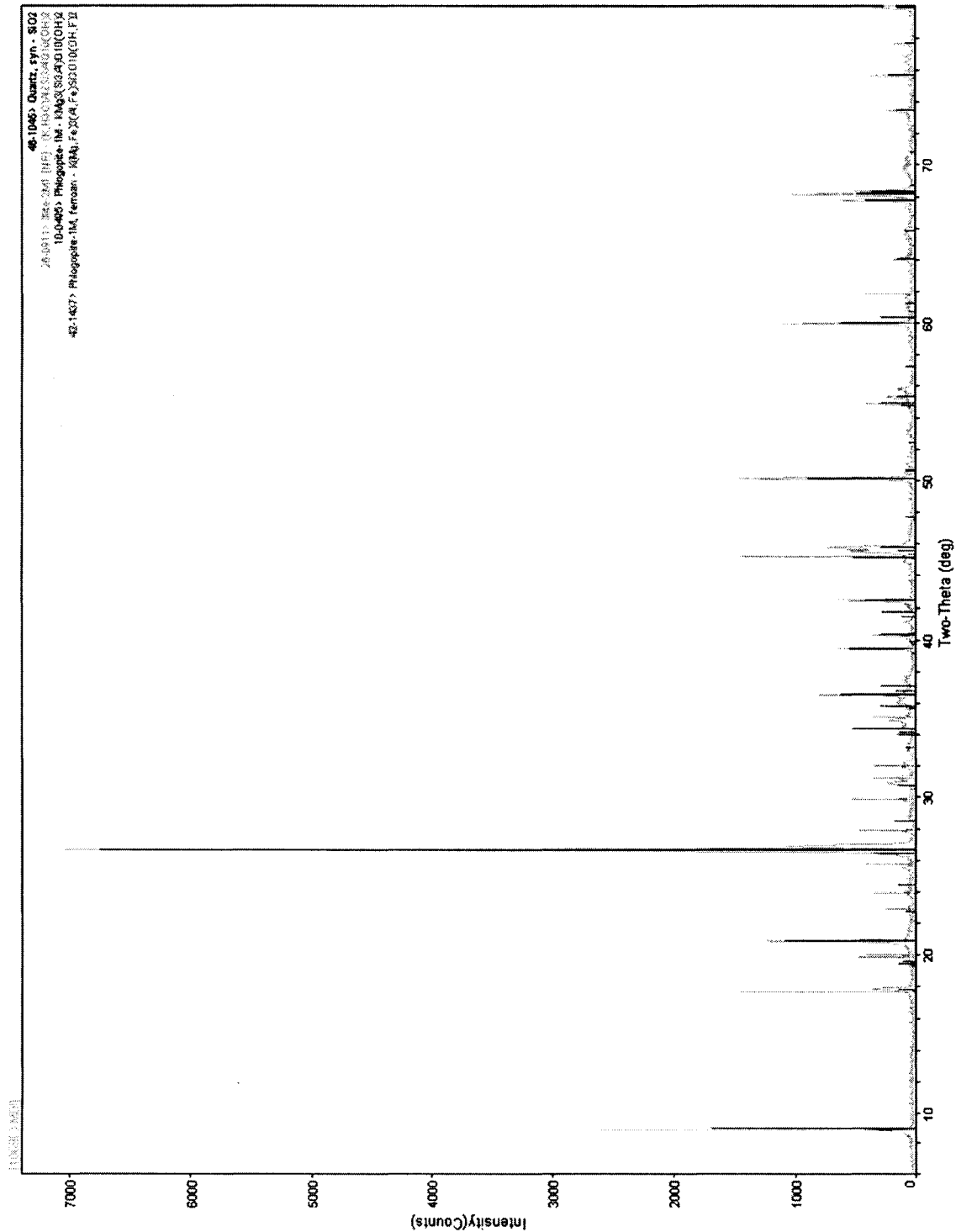


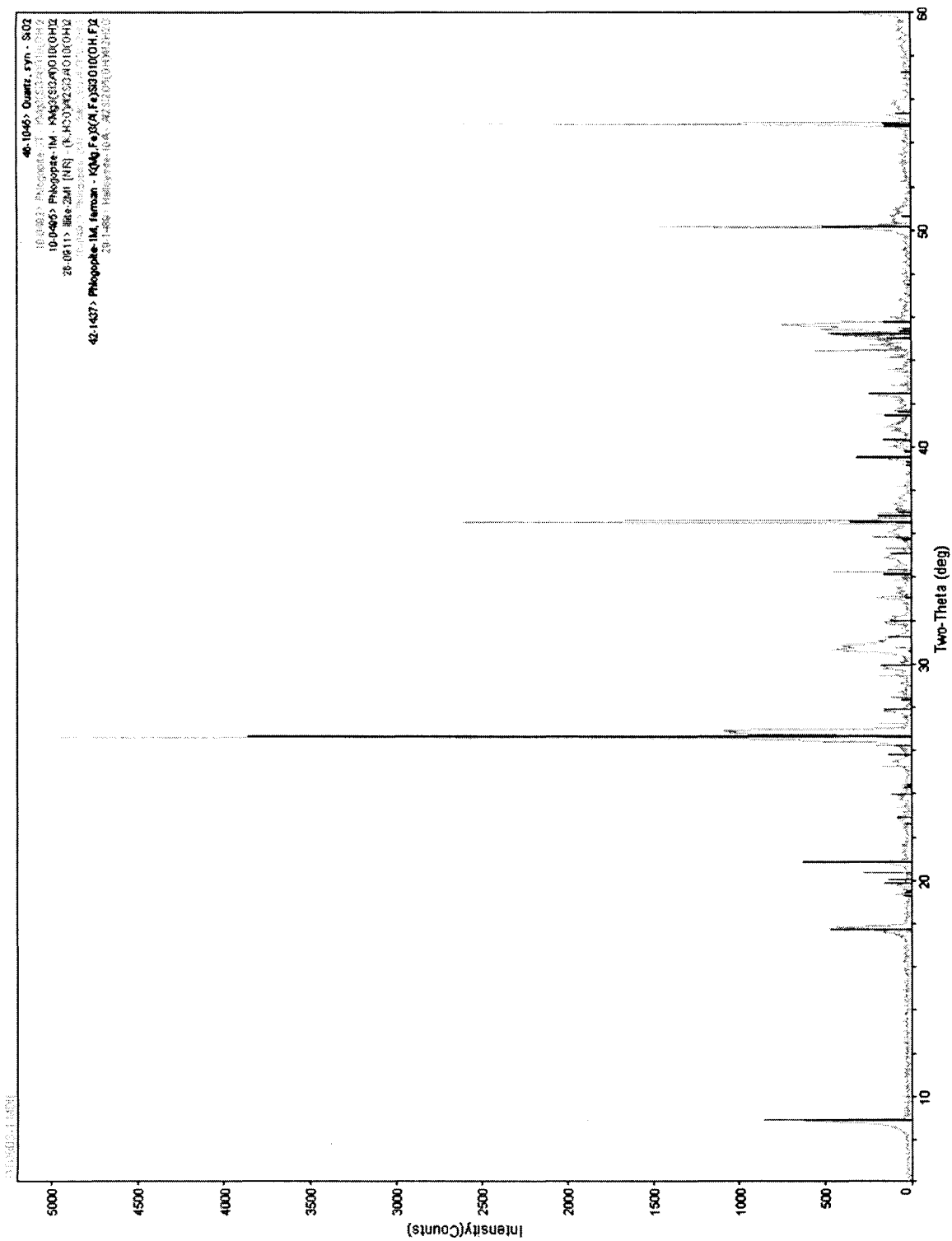
**Appendix A: Part 2.****Biotite (phlogopite) weathering**

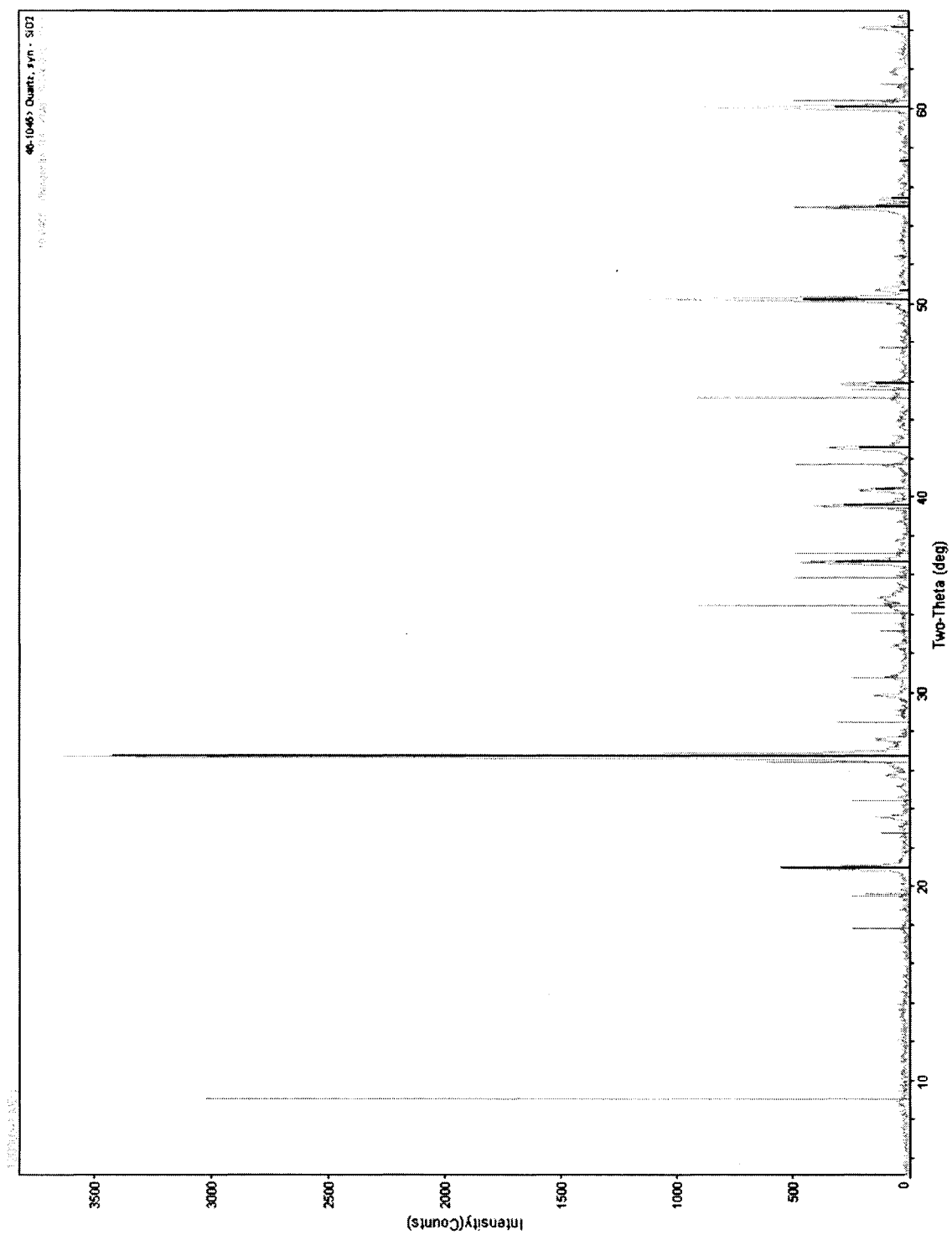


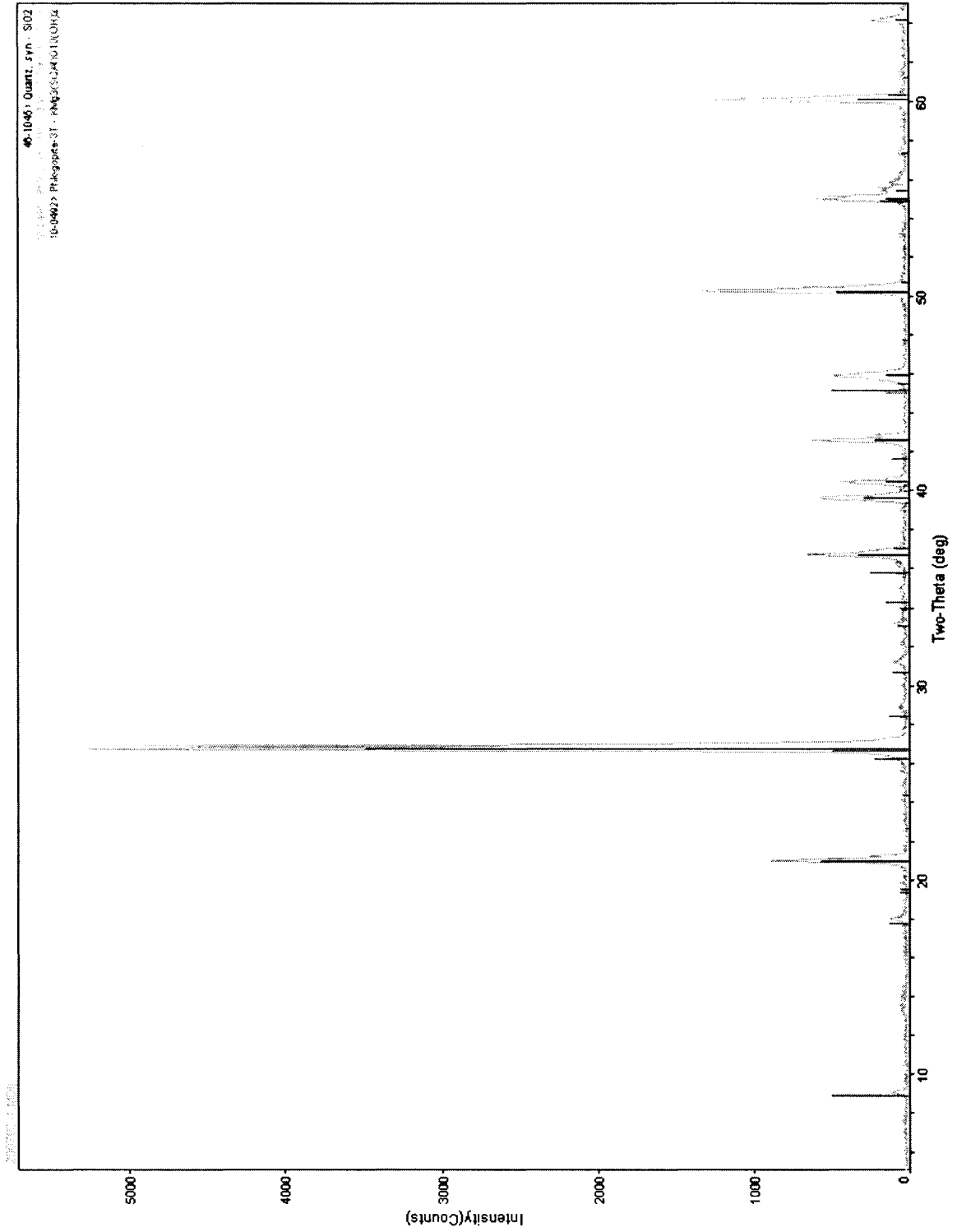


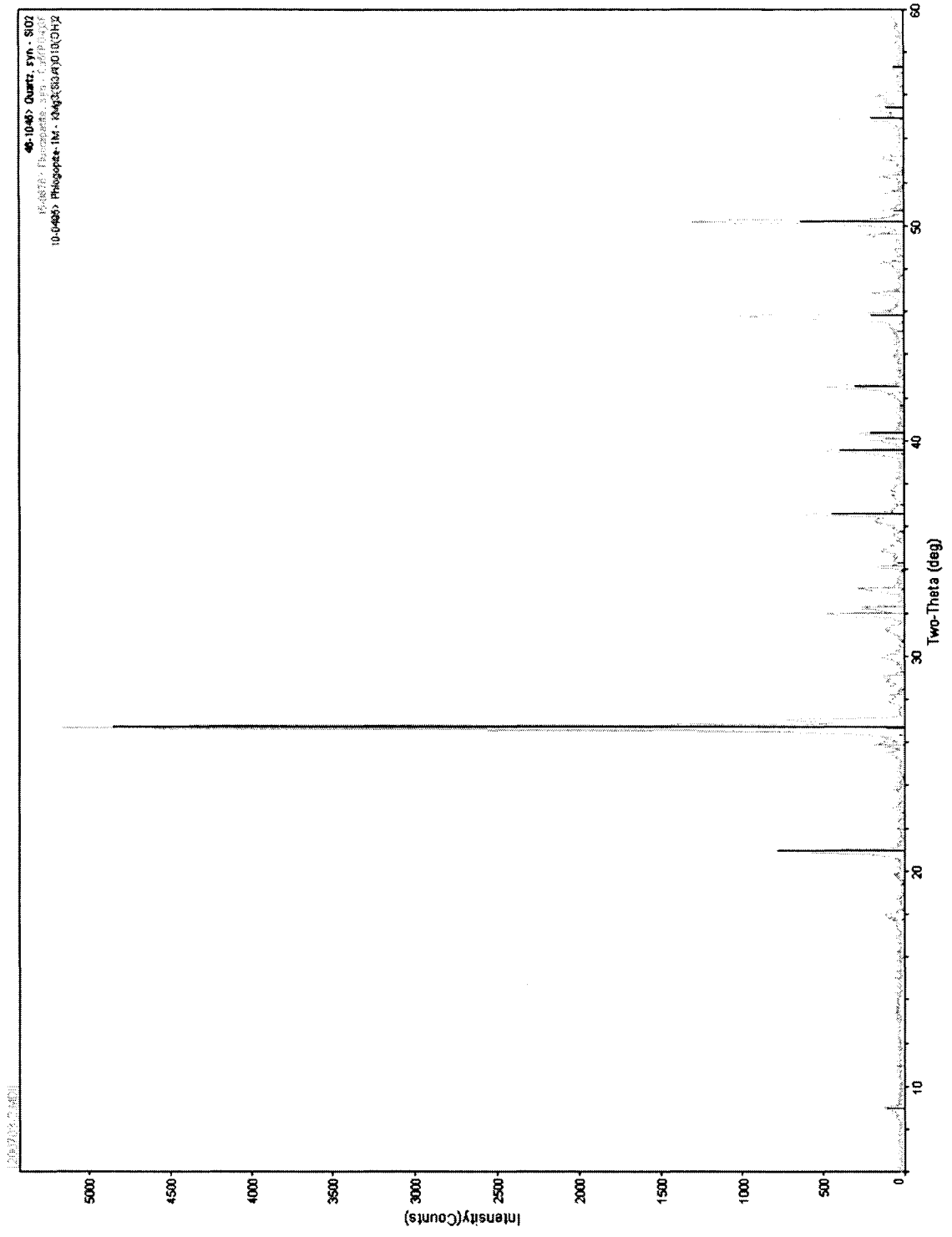


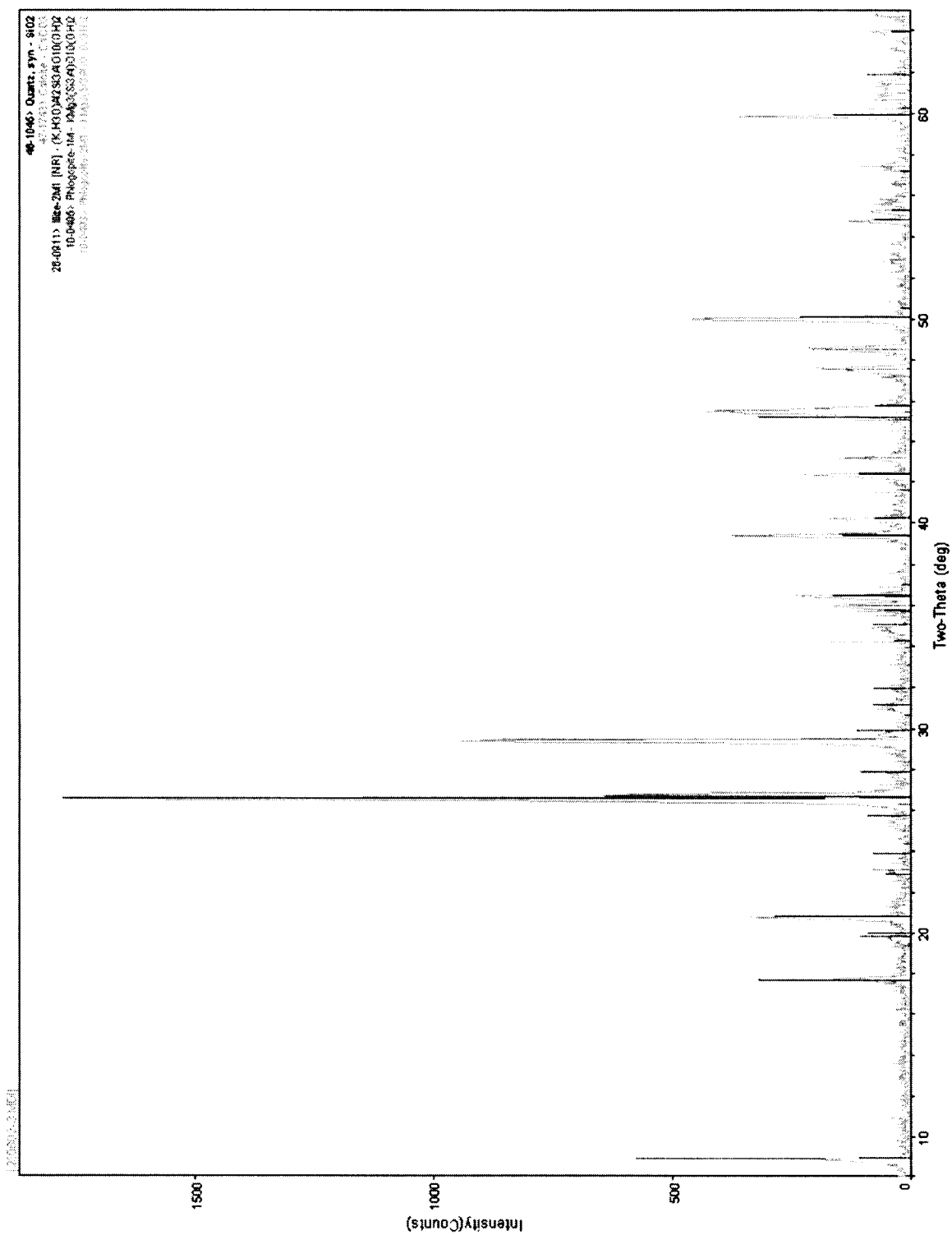




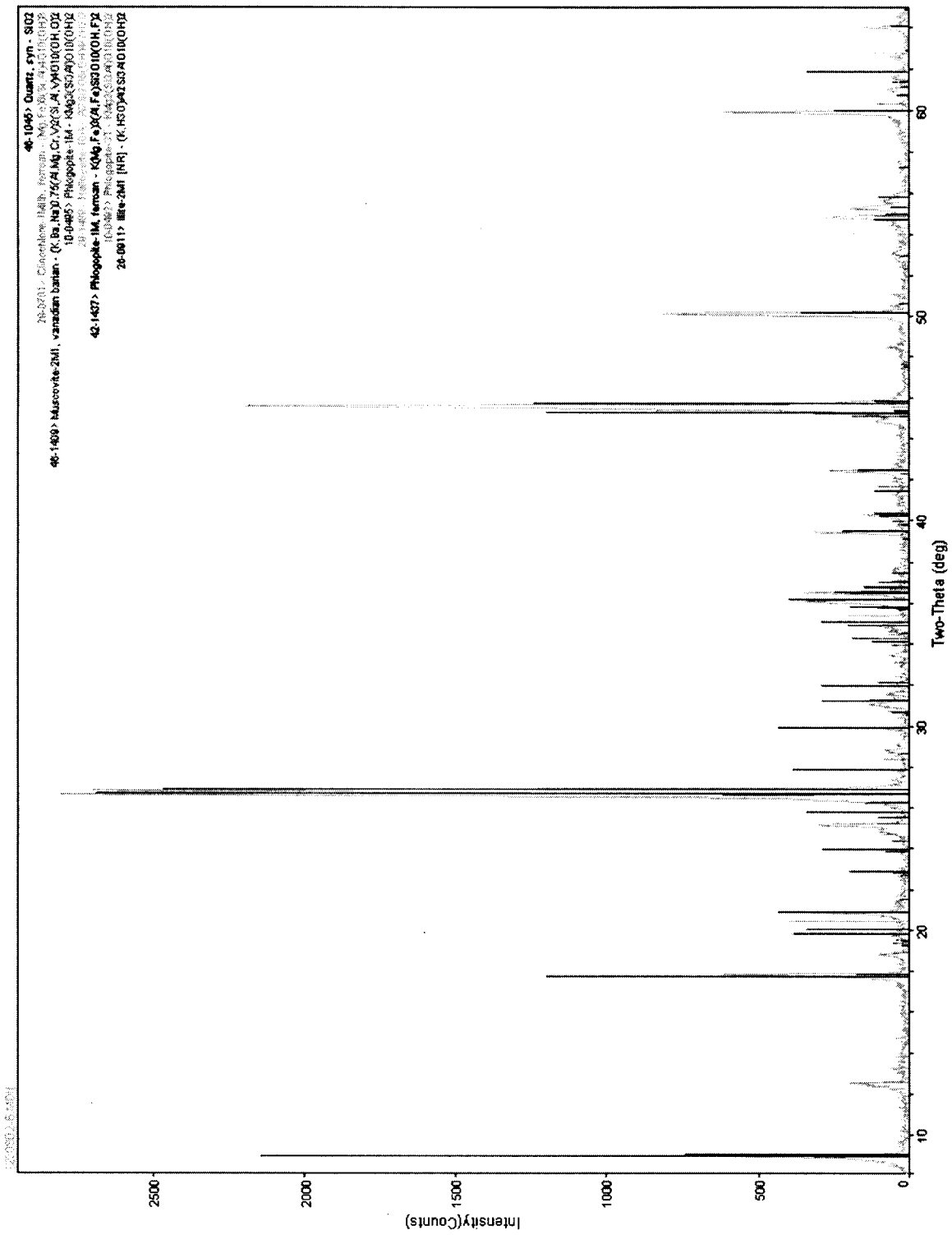


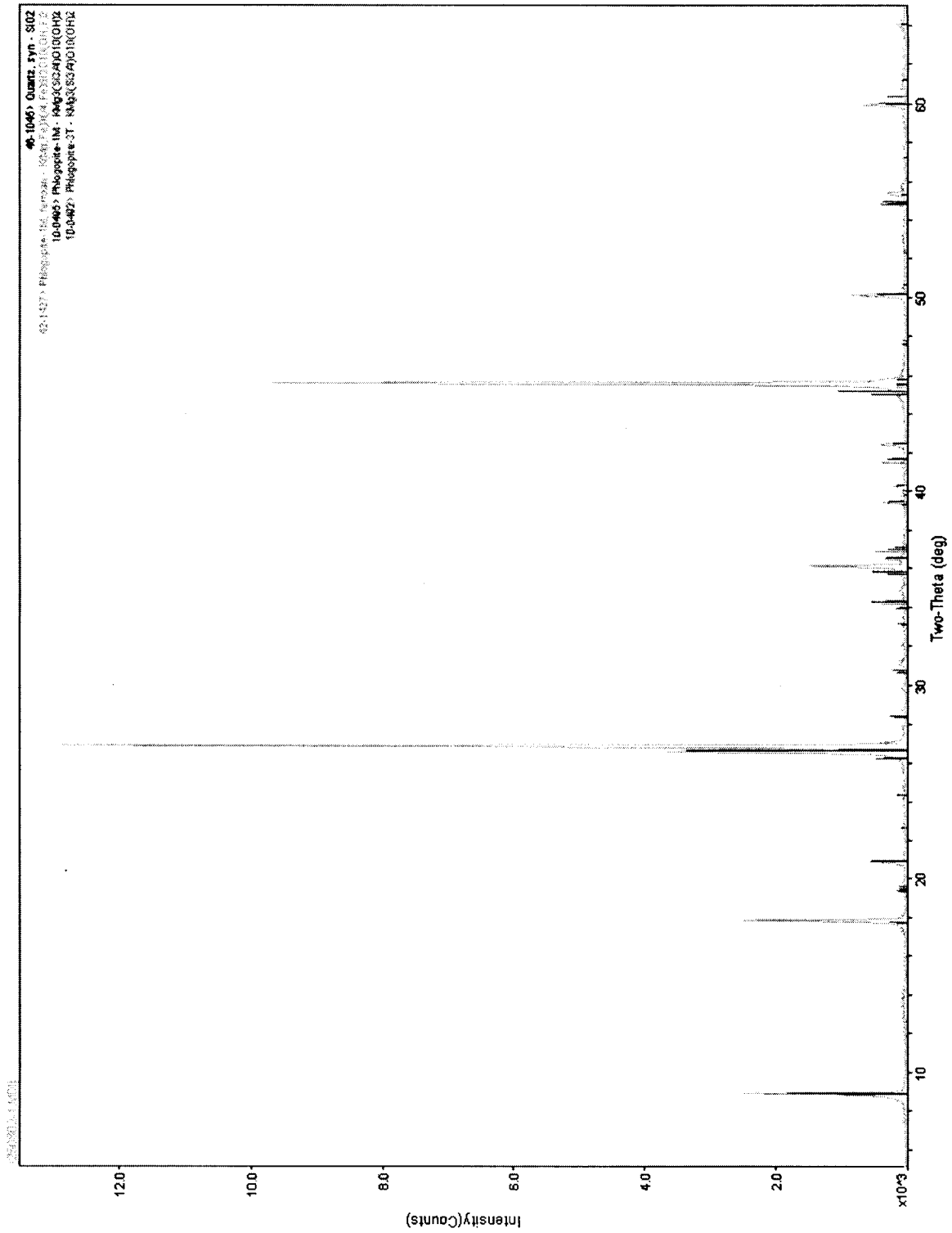


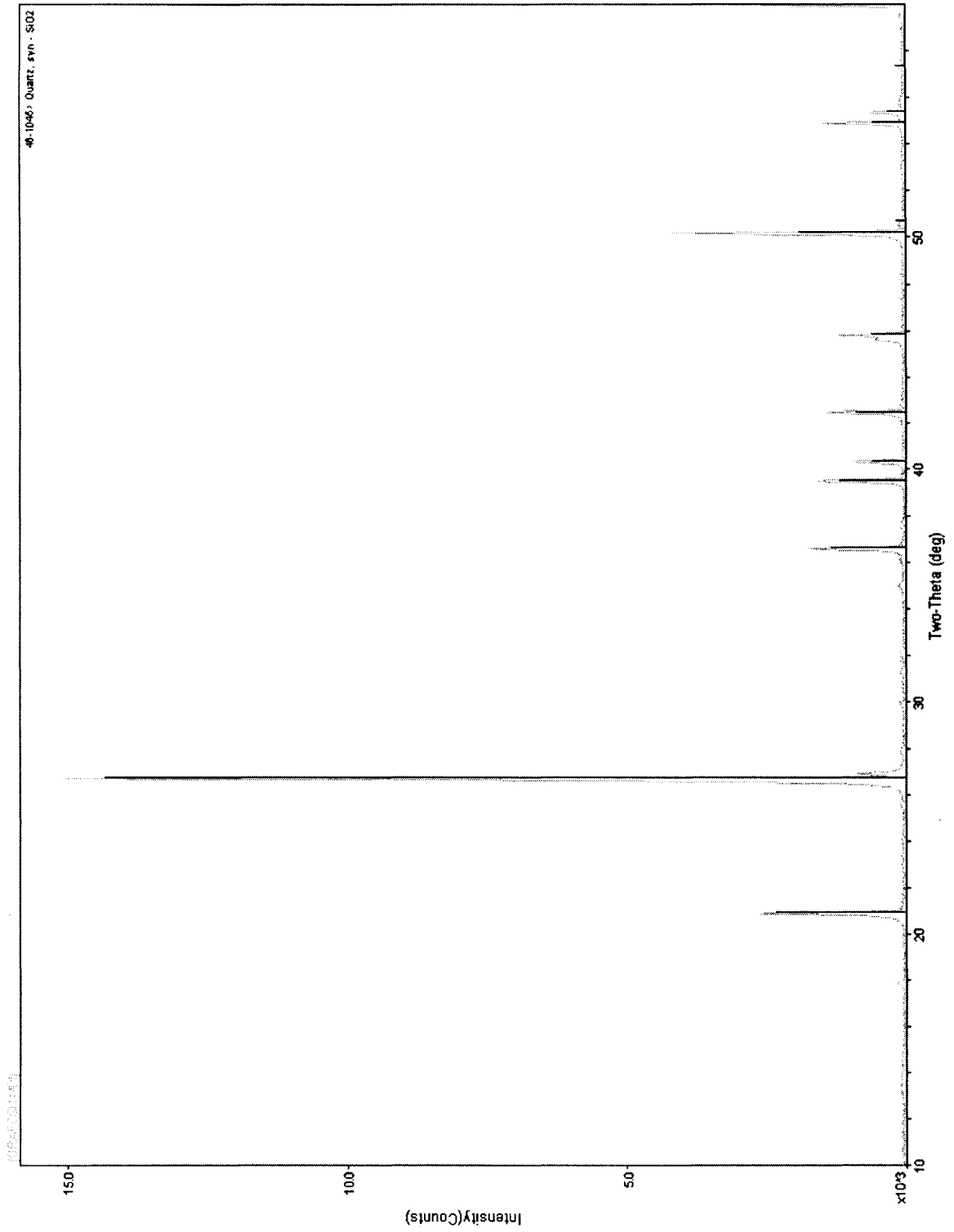






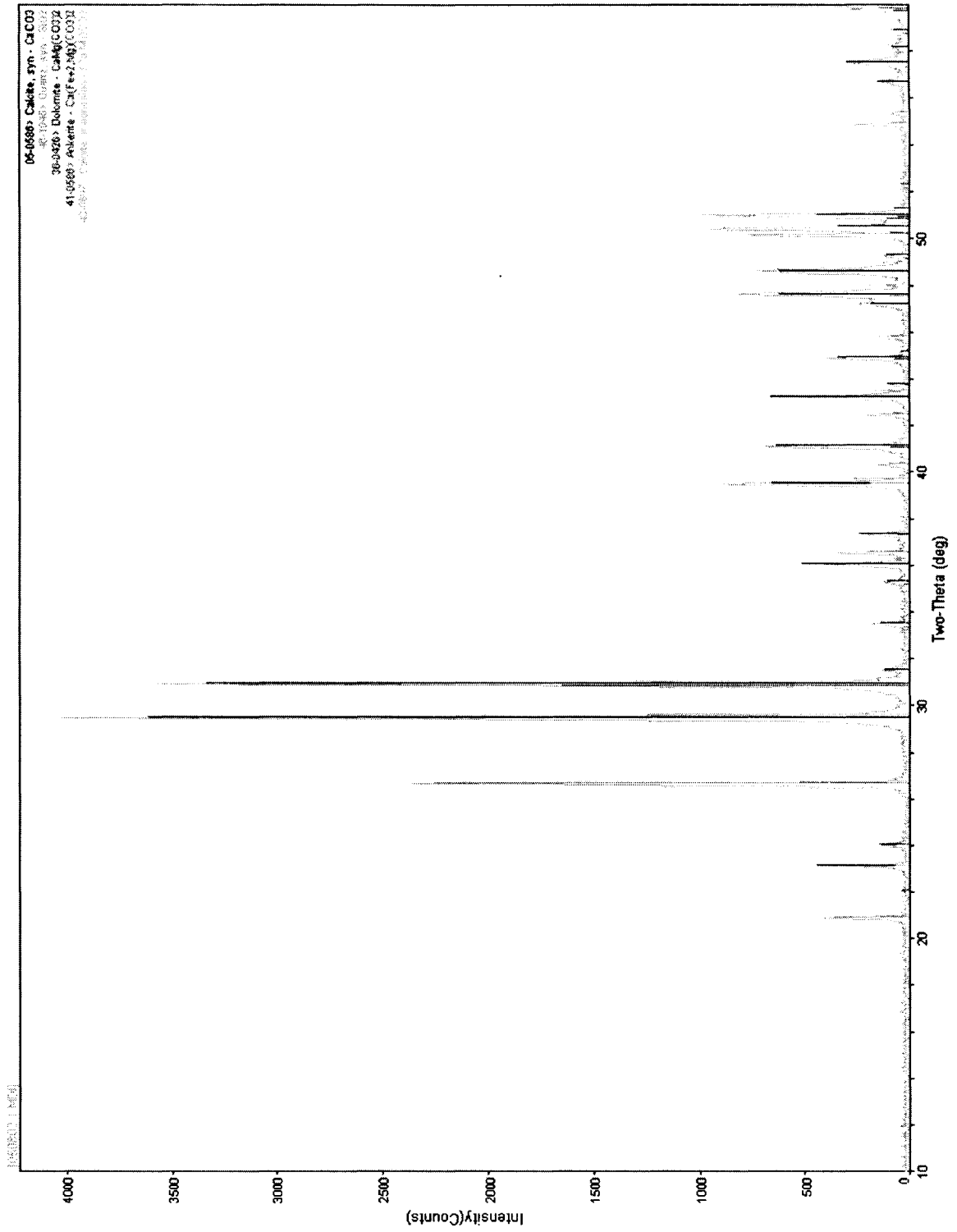


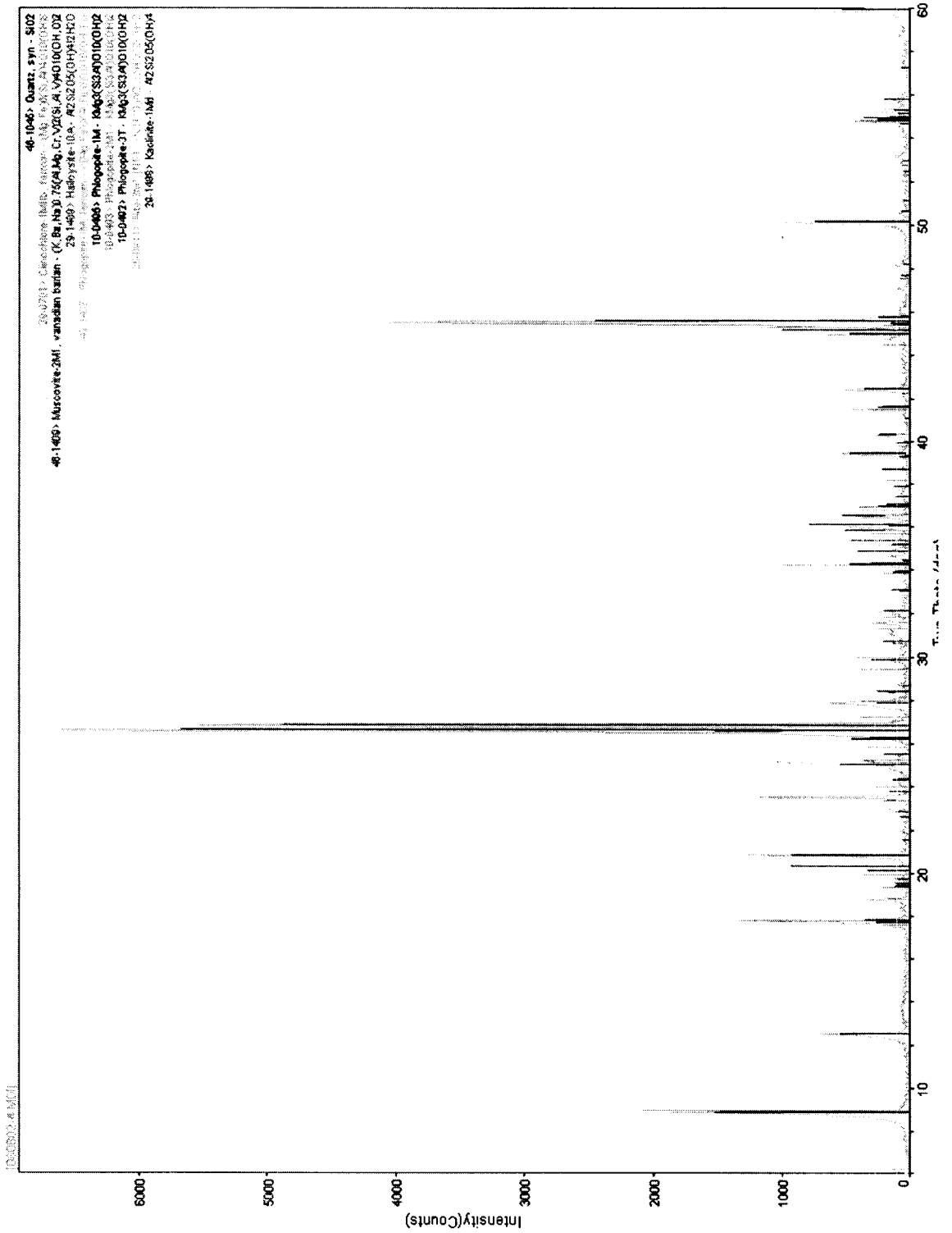


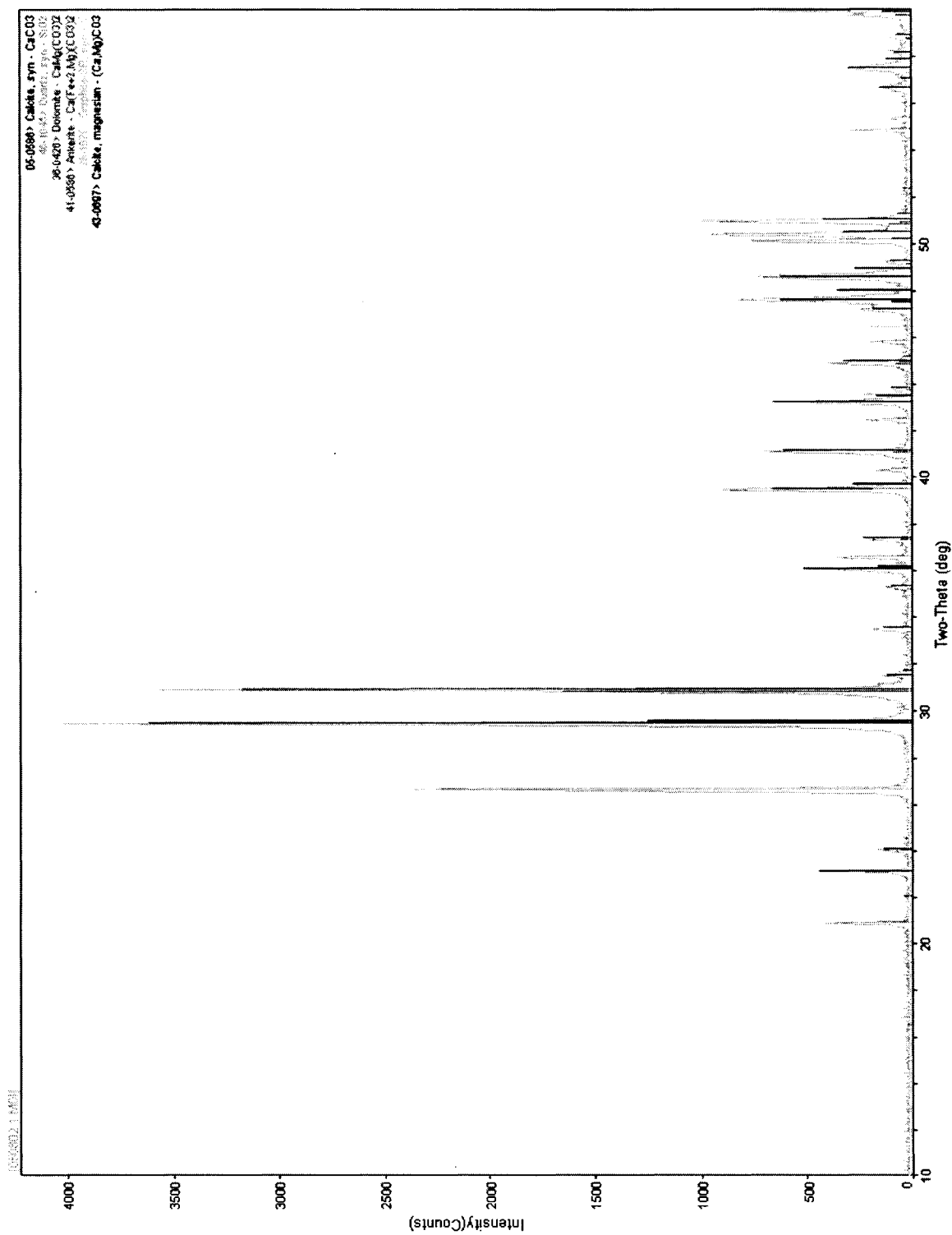


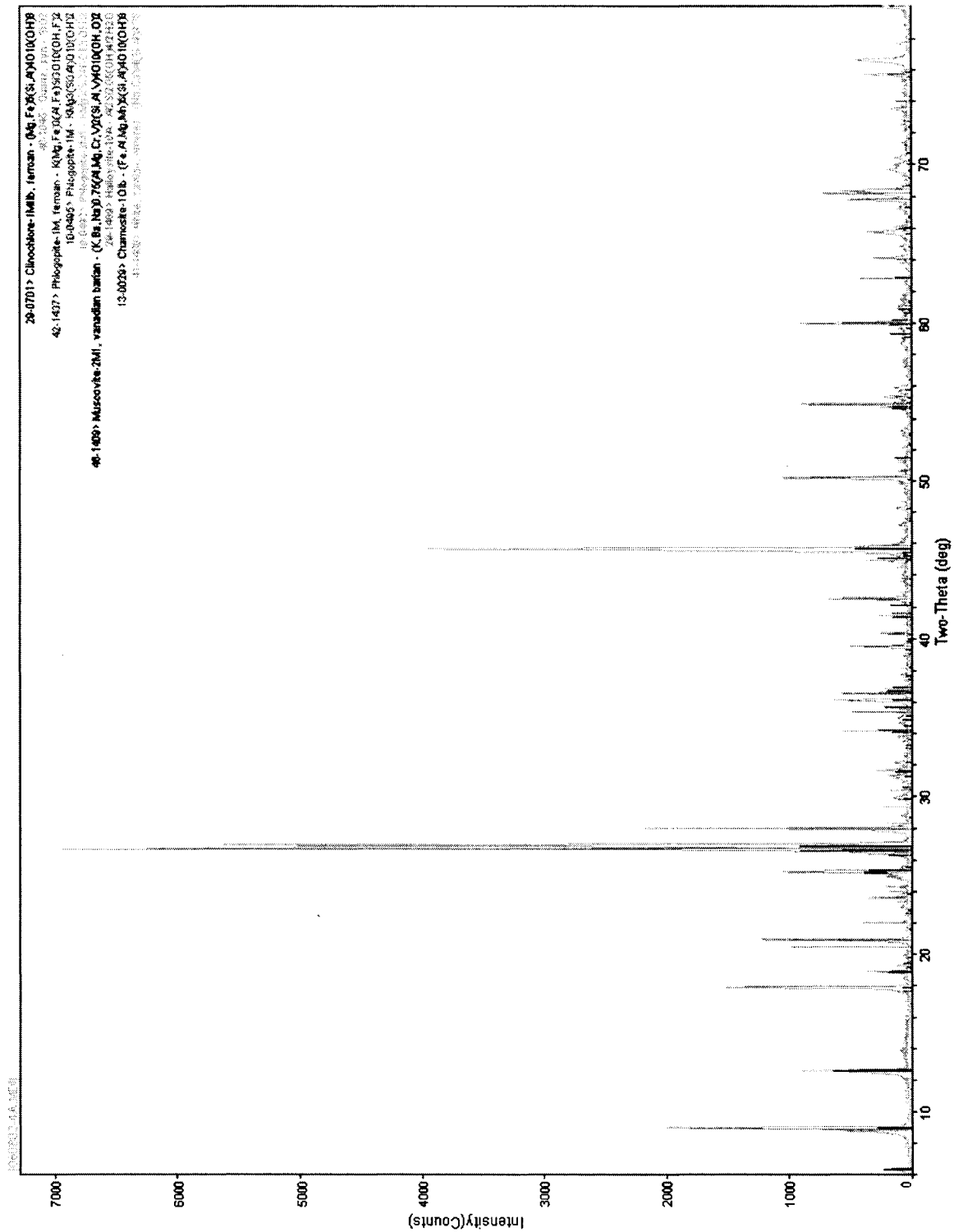
**Appendix A: Part 3**

**Alteration**

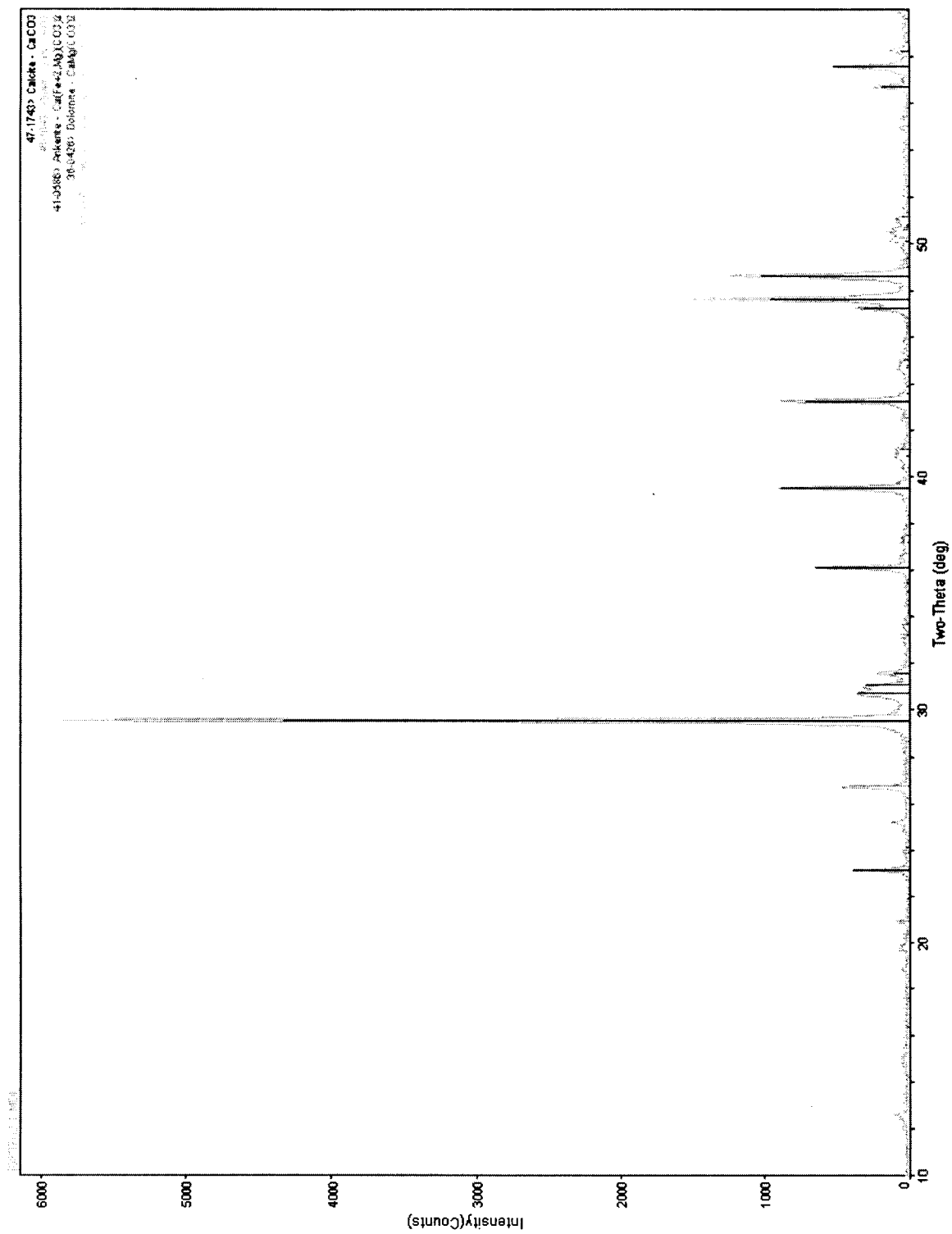


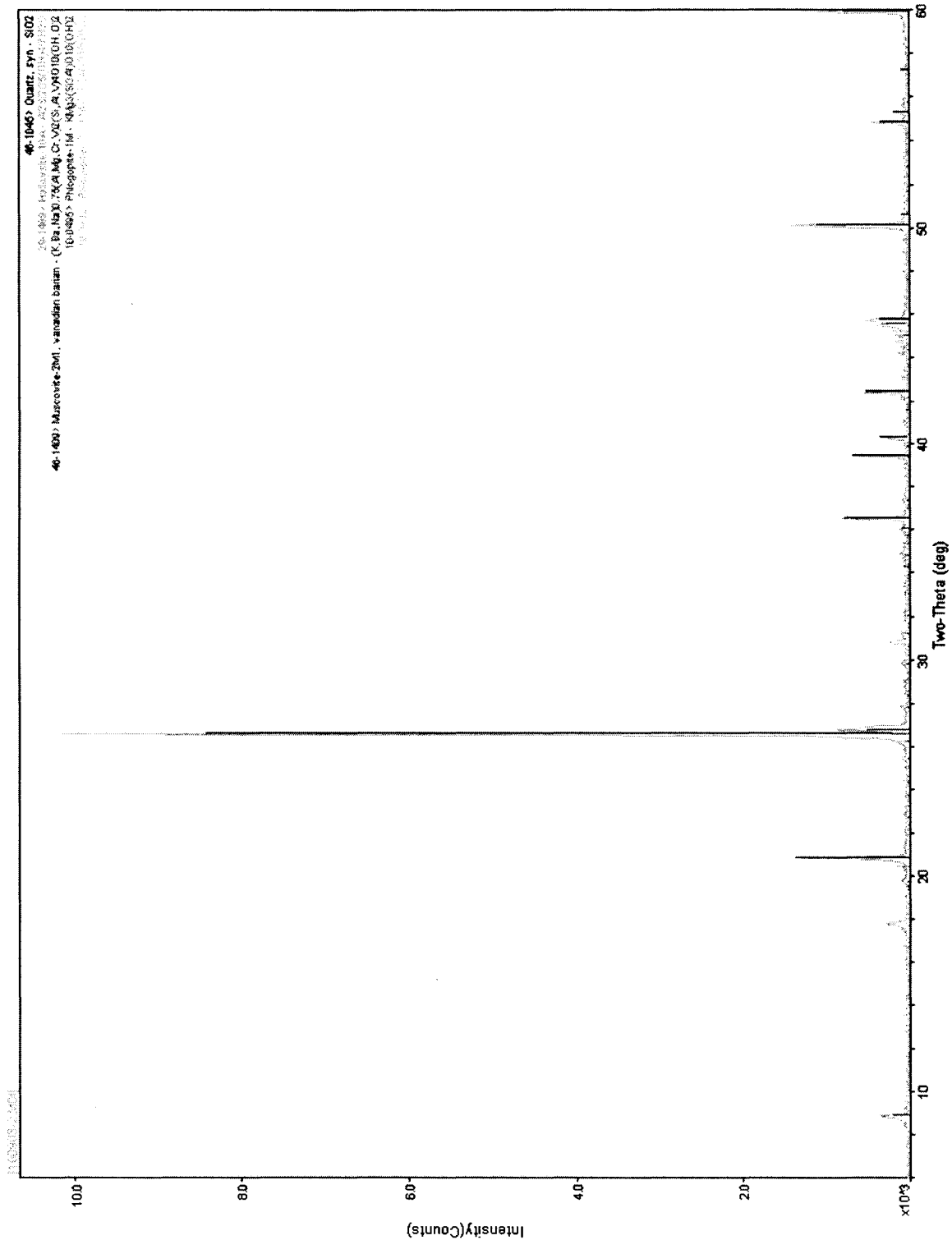


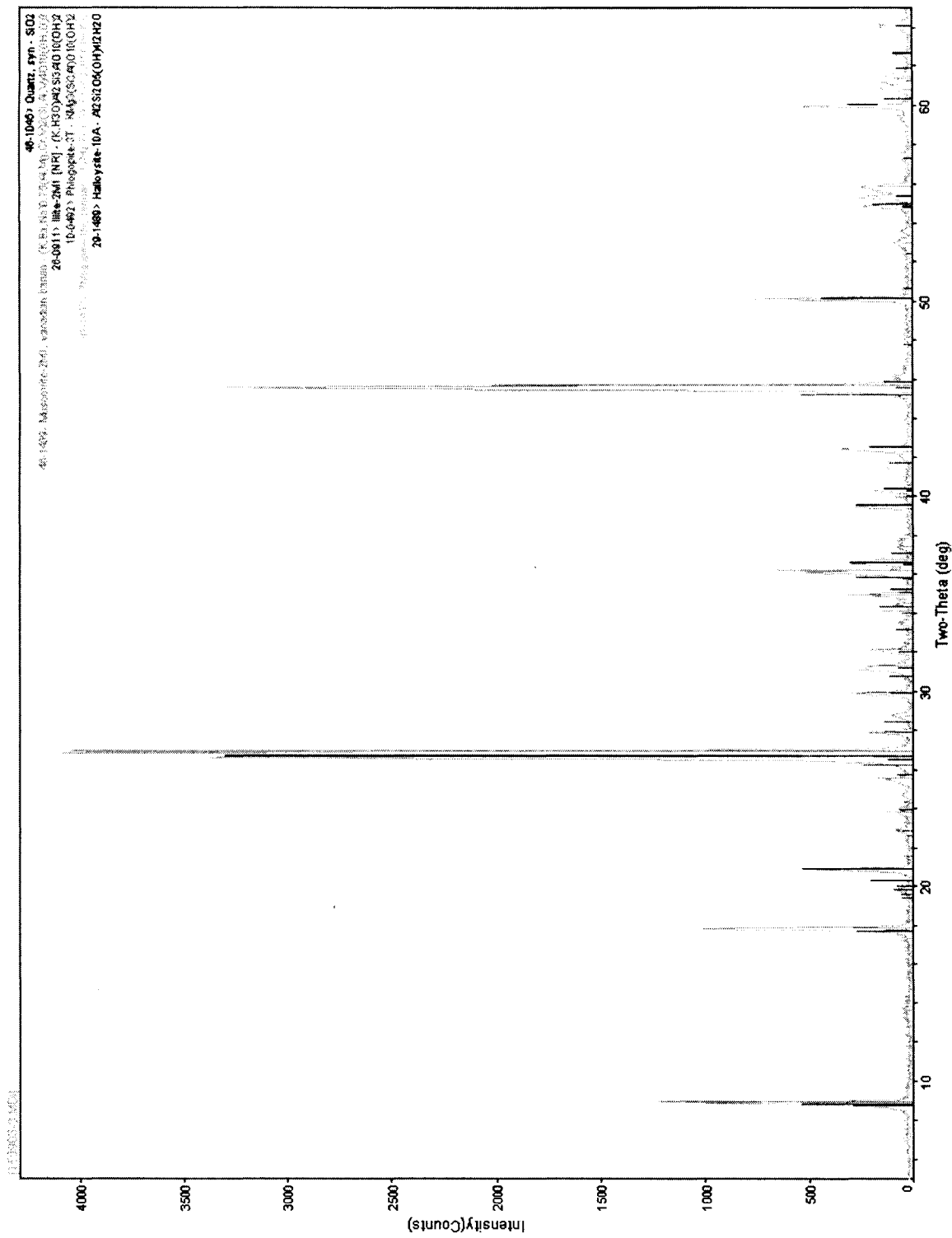


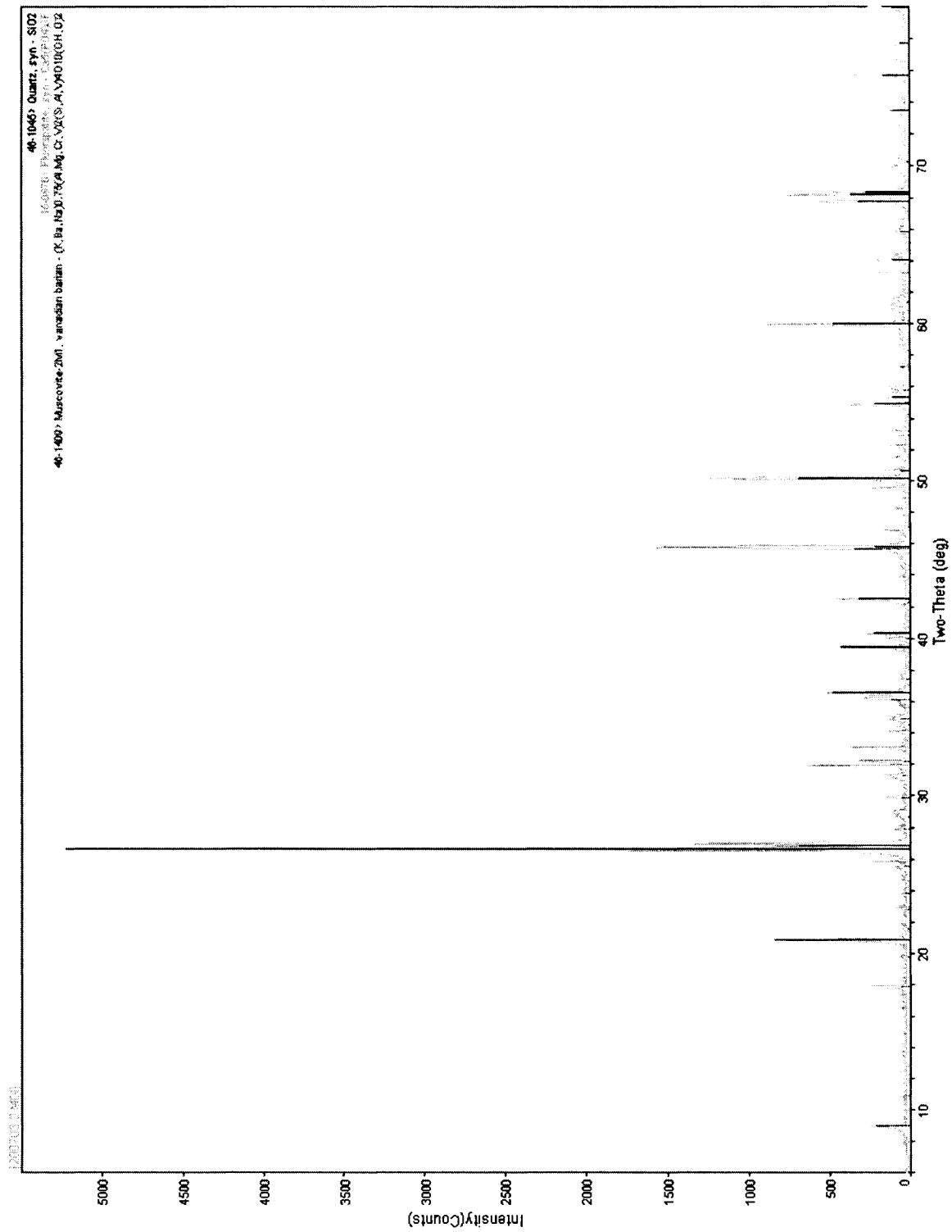


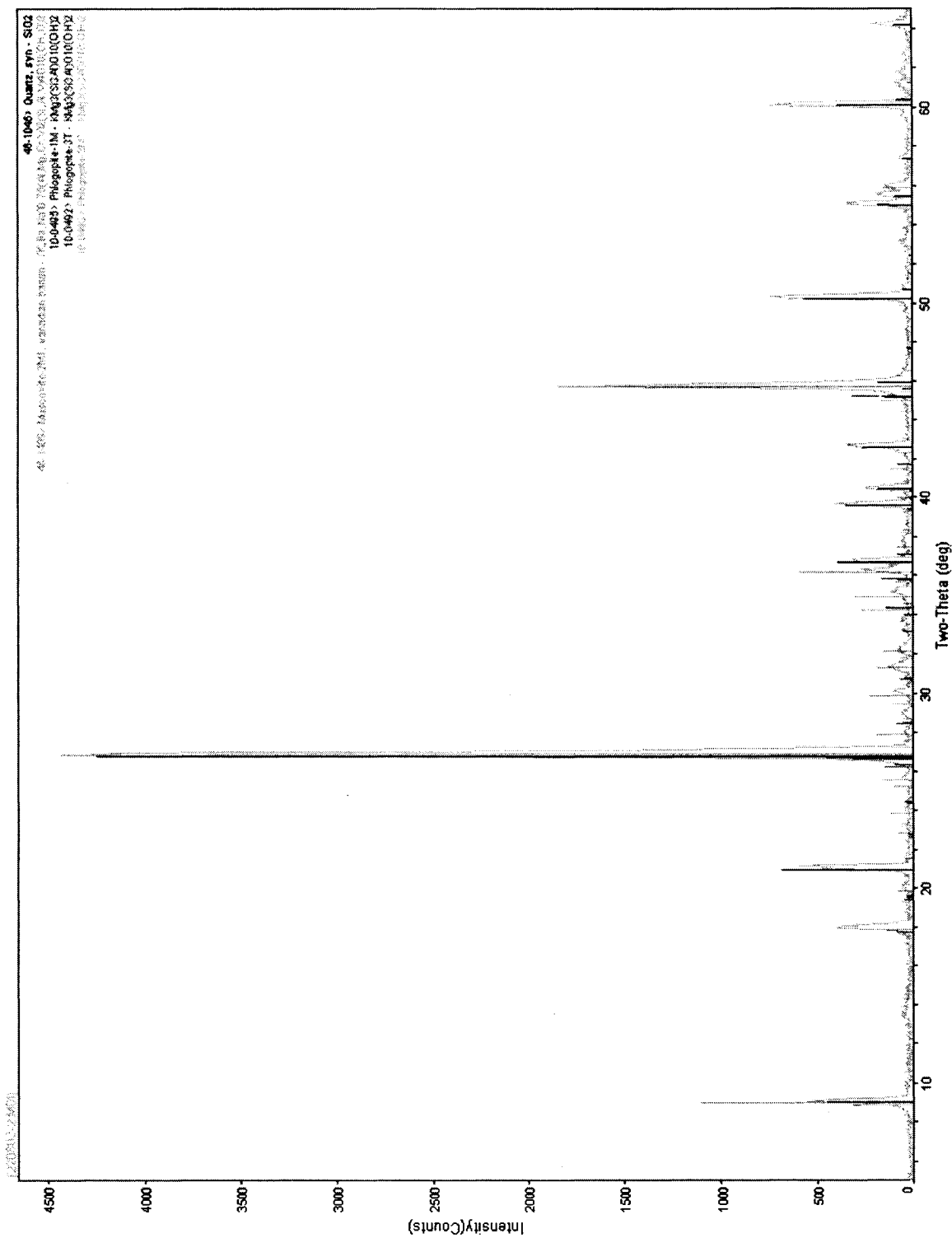


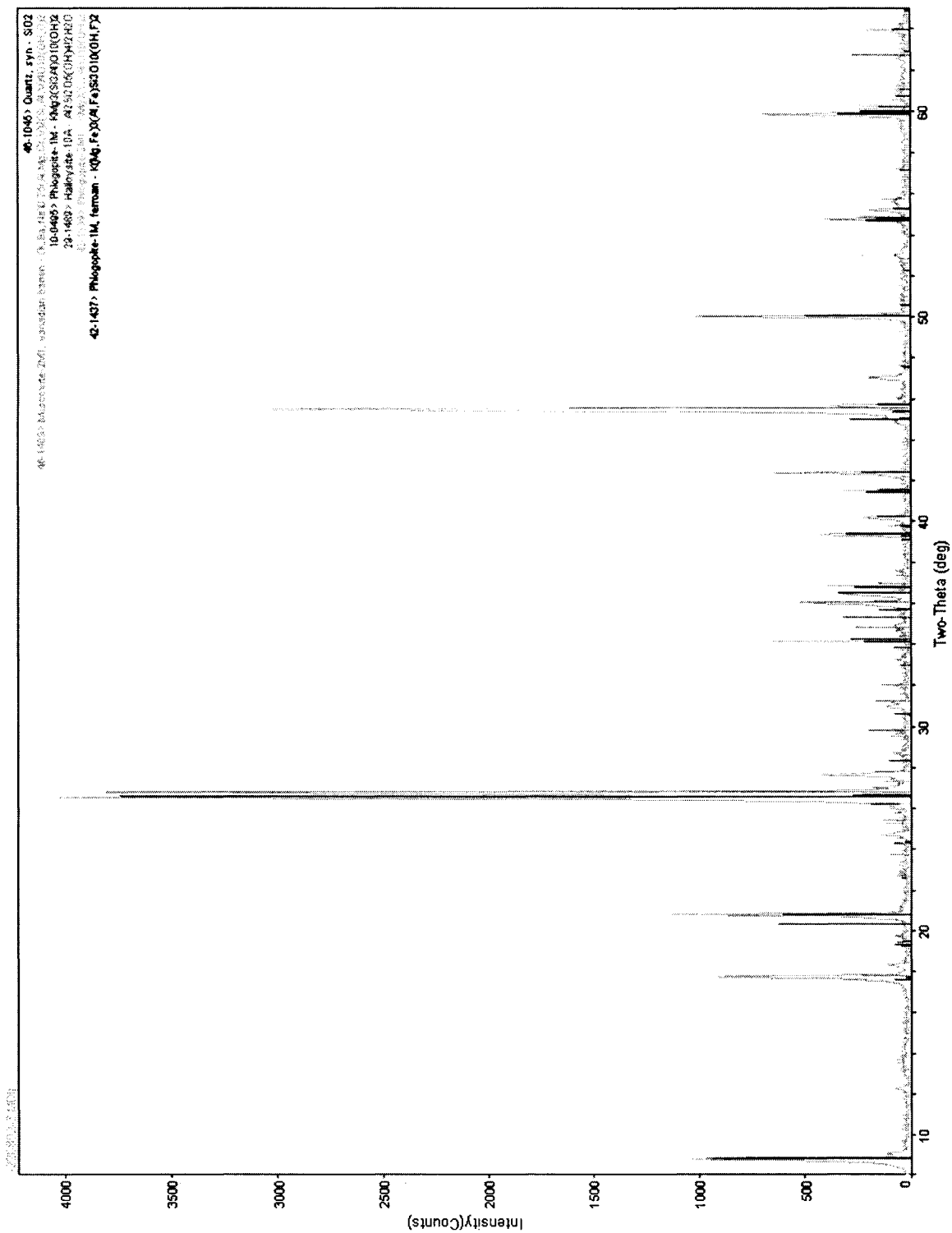


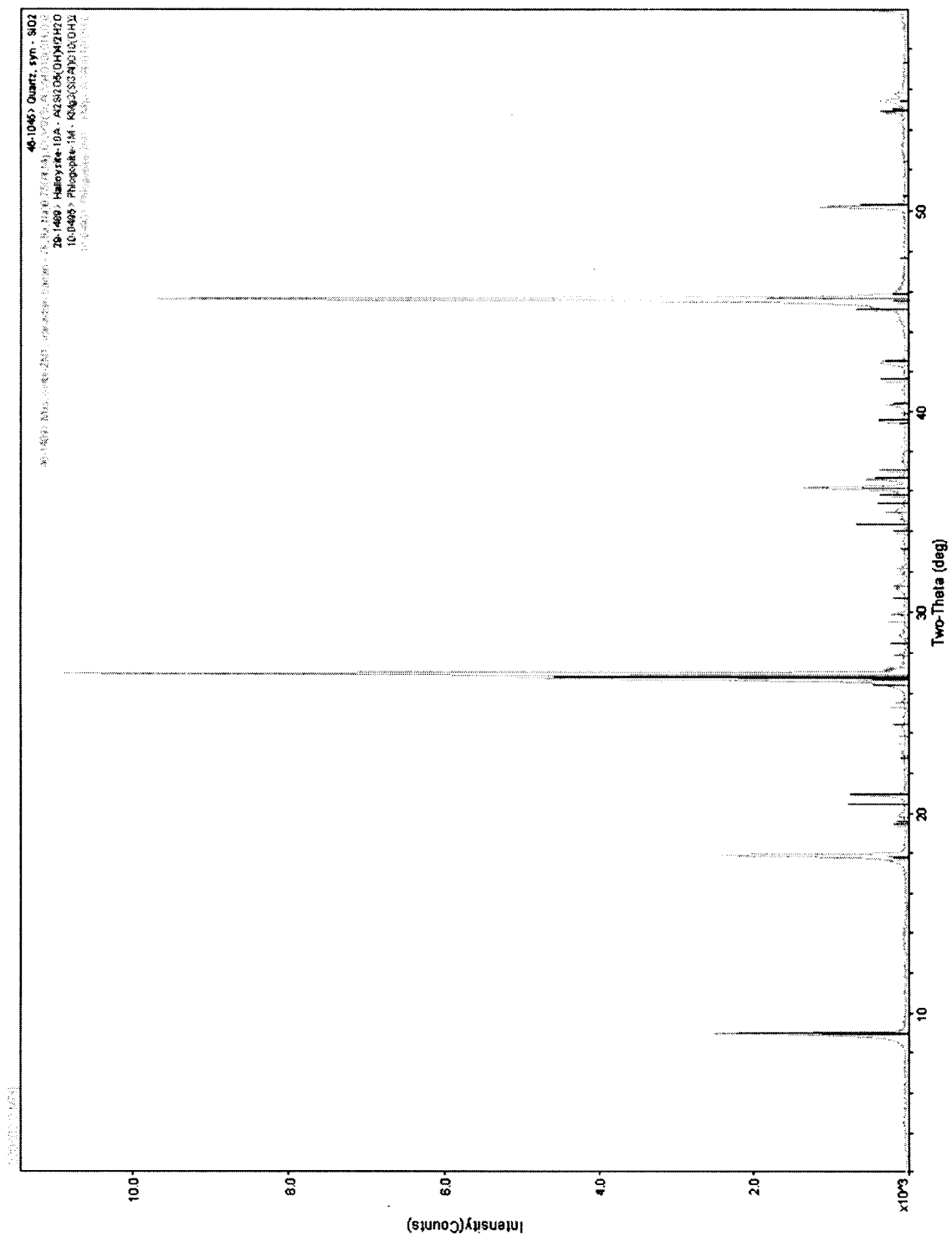


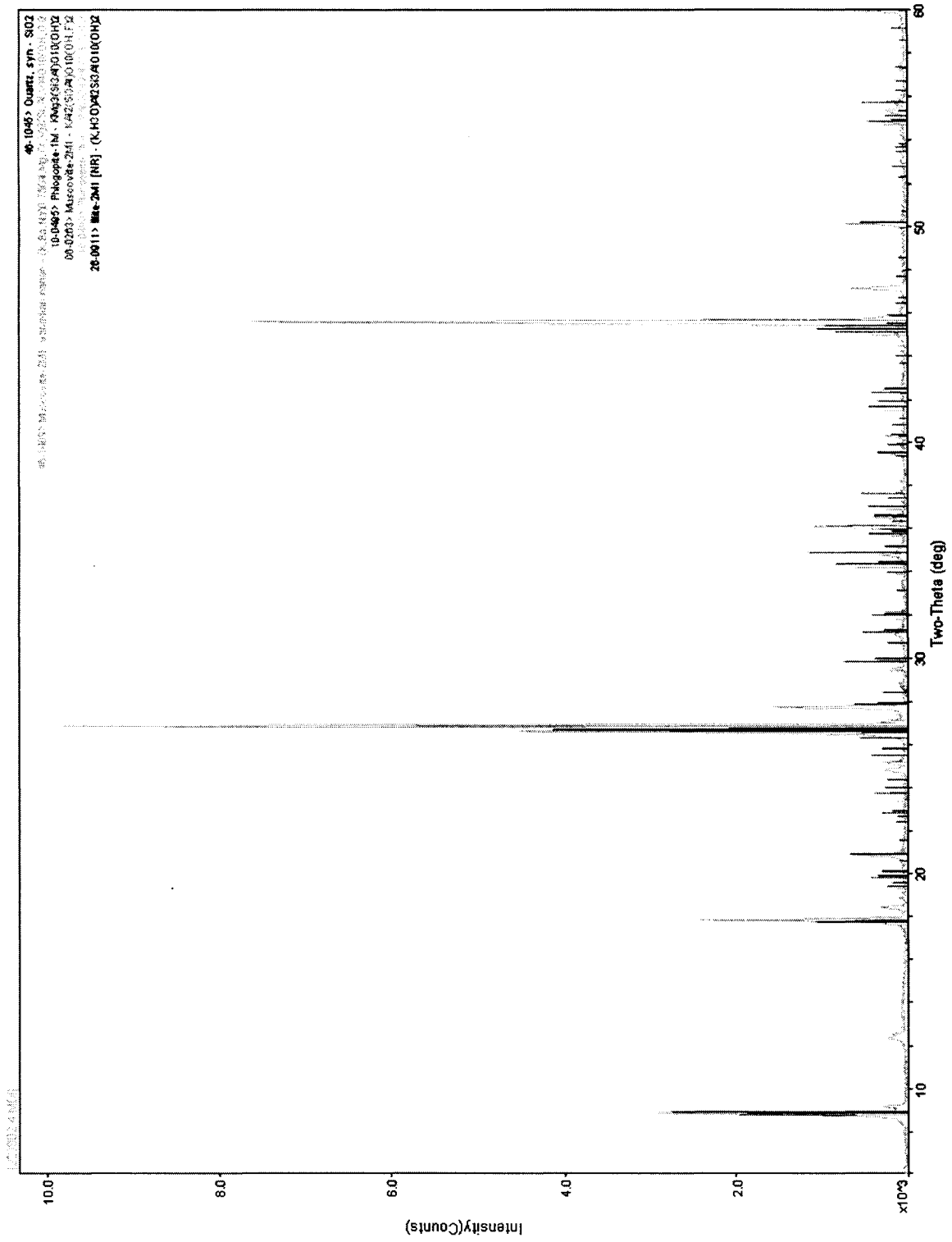




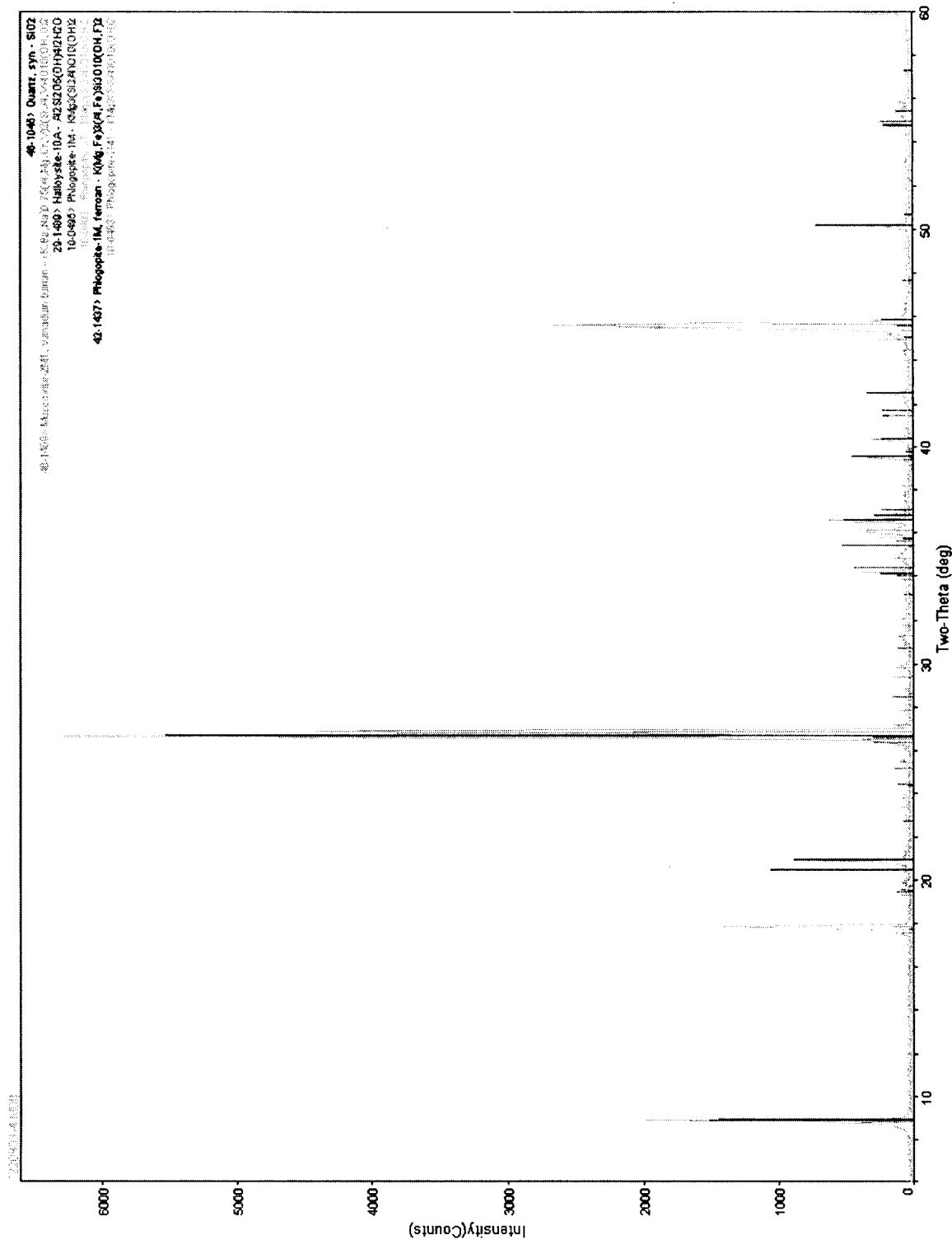


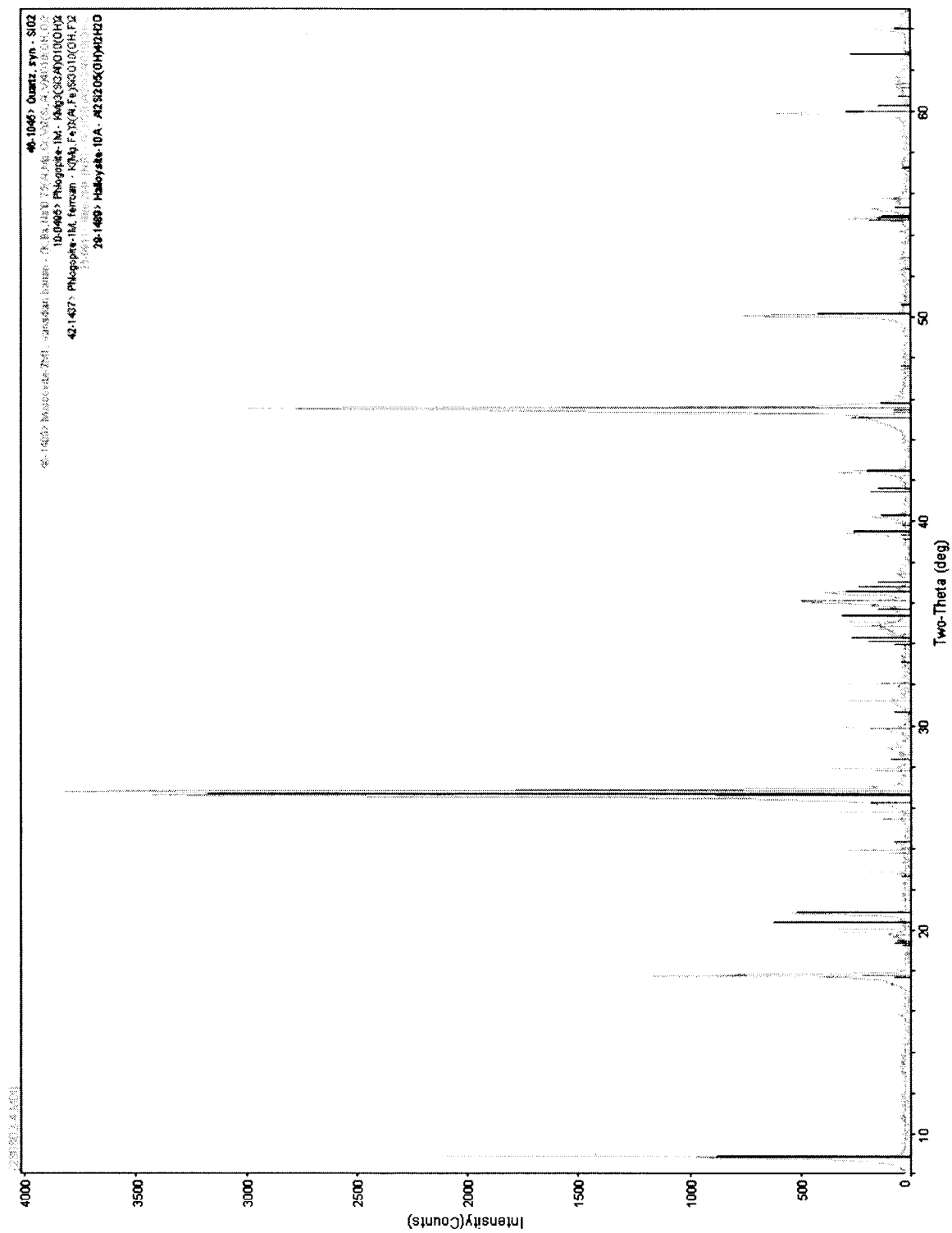


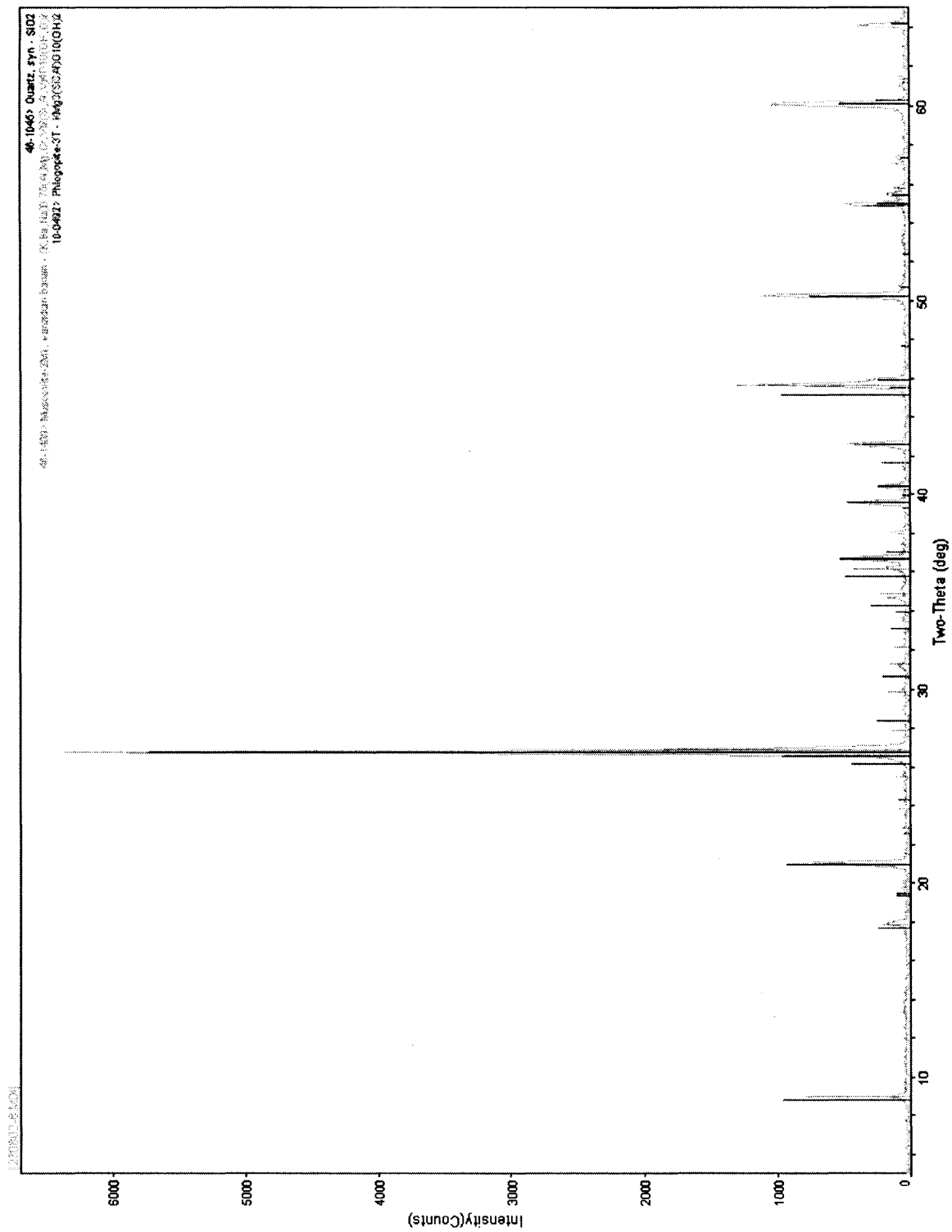


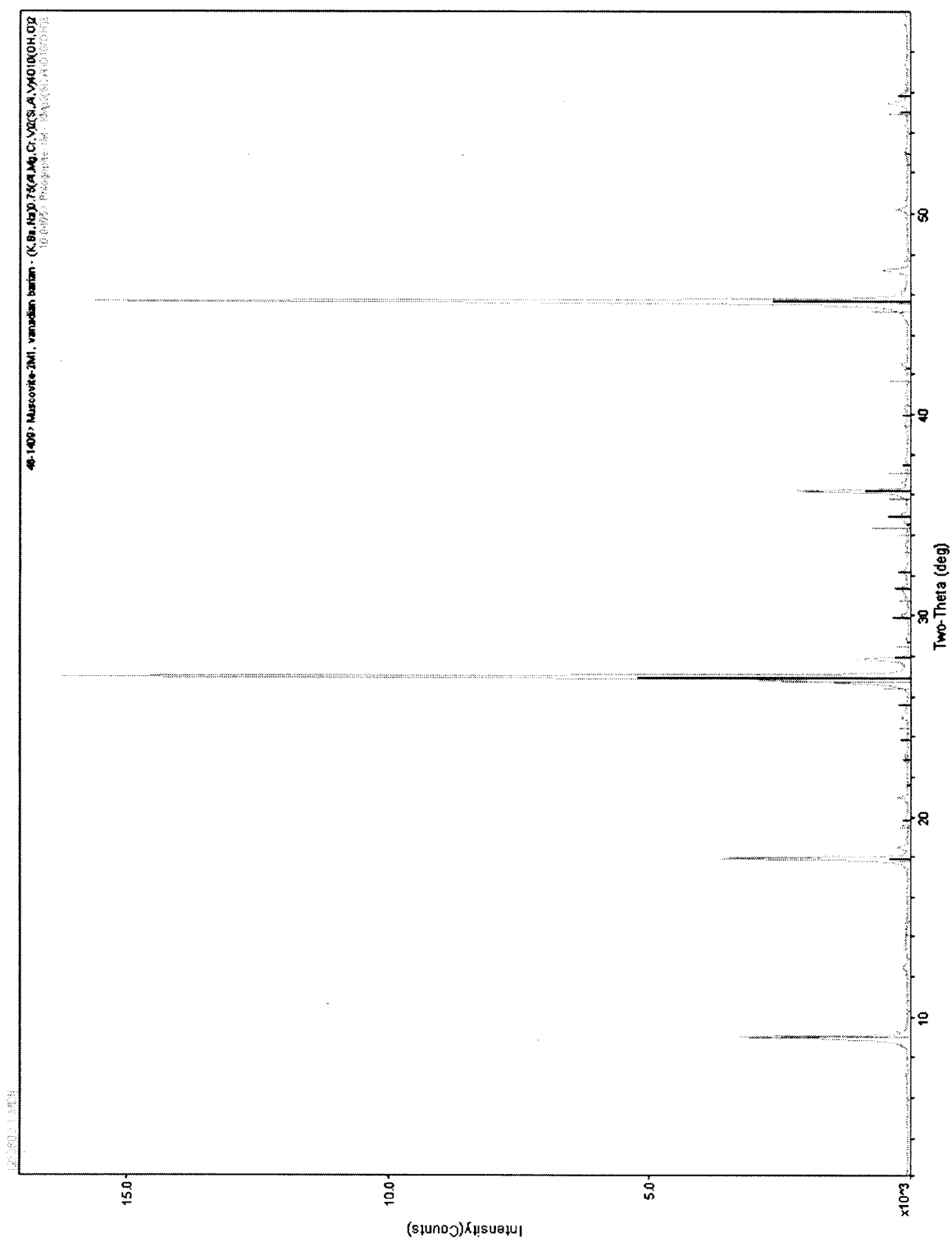




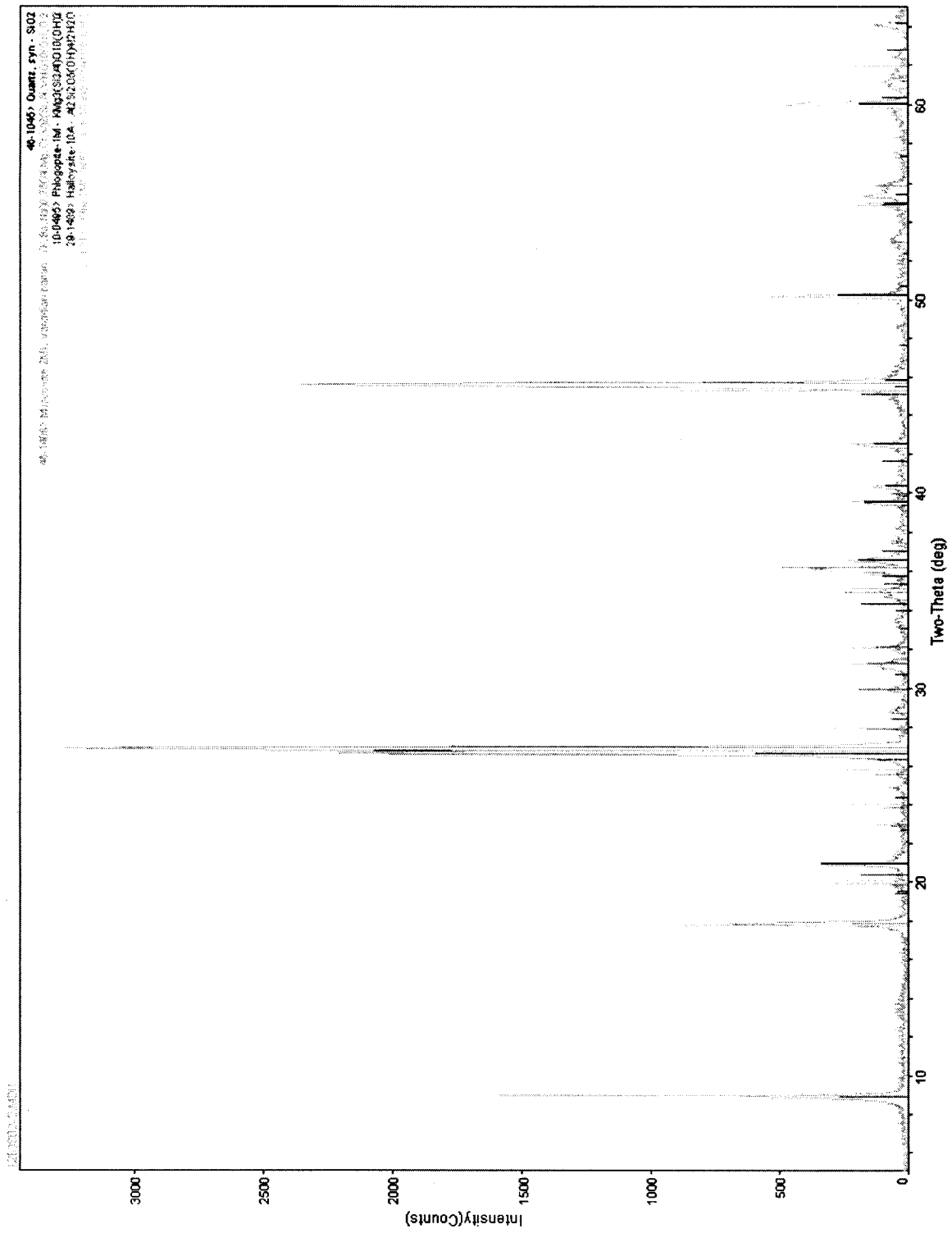


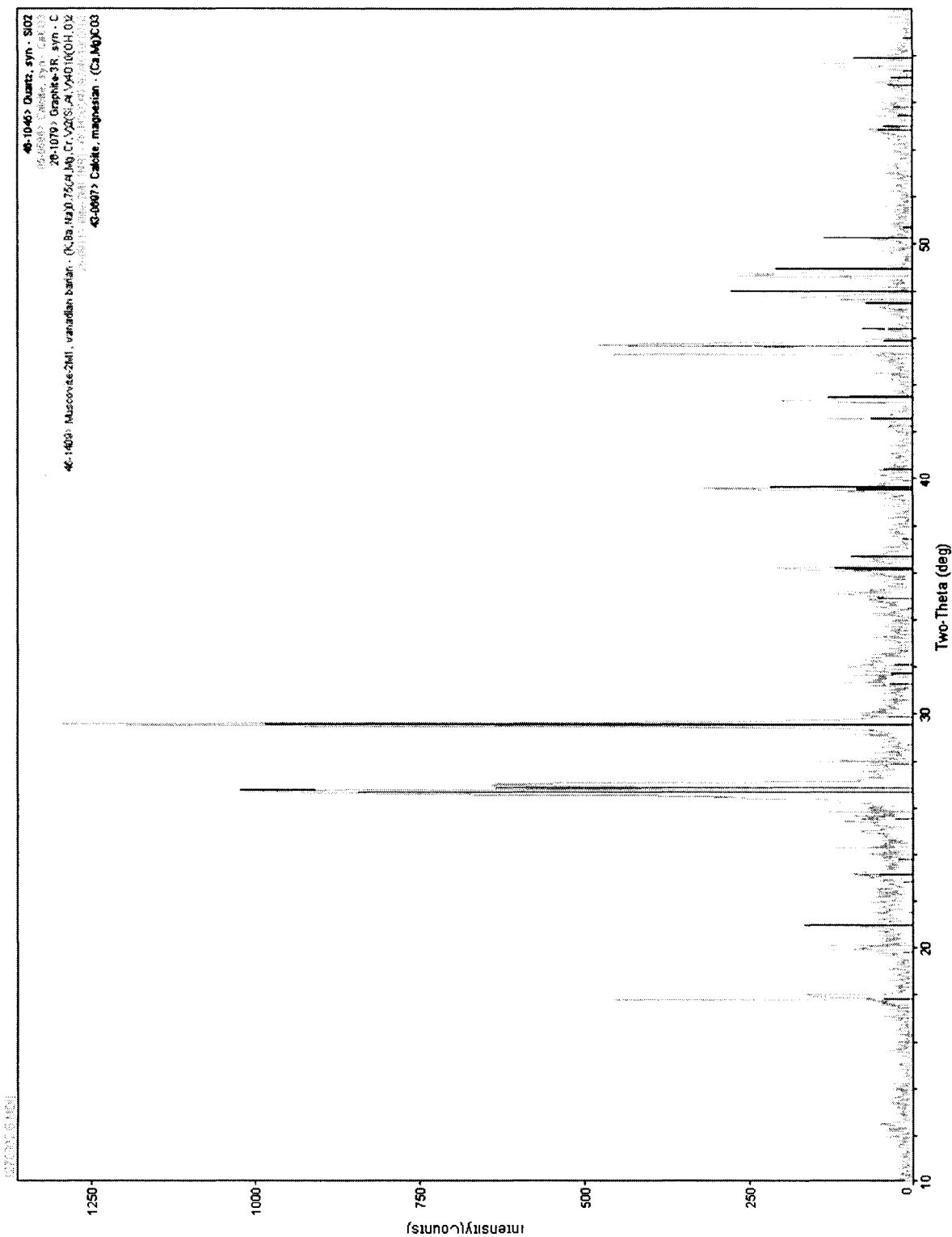


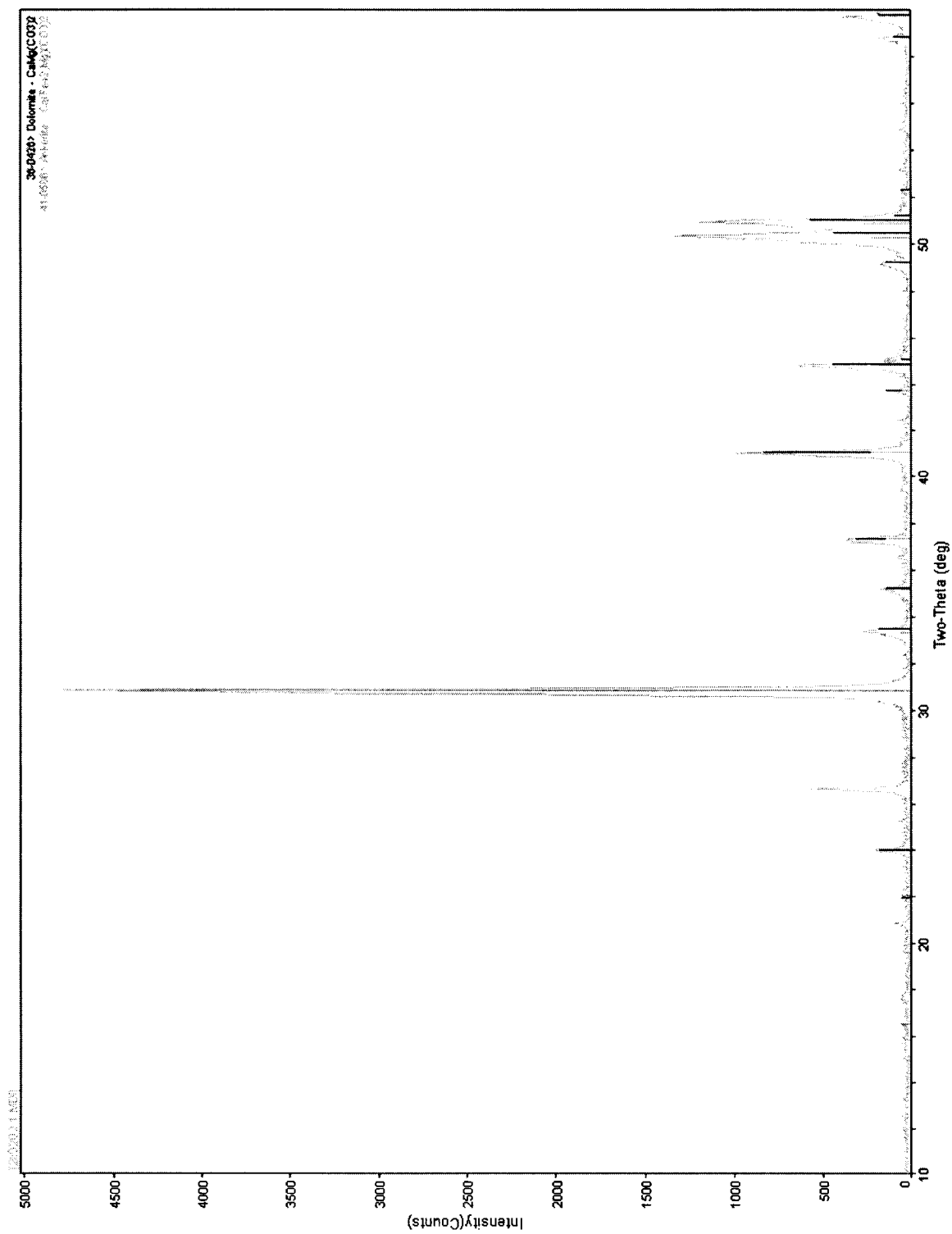




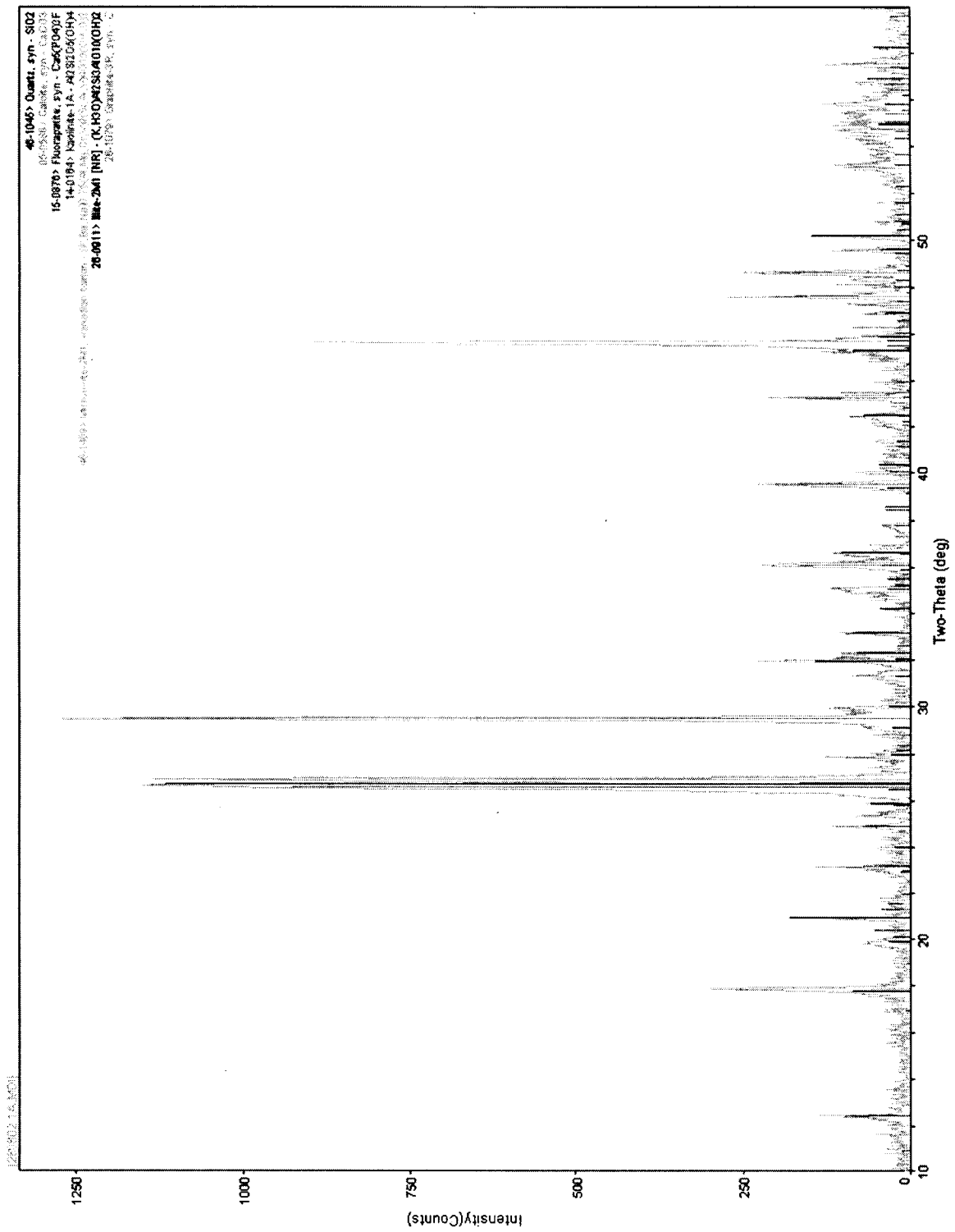


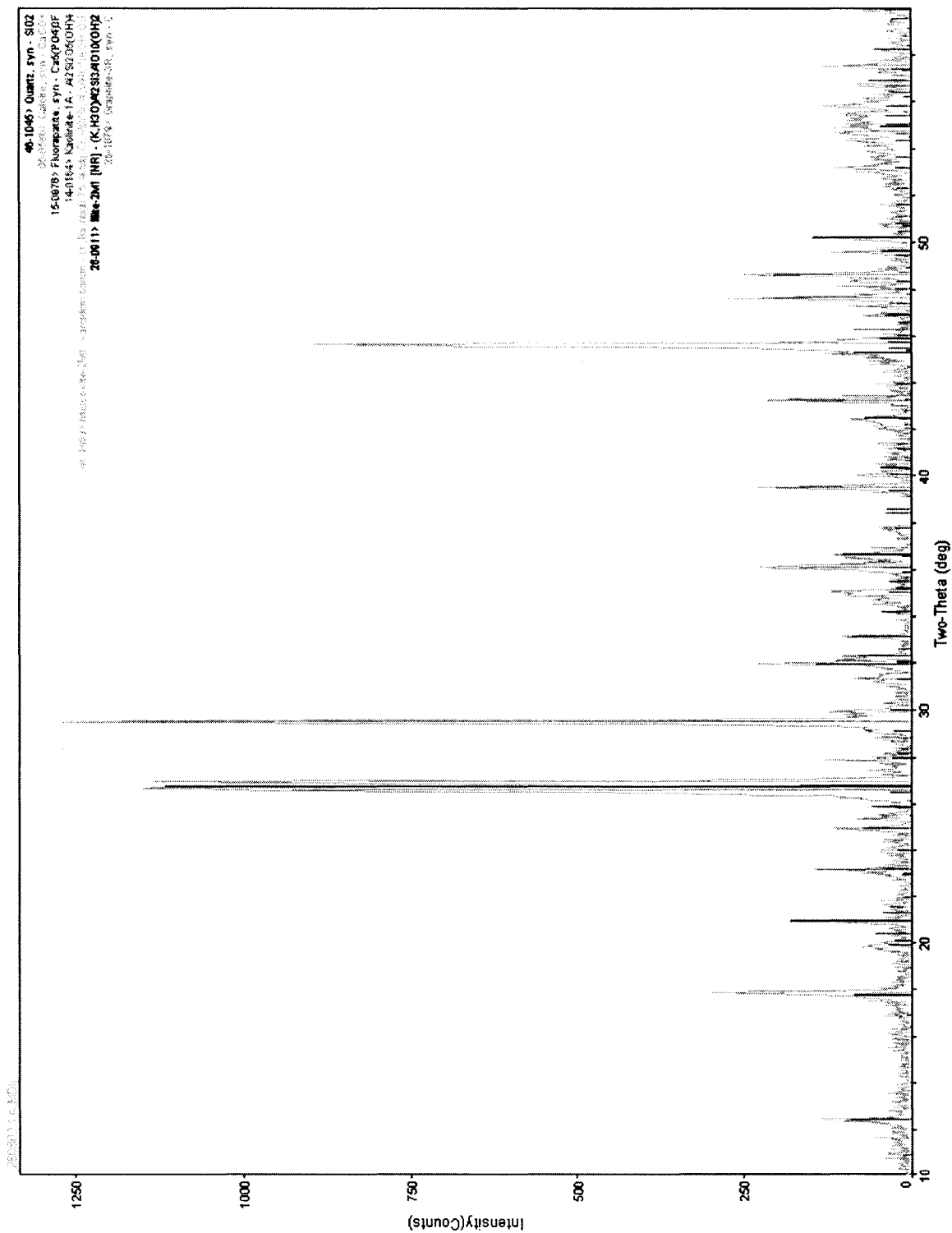


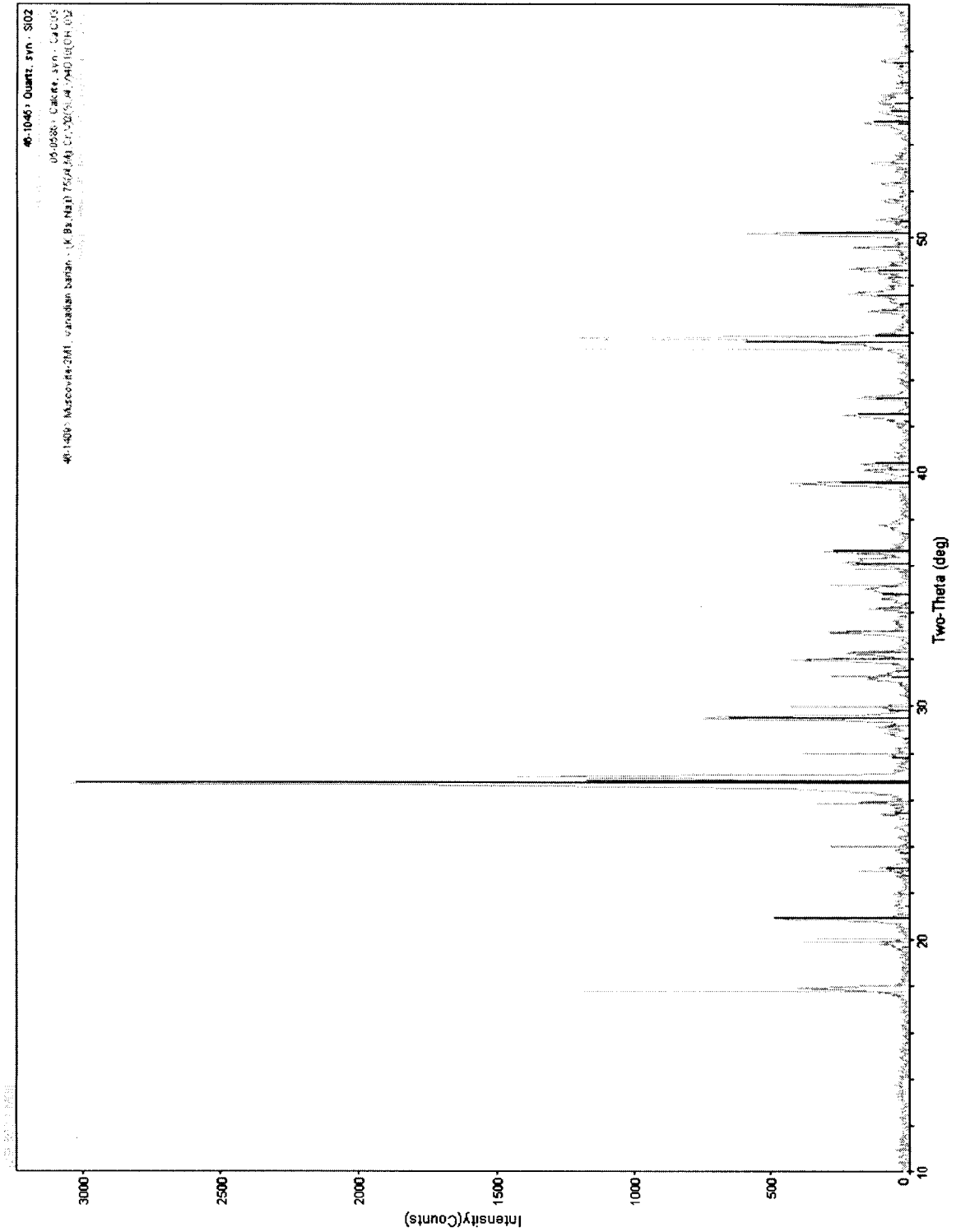


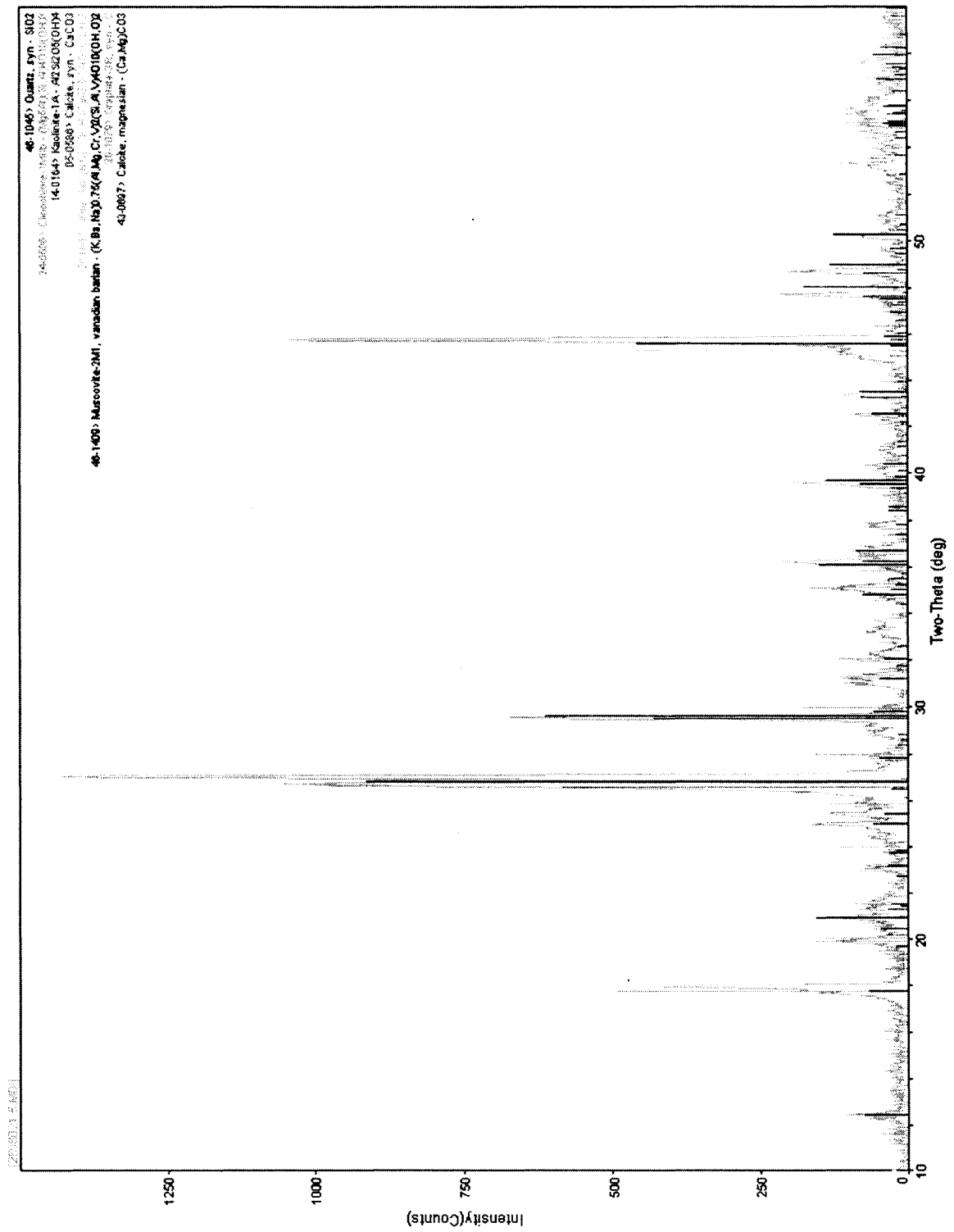


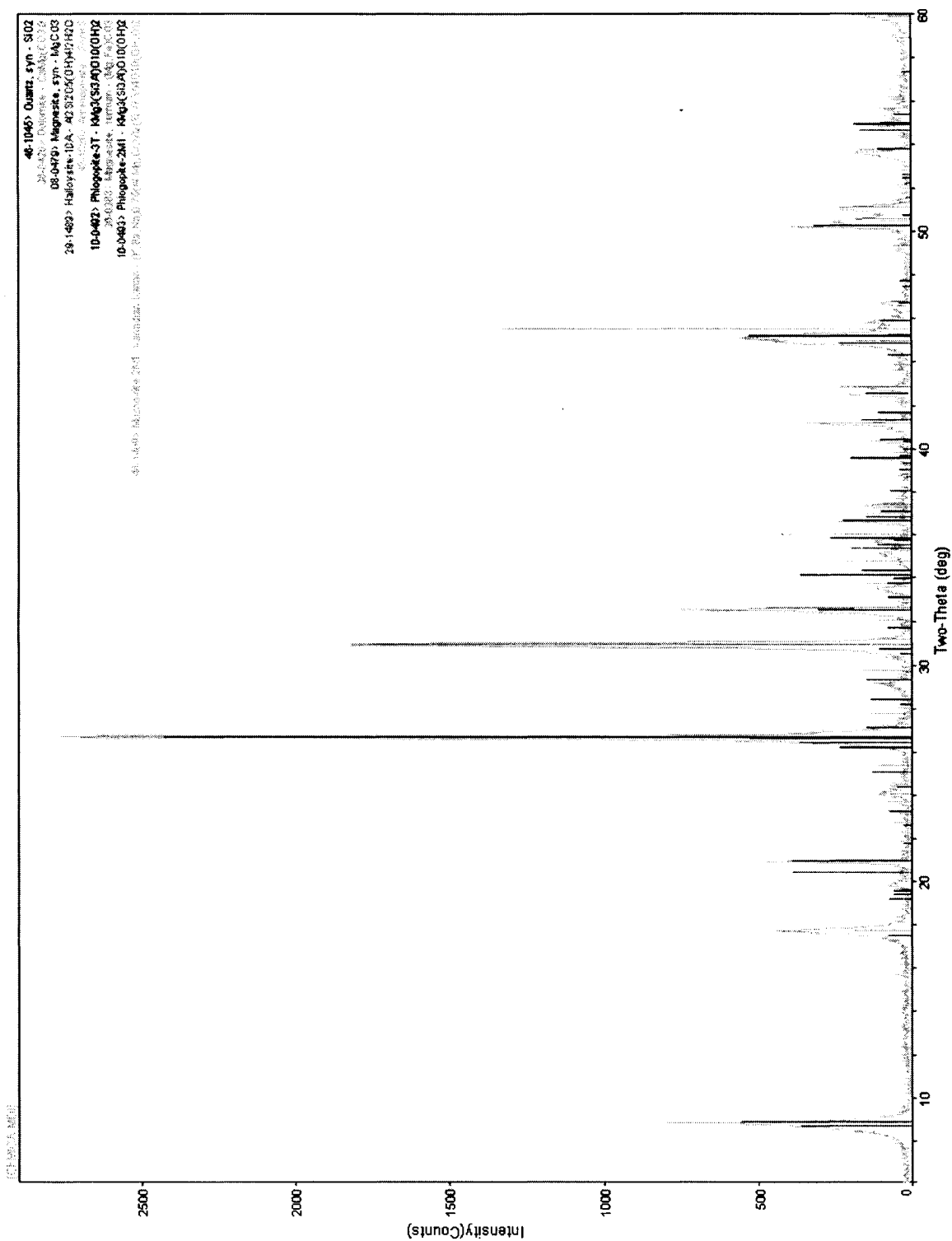


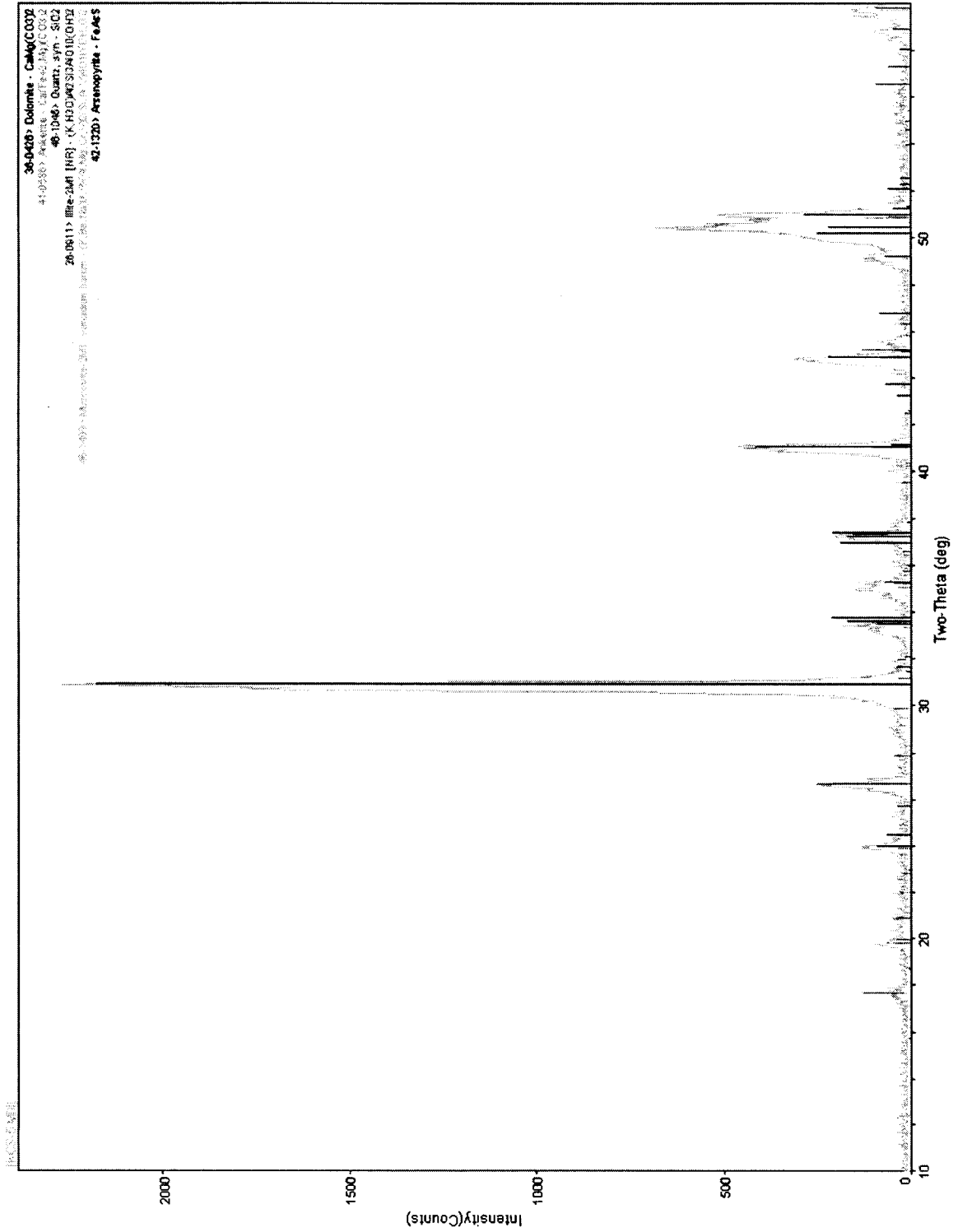


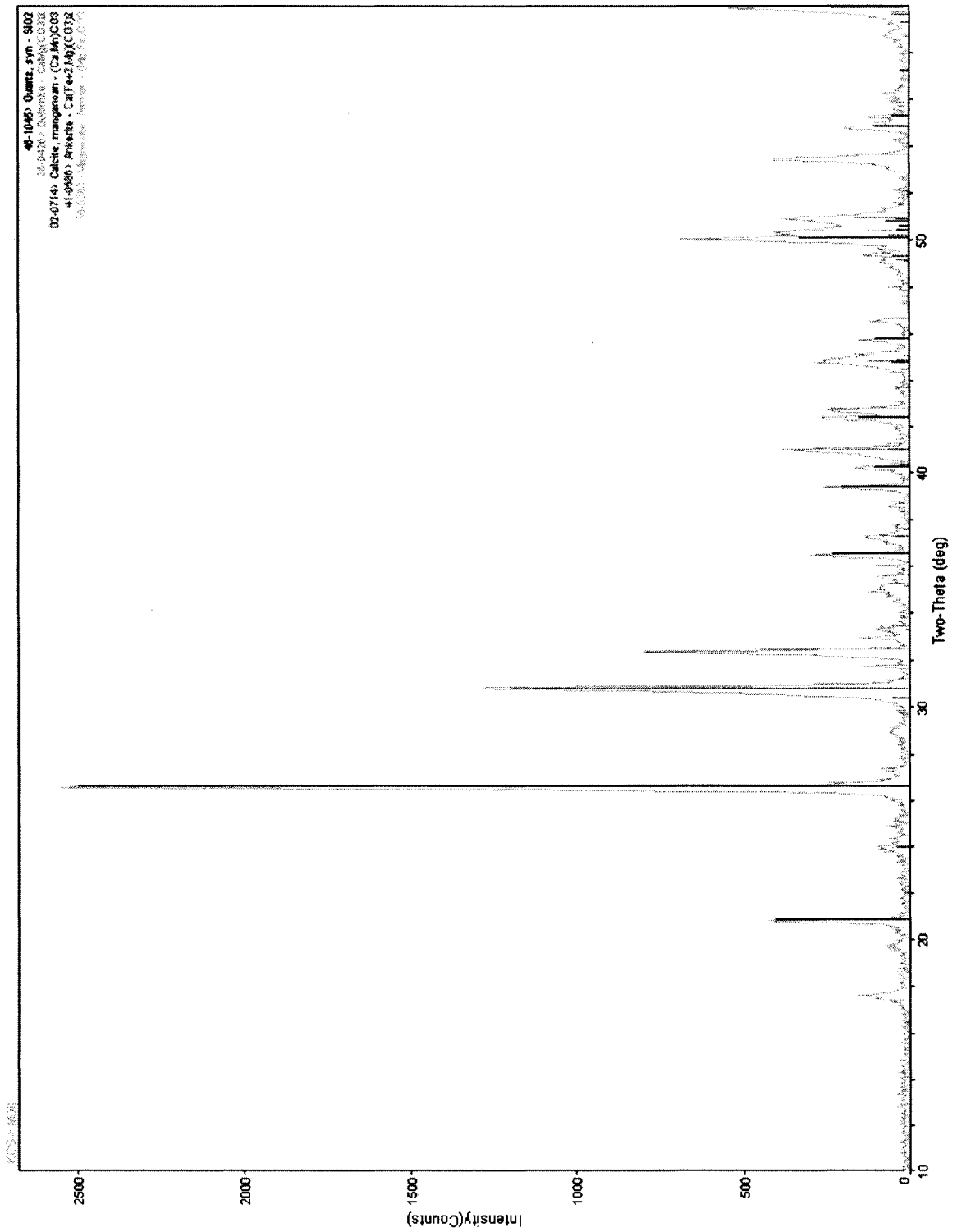


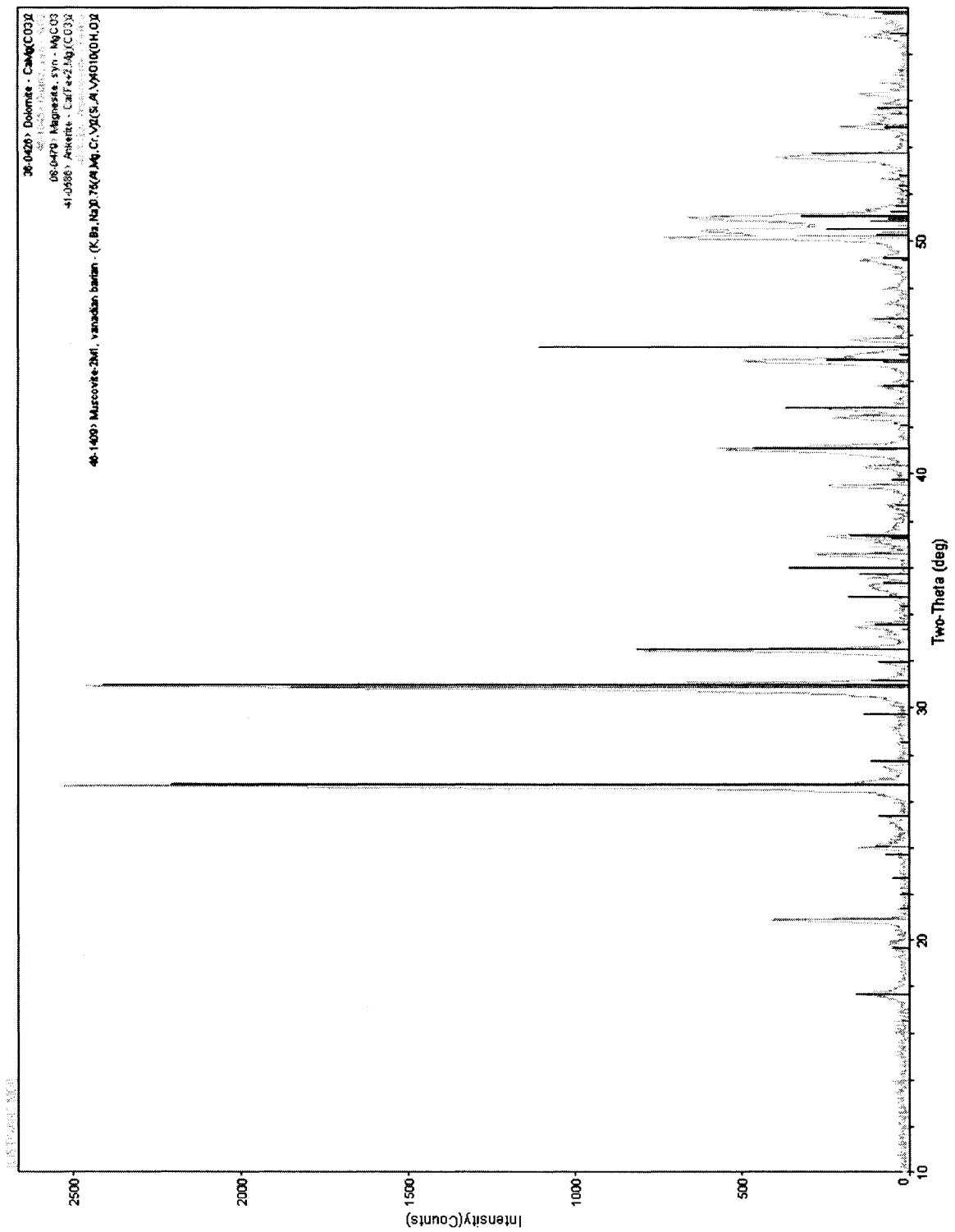






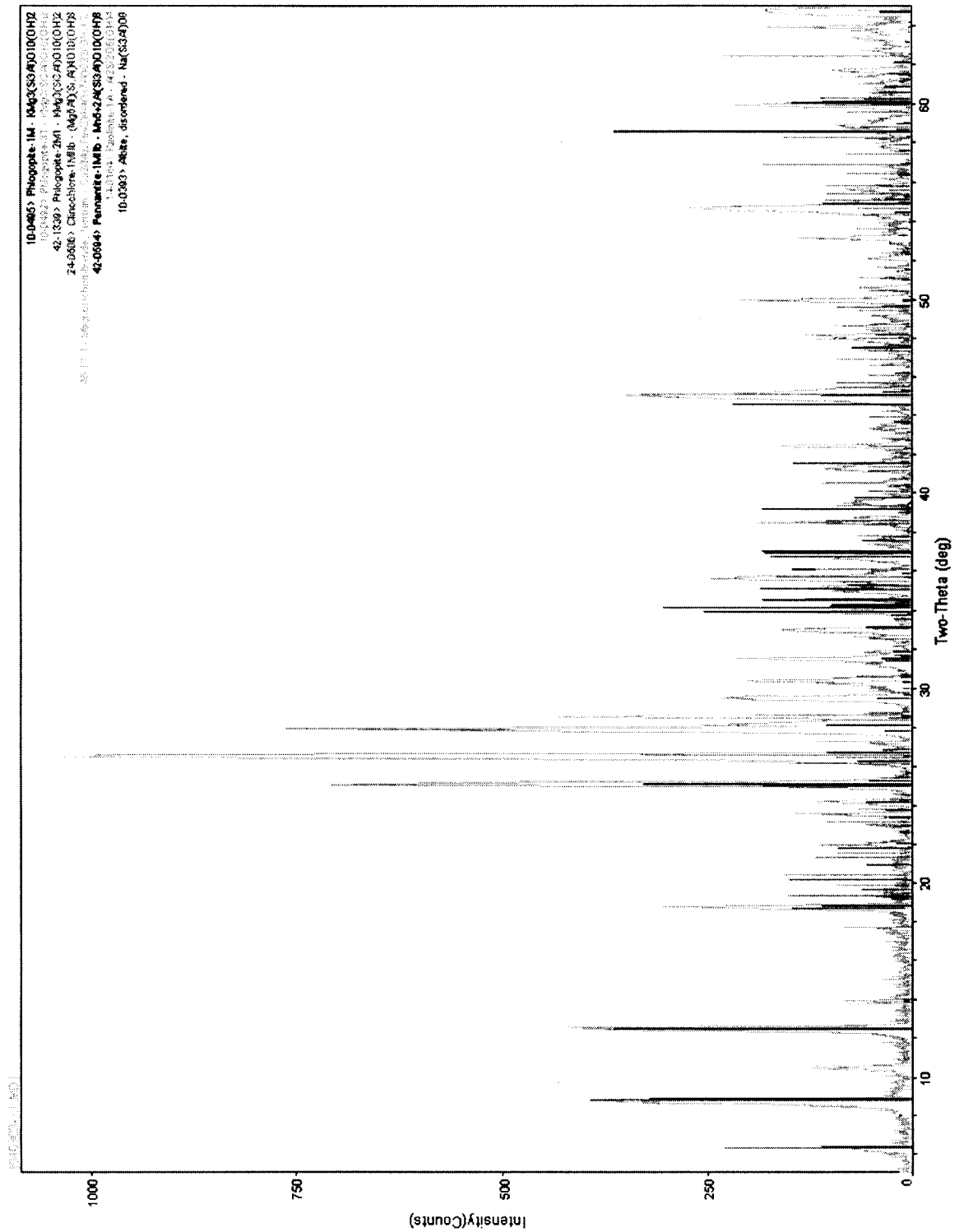


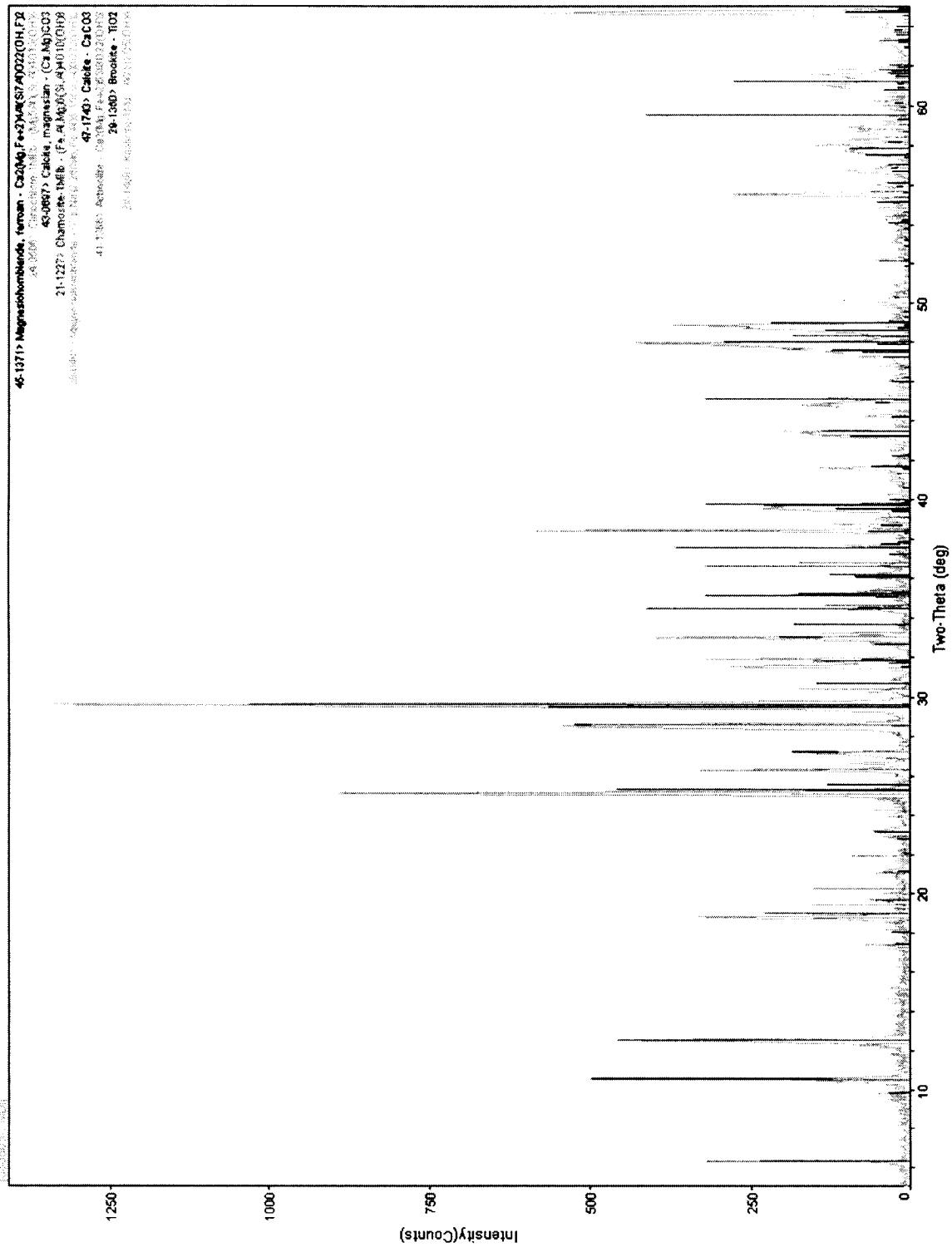


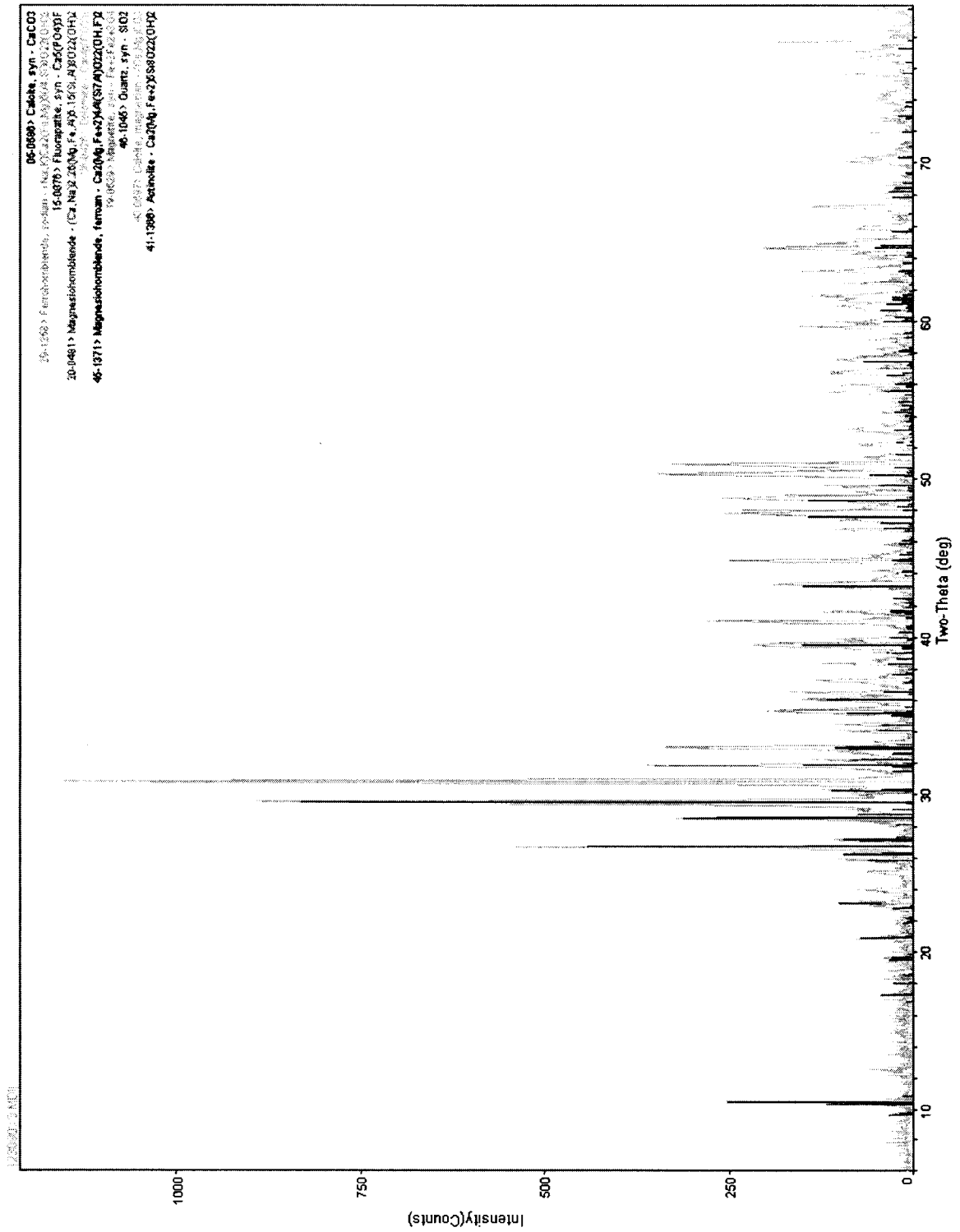




**Appendix A: Part 4.****Amphibolite**







## **Appendix B**

### **Petrographic Summary Tables**

Petrographic analyses for this study utilized transmitted and reflected light.

Both standard thin sections, with cover slips and polished thin sections were studied.

An Olympus BX51 research petrographic microscope equipped with a vertical illumination system and an Olympus digital imaging system was used for petrographic analysis and documentation.

## Bañales schist-quartzite N#24

sample#	%present											MFS	FS-1
	280802-8	280802-12	280802-1	270802-24	270802-28	270802-16	270802-15	080802-4	010802-2	280802-5	280802-2		
quartz	90	76	4	20	72	34	65	1	80	70	20	85	
biotite	3	22	45	45	25	60	15	30	20	30	68	10	
plagioclase	-	-	tr	tr	tr	tr	tr	6	-	tr	-	-	
calcite	-	-	20	30	-	-	-	40	-	-	10	-	
graphite	7	2	1	3	-	-	-	-	-	-	-	-	
FeOx	-	5	-	-	-	-	-	-	-	-	-	-	
tourmaline	-	tr	-	-	tr	-	tr	-	-	-	-	-	
magnetite	-	-	-	-	-	1	tr	-	-	-	-	-	
actinolite	-	-	-	-	-	-	-	-	-	-	-	-	
amphibole	-	-	5	-	-	-	-	20	-	-	-	-	
spinel	-	-	tr	-	tr	-	-	3	-	-	-	-	
epidote	tr	tr	-	-	tr	-	tr	-	-	-	2	-	
garnet	-	-	25	2	3	5	10	-	-	tr	-	5	
pyrite	-	-	-	-	-	-	tr	tr	-	-	-	-	

week/Alt

## Bitterschist-quartzite

sample#	Mineral	%present													
		FS-2	2007085	280808-4	280808-4	280808-1	100908-2	100908-11	100908-4	280808-6	100908-12	090908-9			
98	quartz	56	7	20	18	80	80	95	90	89	100				
5	biotite	4	85	80	80	15	3	10	11	tr					
	plagioclase	30													
	calcite					tr	1								
	graphite						2	1							
	FeOx						1								
	tourmaline		1		2										
	magnetite		7												
	actinolite	10													
	amphibole														
	sphene	tr													
	apatite														
	garnet	3			tr	2									
	Pyrite														

Eclogite N=9

sample #	Mineral	% present									
		EG-1	210703-1	200903-6	130603-4	EG-5	EG-4	EG-2	EG-1	290802-3	
	garnet	6	2	15	6	20	30	25	15	2	
	biotite	10	-	-	-	30	3	4	-	53	
	calcite	45	70	25	35	-	35	30	30	30	
	sphene	5	-	-	-	-	-	-	-	-	
	amphibole	20	3	-	-	5	28	-	15	-	
	actinolite	-	2	40	55	-	-	2	-	-	
	pyroxene	2	-	-	-	-	-	-	-	-	
	quartz	7	1	-	-	5	1	10	5	10	
	Magnetite	5	8	-	1	-	-	-	-	-	
	apatite	-	2	2	-	tr	2	-	7	tr	
	tourmaline	-	-	-	-	-	-	-	-	tr	
	graphite	-	-	-	-	-	1	-	-	5	
	stibnomaline	tr	-	-	-	-	-	-	-	-	
	pyrite	-	2	-	-	-	-	-	-	-	
	plagioclase	-	-	1	1	-	-	4	3	-	



Marble N=5

sample #	Mineral	% present				
		230903-5	ZEP	300802-2	250802-2a	080803-5
	Actinolite	90	-	3	-	-
	calcite	8	80	85	80	85
	biotite	-	3	-	3	1
	quartz	-	1	-	-	-
	garnet	-	3	-	-	1
	apatite	-	-	tr	-	3
	sphene	-	7	-	5	-
	chlorite	-	1	-	-	-
	tourmaline	-	-	tr	-	-
	pyroxene	tr?	-	-	-	-
	ankerite vn	2	-	-	-	-
	opaques	-	5	7	3	-
	plagioclase	-	-	-	10	-
	amphibole	-	-	-	tr	10

graphitischist N#12

sample#	Mhard										%presart			
	070708-2	180908-13	180908-13	100908-1	180908-3a	M#1	A-1	100702-6	290802-2	270602-2	220802-1d	200708-2		
quartz	7	1	2	80	5	80	90	60	65	80	90	75		
graphite	3	7	5	5	5	2	8	10	5	2	1	10		
biotite	90	92	98	1	90	1	2	30	15	14	5	13		
calcite	-	-	-	4	-	17	-	-	-	-	1	-		
garnet	-	-	-	5	-	-	-	-	-	1	-	-		
spinel	-	-	-	-	tr	-	-	-	-	-	-	-		
apatite	-	-	-	-	-	-	-	1	-	-	-	-		
plagioclase	tr	-	-	-	-	-	-	-	5	tr	3	-		
magnetite	-	-	-	-	-	-	-	-	-	tr	tr	-		
	Atrd	Atrd	Atrd	attds.per	s.per	s.per	s.per	s.per	wks.per	s.per	s.per	s.per		

s.per = s.pergeneration

Alteration fuchsite-ankerite		N=9		% present									
sample #	Mineral	090903-3	070703-1	070703-2a	070703-2b	070703-2a	100903-13	M-2	050703-2	280802-9b	280802-9a		
	quartz	tr	2	30	50	50	3	40	1	1	1	1	1
	ankerite	35	76	63	50	50	45	50	50	60	78		
	fuchsite	12	20	5	tr	tr	45	10	30	37	20		
	biotite	40		tr	tr	tr	7	tr	1	-	-		
	py	2	1.5	tr	1	1	-	-	10	2	-		
	aspy	1	0.5	tr	-	-	-	-	-	-	-		
	plagioclase	10	-	-	-	-	-	-	-	-	-		
	garnet	-	-	-	-	-	-	-	tr	-	-		
	apatite	-	tr	-	-	-	-	tr	2	tr	1		
	tourmaline	-	-	-	-	-	-	-	2	tr	tr		
	FeOx	-	-	-	-	-	-	-	10	-	-		
	graphite	-	-	2	tr	tr	-	tr	-	-	-		
			ox	ox	ox	strg ox	wk ox		strg ox	ox			

ox = supergene alteration

State-argillite N=10

Mineral	% present									
	270903-6a	250603-6	190903-1	120903-3	ABBS	180903-4	270903-2	180903-3b	CBX	270903-2a
quartz	100	100	30	80	35	70	50	88	45	60
graphite	tr	-	2	10	5	5	10	2	5	2
calcite	-	-	68	-	-	-	-	-	20	-
pyrite	-	-	1	-	-	-	-	-	-	-
biotite	-	-	-	10	60	25	40	10	30	38

10% calcareous grain:

## Appendix C

### Stable Isotope Data Tables

Stable isotope analyses were performed by the Nevada Stable Isotope Laboratory.

Sulfur isotope and graphite carbon isotope analyses were performed in continuous flow mode, using an Eurovector model 3028 elemental analyzer interfaced to a Micromass IsoPrime stable isotope ratio mass spectrometer. Sulfur isotope analyses were performed after the method of Giesemann et al. (1994) and Grassineau et al. (2001).  $\delta^{34}\text{S}$  results are reported in units of ‰ vs. VCDT. An uncertainty of  $\pm 0.2\text{‰}$  is recommended. Sulfur is extracted from bulk samples using Kiba reagent, after the technique of Sasaki et al. (1979). Graphite carbon isotope analyses were performed after the method of Preston and Owens (1983). Graphite- $\delta^{13}\text{C}$  results are reported in units of ‰ vs. VPDB, and an uncertainty of  $\pm 0.1\text{‰}$  is recommended.

Carbonate isotope analyses were performed in dual inlet mode, using a Micromass MultiPrep preparation device interfaced Micromass IsoPrime stable isotope ratio mass spectrometer, using the phosphoric acid reaction method of McCrea (1950), except that the reaction was performed at  $90^\circ\text{C}$ .  $\delta^{13}\text{C}$  results are reported in units of ‰ vs. VPDB, and  $\delta^{18}\text{O}$  results are reported in units of ‰ vs. VSMOW. An uncertainty of  $\pm 0.1\text{‰}$  is recommended for both  $\delta^{13}\text{C}$  and  $\delta^{18}\text{O}$ .

Giesemann A., Jager H.J., Norman A.L., Krouse H.P. and Brand W.A. (1994) On-line sulfur-isotope determination using an elemental analyzer coupled to a mass spectrometer. *Analytical Chemistry*, 66: 2816-2819.

Grassineau N.V., Matthey D.P. and Lowry D. (2001) Sulfur Isotope Analysis of Sulfide and Sulfate minerals by Continuous Flow-Isotope Ratio Mass Spectrometry. *Analytical Chemistry*, 73: 220-225.

McCrea J.M. (1950) On the isotope chemistry of carbonates and a paleotemperature scale. *Journal of Chemical Physics*, 18: 849-857.

Preston T. and Owens N.J.P. (1983) Interfacing an automatic elemental analyzer with an isotope ratio mass spectrometer: the potential for fully automated total nitrogen and nitrogen-15 analysis, *Analyst*, 108: 971-977.

Sasaki A., Arikawa Y. and Folinsbee R.E. (1979) Kiba reagent method of sulfur extraction applied to isotopic work. *Bulletin of the Geological Survey of Japan*, 30: 241-245.

True North  
Carbonate samples for oxygen and carbon isotopes  
Sample Number

count	Lab	True North	location	Type	$\delta^{13}\text{C}$ (‰, VPDB)	$\delta^{18}\text{O}$ (‰, VPDB)	$\delta^{18}\text{O}$ (‰, VSMOW)
1	KC-1	050802-1	H11460E CG-6	Calcite vein	-8.6	-12.9	17.6
2	KC-2	070204-1	Hind	Vein, coarse xtline calcite (late?)	-0.2	-26.2	3.9
3	KC-3	100702-1	H11340E	Late(?) calcite vns w/dog tooth spar in alt bio-schist	-3.7	-13.3	17.2
4	KC-4	100702-3Ast1	H11340E	multi-vns Trmsicnt sikwk x-cut by cream ankerite	-5.3	-13.4	17.1
5	KC-5	100702-3Ast2	H11340E	multi-vns Trmsicnt sikwk x-cut by cream ankerite	-3.5	-17.5	12.9
6	KC-6	100702-3st1	H11340E	multi-vns Trmsicnt sikwk x-cut by cream ankerite	-6.4	-12.8	17.8
7	KC-7	100702-3st2	H11340E	multi-vns Trmsicnt sikwk x-cut by cream ankerite	-4.6	-18.3	12.1
8	KC-8	100702-3st3	H11340E	multi-vns Trmsicnt sikwk x-cut by cream ankerite	-4.1	-24.3	5.9
9	KC-9	130603-4	S1340	Whole rock, Shepard eclogite??	-8.9	-14.5	15.9
10	KC-10	230903-3	H11360N	Whole rock, eclogite??	-6.7	-15.9	14.6
11	KC-11	260603-2	S1340	Calcite vein, Shepard	1.6	-25.9	4.2
12	KC-12	270802-10mbx	H11340N	matrix, listwaenite float (ankerite)	-6.0	-14.6	15.8
13	KC-13	270802-10vn	H11340N	Vein, listwaenite float (ankerite)	-3.1	-19.6	10.7
14	KC-14	270802-3	H11340N	banded calcite vein (with graphite)	1.8	-29.6	0.4
15	KC-15	270802-6	H11340N	Calcite/Qtz bx from sheared vn	-1.6	-25.9	4.2
16	KC-16	280802-9Ambx	H11340S	matrix, weathered ankerite alt	-5.3	-15.4	15.0
17	KC-17	280802-9Avn	H11340S	Vein, from weathered ankerite alteration	-1.5	-17.3	13.0
18	KC-18	CBX	Central	Carb sep. (calcite)	-8.1	-12.4	18.2
19	KC-19	EG-0	Hind	Whole rock, eclogite	-4.1	-13.9	16.5
20	KC-20	EG-1	Hind	Whole rock, eclogite	-4.5	-10.9	19.7

True North Sulfur isotope samples	$\delta^{34}\text{S}_{\text{SO}_4}$ (‰)
Sample# Type and location	
KCS1 Nail's zone 1480S; stibnite	-1.9
KCS2 Stibnite in Qz	-1.3
KCS3 Stibnite in Qz; 180803.5	0.3
KCS4 aspy, Ft. Knox	2.0
KCS5 Blackmtx. bx, whole rock	nfd
KCS6 aspy concentrate w/ mica and carbonate	1.8
KCS7 EGQ, whole rock	0.9
KCS8 EG-1, whole rock	-0.8
KCS9 aspy separate; 100803.5	1.2
KCS-10 aspy separate; 100803.5; ox	1.1
KCS-11 whole rock; Pedro Dome; clastic	2.4

nfd = no data

$\delta^{34}\text{S}_{\text{SO}_4}$  (‰)

stibnite  
stibnite  
stibnite  
arsenopyrite  
aspy concentrate w/ mica and carbonate  
aspy concentrate w/ mica and carbonate  
edogite, whole rock  
edogite, whole rock  
arsenopyrite  
arsenopyrite

stibnite  
stibnite  
stibnite  
arsenopyrite  
aspy concentrate w/ mica and carbonate  
EGQ, whole rock  
EG-1, whole rock  
aspy separate; 100803.5  
aspy separate; 100803.5; ox  
whole rock; Pedro Dome; clastic

nfd = no data

Graphite isotope samples  
True North

count	ID	sample no.	$\delta^{13}\text{C}_{\text{VPDB}} (\text{‰})$	location	type
1	KOG-1	060802-4	-39.1	H1360	graphite schist
2	KOG-5	160903-2	-28.6	C1260	graphite schist
3	KOG-4	140903-1	-25.2	Birch Hill	argillite/slate
4	KOG-2	100903-2	-23.6	H1280	graphite schist
5	KOG-7	200703-2	-23.0	H1400S	graphite schist
6	KOG-6	180903-4	-22.1	C1260	argillite/slate
7	KOG-3	120803-5	-22.0	S1300	argillite/slate
8	KOG-10	280802-15	-21.1	H1340S	graphite from fault
9	KOG-8	250603-5	-20.8	S1340	graphite from around qtz pod (in mineralized fault)
10	KOG-9	250603-8	-20.7	S1340	graphite from fault
11	KOG-11	270802-6	-18.3	Hnd	fault graphite for calcite-graphite geotherm
12	KOG-12	270802-3	-19.0	Hnd	fault graphite for calcite-graphite geotherm



## Appendix D

### Age Dates and Argon Release Data

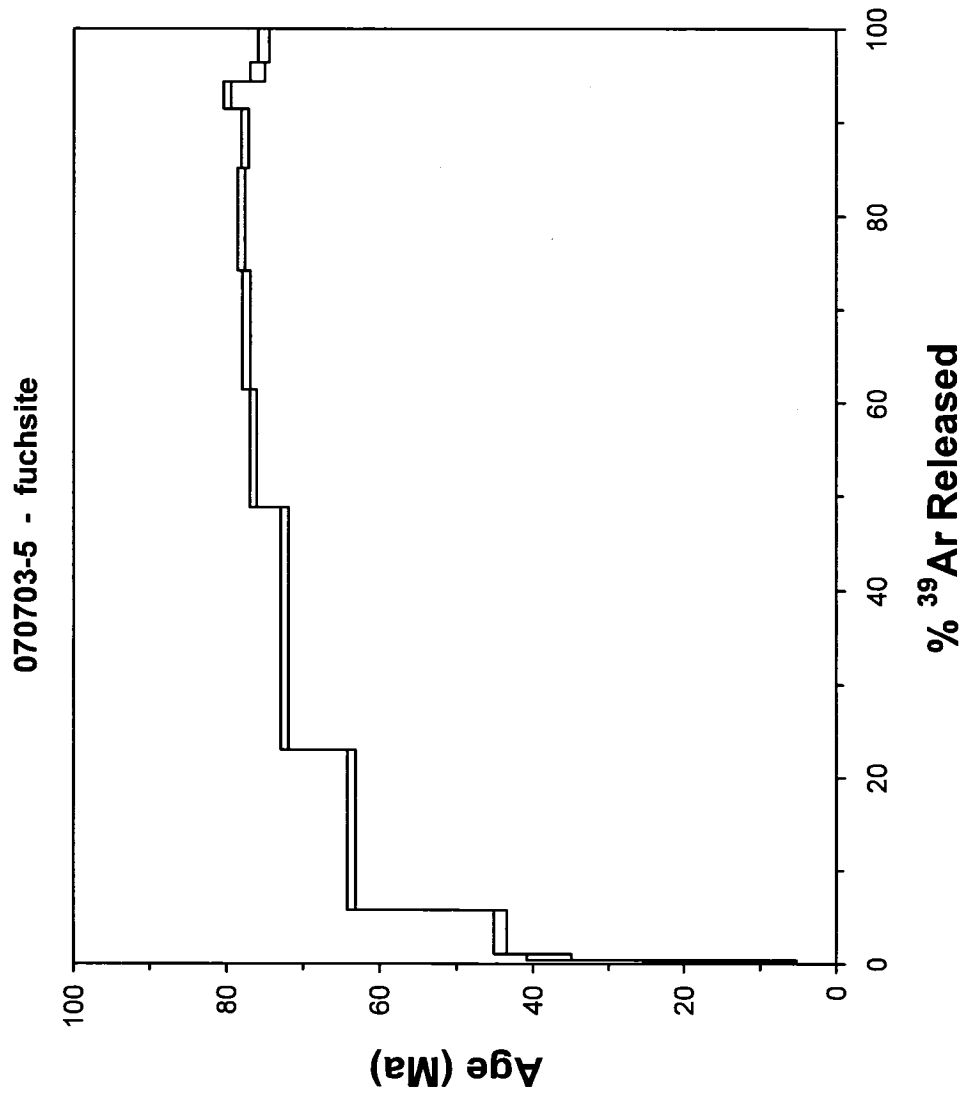
$^{40}\text{Ar}/^{39}\text{Ar}$  geochronology reported in this study was performed by the University of Nevada, Las Vegas Geochronology laboratory, under the direction of Dr. Terry Spell.

For discussion of the techniques used see, Spell et al., (2001) and Reiners et al., (2004).

Thompson-CREG 070703-6, Initials 809mg, J=0.001678±0.45%  
 4-amu discrimination = 1.0140±0.24%, 403K=0.0001 ± 10.0%, 3637Ca = 0.000282±2.28%, 3937Ca = 0.000669±0.44%

step	T (C)	t (min)	38A	37A	38A	39A	40A	%40A*	%39A/r1sd	Calc	40A/39A/K	Age (My)	r1sd
1	455	12	1.255	0.049	0.238	0.364	367.68	0.6	0.2	1.2890724	5563865	1674	8.69
2	475	12	0.414	0.033	0.070	0.386	121.663	1.5	0.2	1.53879976	4408940	1330	8.09
3	515	12	0.320	1.320	0.138	1.271	207.784	8.0	0.6	9.81604448	12638806	37.86	2.92
4	560	12	1.837	3.215	0.466	9.268	672.449	20.8	4.7	3.27227538	14801392	44.26	0.82
5	646	12	2.897	29.881	0.897	33.947	1577.8	46.5	17.2	8.31584638	21.47133	63.70	0.54
6	700	12	2.573	201.534	1.138	50.639	1922.38	64.6	25.8	37.782197	24.416268	72.44	0.50
7	740	12	0.835	70.249	0.455	24.832	851.819	75.9	12.6	28.6752861	25.813280	76.50	0.48
8	780	12	0.426	0.664	0.388	25.101	783.886	86.1	12.7	0.21175971	26.124670	77.40	0.48
9	820	12	0.320	0.289	0.330	21.715	666.670	87.2	11.0	0.12542439	26.361844	78.05	0.46
10	870	12	0.204	0.240	0.216	12.666	389.838	88.7	6.4	0.18001134	26.178708	77.66	0.47
11	920	12	0.108	0.213	0.094	5.721	195.917	87.2	2.9	0.36088816	26.991348	78.91	0.51
12	1000	12	0.127	0.276	0.072	4.060	140.418	78.7	2.1	0.64234088	25.623412	75.95	0.93
13	1400	12	0.863	0.667	0.244	7.062	431.418	43.5	3.6	0.74346073	25.346221	75.15	0.73
											Total gas age =		71.64
											no plateau		
											no isodron		

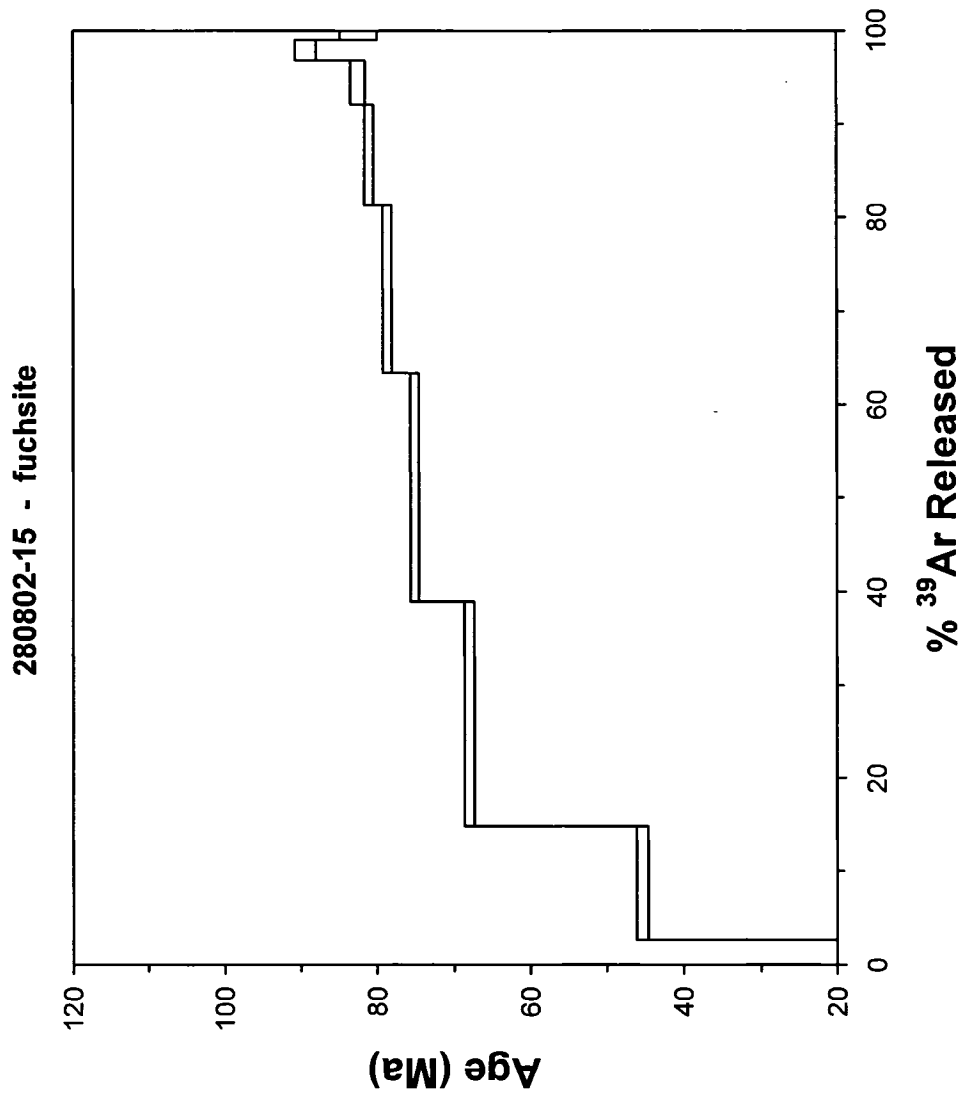
Cumulative % 68A r1sd = 100.0  
 Under isotope beams in mV, r1sd = released, error in age includes J error, all errors 1 sigma  
 (38A through 40A are measured beam intensities, corrected for decay for the age calculations)



Thompson CP6572808216, 1.14416, 127mg, J=0.001668810417%  
 4amidobenzoinitor=101422±0.18% 4039<=0.001±1.000% 3533Ca=0.00167±3.88% 393Ca=0.0010±0.63%

step	T(O)	t (min)	35A	36A	37A	38A	39A	40A	%40A*	%28A1isd	CaK	40A/39A/K	Apa(1A)	1sd
1	50	12	1859	0072	0542	0361	1238	527415	-28	26	060189016	-11.408153	-3458	-820
2	60	12	1494	0542	0542	0367	5977	536515	17.5	122	097288817	16308739	4541	074
3	60	12	1376	2348	4315	0401	11789	671286	40.7	241	21374018	23016649	6796	066
4	60	12	0986	4315	0301	0339	11915	593916	52.4	244	368801338	2530380	7510	069
5	70	12	0675	0301	0301	0239	8787	460944	55.0	179	038821037	2576800	7865	055
6	70	12	0421	0304	0034	0156	5229	257475	55.3	106	00811675	27581894	8100	069
7	80	12	0176	0039	0039	0050	2318	115485	58.6	47	01946568	2805738	8246	068
8	80	12	0100	0015	0015	0058	1103	61985	58.7	23	01468895	3047296	8929	1.39
9	90	12	0060	0032	0032	0084	0465	30376	52.7	10	073811872	28031066	8236	242
									Cumulative %88A1isd=	1000		Total gasage=	6888	054

nde; isotope beam sin mV; (fscd=released) error in age in d. u. s. J. error; all error 1 sigma  
 (36A through 40A are measured beam intensities; corrected for decay for the age calculation)

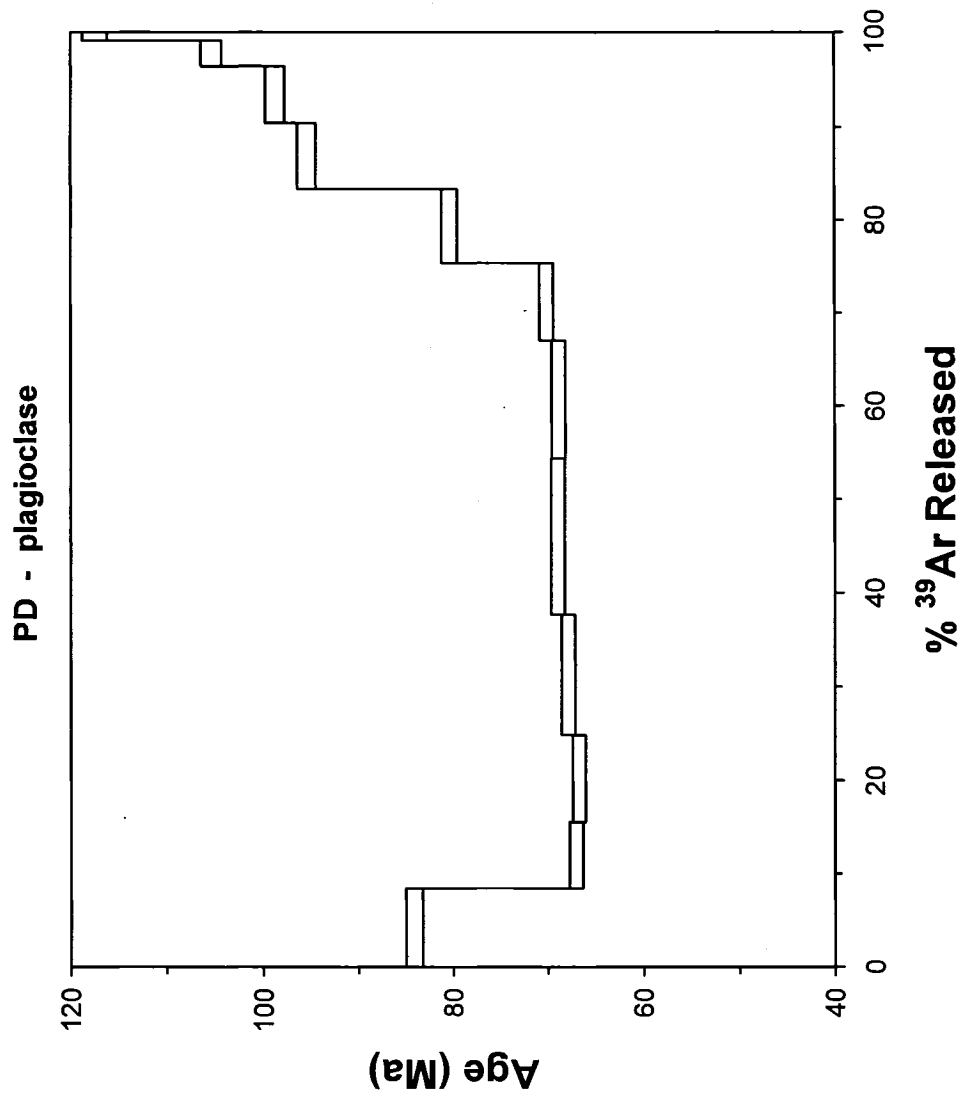


Thompson-CREG FD, plagioclase, 21.95 mg, J = 0.001688 ± 0.087%  
 4 amu discrimination = 1.0159 ± 0.26% 40Ar/39Ar = 0.0001 ± 100.0% 39Ar/40Ar = 0.000287 ± 3.63% 39Ar/40Ar = 0.00070 ± 0.63%

step	T (C)	t (min)	36Ar	37Ar	38Ar	39Ar	40Ar	%40Ar*	%39Ar/40Ar	CaK	40Ar/39ArK	Age (Ma)	1sd
1	660	12	3.387	36.009	1.738	61.866	2720.98	64.3	8.5	5.63019681	28.270565	84.10	0.89
2	730	12	2.242	33.782	1.158	51.502	1782.54	64.2	7.1	6.53837796	22.430909	67.05	0.71
3	810	12	1.280	28.573	1.066	67.604	1868.6	81.3	9.3	4.21006218	22.330719	66.75	0.69
4	880	12	1.676	31.280	1.527	92.750	2577.21	81.7	12.8	3.35528667	22.710778	67.87	0.70
5	960	12	1.512	33.437	1.863	121.115	3214.7	86.9	16.7	2.74880388	23.071986	68.93	0.71
6	1020	12	1.072	25.425	1.411	91.391	2402.93	87.6	12.6	2.77027071	23.048767	68.86	0.71
7	1080	12	1.003	14.457	1.031	60.799	1710.04	83.6	8.4	2.35726179	23.478770	70.12	0.72
8	1150	12	1.881	17.678	1.302	57.975	2103.96	74.5	8.0	3.03629701	26.973668	80.33	0.84
9	1220	12	1.688	18.174	1.263	51.166	2123.67	77.6	7.0	3.53748689	32.178542	95.42	0.99
10	1290	12	0.807	13.713	0.859	43.650	1682.52	86.7	6.0	3.12832884	33.319317	98.72	1.01
11	1360	12	0.523	14.891	0.457	19.351	833.597	84.0	2.7	7.67321127	36.624527	105.36	1.08
12	1400	12	0.329	13.432	0.202	6.807	360.275	78.4	0.9	19.7475233	39.680628	117.45	1.29
										Total gas age =		75.84	
										no plateau			
										no isochron			

Cumulative %39Ar/40Ar = 100.0  
 note: isotope beams in mV, 1sd = released, error in age includes 0.99%-J error, all errors 1 sigma  
 (38Ar through 40Ar are measured beam intensities, corrected for decay for the age calculations)

FD = Pedro Dobre



## Appendix E

### Geochemical Data

Drill hole geochemical data presented in this study is from data generated by Kinross U.S.A (Fairbanks Gold) and used by permission.

Geochemical samples in the 'True North Mine Geochemistry' database were collected by the author and analyzed in the same laboratories and by the same techniques as routine drill hole geochemical samples by Fairbanks Gold exploration and development geologic programs. Sample preparation, laboratories, and analytical packages (elemental data returned and analytical techniques) varied over the course of the exploration and development of True North.



Correlation matrix for Kinross multi-element drill-hole database

	Au	Ag	Cu	Pb	Zn	Mo	Ni	Co	Cd	Bi	As	Sb	Hg	Fe	Mn	Te	Ba
Au	1																
Ag	0.286422	1															
Cu	0.025343	0.330749	1														
Pb	0.143313	0.802185	0.188625	1													
Zn	0.050367	0.270058	0.335425	0.118894	1												
Mo	-0.0368	0.178354	0.280104	-0.0025	0.548987	1											
Ni	-0.04909	-0.02284	0.274015	-0.03344	0.21187	-0.00405	1										
Co	-0.0447	-0.11151	0.216913	-0.0447	-0.05671	-0.2579	0.8009	1									
Cd	0.311661	0.391936	0.131276	0.242781	0.211881	0.113349	-0.03331	-0.09545	1								
Bi	0.136557	0.698554	0.167715	0.797997	0.090556	-0.03132	-0.01717	-0.03147	0.205895	1							
As	0.800781	0.111655	0.043854	0.266795	0.036991	-0.04025	-0.06388	-0.11417	0.590282	0.272933	1						
Sb	0.108845	0.311418	0.038763	0.260202	0.068535	0.013736	-0.01974	-0.01369	0.145759	0.121869	0.183246	1					
Hg	0.415208	0.335478	0.174817	0.246716	0.291581	0.135966	0.007728	-0.07722	0.327238	0.170687	0.40001	0.085842	1				
Fe	0.070334	-0.00388	0.198917	0.033075	-0.01	-0.23863	0.58653	0.701869	0.040174	0.103247	0.097068	0.011268	0.06813	1			
Mn	0.050541	-0.03642	-0.07103	0.013975	-0.02895	-0.23425	0.323549	0.346965	0.055031	0.069933	0.106449	0.020122	0.05142	0.713786	1		
Te	-0.01427	0.064052	0.035716	-0.00383	0.194559	0.218913	0.061916	-0.0423	0.049071	0.002681	-0.0285	-0.00675	0.025534	-0.05092	-0.01275	1	
Ba	-0.11184	-0.02621	0.17905	-0.03103	0.05122	-0.00831	0.469065	0.489403	-0.10696	-0.01444	-0.21307	-0.04395	-0.10746	0.29773	0.104113	0.15384	1
Cr	-0.06315	-0.05065	0.211495	-0.00254	-0.0334	0.10932	0.475811	0.416061	-0.05874	-0.1527	-0.02641	-0.02641	-0.03432	0.157506	-0.04275	0.058269	0.376185
V	-0.08051	0.063937	0.317795	-0.01869	0.490731	0.380503	0.44508	0.314265	0.026347	0.007222	-0.15149	-0.02573	0.042638	0.201805	0.057308	0.417796	0.51367
W	0.486284	0.018694	-0.01522	-0.0014	-0.00891	-0.01758	0.008522	0.080016	0.05822	0.032232	0.067152	0.021759	0.0302	0.035118	0.013933	-0.00216	0.01863
La	-0.03188	-0.13638	-0.21314	-0.02211	-0.03173	-0.13693	0.063552	0.076435	-0.02492	-0.02444	0.013552	-0.01121	0.019412	0.45429	0.699131	-0.0103	0.06525
Al	-0.16106	-0.15408	0.163231	-0.06004	0.025772	-0.19468	0.402587	0.56418	-0.19081	-0.04436	-0.31622	-0.06715	-0.18259	0.364656	0.086618	0.009712	0.819936
Mg	0.00195	-0.01993	0.061456	-0.02203	-0.06979	-0.25921	0.500813	0.55841	-0.03284	0.043086	-0.02343	-0.00189	-0.104	0.583946	0.494234	0.006786	0.406262
Ca	0.040304	0.110742	-0.05385	0.006343	0.004555	-0.16225	0.351081	0.336623	0.044642	0.115626	0.072685	0.025504	-0.01708	0.417731	0.519062	0.010317	0.288014
Na	-0.11354	-0.14363	-0.04129	-0.04114	-0.08818	-0.1032	0.144539	0.24398	-0.14072	-0.05523	-0.20724	-0.04994	-0.15465	0.044786	-0.0777	0.057853	0.390311
K	-0.12042	-0.11018	0.127865	-0.04841	0.022011	-0.12116	0.100388	0.273276	-0.13827	-0.04444	-0.24059	-0.05519	-0.15468	0.087185	-0.07128	0.012172	0.54382
Sr	0.005418	-0.02011	-0.13485	-0.00037	-0.01651	-0.13928	0.241824	0.181491	0.041361	0.113372	0.047753	0.008825	-0.0028	0.558453	0.812026	0.028516	0.063988
Y	0.005564	0.062901	0.061291	0.01303	0.249416	0.0762	0.194147	0.090064	0.06304	0.101319	0.035673	0.016425	0.103993	0.510394	0.751145	0.077279	0.001559
Ga	-0.04714	-0.16562	-0.05541	-0.00754	0.044717	-0.10989	0.136251	0.163624	-0.11444	0.008159	-0.10241	-0.03724	0.006715	0.246988	0.192866	0.012531	0.154571
Li	-0.16457	-0.15326	0.12398	-0.05444	0.015196	-0.16991	0.431598	0.565965	-0.19598	-0.04767	-0.31819	-0.06375	-0.16867	0.326629	0.057729	0.016217	0.626886
Nb	-0.06796	0.080362	0.249483	-0.0066	0.398168	0.3465594	0.398369	0.252768	0.037414	0.014073	-0.12916	-0.02274	0.0822	0.222031	0.119428	0.452273	0.453959
Sc	0.007238	-0.0192	0.207829	-0.02986	-0.004164	-0.16707	0.549484	0.70942	-0.03703	-0.02363	-0.02486	0.030666	0.021015	0.583602	0.273306	-0.01309	0.293671
Ta	-0.0104	-0.00181	-0.02068	-0.00339	0.002513	0.017862	0.017076	0.006692	-0.00963	-0.01922	-0.0037	-0.01979	-0.019	-0.00397	-0.00715	-0.00397	-0.0126
Zr	-0.02371	0.004823	0.077544	-0.00052	0.24845	0.187867	-0.19028	-0.23588	-0.01904	-0.02114	-0.06482	-0.02749	0.058268	-0.20558	-0.06973	0.013014	-0.05057
S	0.140861	0.086845	0.076573	0.005821	0.072743	0.091258	0.027788	0.048918	0.230128	0.001491	0.153329	0.085448	0.032121	0.122494	0.058471	-0.01504	-0.11688
Ti	-0.03498	-0.05459	-0.02832	-0.01059	0.030931	-0.04177	-0.02039	0.033974	-0.04149	-0.02269	-0.07293	-0.01514	-0.0657	-0.01227	-0.03517	-0.01317	0.109396

	Cr	V	W	La	Al	Mg	Ca	Ni	K	Sr	Y	Ga	Li	Nb	Sc	Ta	Zr
Au																	
Ag																	
Cu																	
Pb																	
Zn																	
Mn																	
Ni																	
Co																	
Cd																	
Bi																	
As																	
Sb																	
Hg																	
Fe																	
Mn																	
Te																	
Ba																	
Cr	1																
V	0.329856	1															
W	-0.00846	-0.0151	1														
La	-0.14427	-0.10753	-0.00879	1													
Al	0.330061	0.426999	-0.01987	-0.10529	1												
Mg	0.171706	0.312454	0.009789	0.080047	0.512907	1											
Ca	-0.06567	0.210436	0.008461	0.127747	0.183904	0.608794	1										
Ni	0.214812	0.137738	-0.00441	-0.05475	0.418181	0.114425	-0.0231	1									
Na	0.185147	0.310652	-0.0151	-0.23201	0.788055	0.324954	0.126859	0.44848	1								
K	-0.08428	0.054483	-0.00336	0.894197	-0.01045	0.430433	0.518861	-0.02139	-0.13139	1							
Sr	-0.1597	0.187988	-0.00074	0.750276	-0.04541	0.259844	0.36476	-0.16937	0.765165	0.156866	1						
Y	0.143178	0.142778	-0.02086	0.225943	0.315578	0.194311	0.026155	0.21551	0.224271	0.178089	0.178089	1					
Ga	0.376923	0.415762	-0.02153	-0.13696	0.856876	0.500487	0.179809	0.494633	0.746375	-0.01364	-0.10223	0.30126	1				
Li	0.283352	0.860516	-0.01923	0.007335	0.324891	0.2535	0.165434	0.128915	0.205985	0.143478	0.241197	0.148257	0.332221	1			
Nb	0.284406	0.33006	0.028843	0.013811	0.360142	0.550545	0.358955	0.058545	0.137068	0.119995	0.062298	0.058637	0.380169	0.301565	1		
Sc	0.023525	0.00495	-0.00167	-0.00605	0.007173	0.008402	0.034351	0.038461	-0.00089	0.000977	0.003027	0.02163	0.041156	0.004799	0.004779	1	
Ta	-0.18726	0.02734	-0.0178	-0.04878	0.088189	-0.11526	-0.13837	0.158952	0.260003	-0.06056	0.034489	0.188806	0.047357	-0.02361	-0.21542	-0.0174	1
Zr	-0.0492	0.037358	0.073822	-0.07168	-0.05189	0.108614	0.143827	0.002554	-0.0275	0.06801	0.04857	-0.04408	-0.0098	0.028884	0.074852	0.023484	0.010867
S	-0.05338	0.081253	-0.00553	-0.06648	0.262058	0.073214	0.085543	0.346862	-0.01811	-0.04486	0.098211	0.263246	0.034254	0.004347	-0.01014	0.260232	
Ti																	

Cr (ppm) in logged lithologies in the True North drill hole geochemical data base

logged lithology	count	mean	max	min	average	Map unit
ARG	44	147.98	455	36		
PHY	27	101.70	294	39		
SLT	179	123.82	525	27		
MYL	33	129.21	303	36	128.80	Slate-Argillite
CBX	57	122.18	515	38		
CBXF	15	148.47	385	35		
CBXM	19	173.53	276	136		
ECLG	136	214.36	570	72	193.93	Eclogite
MGEC	27	91.04	213	58		
MBL	25	217.44	344	23		
MGMB	50	136.28	218	53	163.33	Marble
GBND	26	222.62	479	65		
GMSC	69	163.88	541	32	178.79	Quartz mica schist
GQSC	742	178.64	1426	15		
QZT	101	197.37	430	25	177.17	Quartzite
GQTZ	153	163.84	374	39		
MFSC	387	237.80	697	11	238.52	Biotite schist/ Amphibolite
MF	5	227.00	308	174		
AMPH	5	306.20	441	182		

True North Mine sample geochemistry														
Sample Number	WEI-21 Recvd Wt. kg	WEI-22 Dry Wt. kg	1449 Au-AA24		Au-AA13		Au-GRA22		ME-ICP41		ME-ICP41		ME-ICP41	
			Au ppm	Au ppm	oz/ton	Au ppm	Au ppm	Ag ppm	Al %	As ppm	B ppm	Ba ppm	Be ppm	
030703-1	4.8	4.7	0.243	0.1745	3	0.24	7530	10	70	<0.5				
050703-3	4	3.9	0.255	0.0133	1.9	0.13	69	<10	30	<0.5				
050703-4	2.7	2.7	0.0037		<0.2	0.03	811	<10	10	<0.5				
050703-5	2.9	2.8	0.0326	0.0184	1.2	0.37	3390	10	150	<0.5				
050703-6	0.6	0.6	0.0203	0.0135	0.6	0.27	1455	10	50	<0.5				
070703-3	4.2	4.2	0.0869	0.0623	0.2	0.12	6650	<10	40	<0.5				
090903-10	2.45		0.007	0.0002	<0.2	3.32	35	10	2710	1.4				
090903-7	1.63		2.24	0.0720	1.4	0.23	287	<10	120	<0.5				
090903-8	1.89		0.009	0.0003	<0.2	0.46	139	10	60	<0.5				
090903-9	1.51		0.963	0.0310	0.7	0.65	3620	10	240	0.8				
100903-1	2.29		0.256	0.0082	1.2	0.4	3110	10	140	<0.5				
100903-2	2.26		0.035	0.0011	0.6	0.51	1080	10	160	<0.5				
100903-3	2.61		1.36	0.0437	0.4	0.3	6460	10	90	<0.5				
100903-4	2.54		1.535	0.0494	1.8	0.64	8170	10	150	0.5				
100903-5	3.66		>10.0	0.9003	28	47.1	>10000	<10	90	<0.5				
100903-6	3.47		5.76	0.1852	1.3	0.49	>10000	10	90	0.6				
100903-7	2.52		1.37	0.0441	14.6	0.47	9970	10	50	0.5				
100903-8	3.33		1.77	0.0569	1.6	0.77	8120	10	150	0.7				
100903-9	3.12		>10.0	0.7621	23.7	1.2	>10000	10	90	0.9				
10703-1	1.6	1.6	0.0006		0.2	0.15	248	<10	30	<0.5				
10703-4	3.9	3.8	0.0972	0.0112	0.7	0.47	>10000	10	70	0.7				
10703-5	2.2	2.2	0.0007		<0.2	0.8	163	20	60	1				
10703-6	1.5	1.5	0.0002		<0.2	3.87	35	<10	880	1.4				
110703-1	2.4	2.3	0.0457	0.0338	1.4	0.08	257	<10	80	<0.5				
110703-11	1.1	1.1	0.189	0.1635	0.4	0.24	9410	<10	40	<0.5				
110703-3	2.4	2.3	0.0247	0.015	1.6	0.48	4730	10	180	<0.5				
110703-4	2.3	2.3	0.0335	0.0358	0.6	0.34	6730	10	60	<0.5				
110703-5	2.5	2.5	0.0065		1.2	0.43	1415	10	90	<0.5				
110703-6	2.1	2.1	0.0003		<0.2	1.5	40	10	70	1				
120803-3	2.1	2.1	0.0003		0.7	2.96	29	<10	960	1.2				
120803-4	3.1	3.1	0.0002		0.8	3.35	24	<10	510	1				
120803-6	2.5	2.5	0.0002		0.8	2.78	21	<10	700	1.1				
140903-1	4.12		0.023	0.0007	2	0.33	57	<10	630	<0.5				

Sample Number	ME-ICP41 Bi ppm	ME-ICP41 Ca %	ME-ICP41 Cd ppm	ME-ICP41 Co ppm	ME-ICP41 Cr ppm	ME-ICP41 Cu ppm	ME-ICP41 Fe %	ME-ICP41 Ga ppm	ME-ICP41 Hg ppm	ME-ICP41 K %	ME-ICP41 La ppm	ME-ICP41 Mg %
030703-1	<2	6.55	0.8	8	200	120	3.17	<10	<10	0.11	10	2.66
050703-3	<2	9.41	0.7	4	165	138	1.56	<10	<10	0.04	<10	2.2
050703-4	<2	2.86	<0.5	1	219	8	0.92	<10	<10	0.01	<10	1.05
050703-5	<2	5.59	0.5	5	182	97	2.49	<10	<10	0.17	10	2.14
050703-6	<2	4.86	<0.5	8	170	23	1.8	<10	<10	0.09	10	1.78
070703-3	<2	8.36	<0.5	3	84	8	2.34	<10	<10	0.05	<10	3.58
080903-10	<2	8.36	<0.5	38	269	59	6.71	20	<1	1.57	40	4.92
090903-7	<2	14	<0.5	9	39	300	2.71	10	1	0.1	<10	6.27
090903-8	<2	5.75	<0.5	33	89	69	5.67	10	<1	0.25	40	7.6
090903-9	<2	4.77	<0.5	47	69	170	6.83	10	<1	0.27	40	2.28
100903-1	<2	5.74	1.5	13	35	102	3.64	10	<1	0.29	20	2.25
100903-2	<2	3.35	1.2	12	34	78	2.73	<10	<1	0.29	20	1.18
100903-3	<2	0.62	<0.5	6	70	66	3.97	<10	<1	0.19	20	0.25
100903-4	2	7.57	2.2	12	41	144	3.78	<10	1	0.32	20	2.43
100903-5	136	4.17	70.2	7	32	846	10.35	<10	2	0.32	<10	0.94
100903-6	2	14	<0.5	5	14	58	4	<10	<1	0.24	10	5.64
100903-7	7	6.4	12	7	48	301	3.32	<10	<1	0.15	10	2.46
100903-8	<2	6.96	1	16	27	120	3.66	<10	<1	0.28	30	2.25
100903-9	<2	6.13	<0.5	41	99	71	6.37	<10	1	0.25	20	2.51
10703-1	<2	5.96	<0.5	5	137	16	1.37	<10	<10	0.06	10	1.7
10703-4	<2	13.45	<0.5	16	46	41	4.46	<10	<10	0.18	10	6.6
10703-5	<2	9.07	<0.5	32	142	81	4.44	<10	<10	0.23	30	4.76
10703-6	<2	6.88	<0.5	38	254	89	6.34	10	<10	1.05	40	4.04
110703-1	3	4.57	1.3	5	114	126	1.21	<10	<10	0.04	<10	1.64
110703-11	<2	1.3	<0.5	3	290	15	2.16	<10	<10	0.14	10	0.48
110703-3	<2	3.91	1.3	5	165	90	2.78	<10	<10	0.23	20	1.52
110703-4	<2	3.95	<0.5	15	76	45	3.93	<10	<10	0.19	20	1.35
110703-5	<2	4.96	0.5	11	166	88	3.21	<10	<10	0.19	20	1.44
110703-6	<2	5.64	<0.5	18	113	45	3.48	<10	<10	0.1	20	2.21
120803-3	<2	7.65	0.8	10	51	54	2.63	10	<10	0.5	10	1.45
120803-4	<2	8.99	0.5	10	72	35	2.9	10	<10	1.4	10	2.3
120803-6	<2	10.2	1.2	10	58	51	2.48	10	<10	0.55	10	1.6
140903-1	<2	0.1	<0.5	1	71	67	0.97	<10	<10	0.16	10	0.06

Sample Number	ME-ICP41 Mn ppm	ME-ICP41 Mo ppm	ME-ICP41 Na %	ME-ICP41 Ni ppm	ME-ICP41 P ppm	ME-ICP41 Pb ppm	Pb-AA46 Pb %	ME-ICP41 S %	ME-ICP41 Sb ppm	ME-ICP41 Sc ppm	ME-ICP41 Sr ppm	ME-ICP41 Ti %
030703-1	846	2	<0.01	36	1450	50		0.09	2840	3	281	<0.01
050703-3	885	<1	0.01	25	50	27		1.58	>10000	<1	230	<0.01
050703-4	225	2	<0.01	11	50	3		0.02	165	<1	73	<0.01
050703-5	603	2	<0.01	20	3160	96		0.36	302	3	275	<0.01
050703-6	463	2	<0.01	27	470	78		0.03	991	2	128	<0.01
070703-3	615	<1	<0.01	12	280	42		0.13	261	2	291	<0.01
090903-10	1340	<1	0.02	95	2060	15		0.18	116	28	443	0.24
090903-7	1165	<1	0.01	42	100	188		1.18	>10000	<1	777	<0.01
090903-8	995	<1	<0.01	154	1820	4		0.03	101	26	348	<0.01
090903-9	1095	1	<0.01	136	1620	65		0.24	638	22	321	<0.01
100903-1	657	9	<0.01	47	4480	76		0.2	198	2	174	<0.01
100903-2	513	7	0.01	47	4330	35		0.16	167	2	142	0.01
100903-3	964	2	<0.01	24	950	7		0.31	102	4	180	<0.01
100903-4	1025	8	0.01	57	7000	118		0.12	217	2	276	<0.01
100903-5	870	4	<0.01	13	430	>10000	1.58	2.11	3340	1	458	<0.01
100903-6	1390	1	<0.01	18	1750	63		0.39	271	4	422	<0.01
100903-7	945	3	<0.01	37	1640	8850		0.13	2190	4	278	<0.01
100903-8	767	5	<0.01	67	2530	21		0.11	151	6	237	<0.01
100903-9	1235	1	<0.01	152	1860	36		1.62	130	25	287	<0.01
10703-1	440	1	<0.01	25	400	3		0.02	25	5	202	<0.01
10703-4	1080	1	<0.01	52	1350	11		1.89	235	10	516	<0.01
10703-5	1155	<1	<0.01	128	2200	9		0.85	168	32	372	<0.01
10703-6	1375	<1	0.02	130	4140	9		0.13	62	24	322	0.22
110703-1	289	<1	0.01	27	200	15		0.34	>10000	<1	273	<0.01
110703-11	354	1	<0.01	16	220	2		0.1	138	2	102	<0.01
110703-3	399	2	<0.01	30	2480	19		0.29	771	4	169	<0.01
110703-4	738	3	<0.01	55	920	12		0.15	426	5	147	<0.01
110703-5	506	5	<0.01	37	3100	20		0.26	314	4	139	<0.01
110703-6	619	<1	0.02	57	1140	5		0.34	70	14	176	0.05
120803-3	387	7	0.05	65	410	9		0.04	15	5	118	0.12
120803-4	385	7	0.06	40	420	11		0.37	12	6	146	0.17
120803-6	615	8	0.01	46	380	9		0.04	15	6	110	0.14
140903-1	13	7	0.01	6	1240	6		0.01	3	1	13	0.01

Sample Number	ME-ICP41		ME-ICP41		ME-ICP41		ME-ICP41		ME-ICP41		ME-ICP41	
	Tl	ppm	U	ppm	V	ppm	W	ppm	Zn	ppm		
030703-1	<10	<10	<10	39	<10	<10	<10	81	H1300 drusy qtz xls			
050703-3	<10	<10	<10	4	<10	<10	<10	82	H1300 composite vn structure			
050703-4	<10	<10	<10	4	<10	<10	<10	6	H1300 FW below vn			
050703-5	<10	<10	<10	27	<10	<10	<10	40	H1300 HW unait amph?			
050703-6	<10	<10	<10	12	<10	<10	<10	37	H1300 qtz-amph bx			
070703-3	<10	<10	<10	11	<10	<10	<10	31	H1300 qv with graphite ox HW			
090903-10	<10	<10	10	242	<10	<10	<10	83				
090903-7	<10	<10	10	17	<10	<10	<10	38				
090903-8	<10	<10	10	46	<10	<10	<10	58				
090903-9	<10	<10	10	60	<10	<10	<10	91				
100903-1	<10	<10	10	29	<10	<10	<10	95				
100903-2	<10	<10	<10	29	<10	<10	<10	72				
100903-3	<10	<10	<10	13	<10	<10	<10	39				
100903-4	<10	<10	<10	54	<10	<10	<10	180				
100903-5	10	10	10	8	<10	<10	<10	820				
100903-6	<10	<10	<10	26	<10	<10	<10	162				
100903-7	<10	<10	10	34	<10	<10	<10	157				
100903-8	<10	<10	<10	33	<10	<10	<10	231				
100903-9	<10	<10	<10	82	<10	<10	<10	133				
10703-1	<10	<10	<10	20	<10	<10	<10	21				
10703-4	<10	<10	<10	39	<10	<10	<10	38				
10703-5	<10	<10	<10	82	<10	<10	<10	49				
10703-6	<10	<10	<10	222	<10	<10	<10	77				
110703-1	<10	<10	<10	6	<10	<10	<10	290				
110703-11	<10	<10	<10	6	<10	<10	<10	31				
110703-3	<10	<10	<10	31	<10	<10	<10	76				
110703-4	<10	<10	<10	11	<10	<10	<10	59				
110703-5	<10	<10	<10	29	<10	<10	<10	58				
110703-6	<10	<10	<10	99	<10	<10	<10	82				
120803-3	<10	<10	<10	65	<10	<10	<10	100				
120803-4	<10	<10	<10	102	<10	<10	<10	124				
120803-6	<10	<10	<10	73	<10	<10	<10	126				
140903-1	<10	<10	<10	18	<10	<10	<10	13				

True North Mine sample geochemistry													
Sample Number	WEI-21 Recvd Wt. kg	WEI-22 Dry Wt. kg	1449 Au-AA24		Au-AA13 Au oz/ton	Au-GRA22 Au ppm	ME-ICP41 Ag ppm	ME-ICP41 Al %	ME-ICP41 As ppm	ME-ICP41 B ppm	ME-ICP41 Ba ppm	ME-ICP41 Be ppm	ME-ICP41 Bi ppm
			Au ppm	LB									
160903-3	3.51				0.0023		1	0.32	345	<10	210	<0.5	
160903-4	2.74			0.084	0.0027		<0.2	1.4	744	10	110	0.7	
160903-8	2.63			0.005	0.0002		0.2	2.67	20	<10	940	<0.5	
180903-1	2.53			0.013	0.0004		1.1	0.86	19	<10	630	0.5	
180903-2	3.02			0.01	0.0003		0.4	2.74	54	<10	1140	0.5	
180903-3	2.81			0.03	0.0010		<0.2	2.36	60	<10	730	0.5	
220903-3	2.87			0.037	0.0012		<0.2	0.53	412	<10	80	<0.5	
220903-4	2.88			0.059	0.0019		<0.2	0.53	1550	10	150	<0.5	
230903-1	1.76			0.574	0.0185		1.2	0.19	2530	10	30	<0.5	
230903-12	1.15			<0.005			<0.2	0.47	427	<10	140	<0.5	
230903-4	2.38			<0.005			<0.2	0.11	21	<10	30	0.6	
230903-5	2.52			<0.005			<0.2	3.45	34	<10	160	2.1	
230903-6	2.65			<0.005			<0.2	1.08	65	<10	70	0.8	
230903-7	0.98			0.059	0.0019		<0.2	2.02	4410	<10	910	2.5	
230903-8	1.79			<0.005			<0.2	0.45	460	10	110	<0.5	
240903-1	2.96			0.008	0.0003		0.3	0.14	57	<10	20	<0.5	
250603-1	5.6	5.6		0.0002			1.1	0.27	255	10	190	<0.5	
250603-2	3.1	3		0.28	0.1355		8.9	0.59	2790	10	160	0.7	
250603-3	3.4	3.3		>0.292	0.389	0.577	3	0.59	3570	20	220	0.5	
250603-4	4	4		0.0098			2.1	0.54	1040	10	280	0.6	
250603-5	4.3	4.3		0.0007			1.1	0.23	227	10	160	<0.5	
250603-6	3.2	3.2		0.0003			1.3	0.29	188	10	420	<0.5	
250603-7	4.3	4.3		0.0003			1.5	0.23	293	10	310	<0.5	
250603-8	2.8	2.8		0.0004			0.8	0.25	230	10	250	<0.5	
250903-1	2.82			0.008			0.4	3.34	26	<10	410	1.1	
260603-1	2.8	2.7		0.0303	0.0206		0.6	0.19	>10000	10	40	<0.5	
260603-1	3.1	3.1		0.0005			0.4	0.12	71	<10	30	<0.5	
260603-11	1.8	1.7		0.0019			1.1	0.46	303	10	100	<0.5	
260603-2	2.9	2.8		0.18	0.1195		0.8	0.23	6920	10	200	<0.5	
260603-3	3.1	3.1		0.107	0.0804		0.9	0.16	7950	<10	30	<0.5	
260603-4	3.5	3.3		0.0006			2.1	0.35	174	10	60	<0.5	
260603-5	2.3	2.3		0.0107	0.0009		1.3	1.21	74	10	250	0.6	
260603-6	1.49			0.03	0.0010		<0.2	0.4	130	10	90	<0.5	



Sample Number	ME-ICP41 Bi ppm	ME-ICP41 Ca %	ME-ICP41 Cd ppm	ME-ICP41 Co ppm	ME-ICP41 Cr ppm	ME-ICP41 Cu ppm	ME-ICP41 Fe %	ME-ICP41 Ga ppm	ME-ICP41 Hg ppm	ME-ICP41 K %	ME-ICP41 La ppm	ME-ICP41 Mg %
160903-3	<2	0.15	0.5	2	51	34	1.54	<10	1	0.3	20	0.04
160903-4	<2	9.47	<0.5	34	196	42	5.29	10	<1	0.26	30	4.83
160903-8	<2	4.83	<0.5	16	106	60	3.59	10	<1	1.49	10	1.74
180903-1	<2	4.3	3.1	7	146	92	0.75	<10	<1	0.37	20	0.2
180903-2	<2	0.69	<0.5	7	63	79	3.33	10	<1	1.35	20	2.03
180903-3	<2	7.66	1.5	6	143	43	2.17	10	<1	1.16	20	1.55
220903-3	<2	0.12	<0.5	4	88	12	1.12	<10	<1	0.13	10	0.1
220903-4	<2	0.14	<0.5	17	25	45	3.97	<10	1	0.29	40	0.07
230903-1	<2	2.21	0.8	4	115	32	1.33	<10	<1	0.12	10	0.87
230903-12	<2	0.12	<0.5	15	32	34	2.96	<10	<1	0.3	40	0.04
230903-4	<2	2.88	<0.5	2	79	3	0.6	<10	<1	0.01	20	0.18
230903-5	<2	11.75	<0.5	15	52	7	6.92	20	1	0.04	40	5.55
230903-6	<2	>15.0	<0.5	20	69	34	5.71	10	<1	0.01	130	3.27
230903-7	<2	8.77	<0.5	36	118	41	11.8	10	1	0.15	280	1.53
230903-8	<2	0.22	<0.5	18	23	20	3.85	<10	<1	0.33	40	0.07
240903-1	<2	1.92	<0.5	2	129	12	0.77	<10	<1	0.08	10	0.58
250603-1	<2	3.78	20.1	2	250	75	0.95	<10		0.12	10	0.05
250603-2	<2	2.43	12.1	7	121	124	2.64	<10		0.21	10	0.08
250603-3	<2	2.77	13.9	11	207	75	2.93	<10		0.24	20	0.06
250603-4	<2	2.19	13.6	4	126	100	1.4	<10		0.16	10	0.04
250603-5	<2	2.22	4.7	2	237	41	0.79	<10		0.07	<10	0.02
250603-6	<2	2.23	7	2	352	61	0.86	<10		0.12	<10	0.03
250603-7	<2	2.63	10.5	1	388	39	0.85	<10		0.1	<10	0.03
250603-8	<2	1.71	12.1	2	352	61	0.85	<10		0.1	<10	0.02
250903-1	<2	1.32	<0.5	14	66	82	3.82	10	1	0.71	30	2.18
260603-1	<2	8.38	<0.5	6	197	28	3.09	<10		0.07	10	0.8
260603-1	<2	>15.0	5.7	3	17	18	0.79	<10		0.04	<10	0.15
260603-11	<2	3.12	4.3	12	120	125	3.62	<10		0.13	20	0.05
260603-2	<2	6.16	<0.5	8	239	38	1.61	<10		0.14	20	0.39
260603-3	<2	5.33	4.6	3	210	27	2.01	<10		0.07	<10	0.18
260603-4	<2	3.11	<0.5	1	103	21	2.25	<10		0.25	30	0.04
260603-5	<2	4.36	3.1	11	134	350	3.08	<10		0.31	30	0.26
260603-6	<2	0.07	<0.5	6	34	3	1.22	<10	<1	0.3	20	0.03

Sample Number	ME-ICP41 Min ppm	ME-ICP41 Mo ppm	ME-ICP41 Na %	ME-ICP41 Ni ppm	ME-ICP41 P ppm	ME-ICP41 Pb ppm	Pb-AA46 Pb %	ME-ICP41 S %	ME-ICP41 Sb ppm	ME-ICP41 Sc ppm	ME-ICP41 Sr ppm	ME-ICP41 Ti %
160903-3	54	10	0.01	12	3220	25		0.18	86	1	126	<0.01
160903-4	1280	2	<0.01	154	2220	2		0.11	125	30	522	<0.01
160903-8	546	3	0.03	63	1700	9		0.23	6	5	79	0.21
180903-1	83	4	0.01	40	>10000	18		<0.01	7	3	163	0.05
180903-2	253	2	0.02	34	1410	7		0.04	15	3	32	0.17
180903-3	291	3	0.02	91	7070	4		<0.01	8	4	110	0.13
220903-3	144	1	0.01	14	250	10		<0.01	124	1	10	<0.01
220903-4	336	1	0.01	42	340	6		0.01	671	5	15	<0.01
230903-1	247	1	<0.01	15	150	41		0.07	66	1	53	<0.01
230903-12	1750	1	0.03	15	300	2		<0.01	76	4	23	0.01
230903-4	300	<1	<0.01	13	2950	7		<0.01	9	1	456	0.03
230903-5	2220	<1	0.01	62	>10000	12		<0.01	2	4	2560	0.02
230903-6	2010	<1	0.01	93	>10000	13		0.12	51	5	3520	0.03
230903-7	7410	1	0.02	169	>10000	30		<0.01	948	17	1590	0.06
230903-8	1960	<1	0.03	20	780	3		<0.01	12	12	29	<0.01
240903-1	228	3	<0.01	11	1570	2		0.02	12	2	72	<0.01
250603-1	207	15	<0.01	65	2290	7		0.03	56	2	51	<0.01
250603-2	618	29	<0.01	104	2000	271		0.01	64	4	32	<0.01
250603-3	338	17	<0.01	81	370	16		0.02	31	3	12	<0.01
250603-4	149	45	<0.01	97	8750	29		0.02	39	3	67	<0.01
250603-5	117	14	<0.01	53	3520	11		0.02	19	1	65	<0.01
250603-6	169	8	<0.01	46	3690	8		0.01	29	2	34	<0.01
250603-7	220	5	<0.01	34	1880	9		<0.01	18	1	53	<0.01
250603-8	163	8	<0.01	48	4180	12		0.02	19	1	38	<0.01
250903-1	661	5	0.01	30	1440	6		0.04	14	6	31	0.05
260603-1	1425	3	<0.01	20	1320	24		0.03	57	4	188	<0.01
260603-1	638	2	<0.01	24	430	2		0.01	9	1	492	<0.01
260603-11	622	12	<0.01	85	2840	11		0.03	29	3	39	<0.01
260603-2	579	1	<0.01	47	1470	2		0.06	35	4	68	<0.01
260603-3	922	4	<0.01	23	600	92		0.06	39	2	51	<0.01
260603-4	17	3	0.01	10	5960	12		2.97	18	4	126	<0.01
260603-5	165	16	0.01	106	>10000	11		0.06	14	4	192	0.01
260603-6	461	1	0.02	7	230	3		<0.01	5	4	14	<0.01

Sample Number	ME-ICP41		ME-ICP41		ME-ICP41		ME-ICP41		ME-ICP41		ME-ICP41	
	Tl	ppm	U	ppm	V	ppm	W	ppm	Zn	ppm		
160903-3	<10	<10	45	<10	80	<10	<10	<10	80			
160903-4	<10	<10	87	<10	89	<10	<10	<10	89			
160903-8	<10	<10	90	<10	94	<10	<10	<10	94			
180903-1	<10	10	400	<10	114	<10	<10	<10	114			
180903-2	<10	<10	75	<10	104	<10	<10	<10	104			
180903-3	<10	<10	272	<10	317	<10	<10	<10	317			
220903-3	<10	<10	3	<10	16	<10	<10	<10	16			
220903-4	<10	<10	5	<10	73	<10	<10	<10	73			
230903-1	<10	<10	5	<10	63	<10	<10	<10	63			
230903-12	<10	<10	17	<10	56	<10	<10	<10	56			
230903-4	<10	<10	6	<10	13	<10	<10	<10	13			
230903-5	<10	<10	51	<10	158	<10	<10	<10	158			
230903-6	<10	<10	48	<10	100	<10	<10	<10	100			
230903-7	<10	<10	110	<10	230	<10	<10	<10	230			
230903-8	<10	<10	9	<10	59	<10	<10	<10	59			
240903-1	<10	<10	17	<10	16	<10	<10	<10	16			
250603-1	<10	<10	267	<10	264	<10	<10	<10	264			
250603-2	<10	<10	74	<10	656	<10	<10	<10	656			
250603-3	<10	<10	28	<10	393	<10	<10	<10	393			
250603-4	<10	<10	358	<10	389	<10	<10	<10	389			
250603-5	<10	<10	183	<10	169	<10	<10	<10	169			
250603-6	<10	<10	315	<10	187	<10	<10	<10	187			
250603-7	<10	<10	313	<10	136	<10	<10	<10	136			
250603-8	<10	<10	222	<10	190	<10	<10	<10	190			
250903-1	<10	<10	78	<10	76	<10	<10	<10	76			
260603-1	<10	<10	24	<10	38	<10	<10	<10	38			
260603-1	<10	<10	16	<10	185	<10	<10	<10	185			
260603-11	<10	<10	30	<10	584	<10	<10	<10	584			
260603-2	<10	<10	19	<10	27	<10	<10	<10	27			
260603-3	<10	<10	55	<10	103	<10	<10	<10	103			
260603-4	<10	<10	17	<10	47	<10	<10	<10	47			
260603-5	<10	<10	246	<10	376	<10	<10	<10	376			
260603-6	<10	<10	4	<10	18	<10	<10	<10	18			

True North Mine sample geochemistry															
Sample Number	WEI-21 Recvd Wt. kg	WEI-22 Dry Wt. kg	1449/Au-AA24		Au-AA13 Au oz/ton	Au-GRA22		ME-ICP41		ME-ICP41		ME-ICP41		ME-ICP41	
			LB	Au ppm		Au ppm	Ag ppm	Al %	As ppm	B ppm	Ba ppm	Be ppm			
260603-7	2.65			0.063	0.0020			<0.2	0.31	124	10	80	<0.5		
260603-8	1.6	1.6		<0.0001				0.5	0.89	8	<10	700	2.1		
260603-9	1	1		0.0001				<0.2	0.13	14	10	30	<0.5		
260903-1	2.56			<0.005				<0.2	1.24	11	<10	120	<0.5		
270803-5	3.35			1.565	0.0503			1.4	0.48	6610	10	150	0.9		
270903-2	2.41			<0.005				<0.2	0.79	11	<10	110	<0.5		
270903-3	1.6			<0.005				<0.2	0.48	12	10	60	<0.5		
270903-4	1.61			<0.005				<0.2	1.56	40	10	510	0.5		
270903-5	2.87			0.005	0.0002			0.6	0.39	487	10	270	<0.5		
300603-1	4.9	4.9		0.0868	0.0664			2.8	0.25	2200	10	40	<0.5		
GC-01	4.2		8.36	2280				0.0665	0.2	1.74	<10	380	1.5		
GC-02	5		9.02	145				0.0042	<2	1.8	<10	4400	1		
GC-03	2.9		4.84	10				<0.005	<2	0.75	<10	220	0.5		
GC-04	4.5		7.92	15				<0.005	<2	2.17	<10	90	0.5		
GC-05	5.6		10.78	<5				<0.005	<2	0.92	<10	260	<5		
GC-06	4.8		9.46	<5				<0.005	<2	1.93	<10	210	0.5		
GC-07	5		9.02	20				0.0006	<2	3.61	<10	1620	1.5		
GC-08	3.8		6.6	7730				0.2255	8.8	0.18	<10	140	<5		
GC-09	2.7		4.62	1405				0.041	1.6	0.22	<10	50	<5		
GC-10	3.8		6.38	2020				0.0589	15.2	0.14	10	40	<5		
GC-11	4		6.16	>10000	0.392			>2917	11.2	0.19	<10	210	<5		
GC-12	3.8		6.38	>10000	0.493			>2917	29.8	0.03	<10	20	<5		
GC-13	2.2		3.08	1425				0.0416	2.8	0.08	<10	10	<5		
GC-14	2.5		3.08	2760				0.0805	1.2	0.31	<10	60	0.5		
GC-15	2		3.52	180				0.0053	1	0.33	<10	180	<5		
GC-16	3.5		6.6	20				0.0006	0.8	0.26	<10	170	<5		
GC-17	4		5.5	5				<0.005	<2	0.47	<10	90	0.5		
GC-18	4.8		7.26	40				0.0012	1	0.31	<10	50	<5		

Sample Number	ME-ICP41 Bi ppm	ME-ICP41 Ca %	ME-ICP41 Cd ppm	ME-ICP41 Co ppm	ME-ICP41 Cr ppm	ME-ICP41 Cu ppm	ME-ICP41 Fe %	ME-ICP41 Ga ppm	ME-ICP41 Hg ppm	ME-ICP41 K %	ME-ICP41 La ppm	ME-ICP41 Mg %
260603-7	<2	0.08	<0.5	1	58	5	0.76	<10	1	0.2	20	0.03
260603-8	<2	>15.0	<0.5	16	49	8	5.62	10		0.41	170	3.8
260603-9	<2	0.11	<0.5	<1	259	4	0.52	<10		0.08	10	0.02
260903-1	<2	0.18	<0.5	5	36	22	2.08	<10	<1	0.33	20	0.51
270803-5	<2	5.26	8.3	6	98	77	1.84	<10	1	0.18	20	0.7
270903-2	<2	0.34	<0.5	11	34	31	3.66	<10	<1	0.25	40	0.2
270903-3	<2	0.18	<0.5	3	77	8	0.96	<10	<1	0.12	10	0.05
270903-4	<2	>15.0	<0.5	7	47	30	1.77	10	<1	0.63	30	0.92
270903-5	<2	3.31	9.8	1	162	38	0.73	<10	1	0.17	10	0.05
300603-1	<2	2.87	0.5	11	215	80	1.79	<10		0.11	10	0.88
GC-01	<2	7.58	2	65	238	66	7.34	<10	<1	0.19	30	2.58
GC-02	<2	11.75	0.5	58	132	64	6.1	<10	<1	0.23	30	1.15
GC-03	4	4.61	1.5	14	72	49	2.85	<10	<1	0.32	20	0.33
GC-04	<2	9.4	1	23	185	40	4.11	<10	<1	0.13	20	2.32
GC-05	4	1.3	<5	12	106	38	1.59	<10	<1	0.46	<10	0.49
GC-06	<2	4.76	<5	17	117	39	2.74	<10	1	0.56	30	1.1
GC-07	6	2.69	2	33	144	236	5.99	10	<1	1.05	30	2.8
GC-08	18	2.31	2.5	8	128	103	4.28	<10	<1	0.15	<10	0.41
GC-09	<2	0.33	1	6	110	73	1.72	<10	1	0.12	10	0.05
GC-10	2	0.4	1.5	3	242	91	1.24	<10	<1	0.1	<10	0.02
GC-11	24	1.65	2.5	9	67	124	5.06	<10	<1	0.16	10	0.25
GC-12	52	2.48	61	5	100	174	8.17	<10	<1	0.19	<10	0.17
GC-13	<2	10.75	0.5	19	26	61	2.04	<10	1	0.05	<10	3.48
GC-14	<2	12.9	2	17	45	66	5.06	<10	<1	0.15	<10	4.62
GC-15	2	2.66	0.5	29	86	66	3.41	<10	<1	0.19	10	0.97
GC-16	4	3.21	11.5	6	119	73	1.29	<10	1	0.16	<10	0.52
GC-17	<2	8.73	1	45	108	119	4.68	<10	<1	0.22	10	6.28
GC-18	<2	12.9	0.5	17	86	104	3.36	<10	<1	0.18	<10	5.31

Sample Number	ME-ICP41 Mn ppm	ME-ICP41 Mo ppm	ME-ICP41 Na %	ME-ICP41 Ni ppm	ME-ICP41 P ppm	ME-ICP41 Pb ppm	Pb-AA46 Pb %	ME-ICP41 S %	ME-ICP41 Sb ppm	ME-ICP41 Sc ppm	ME-ICP41 Sr ppm	ME-ICP41 Tl %
260603-7	37	1	<0.01	5	150	10		0.03	9	1	32	<0.01
260603-8	3110	<1	0.01	55	>10000	17		0.01	3	7	3650	0.04
260603-9	42	1	<0.01	9	160	11		0.01	5	<1	19	<0.01
260903-1	100	1	0.02	15	570	6		0.01	10	2	20	0.02
270803-5	819	5	<0.01	48	4240	30		0.02	40	3	162	<0.01
270903-2	216	1	0.01	33	300	5		<0.01	<2	3	24	<0.01
270903-3	89	1	<0.01	10	210	6		<0.01	3	1	12	<0.01
270903-4	647	2	0.01	24	1150	11		0.01	10	5	251	0.05
270903-5	178	8	<0.01	25	6340	4		0.02	11	2	47	<0.01
300603-1	305	2	0.01	80	1750	<2		1.12	>10000	1	178	<0.01
GC-01	1070	<1	<0.01	422	3270	8		0.02	2010	22	212	<0.01
GC-02	1445	1	0.01	207	4390	10		0.01	858	16	166	0.01
GC-03	370	5	<0.01	69	5020	10		0.01	1115	3	86	0.01
GC-04	805	1	<0.01	124	1830	12		0.01	654	10	237	<0.01
GC-05	245	2	0.01	27	1050	6		<0.01	438	1	33	0.05
GC-06	495	2	0.01	43	1170	16		<0.01	16	4	158	0.05
GC-07	545	1	0.01	166	4390	14		0.18	18	11	171	0.16
GC-08	730	4	0.01	45	810	172		0.17	>10000	3	253	<0.01
GC-09	265	1	<0.01	20	200	122		<0.01	166	1	38	<0.01
GC-10	115	6	0.01	20	90	606		0.03	4630	1	50	<0.01
GC-11	640	1	<0.01	40	970	384		0.14	256	5	192	<0.01
GC-12	330	4	<0.01	17	240	5760		1.64	3400	<1	425	<0.01
GC-13	785	<1	0.01	88	320	12		3.53	>10000	<1	366	<0.01
GC-14	1035	<1	<0.01	55	1940	26		0.83	1080	11	536	<0.01
GC-15	315	12	<0.01	122	1100	42		0.09	184	2	78	<0.01
GC-16	130	18	<0.01	70	5970	6		0.16	142	3	65	<0.01
GC-17	1040	<1	<0.01	186	2080	6		0.24	84	32	362	<0.01
GC-18	1135	<1	<0.01	64	1910	2		0.12	130	29	724	<0.01

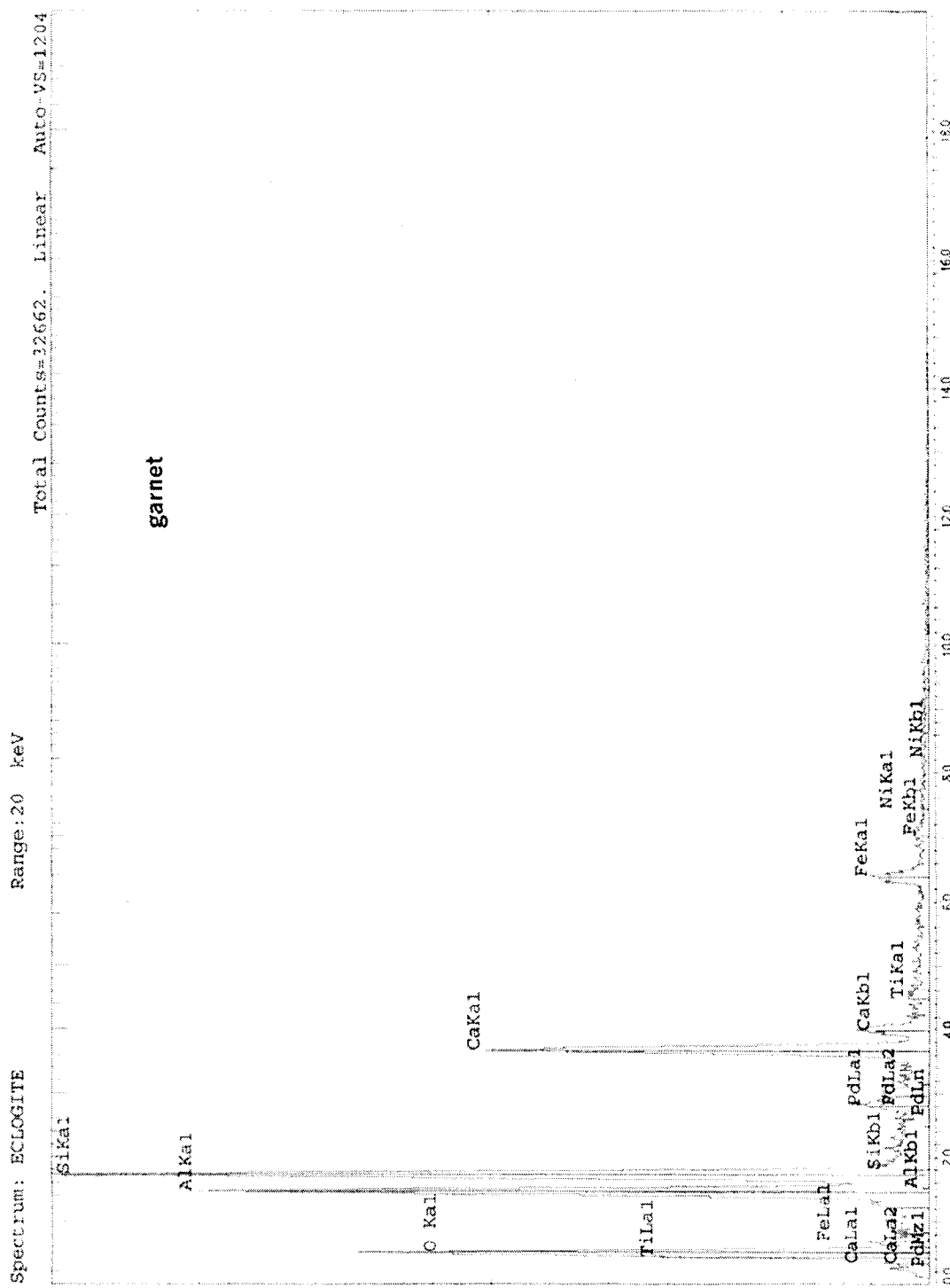
	ME-ICP41	ME-ICP41	ME-ICP41	ME-ICP41	ME-ICP41	ME-ICP41	ME-ICP41	ME-ICP41
Sample Number	Ti ppm	U ppm	V ppm	W ppm	Zn ppm			
260603-7	<10	<10	3	<10	10			
260603-8	<10	<10	49	<10	103			
260603-9	<10	<10	1	<10	3			
260903-1	<10	<10	9	<10	52			
270803-5	<10	<10	164	<10	288			
270903-2	<10	<10	8	<10	67			
270903-3	<10	<10	3	<10	12			
270903-4	<10	<10	42	<10	68			
270903-5	<10	<10	241	<10	112			
300603-1	<10	<10	28	<10	97			
GC-01	<10	<10	112	<10	140			1460E fault HW deep red/brown
GC-02	<10	<10	65	<10	76			1460E fault Hw yellow ox
GC-03	<10	<10	93	<10	134			1460E fault fault plane graphite-FeOx
GC-04	<10	<10	70	<10	92			1460E calcite veins
GC-05	<10	<10	35	<10	36			1460E quartz vein
GC-06	<10	<10	49	<10	74			1460E FW mica schist bx
GC-07	<10	<10	135	<10	312			1460E FW wk-rmd FeOx + graphite
GC-08	<10	<10	11	<10	186			1360N Composite below
GC-09	<10	<10	4	<10	70			1360N FW only
GC-10	<10	<10	5	<10	68			1360N Vein
GC-11	<10	<10	12	<10	122			1360N HW deep red
GC-12	<10	<10	7	<10	1875			1360 quartz vein open space filling
GC-13	<10	<10	19	<10	242			1340NE vein
GC-14	<10	<10	37	<10	96			1340NE HW
GC-15	<10	<10	17	<10	148			1340NE FW
GC-16	<10	<10	201	<10	326			1340NE unaltered mafic schist
GC-17	<10	<10	74	<10	68			1340NE Listwanite
GC-18	<10	<10	49	<10	24			1340NE strong oxidation

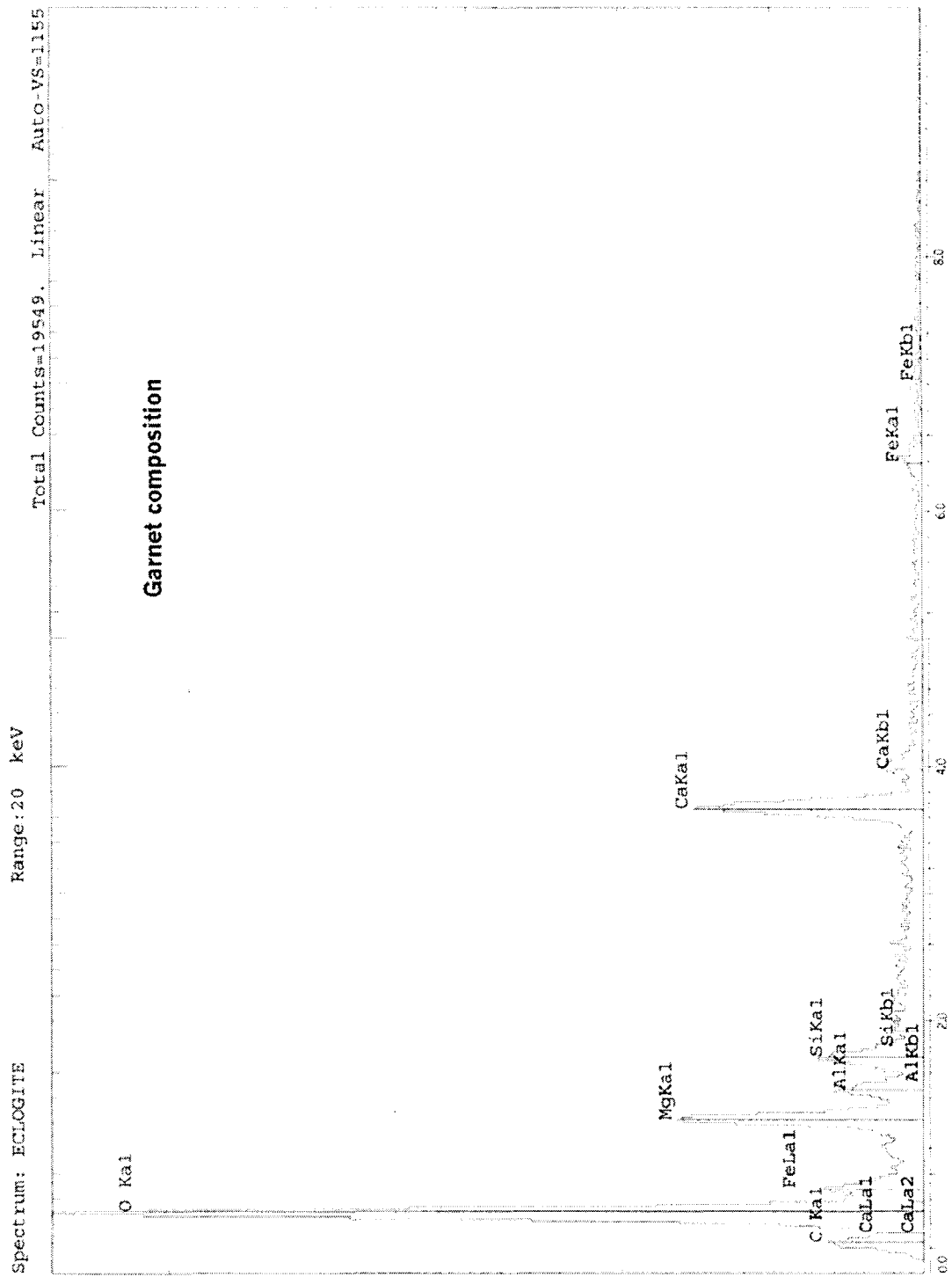
## Appendix F

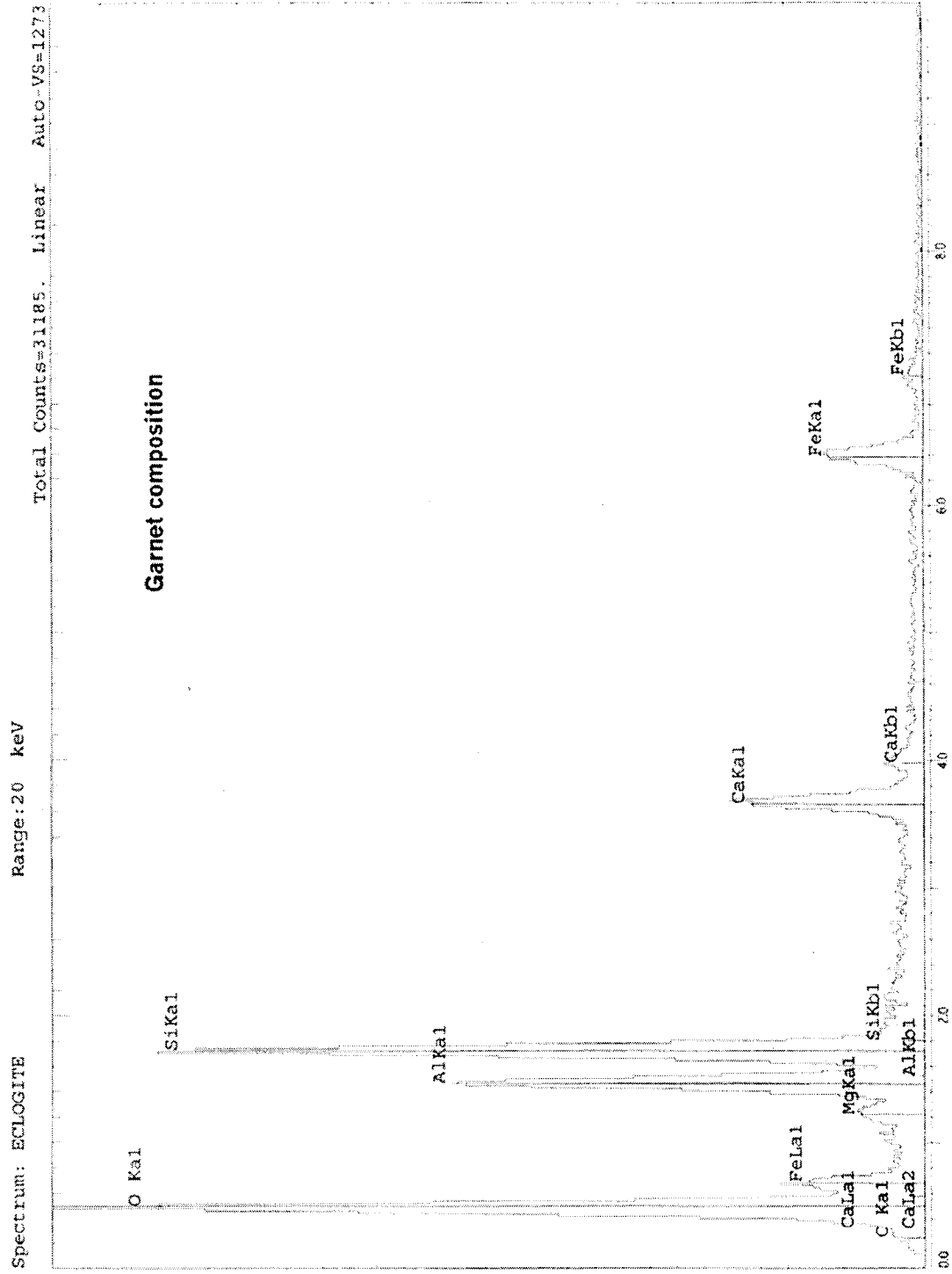
### SEM EDX Data

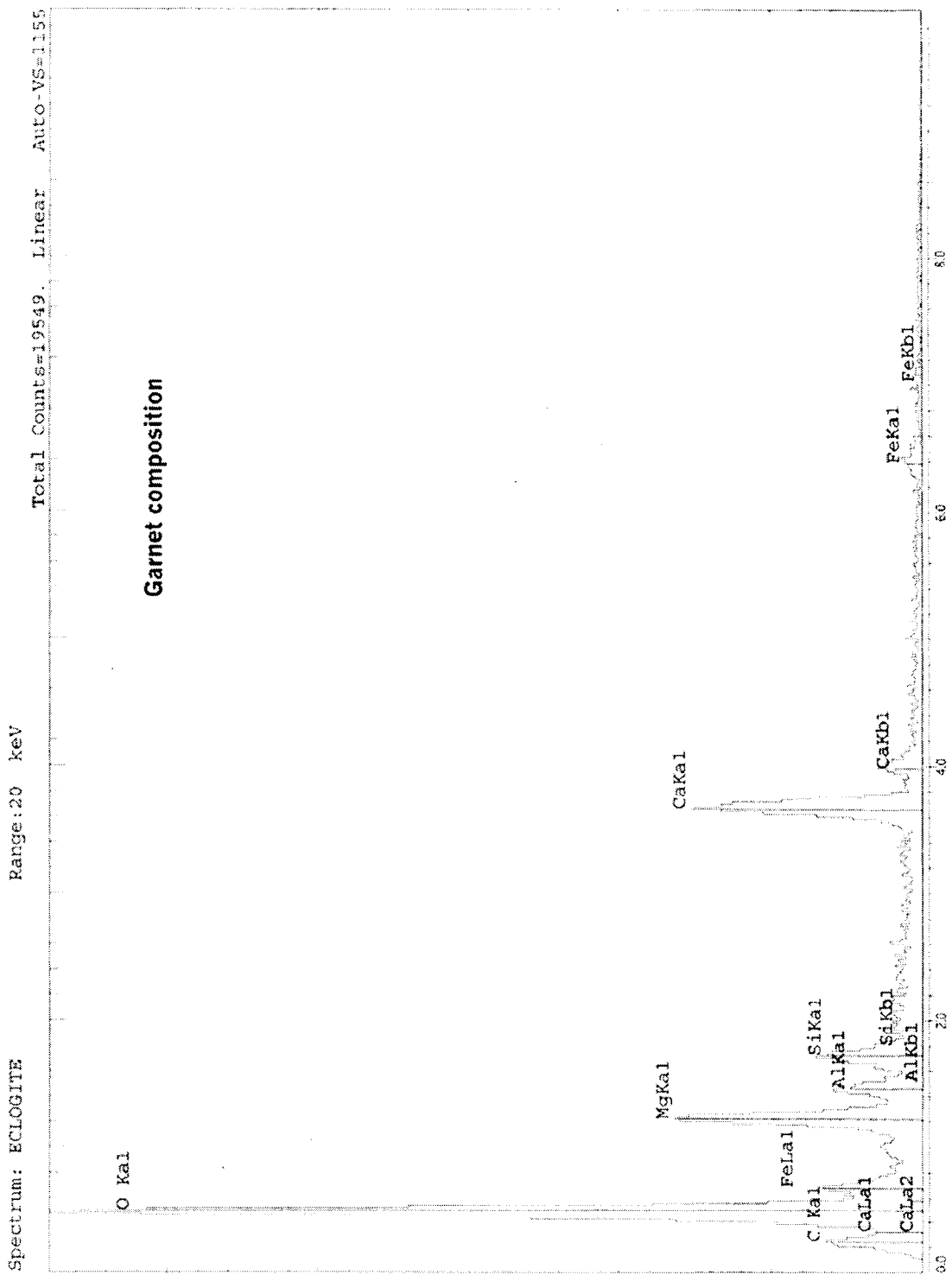
SEM/EDX data was collected with a Jeol JSM 840A SEM equipped with EDX system. The system was operated by Dr. John McCormack, Director of the UNR Electron Microbeam Facility.

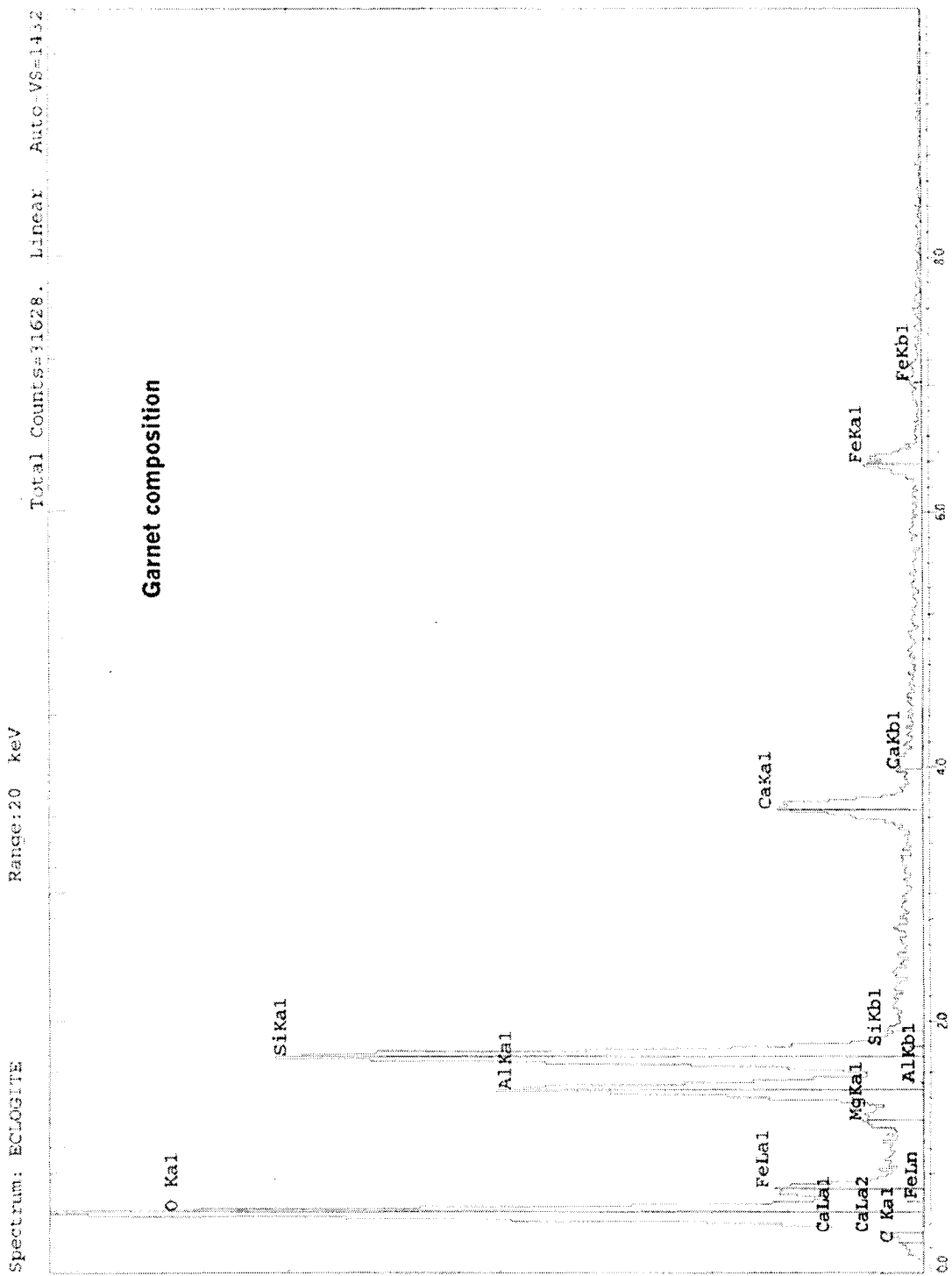


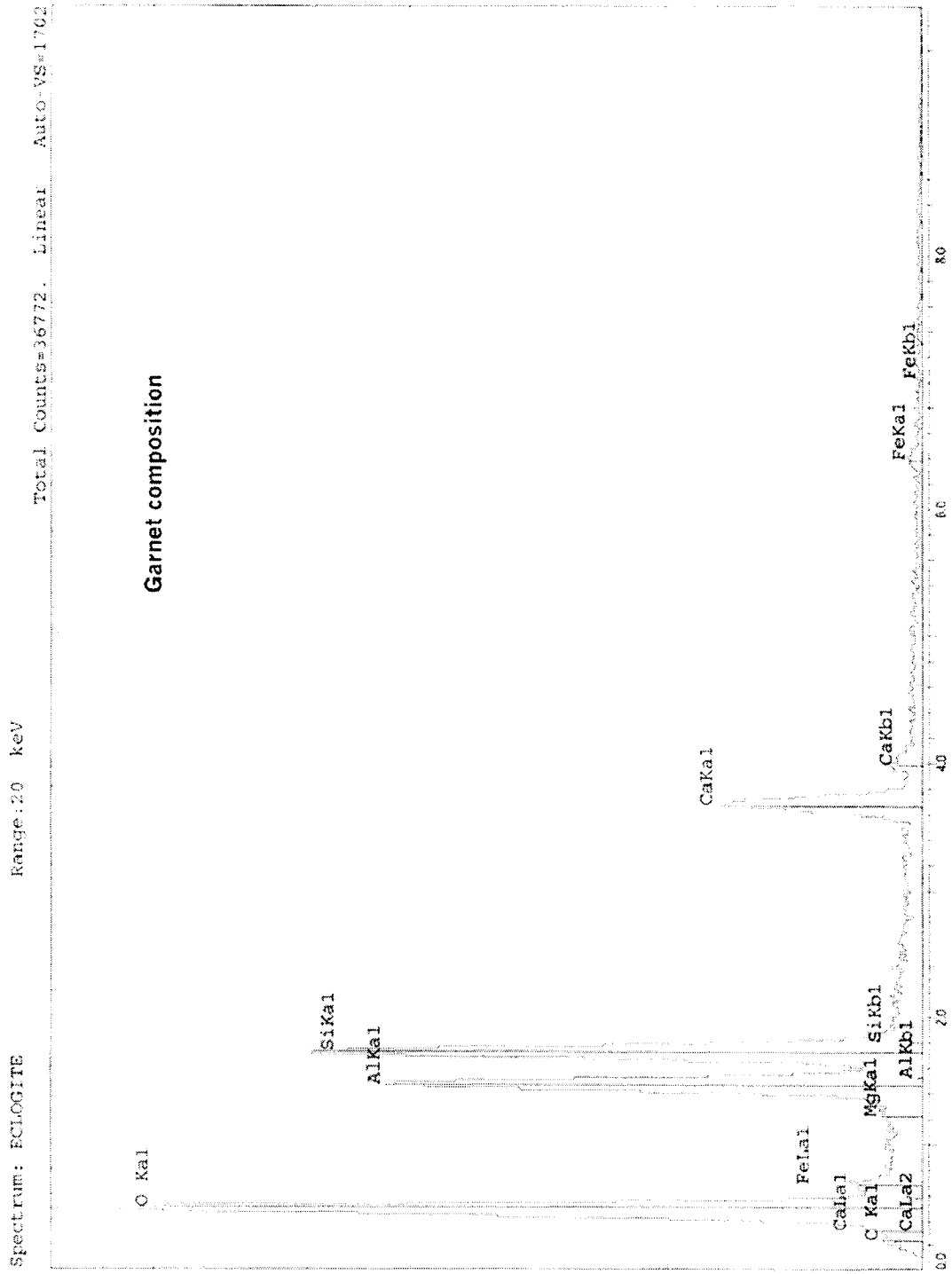


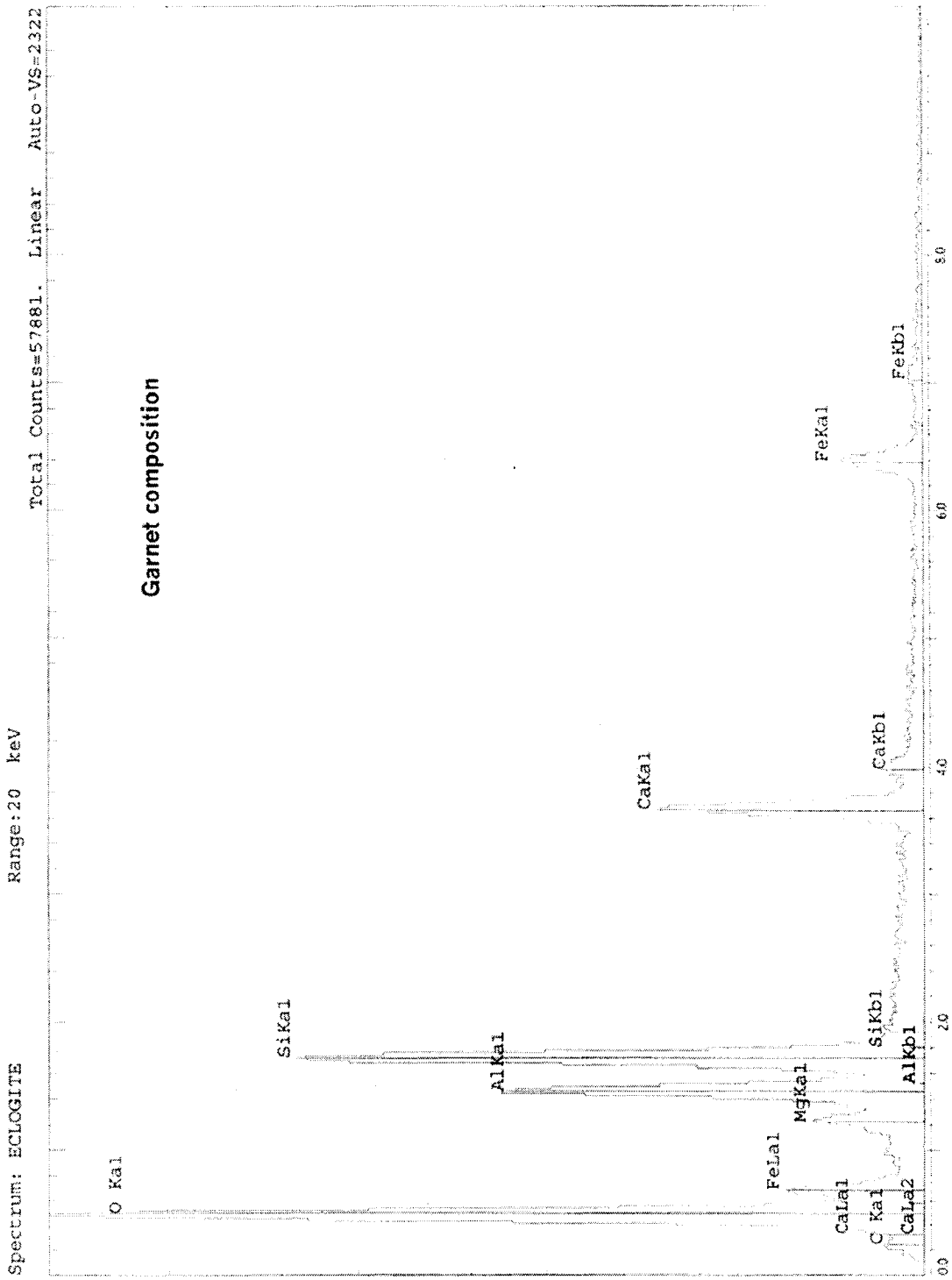


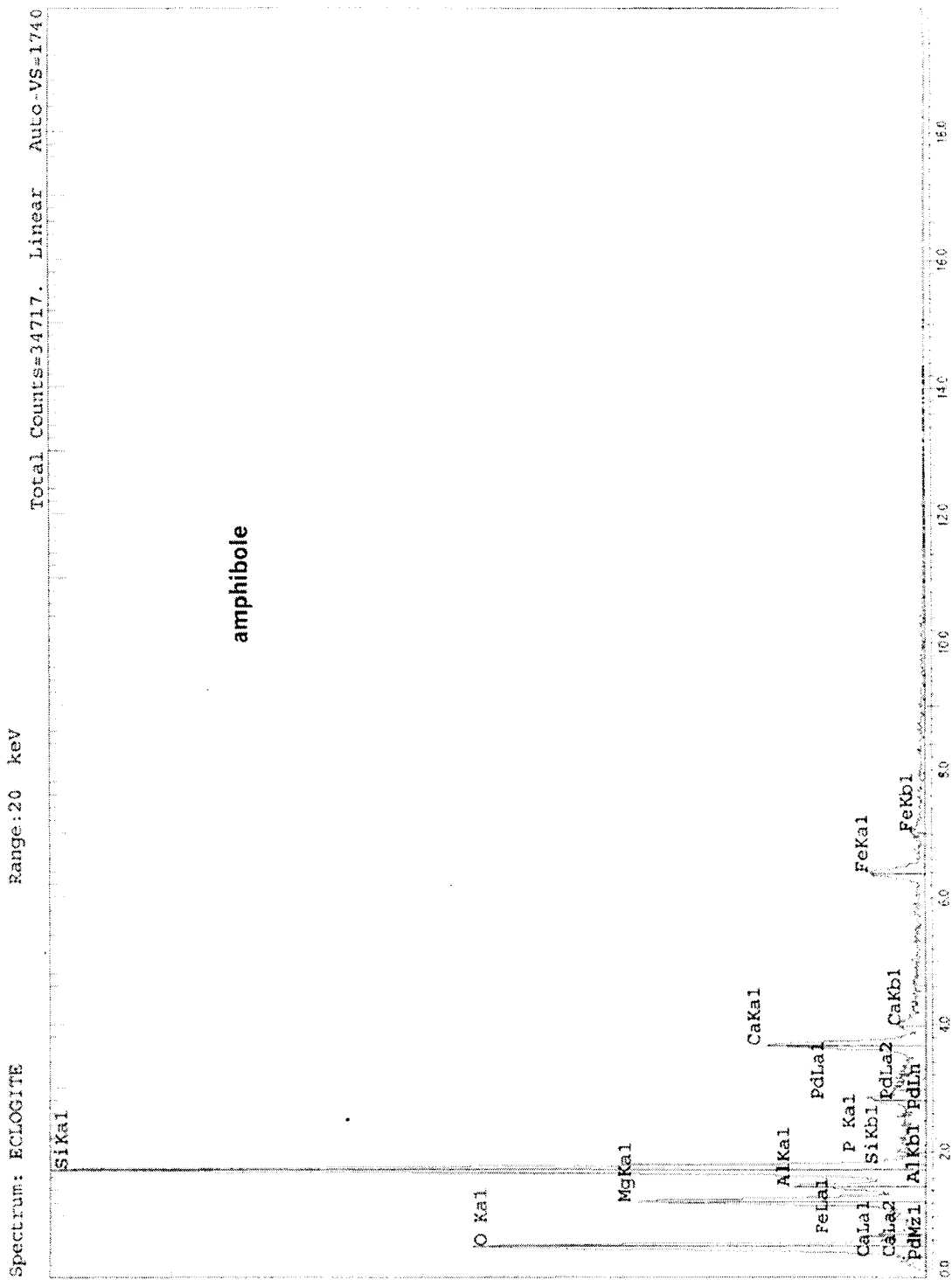




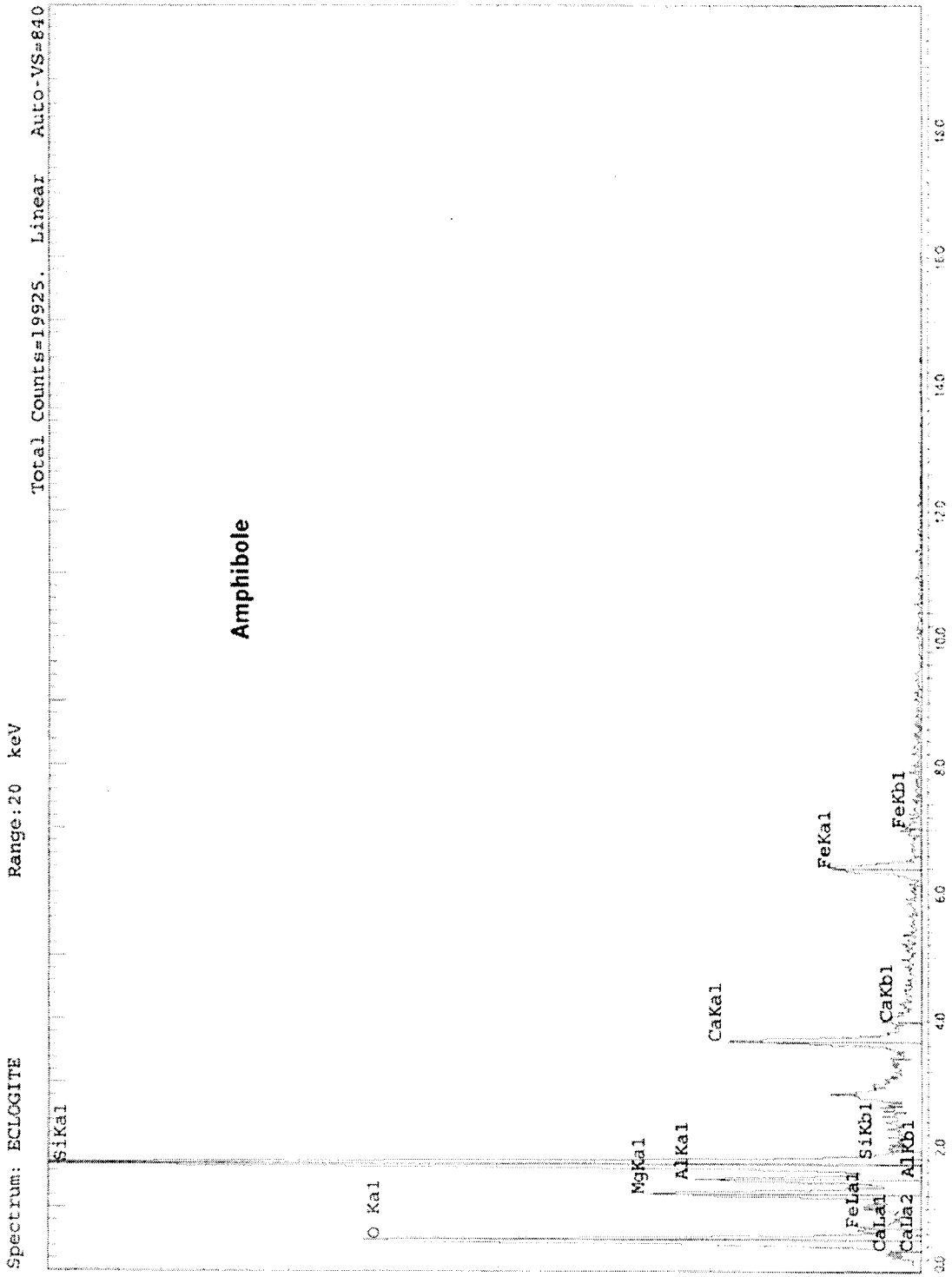


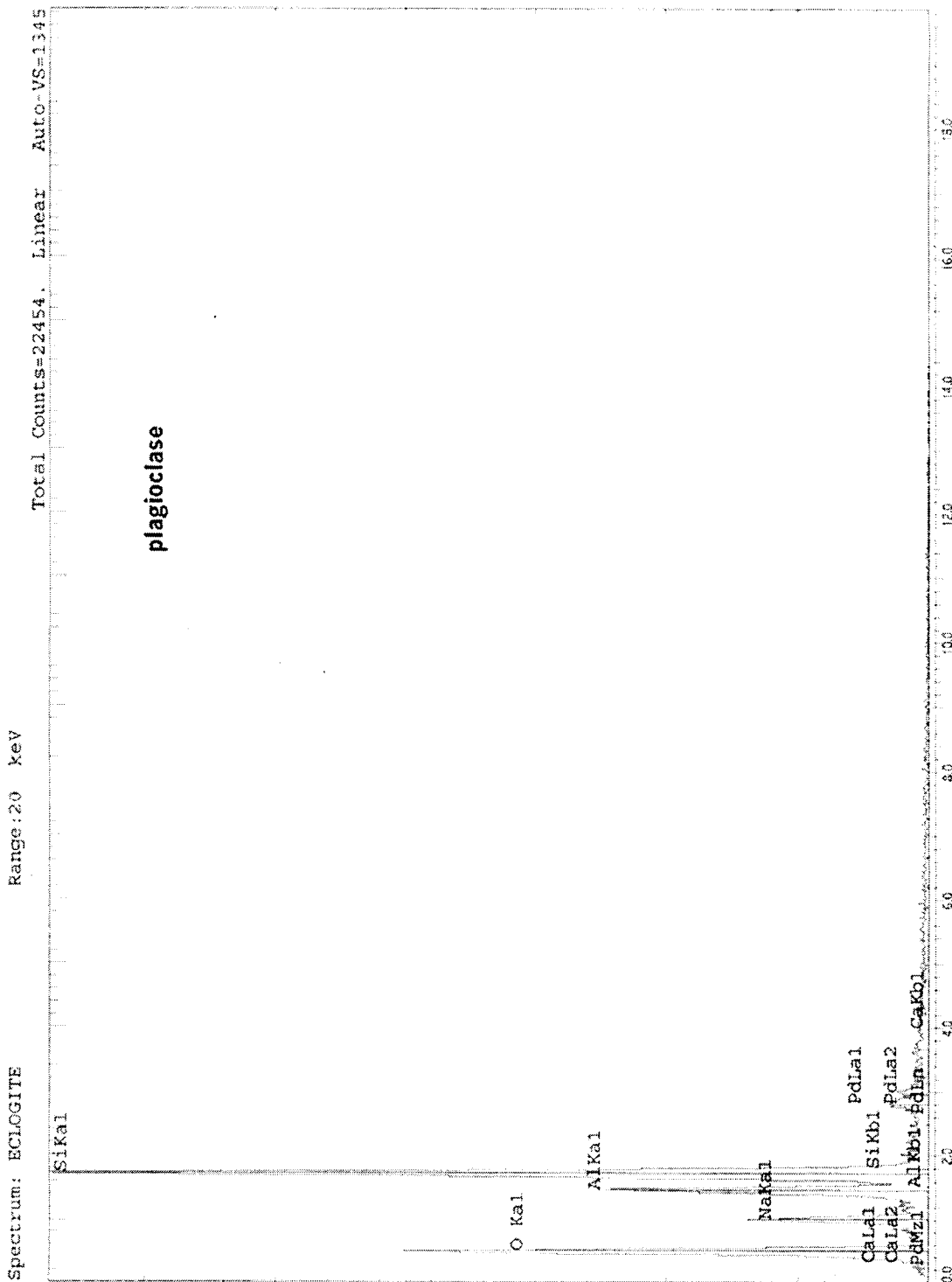


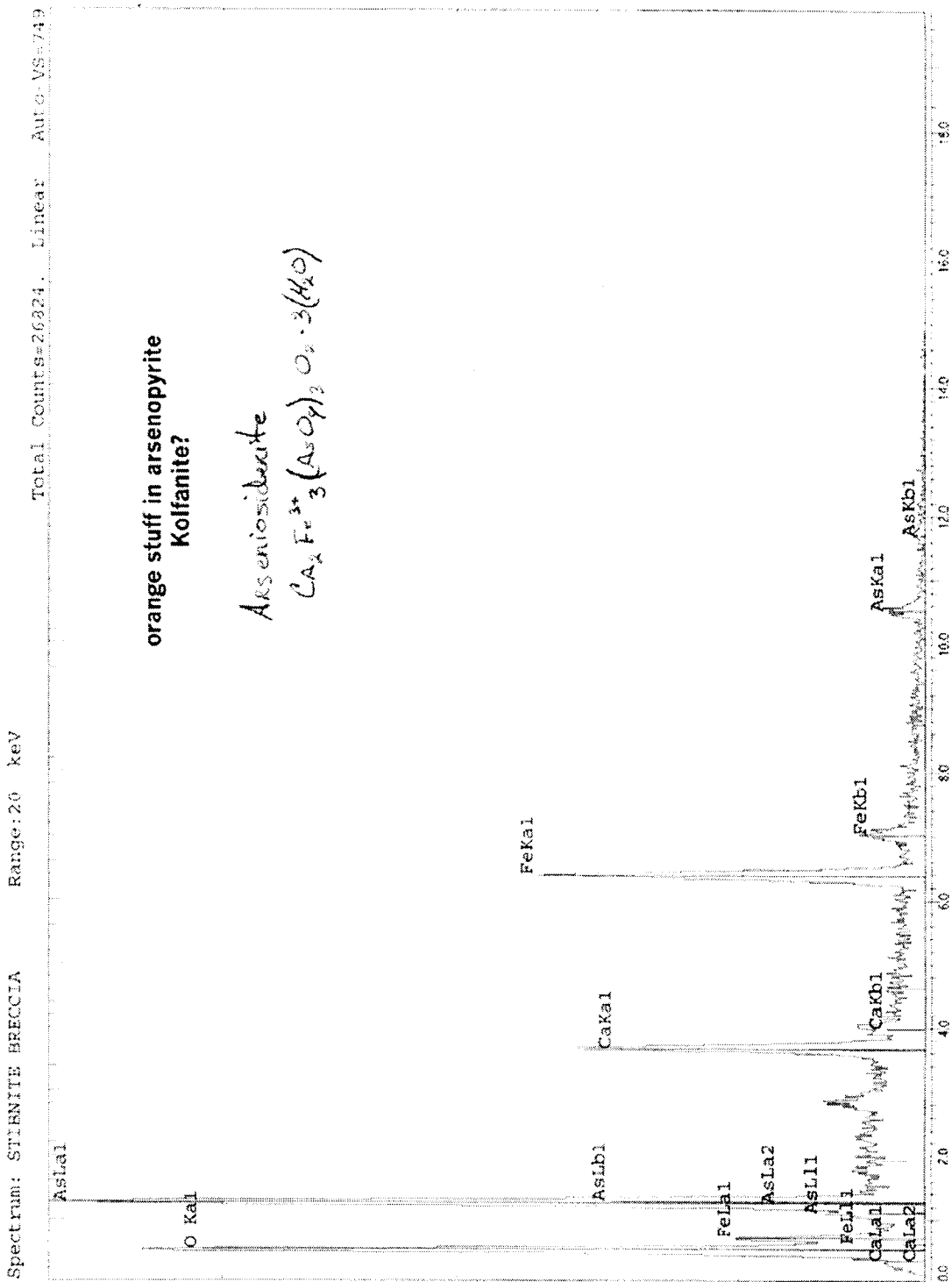


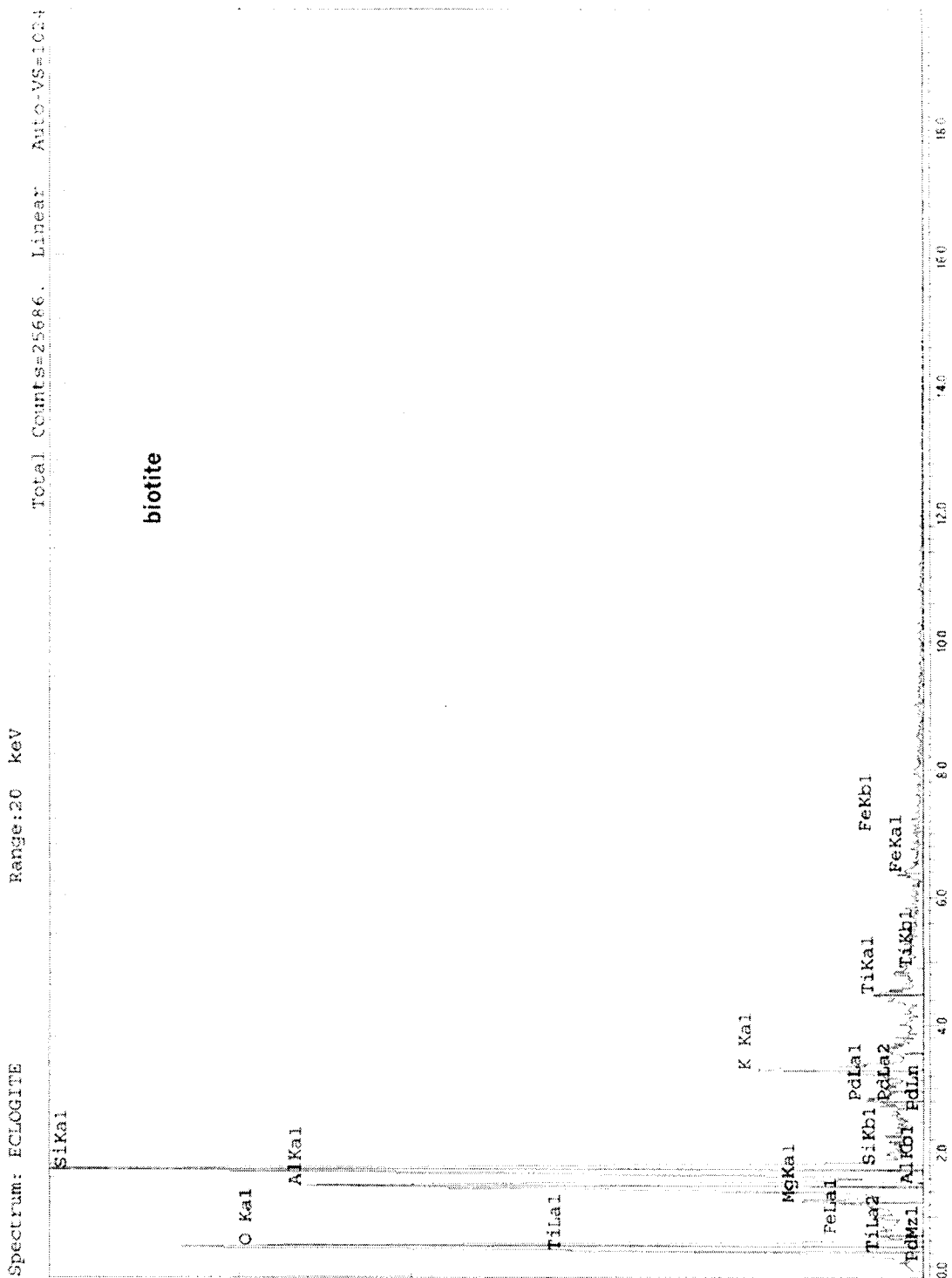


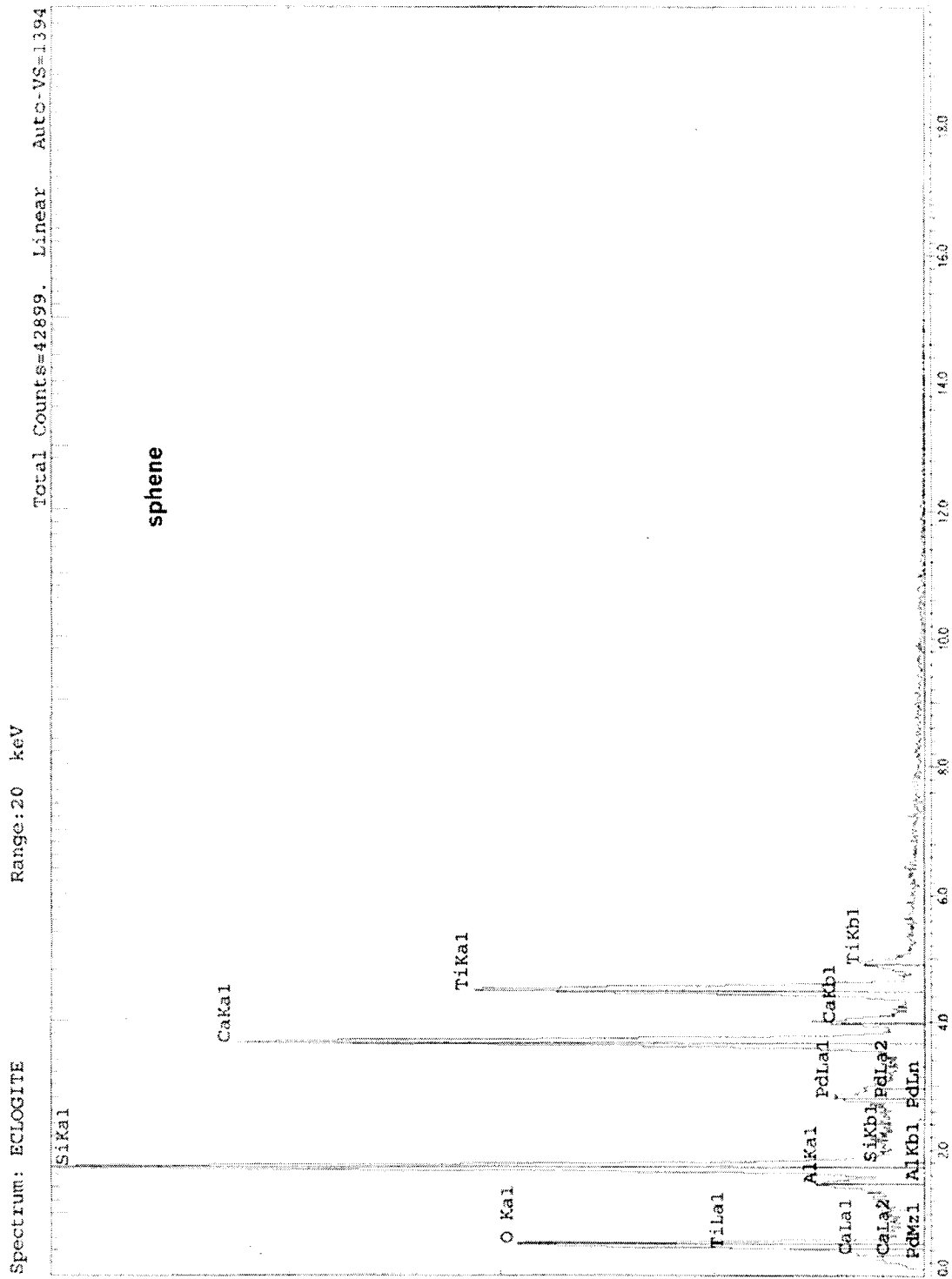


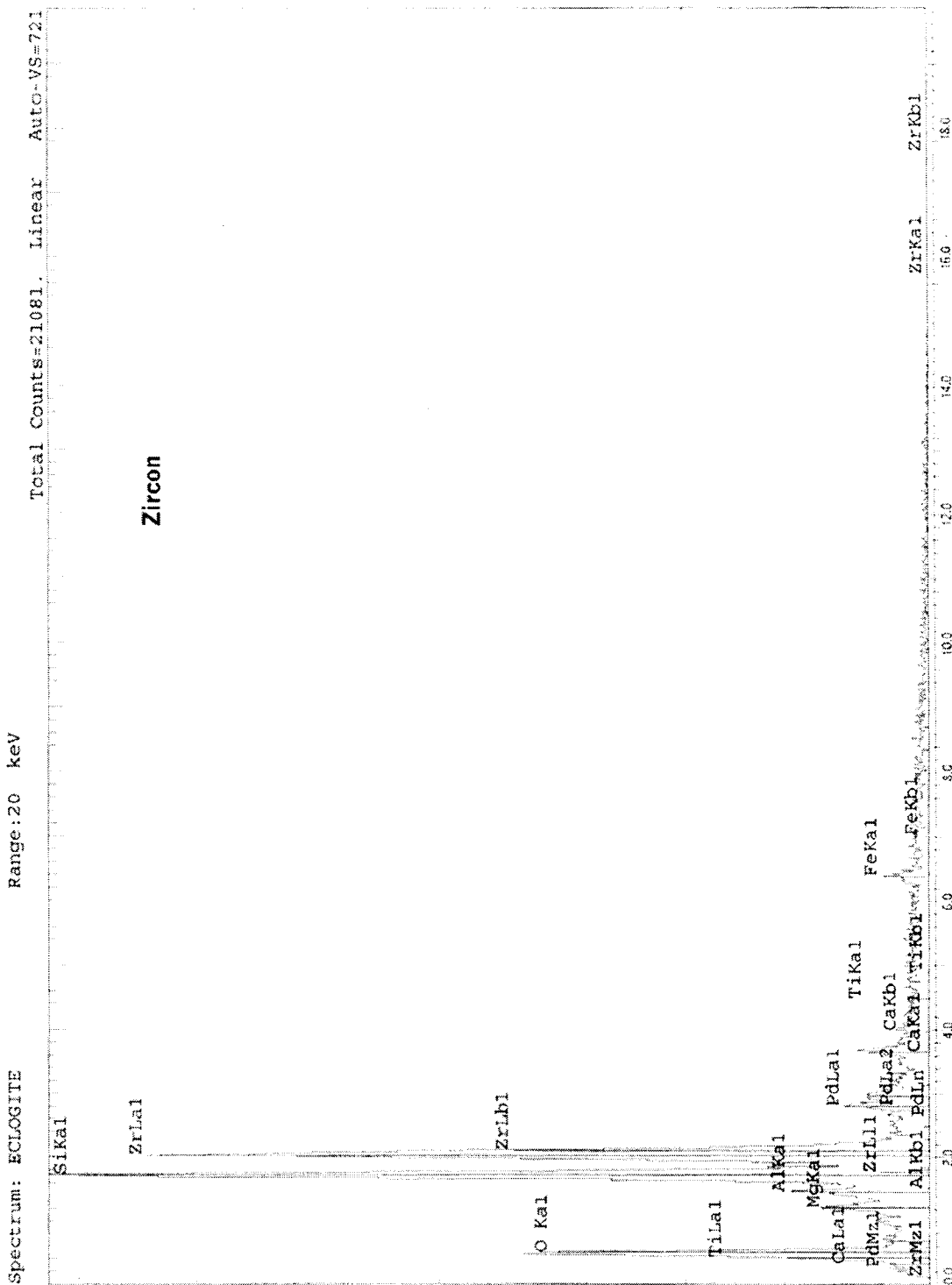


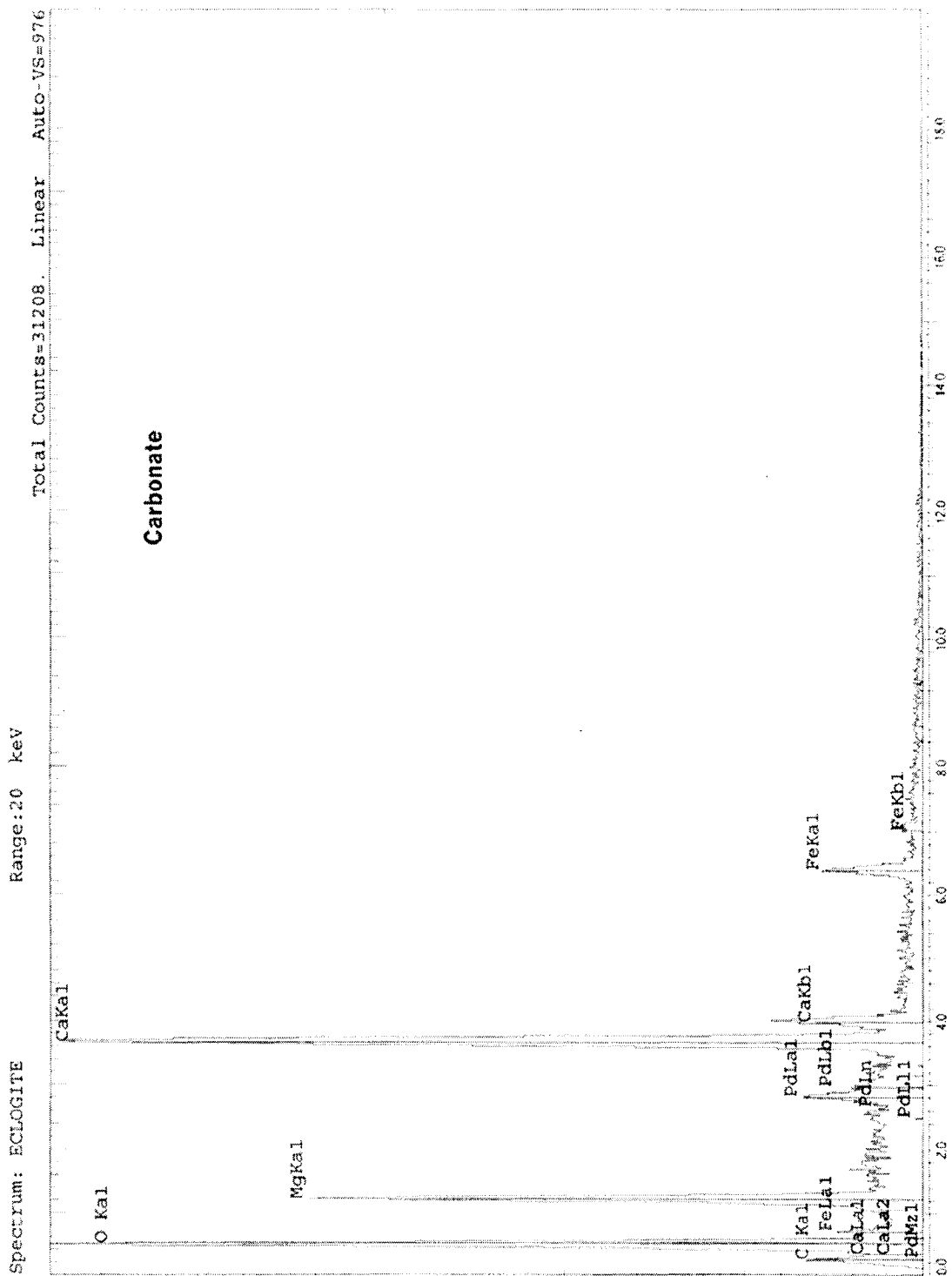


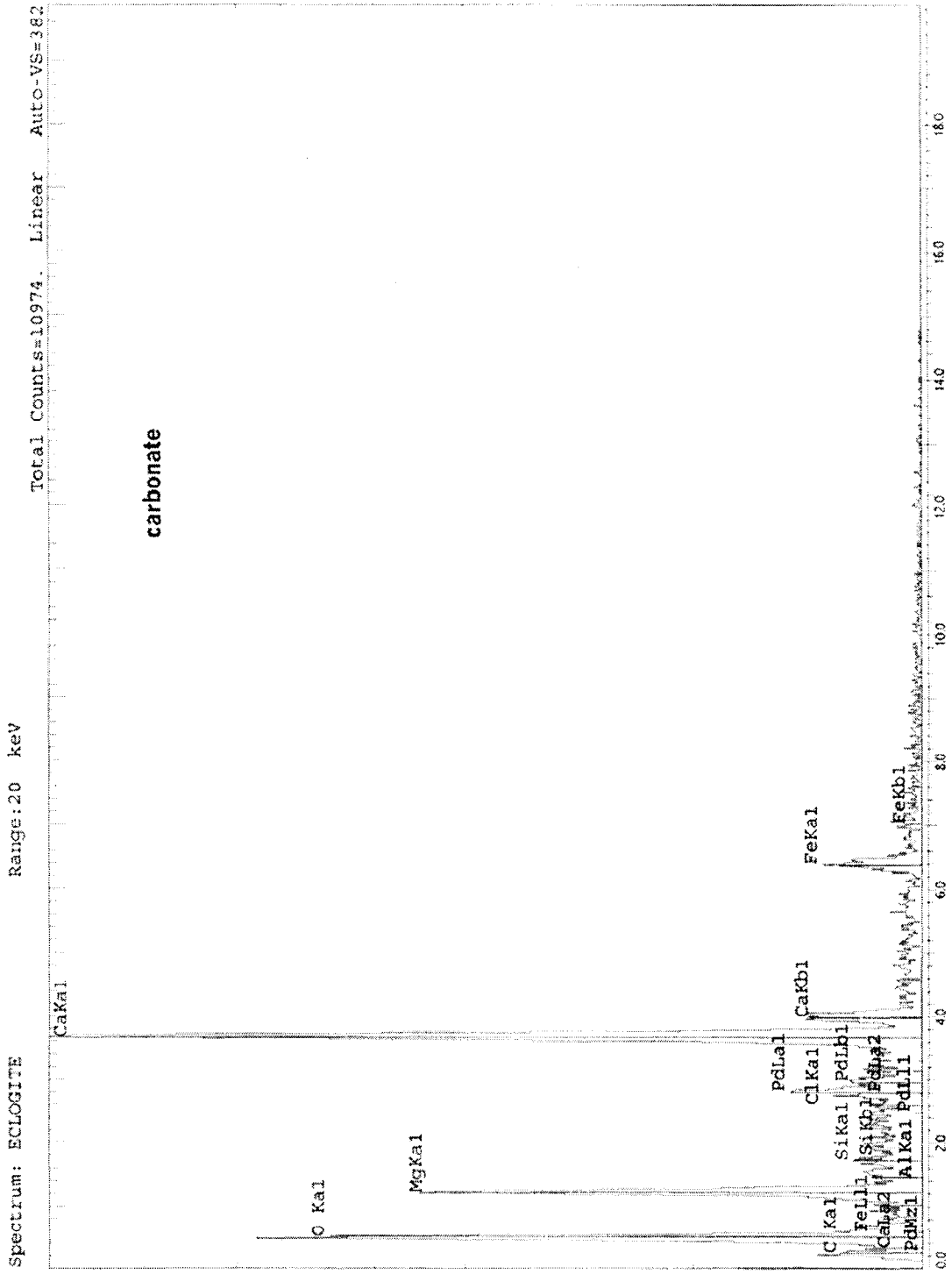




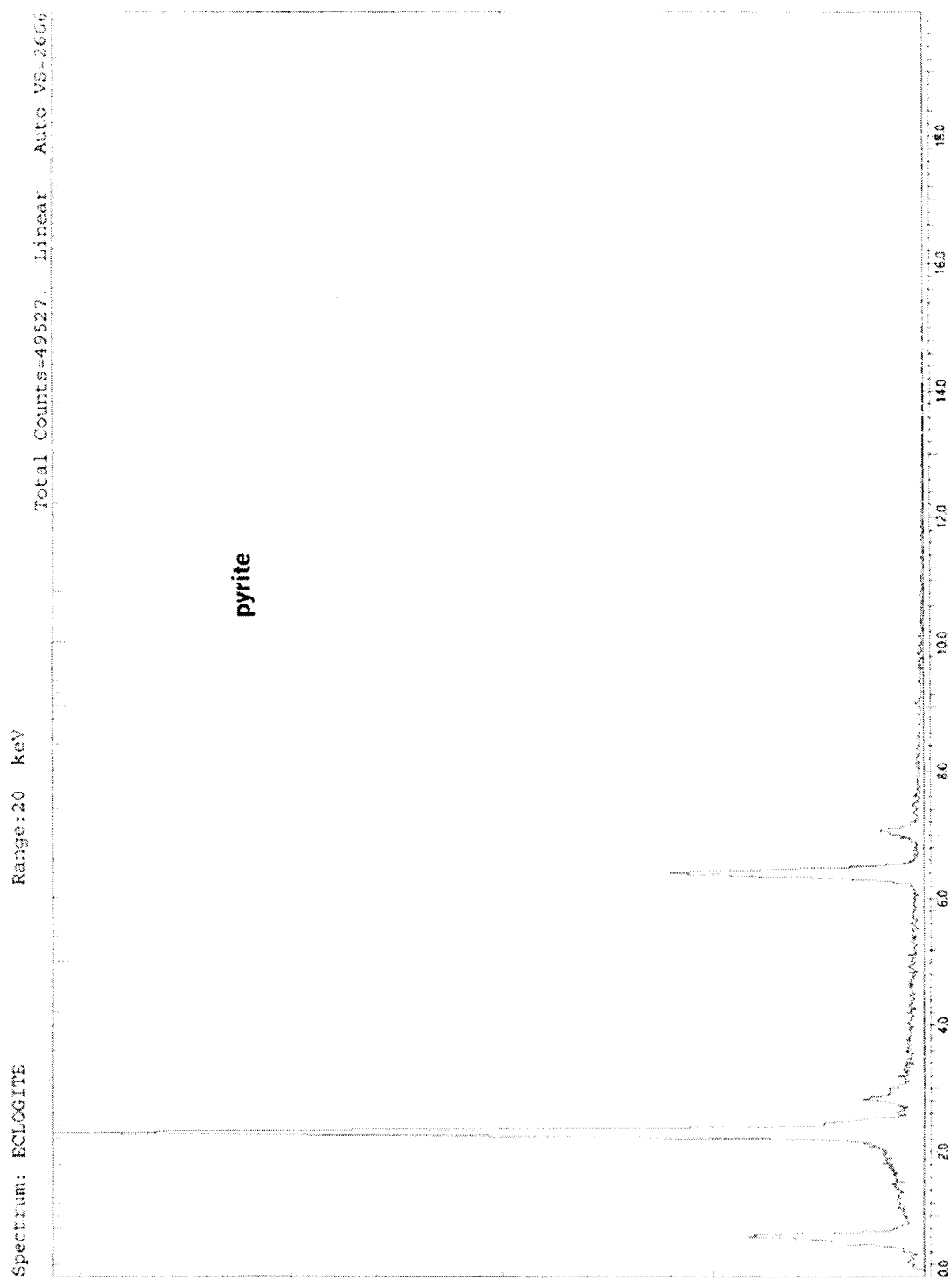


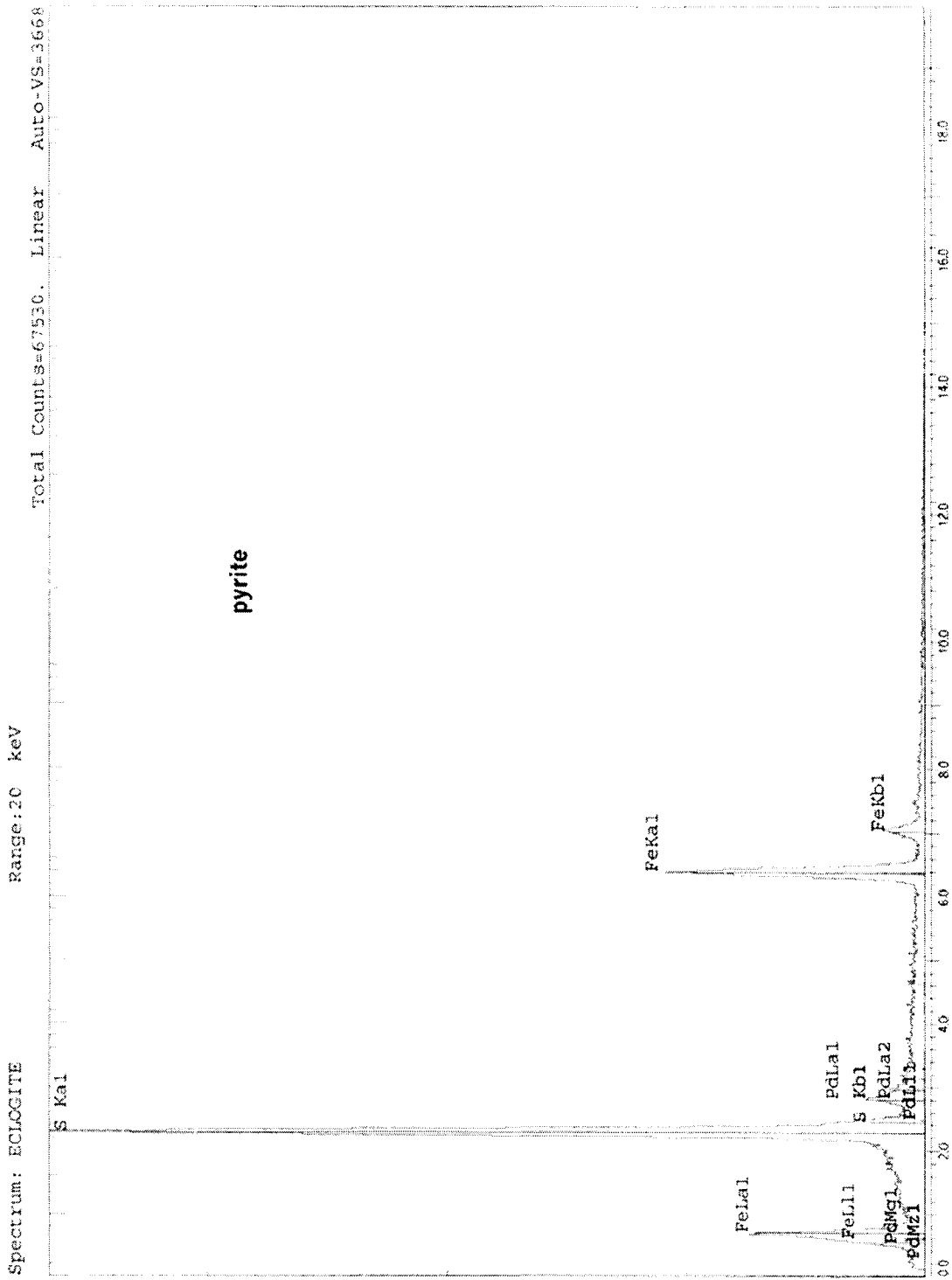


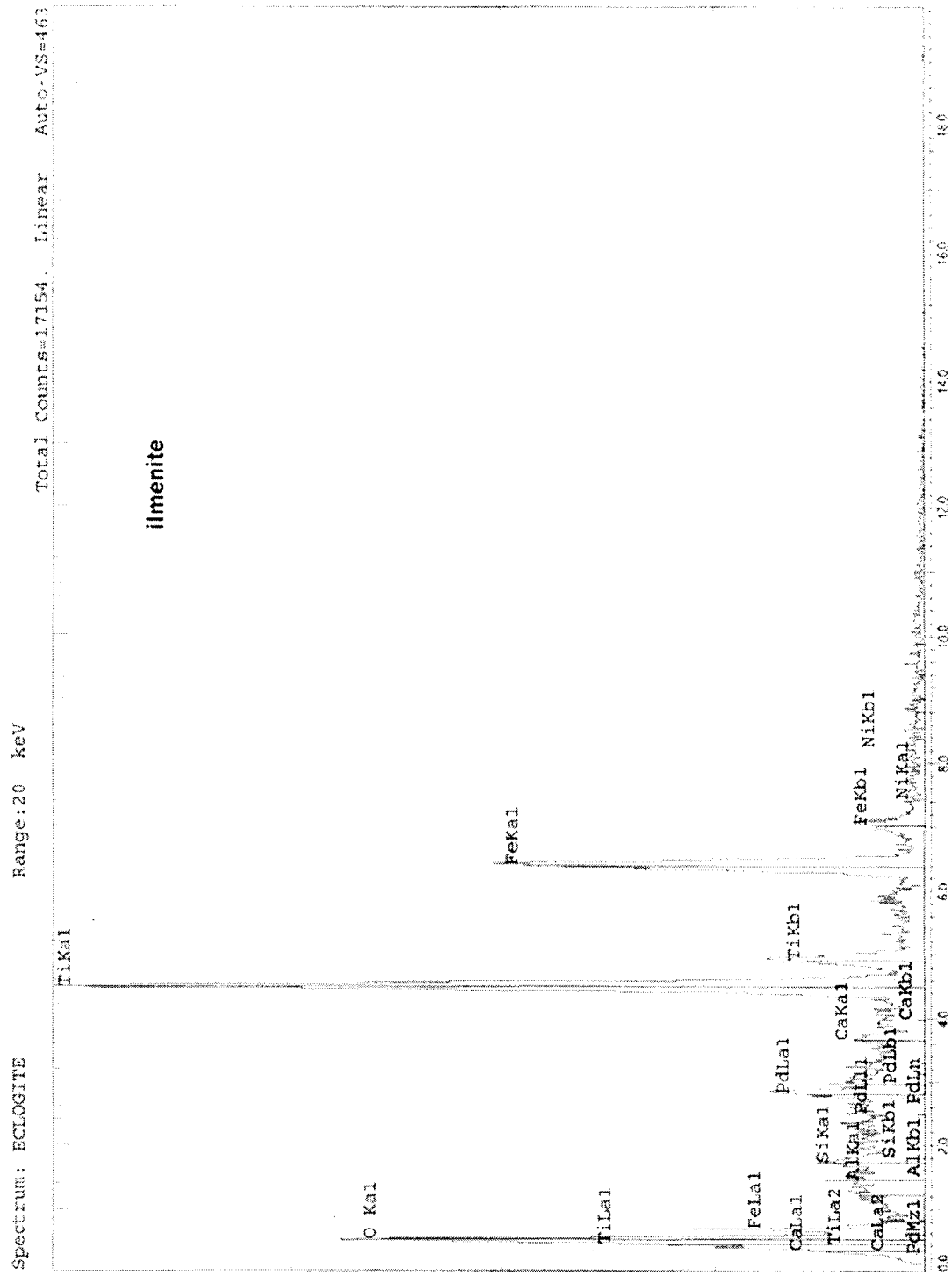












Mar 07 20:34 2006 /tmp/x\_text.pri Page 1

Asynchronous Mode.

\*\*\*\*\*  
 UNK No. = 1 ./rick/cl-storm dated Tue Mar 7 20:14:37 2006  
 14 Elements WDS only X= 75.624 Y= 46.186 Z= 11.338  
 Acc. Voltage = 15.0 (kV) Probe Dia. = 5 Scan On Mag= 5000  
 Probe Current = 3.024E-08 (A)  
 \*\*\*\*\*

Channel	Element	Acm	Peak	Peak cnt sec	BG L cnt sec	BG U cnt sec
2	LIFH Cu T	1	106.350	8818.6 ( 30.0)	4735.5 ( 15.0)	4233.2 ( 15.0)
1	TAP Au T	1	63.656	304719.0 ( 30.0)	18962.9 ( 15.0)	4010.1 ( 15.0)
3	PETJ Ag T	1	133.125	21075.8 ( 30.0)	550.0 ( 15.0)	514.0 ( 15.0)
2	LIFH Fe T	1	133.779	53869.6 ( 30.0)	1759.3 ( 10.0)	1189.1 ( 10.0)
1	TAP Se T	1	97.733	2476.2 ( 30.0)	1613.2 ( 15.0)	2559.4 ( 15.0)
3	LIF Zn T	1	99.834	2864.3 ( 30.0)	1662.2 ( 15.0)	1290.1 ( 15.0)
1	TAP Si T	1	77.537	6762.5 ( 30.0)	1908.4 ( 10.0)	3835.5 ( 10.0)
3	PETJ Sb T	1	110.238	6231.4 (100.0)	3219.2 ( 50.0)	3107.2 ( 50.0)
1	TAP As T	1	105.147	32600.4 ( 30.0)	1155.1 ( 15.0)	773.0 ( 15.0)
3	LIF Hg T	1	86.310	3659.4 ( 30.0)	1979.3 ( 15.0)	1746.2 ( 15.0)
3	PETJ S T	1	172.151	16740.3 ( 30.0)	197.0 ( 10.0)	146.0 ( 10.0)
3	LIF Cr T	1	159.347	470.0 ( 30.0)	172.0 ( 10.0)	159.0 ( 10.0)
3	PETJ Ca T	1	107.686	4407.6 ( 30.0)	813.1 ( 10.0)	616.0 ( 10.0)
3	PETJ Te T	1	105.437	2039.1 ( 30.0)	1232.1 ( 15.0)	914.1 ( 15.0)

Measurement over  
 Correction starts

## Standard Data

Element	Standard name	Wt. (%)	ZAF Fac.	Z	A	F	
1	Ag	99.9900	1.5455	1.7832	0.8667	1.0000	
2	Cu	MAC-Chalcopyr	34.4400	0.0876	0.0900	0.9734	1.0000
3	Zn	MAC-ZnS	67.1000	0.0633	0.0640	0.9904	1.0000
4	Sb	CM2-InSb	51.4600	1.0594	1.1761	0.9008	1.0000
5	Hg	CM2-HgS	86.2200	0.0153	0.0155	0.9899	1.0000
6	Au	CM1-Au	99.9000	3.3936	4.5502	0.7458	1.0000
7	Se	CM1-Se	99.9900	5.7742	8.4543	0.6830	1.0000
8	S	MAC-Pbs	13.4000	2.7570	3.5246	0.7822	1.0000
9	Fe	SMTH-Chromite	10.1362	0.2006	0.2118	0.9471	1.0000
10	Cr	MAC-Cr2O3	68.2158	0.3636	0.3706	0.9811	1.0000
11	Si	SMTH-Pyrope	19.3811	2.8775	4.4341	0.6489	1.0002
12	Ca	SMTH-Kaersut	7.4471	0.8781	0.9487	0.9204	1.0057
13	Te	CM2-ZnTe	66.1200	0.9179	1.0249	0.8947	1.0010
14	As	MAC-GaAs	51.8000	3.4462	9.3860	0.3672	1.0000

## Standard Intensity of WDS

Element	Curr. (A)	Net (cps)	Bg- (cps)	Bg+ (cps)	S.D. (%)	Date
1	2.948E-08	10161.3	58.3	37.5	0.18	Feb 21 12:09 2006
2	2.964E-08	5726.0	138.4	112.8	0.25	Feb 21 11:25 2006
3	2.958E-08	3046.3	44.7	33.7	0.34	Feb 21 11:36 2006
4	2.960E-08	5964.9	325.4	150.6	0.13	Feb 21 11:30 2006
5	2.943E-08	690.5	132.3	118.4	0.82	Feb 21 12:17 2006
6	2.950E-08	13689.9	1764.8	326.6	0.18	Feb 21 11:57 2006
7	2.967E-08	22718.4	127.4	83.1	0.12	Feb 21 11:02 2006
8	2.951E-08	2761.9	35.0	15.6	0.35	Feb 21 12:03 2006
9	2.799E-08	1818.6	47.0	30.9	0.44	Mar 2 08:51 2006
10	2.942E-08	3003.7	8.0	7.4	0.33	Feb 21 12:20 2006

Mar 07 20:34 2006 /tmp/x\_text.pri Page 2

11 Si	2.800E-08	10389.8	102.1	41.0	0.18	Mar 2 08:56 2006
12 Ca	2.924E-08	2043.4	24.6	40.2	0.41	Feb 7 19:28 2006
13 Te	2.949E-08	7507.8	77.2	68.3	0.21	Feb 21 12:06 2006
14 As	2.965E-08	5640.7	54.4	47.5	0.25	Feb 21 11:17 2006

Unknown Specimen No. 1

Group : rick Sample : cl-storm  
 UNK No. : 1 Comment :  
 Stage : X= 75.6240 Y= 46.1860 Z= 11.3375  
 Acc. Voltage : 15.0 (kV) Probe Dia. : 5 Scan : On Mag : 5000  
 Dated on Mar 7 20:29 2006  
 WDS only No. of accumulation : 1

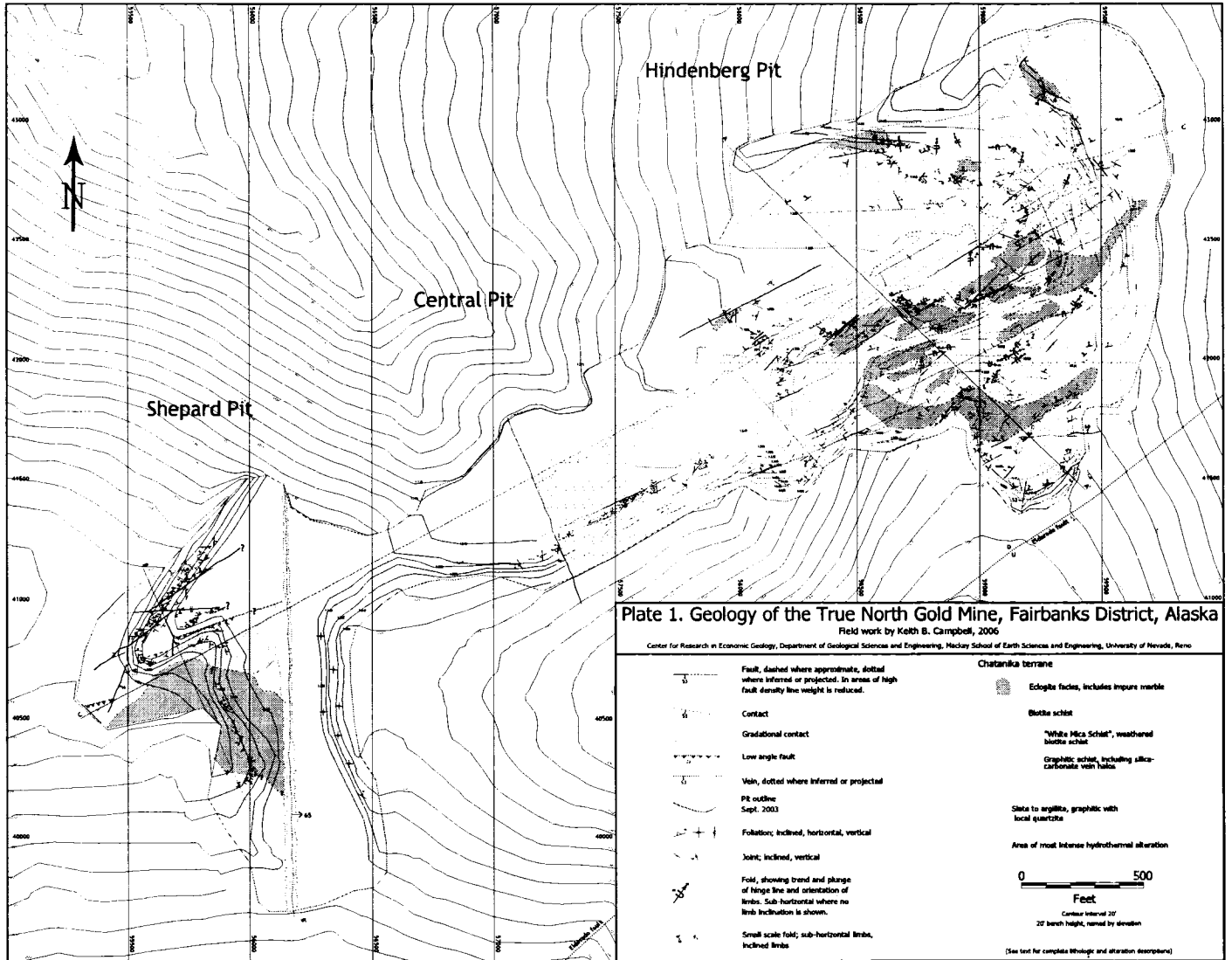
Curr. (A) : 3.024E-08

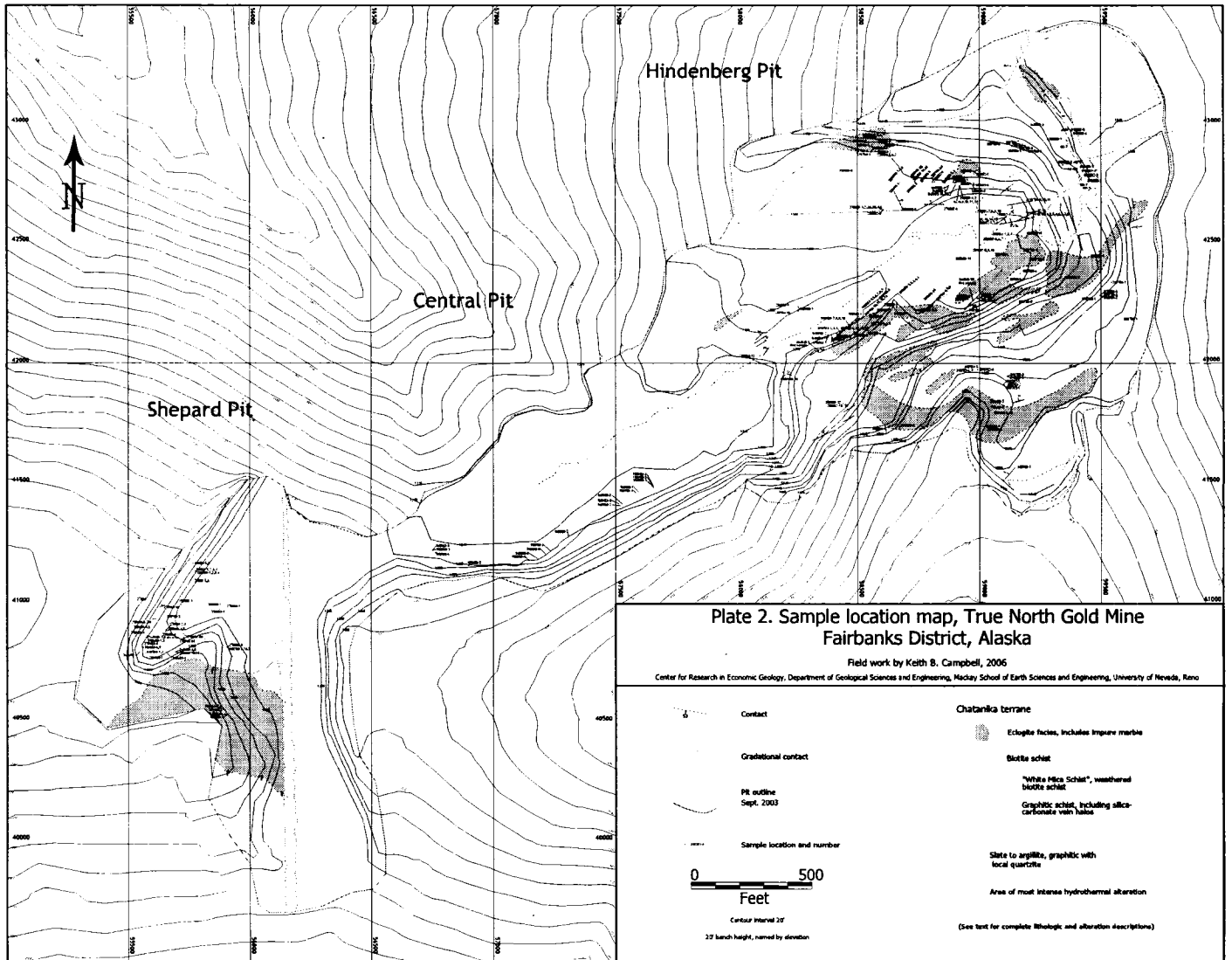
Element	Peak (nm)	Net (cps)	Bg- (cps)	Bg+ (cps)	S.D. (%)	D.L. (ppm)
1 Ag	133.125	667.1	36.7	34.3	0.74	148
2 Cu	106.350	-5.0	315.7	282.2	100.00 ?	263
3 Zn	99.834	-3.6	110.8	86.0	100.00 ?	554
4 Sb	110.238	-1.0	64.4	62.1	100.00 ?	95
5 Hg	86.310	-4.1	132.0	116.4	100.00 ?	3524
6 Au	63.656	9123.1	1264.2	267.3	0.22	591
7 Se	97.733	-59.4	107.5	170.6	100.00 ?	133
8 S	172.151	541.0	19.7	14.6	0.82	62
9 Fe	133.779	1645.6	175.9	118.9	0.50	200
10 Cr	159.347	-0.9	17.2	15.9	100.00 ?	284
11 Si	77.537	-61.8	190.8	383.5	100.00 ?	93
12 Ca	107.686	75.5	81.3	61.6	3.86	94
13 Te	105.437	-3.6	82.1	60.9	100.00 ?	188
14 As	105.147	1022.4	77.0	51.5	0.61	186

ZAF Metal

Element	Wt. (%)	Atom (%)	K (%)	K-raw (%)	ZAF	Z	A	F
Ag	7.716	9.4281	6.399	6.400	1.2058	0.9305	1.2962	0.9997
Cu	0.000	0.0000	0.000	0.000	0.0000	0.0000	0.0000	0.0000 ?
Zn	0.000	0.0000	0.000	0.000	0.0000	0.0000	0.0000	0.0000 ?
Sb	0.000	0.0000	0.000	0.000	0.0000	0.0000	0.0000	0.0000 ?
Hg	0.000	0.0000	0.000	0.000	0.0000	0.0000	0.0000	0.0000 ?
Au	71.915	48.1236	64.946	65.011	1.1073	1.0716	1.0333	1.0000
Se	0.000	0.0000	0.000	0.000	0.0000	0.0000	0.0000	0.0000 ?
S	3.638	14.9548	2.561	19.114	1.4202	1.0103	1.4067	0.9993
Fe	6.481	15.2943	8.490	83.755	0.7634	0.7533	1.0186	0.9949
Cr	0.000	0.0000	0.000	0.000	0.0000	0.0000	0.0000	0.0000 ?
Si	0.000	0.0000	0.000	0.000	0.0000	0.0000	0.0000	0.0000 ?
Ca	0.255	0.8381	0.266	3.571	0.9583	0.7411	1.2864	1.0052
Te	0.000	0.0000	0.000	0.000	0.0000	0.0000	0.0000	0.0000 ?
As	6.458	11.3610	9.206	17.772	0.7015	0.8937	0.7849	1.0000
Total	96.463	100.0000	91.867	195.623	Iteration = 5			

UNK Measurement over





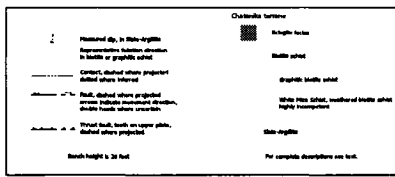
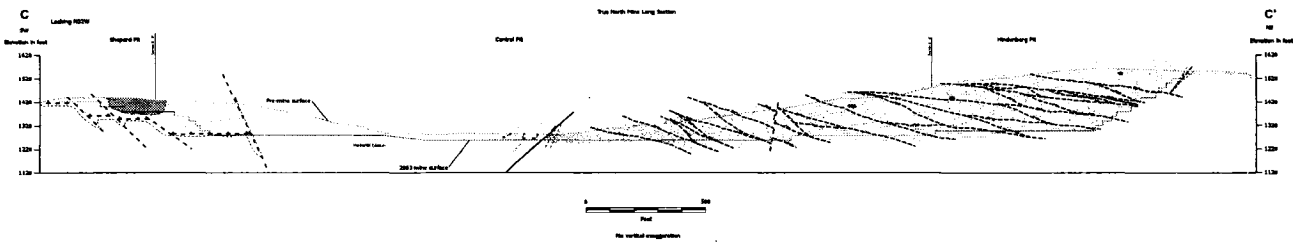
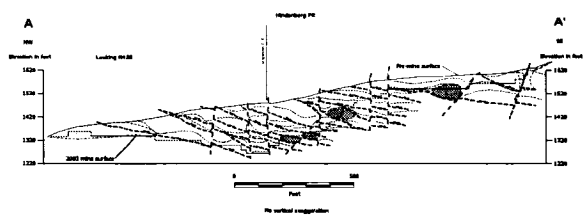
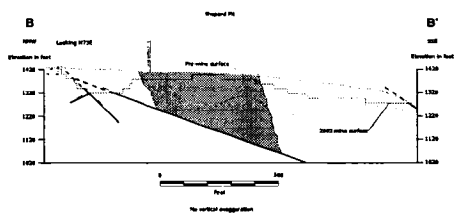


Plate 3. True North interpretive sections

Sketches and Interpretation by Mark S. Conrath, 2006  
 Center for Research in Terrestrial Ecology  
 Department of Geological Sciences and Engineering  
 Husky School of Earth, Science and Engineering  
 University of Hawaii, Hilo